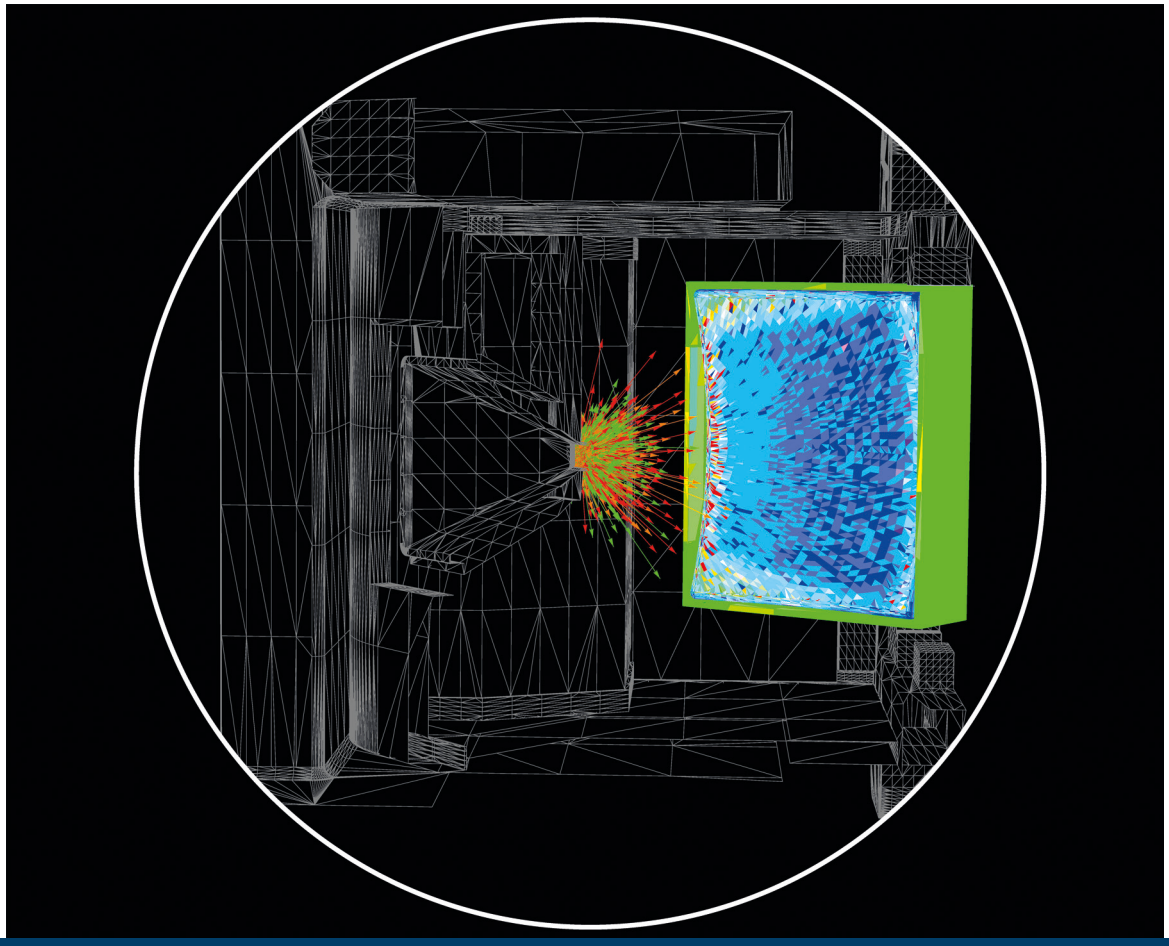

Assessment of erosion in recessed areas of fusion devices using multi-scale computer simulations

Sebastian Rode

Energie & Umwelt / Energy & Environment
Band / Volume 683
ISBN 978-3-95806-867-4

Mitglied der Helmholtz-Gemeinschaft

JÜLICH
Forschungszentrum

Schriften des Forschungszentrums Jülich
Reihe Energie & Umwelt / Energy & Environment Band / Volume 683

Forschungszentrum Jülich GmbH
Institute of Fusion Energy and Nuclear Waste Management (IFN)
Plasma Physics (IFN-1)

Assessment of erosion in recessed areas of fusion devices using multi-scale computer simulations

Sebastian Rode

Schriften des Forschungszentrums Jülich
Reihe Energie & Umwelt / Energy & Environment Band / Volume 683

ISSN 1866-1793 ISBN 978-3-95806-867-4

Bibliografische Information der Deutschen Nationalbibliothek.
Die Deutsche Nationalbibliothek verzeichnet diese Publikation in der
Deutschen Nationalbibliografie; detaillierte Bibliografische Daten
sind im Internet über http://dnb.d-nb.de abrufbar.

Herausgeber und Vertrieb:	Forschungszentrum Jülich GmbH Zentralbibliothek, Verlag 52425 Jülich Tel.: +49 2461 61-5368 Fax: +49 2461 61-6103 zb-publikation@fz-juelich.de www.fz-juelich.de/zb
Umschlaggestaltung:	Grafische Medien, Forschungszentrum Jülich GmbH
Druck:	Grafische Medien, Forschungszentrum Jülich GmbH
Copyright:	Forschungszentrum Jülich 2025

Schriften des Forschungszentrums Jülich
Reihe Energie & Umwelt / Energy & Environment, Band / Volume 683

D 61 (Diss. Düsseldorf, Univ., 2024)

ISSN 1866-1793
ISBN 978-3-95806-867-4

Vollständig frei verfügbar über das Publikationsportal des Forschungszentrums Jülich (JuSER)
unter www.fz-juelich.de/zb/openaccess.

This is an Open Access publication distributed under the terms of the Creative Commons Attribution License 4.0,
which permits unrestricted use, distribution, and reproduction in any medium, provided the original work is properly cited.

Abstract

The development of fusion reactors is a promising research field that leads to a green energy source with virtually infinite fuel. By confining a hot plasma in a magnetic field, the massive energy stored in hydrogen isotopes' nuclei can be released and made available for human use. The current fusion reactor experiments successfully manage to heat a plasma to the extremely high temperatures needed for nuclear fusion, but the machines still serve as stepping stones to a fusion power plant with electricity generation. The confinement of a fusion plasma requires technologies with high precision, power input and durability, which currently prevent economic efficiency that a power plant must provide. Two of the most important devices in this field are the Joint European Torus (JET) and the International Thermonuclear Experimental Reactor (ITER), currently under construction.

In an experimental fusion reactor, a large range of diagnostics is needed on the one hand to provide input to active control methods of the plasma, but on the other hand to learn more about the physics of a magnetically confined fusion plasma. Optical diagnostics with mirror systems adopt a key role in the operation of fusion experiments and are placed in the outer regions of the fusion device. The location of the optical diagnostics is recessed behind the main wall so that incoming heat and particle fluxes from the main plasma are minimized and damage to the diagnostic systems is prevented as good as possible. However, erosion of the mirror and deposition of impurity particles are still likely and could negatively impact the performance of the diagnostics and thus lead to critical issues for the tokamak operation. Additionally, in ITER the diagnostics likely cannot be manually accessed once fusion power operation starts due to activation of the materials caused by the high-energy fusion neutron flux, so long-term operability under the expected plasma conditions needs to be secured. Predictions of the life-time of the optical diagnostics with validated tools are needed.

The ERO2.0 impurity transport and plasma-wall interaction code can provide such numeric simulations of materials exposed to plasmas in fusion devices. However, in the recessed areas of the diagnostic mirrors, the Monte-Carlo code is approaching its limits due to the limited amount of statistics: only a minuscule fraction of sim-

ulated test particles reaches the areas relevant for diagnostics. To correctly resolve these areas, an unreasonably large amount of test particles and thus computation time would be required if ERO2.0 is used in its standard setup.
In this thesis, the erosion and deposition on diagnostic first mirrors in JET and ITER have been numerically analysed, by the development and application of a workflow for ERO2.0 simulations of recessed areas in fusion devices with adequate resolution. Firstly, code updates focussing on runtime optimizations of the recently developed ERO2.0 Guiding-Centre Approximation (GCA) tracing methods are implemented, bringing large improvements in code efficiency so that a larger amount of particles can be simulated in a reasonable computation time. As this is not sufficient to solve the statistics problems in the Monte-Carlo code, a three-stage simulation approach is introduced, in which the simulation volume is successively focussed more and more to the volume around the mirrors.
This multi-stage workflow is first applied to JET, where an ITER-like mirror test assembly (ILMTA) was exposed in an experimental campaign operating with beryllium (Be) first wall and tungsten (W) divertor PFCs. The results of the simulation are compared to the experimental findings. The deposition of impurities on three mirrors located in the ILMTA matches to a satisfactory degree between numeric simulation and experimental measurement, therefore the validity of the approach is confirmed.
Afterwards, the workflow is applied to ITER, where mirror systems are planned in the diagnostic first wall (DFW) in the Equatorial and Upper Port Plug (EPP/UPP). This predictive modelling is used to assess the impinging fluxes onto the molybdenum (Mo) First Mirrors (FMs) located in both ports, assuming a Be first wall, a W divertor and a steel DFW, for which pure iron (Fe) is used as a proxy in the modelling. The full workflow is evaluated in three plasma scenarios over the complete expected ITER experimental operation time, two H-mode scenarios and one L-mode scenario assuming constant plasma conditions in divertor configuration over the full simulation time, respectively. The main finding is that even after more than 2000 h of operation in a high-power H-mode plasma case, the centre of both FMs accumulates less than 0.5 nm impurity materials, while erosion of the Mo mirrors is not expected to exceed 2.5 nm in all scenarios. A strong geometric influence of the cone-shaped aperture located in the front of the mirrors is found, leading to increased impurity deposition on the edges of the FMs. Multiple additional case studies with different material assumptions are performed in this work to assess the credibility of the results and give further outlook of the impact of different wall material combinations on the first mirror erosion and deposition.

Kurzfassung

Die Entwicklung von Fusionsreaktoren zur Stromerzeugung ist ein vielversprechendes Forschungsgebiet, das letztendlich zu einer CO_2-freien Energiequelle mit praktisch unerschöpflichem Brennstoffvorrat führt. Durch den Einschluss eines heißen Plasmas in einem Magnetfeld mit hoher Stärke kann die enorme Energie, die im Kern von Wasserstoffisotopen gespeichert ist, kontrolliert freigesetzt und für den menschlichen Gebrauch verfügbar gemacht werden. In den aktuellen Fusionsexperimenten gelingt es, ein Plasma auf die erforderlichen hohen Temperaturen von mehr als 100 Millionen Kelvin zu erhitzen, die für die Kernfusion erforderlich sind. Die gegenwärtigen Maschinen sind jedoch als physikalische und technische Experimente anzusehen und stellen einen Zwischenschritt auf dem Weg zu einem Fusionskraftwerk zur Stromerzeugung dar. Die Einschließung eines Fusionsplasmas stellt technologische Herausforderungen im Bereich der Herstellung der Komponenten, und erfordert Technologien mit hoher Leistung und einer langen Lebensdauer, die derzeit die wirtschaftliche Effizienz, die ein Kraftwerk bieten muss, verhindern. Zwei der wichtigsten Geräte in diesem Bereich sind der *Joint European Torus* (JET), der den Weltrekord bei der freigesetzten Fusionsenergie hält, und der *International Thermonuclear Experimental Reactor* (ITER), welcher sich derzeit im Bau befindet. In einem experimentellen Fusionsreaktor ist eine Vielzahl von Diagnoseverfahren erforderlich, einerseits, um die aktiven Kontrollmethoden des Plasmas sicherzustellen, und andererseits, um mehr über die Physik eines magnetisch eingeschlossenen Fusionsplasmas zu erfahren.

Optische Diagnostiken mit Spiegelsystemen spielen eine Schlüsselrolle beim Betrieb dieser Fusionsexperimente, indem sie Möglichkeiten zur passiven und aktiven Spektroskopie oder tomografischen Rekonstruktion des Plasmas bieten. Elektromagnetische Wellen und insbesondere Licht werden durch ein Labyrinth von Spiegeln geleitet, welches in den äußeren Bereich der Fusionsanlage platziert ist, um die Detektoren vor Neutronen und Magnetfeldern abzuschirmen. Die optischen Diagnostiken sind in Bezug auf das eingeschlossene Plasma zurückgesetzt in der Hauptwand eingelassen, sodass auch Wärme- und Teilchenflüsse aus dem Hauptplasma minimiert werden und Schäden an den Diagnosesystemen, beste-

hend insbesondere aus der Ummantelung und den Spiegeln, so gut wie möglich verhindert werden. Dennoch ist eine Erosion der Spiegel und Deposition von Verunreinigungspartikeln im Laufe der Betriebszeit wahrscheinlich, was sich negativ auf die Einsatzfähigkeit der Diagnostik auswirken kann und zu Problemen im Tokamakbetrieb und in der Plasmakontrolle führen könnte. Darüber hinaus ist es wahrscheinlich, dass bei ITER nach Beginn der Plasmaoperation mit Deuterium-Tritium aufgrund der Aktivierung der Strukturmaterialien durch den hochenergetischen Fusionsneutronenfluss nur ein eingeschränkter oder gar kein manueller Zugriff auf die Diagnostikkomponenten mehr möglich ist. Es verbleibt nur ein kostspieliger Austausch. Deswegen muss die langfristige Funktionsfähigkeit unter den zu erwartenden Plasmabedingungen sichergestellt werden. Verlässliche Vorhersagen zur Lebensdauer und Eigenschaften der optischen Diagnostiken mit validierten Simulationsprogrammen sind erforderlich.
Der Monte-Carlo-Code ERO2.0 für den Transport von Verunreinigungen und die Plasma-Wand-Wechselwirkung kann solche numerischen Simulationen von Komponenten der ersten Wand, die dem Fusionsplasma ausgesetzt sind, bereitstellen. In den plasmafernen Bereichen, wo die Diagnostikspiegel sich befinden, stößt der Monte-Carlo-Code jedoch aufgrund der begrenzten Statistik an die Grenzen der Einsetzbarkeit: Nur ein verschwindend geringer Teil der simulierten Testteilchen erreicht die für die Diagnostiken relevanten Bereiche. Um diese Bereiche mathematisch korrekt zu beschreiben, wäre eine unverhältnismäßig große Menge an Testteilchen und damit Rechenzeit erforderlich, wenn der ERO2.0-Code in seiner Standardkonfiguration mit Simulation der voll aufgelösten Teilchentrajektorie gemäß der Gyration der geladenen Teilchen verwendet wird.
In dieser Arbeit wird die Erosion und Ablagerung auf diagnostischen ersten Spiegeln in JET und ITER numerisch analysiert, indem ein neuer Arbeitsablauf für ERO2.0-Simulationen von plasmafernen Bereichen in Fusionsanlagen mit angemessener statistischer Auflösung entwickelt und angewendet wird. Zunächst wurden Code-Updates mit Schwerpunkt auf Laufzeitoptimierungen der kürzlich entwickelten GCA-Tracing-Methoden (Führungszentrumnäherung oder *Guiding-Centre-Approximation*) in ERO2.0 implementiert, die die Code-Effizienz des bereits vollständig parallelisierten Codes erheblich verbessern, sodass eine größere Anzahl von Teilchen in einer angemessenen Rechenzeit simuliert werden kann. Da diese Optimierung nicht ausreicht, um die statistischen Probleme des Monte-Carlo-Codes in den plasmafernen Regionen der Wand zu lösen, wurde ein dreistufiger Simulationsansatz eingeführt, bei dem das Simulationsvolumen sukzessive in mehreren Schritten immer stärker auf das Volumen um die Spiegel herum fokussiert wird. Dieser mehrstufige Arbeitsablauf wird zunächst auf den Tokamak JET interpretativ

angewendet, wo ein Testspiegelsystem (*ITER-Like Mirror Test Assembly*, ILMTA) in einer experimentellen Kampagne mit Beryllium (Be)-Hauptwand und Wolfram (W)-Divertor eingesetzt wurde. Die Ergebnisse der Simulation aus dieser Arbeit werden mit den bereits vorhandenen experimentellen Erkenntnissen verglichen. Die Ablagerung von Verunreinigungen auf drei Spiegeln bestehend aus Molybdän in dem Inconel-Gehäuse des ILMTA stimmt in zufriedenstellendem Maße zwischen der numerischen Simulation und der experimentellen Messung überein, sodass die Gültigkeit des Ansatzes bestätigt wird. Anschließend wird dieser neuartige Arbeitsablauf auf ITER angewendet, wo Spiegelsysteme in der sogenannten diagnostischen Hauptwand (*Diagnostic First Wall*, DFW) im äquatorialen und oberen Öffnungszugang (*Equatorial Port Plug*, EPP/ *Upper Port Plug*, UPP) geplant sind. Diese vorhersagende Modellierung wird verwendet, um die auf die Molybdän-Spiegel auftreffenden Flüsse zu bewerten, wobei eine Be-Hauptwand, ein W-Divertor und eine DFW aus reinem Eisen (Fe), stellvertretend für den Spezialstahl von ITER, angenommen werden. Der vollständige Arbeitsablauf wird in drei Plasmaszenarien repräsentativ für die Betriebsmodi in Divertorkonfiguration von ITER über die gesamte erwartete Operationsdauer von ITER evaluiert: zwei Szenarien in H-Mode und eine in L-Mode unter der Annahme konstanter Plasmabedingungen über die gesamte Simulationszeit. Das Hauptergebnis ist, dass selbst nach mehr als 2000 Betriebsstunden in einem Hochleistungs-H-Mode-Plasma das Zentrum beider Erstspiegel weniger als 0.5 nm Verunreinigungsmaterialien auf der Oberfläche akkumuliert, während die Erosion der ersten Spiegel aus Molybdän in allen Szenarien voraussichtlich 2.5 nm nicht überschreiten wird. Eine vollständige Deposition und damit ein Verlust der optischen Eigenschaften ist nicht zu erwarten. Weiterführend wurde ein starker geometrischer Einfluss der kegelförmigen Öffnung der DFW auf die Deposition der Spiegel festgestellt, welcher zu einer erhöhten Ablagerung von Verunreinigungen an den Rändern der ersten Spiegel führt. Darüber hinaus werden in dieser Arbeit mehrere zusätzliche Fallstudien mit unterschiedlichen Annahmen über die Materialkomposition der ersten Wand (Be, W, B) durchgeführt, um den Vertrauensbereich der Simulationsergebnisse zu bewerten, und einen weiteren Ausblick auf die Auswirkungen verschiedener möglicher Wandmaterialkombinationen in ITER auf die Erosion und Ablagerung auf den ersten Spiegeln zu geben.

Contents

Chapter 1

Introduction

1.1 Nuclear Fusion

In a nuclear fusion reaction, the nuclei of two atoms fuse together to form one heavier nucleus. In this process, the binding energy of nucleons can be released. In the universe, fusion reactions can be observed in stars, where typically hydrogen nuclei fuse to helium. Since the 1950s, mankind has been working on making fusion reactions achievable on earth to provide a new source of energy production with nearly infinite fuel. In the DT-reaction

$$\mathrm{D} + \mathrm{T} \rightarrow {}^4\mathrm{He} + n^0 + 17.6\,\mathrm{MeV}$$

the two hydrogen isotopes deuterium (D) and tritium (T) fuse to form a stable helium (He) nucleus and an unbound neutron n^0, while the decrease in mass during the reaction is released as kinetic energy according to the laws of the mass defect. The DT-fusion reaction is the most achievable reaction for energy generation on earth, as it has a comparably high reaction cross-section with an optimum temperature range around 10 keV ($\sim 10^8$ K)[1]. At this high temperature, the hot gas is in a plasma state, where the largest fraction of the particles is fully ionized. The uncharged neutron is assumed not to interact with the fusion plasma, but the fusion product He, which carries around 20 % of the released kinetic energy, can heat the plasma further. The heating to sustain the fusion temperature can theoretically be completely provided by the fusion product. This point of self-sustained fusion plasma heating is called ignition, and the condition to reach this state is estimated

[1]The unit eV (electron volts) is commonly used in plasma physics as a unit of temperature, although by strict definition it declares an energy. The proportionality constant is the Boltzmann-constant k_B, thus 1 eV is equivalent to a temperature of around $1/k_B \simeq 11\,500$ K.

by the fusion triple product [128, p. 11]

$$n \cdot T \cdot \tau_E > 3 \times 10^{21}\,\mathrm{m}^{-3}\,\mathrm{keV\,s} \tag{1.1}$$

with the plasma density n, plasma temperature T (given in keV) and energy-confinement time τ_E, which represents a timescale on which the plasma loses its energy, e.g. by radiation losses.
The extremely high temperature needed for ignition however is a critical issue, because no material known to mankind can withstand the corresponding heat – confinement is needed. Two basic approaches to solve this problem are pursued: on the one hand Inertial Confinement Fusion (ICF), where a frozen sphere containing the hydrogen isotopes D and T is symmetrically compressed and heated via powerful lasers in a hohlraum [1]. On the other hand, in Magnetic Confinement Fusion (MCF) an ionized DT-plasma is confined via strong magnetic fields and heated by an induced plasma current, resonant electromagnetic waves or neutral beam injection (NBI).

1.2 Magnetically Confined Fusion and Tokamaks

Magnetic fields can confine charged particles by the physical law of the Lorentz force. A charged particle's momentum in the plane perpendicular to the local magnetic field is continuously rotated by the Lorentz force, while the momentum parallel to the magnetic field line is unaffected. This leads to a helical trajectory called gyration. Due to the unperturbed parallel transport, confinement is not achieved in a linear magnetic field. Bent magnetic field lines are necessary, and the mathematical so-called "Hairy-Ball Theorem" leaves a toroidal shape (see Figure 1.1) as the only option to confine a plasma volume in a shape enclosed by a continuous magnetic field. Despite that, inherent charge-separation of the particle species inside the spatially inhomogeneous toroidal magnetic field gives rise to electric fields, which result in a drift radially outward for all charged particles. This intrinsic effect makes an exclusively toroidal magnetic field still an unfitting option for a magnetic confinement device. An additional poloidal magnetic field is needed to offset this effect and create a potentially stable plasma in the resulting helical total magnetic field. Two approaches to create this magnetic structure are commonly used, defining the two main classes of toroidal magnetic confinement devices: stellarators and tokamaks (see Figure 1.2).
In a stellarator, the entire helical magnetic field can be generated by its external magnetic field coils. This requires either two sets of coils, toroidal and helical

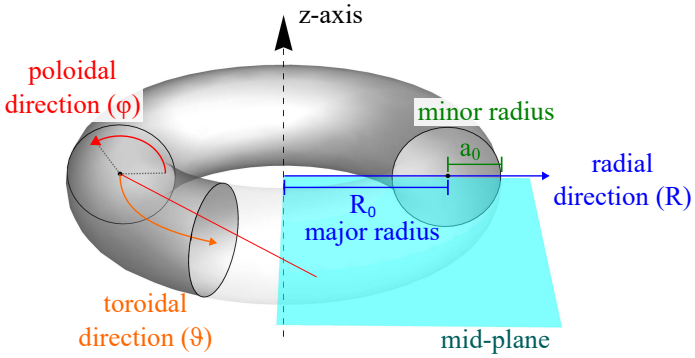

Figure 1.1: Overview of toroidal geometry, defined by the major radius R_0 and the minor radius a_0.

magnetic field coils as in a heliotron, or a complex 3D structure of the field coils as in the HELIAS advanced stellarator concept. The complex 3D shape of the coils is the reason why advanced stellarator designs have only been made possible once sufficiently powerful computers enabled the 3D optimization of the problem. Examples of operational devices of the stellarator class are the advanced stellarator Wendelstein 7-X (W7-X; Greifswald, Germany) [63, 85] and the heliotron Large Helical Device (LHD; Toki, Japan) [64, 115]. Stellarators have an advantage of intrinsic steady-state operation as desired in a fusion reactor and are less prone to plasma instabilities caused by the plasma current. Disadvantages of the design are the significantly more complex engineering due to the necessary 3D magnetic field coils, which also makes remote handling capabilities inside the device significantly more complicated [3, 127]. Stellarators are however not the focus of this work. Nevertheless, the physics and applied simulation techniques can in principle be transferred from the devices studied in this work to stellarator fusion device concepts.

The second class of toroidal magnetic confinement devices are tokamaks. In a tokamak, the magnetic field line structure is initially only generated by planar toroidal field coils, which have a much simpler geometry than the shaped field coils in stellarators. In modern tokamaks, superconducting magnetic field coils are used to permit a permanent magnetic field. The essential poloidal magnetic field component is induced by a current in the plasma, which itself is induced owing to the transformer concept. This transformer-like type of current drive, however, requires a continuous change in magnetic field strength in the central solenoid (the inducing part of the transformer) due to Ampere's law. Because the magnetic field strength is limited by material and engineering constraints, tokamaks are

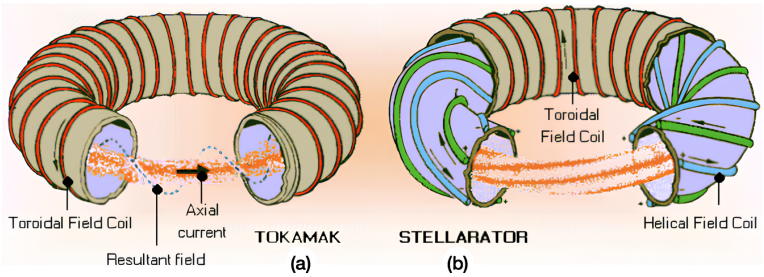

Figure 1.2: Simplified geometry in (a) tokamaks and (b) stellarators, shown with the resulting helical field that is necessary for confining a plasma. Magnetic field coils are shown in red and green. Image taken from http://www-fusion-magnetique.cea.fr/gb/fusion/principes/principes02.htm

inherently pulsed devices, in contrast to stellarators. Other methods of current drive are however also possible, which can extend the pulse duration in a tokamak – pulses with more than 300 s have recently been achieved [47] using superconducting magnetic field coils and non-inductive current drive mechanisms.
The confinement time in a fusion plasma has been experimentally found to scale with roughly the square of the major radius of a fusion device [126], and thus the fusion triple product (Equation 1.1) likewise scales with the major radius. Therefore, larger and larger devices are built as part of an iterative approach to a fusion power plant. However, impurity particles inside the plasma remain a critical aspect in the operation of fusion devices, since heavy impurities can cool down the core plasma by excessive radiation or by diluting the plasma to the point where DT-reactions are significantly less likely. A main source of impurity particles is the erosion of the plasma-facing components (PFCs). Excessive erosion limits the life-time of PFCs, causing material migration and degradation in the armour. Therefore, both tokamaks and stellarators need to be designed to minimize the impurity flux to the core plasma, and thus the erosion of PFCs.

1.3 JET and ITER

The road to a fusion power plant is long due to the extreme conditions present in such a device, requiring constant innovations in physics and enormous precision in engineering. Two of the most important devices in the field of MCF are the tokamaks JET and ITER, both of which are directly relevant to this work.
JET ("Joint European Torus", see Figure 1.3) is an experimental fusion device located in Culham, UK. The tokamak was built as a European device aiming at a power amplification factor $Q = 1$ [86], thus, the fusion power of the plasma

was intended to equal to the additional heating power injected. Operating for more than 40 years from 1983 to 2023, the world record of released fusion energy in a single plasma pulse has been achieved multiple times in this device [75], currently lying at 69.26 MJ during a five-second pulse[2]. The best amplification factor achieved in a JET DT-plasma discharge was $Q = 0.65$, holding the current record for MCF [118][3]. JET has a major radius of 2.96 m with an on-axis magnetic

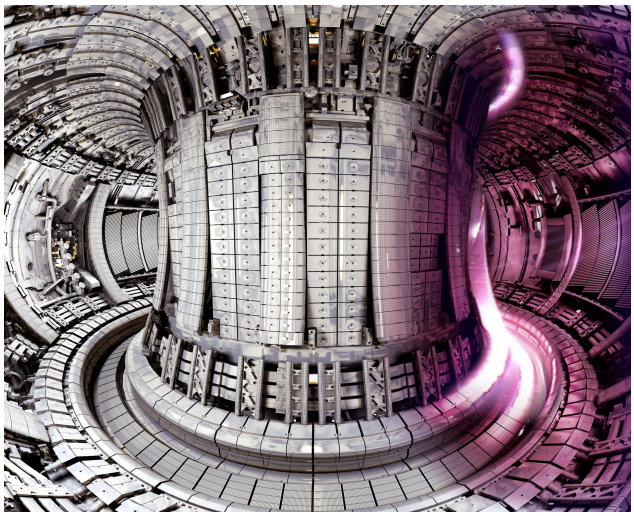

Figure 1.3: Inside view of the Joint European Torus (JET) tokamak with "ITER-like wall". This image is combined from a picture taken during operation (right side) and one taken outside of operation (left side). Image taken from https://euro-fusion.org/

field of 3.4 T and a plasma current of up to 5 MA [86]. A plasma volume of more than 90 m^3 is enclosed[4]. A total auxiliary heating power of up to 37 MW can be injected in a mix of neutral beam and ion cyclotron radiation heating [98]. The device is using conventional magnetic field coils and is inertially cooled, which limits the pulse duration. JET was originally equipped with graphite-based first wall components, but underwent a major change in wall material: starting from 2011, JET operated with a beryllium (Be)/tungsten (W) wall (labelled "ITER-like wall", JET-ILW) [87], which significantly reduced the primary erosion in the device [12] due to omission of chemical erosion of graphite. This was detected by the wide range of diagnostics available in JET, providing data of more than 100.000 performed plasma discharges. These data can be accessed for analysis and

[2]https://www.iter.org/newsline/-/3998

[3]For ICF, an amplification factor of $Q \simeq 2.4$ [68] was achieved in 2023 at the NIF facility, where 5.2 MJ fusion power was measured with an incident laser energy of 2.2 MJ. The electric energy used to generate the laser beams (~ 300 MJ) is not included in this number

[4]https://euro-fusion.org/devices/jet/

can be used to benchmark all types of plasma codes covering the plasma core to the wall of the plasma. The codes are then used to predict the behaviour in future devices.
ITER ("International Thermonuclear Experimental Reactor", Latin: "the way") is a tokamak currently under construction in Cadarache, France. ITER is built in an international endeavour jointly between the EU, the USA, Russia, Korea, Japan, China, and India. The start of research operations[5] is expected in 2034 and full magnetic power is scheduled for 2036. The device is significantly larger than JET, with a major radius of 6.2 m. ITER was for a long time planned to be built with a Be first wall and W divertor (as it was experimentally tested in the JET-ILW), but recently it was decided to realize ITER as a full-W device[5], partially due to the low erosion in W devices [42]. ITER will, in contrast to JET, include superconducting magnets operating at 5.3 T and plasma currents up to 15 MA [51], with the aim to reach a discharge length of around 400 s in high-power operation. In the significantly larger plasma volume of ITER (840 m^3, see Figure 1.4), around 500 MW fusion power is set to be generated from 50 MW heating power ($Q = 10$)[6]. Although roughly twice as large in radius in comparison to JET and four times as large in surface area, JET is still the closest fusion device worldwide to ITER and is the main facility used for extrapolation.

1.4 Optical Plasma Diagnostics

Current tokamaks are experimental devices and as such, they are equipped with a wide range of diagnostics to characterise the plasma, the plasma-wall interaction, and the state of the PFCs, thus, to deepen the overall understanding of the physical effects present. Moreover, diagnostics are also used a step further in complexity in active control systems to manipulate the state of the plasma [49, 78], e.g. by triggering additional heating if the desired plasma temperature has not been reached or if plasma instabilities are detected.
However, the conditions present in an experimental fusion reactor are extreme – the confinement of a plasma in a magnetic field is not perfect, so plasma-wall interactions are an important part of the considerations, when designing a tokamak, defining the PFCs, and planning the diagnostics to study or control the states of both. High heat loads and ion or neutral particle fluxes reaching PFCs put significant restraints on the possible materials used in such a device (see chapter 2 for an overview of plasma-wall interactions).

[5] ITER press conference from July 3rd 2024, https://www.iter.org/newsline/-/4056
[6] https://www.iter.org/mach

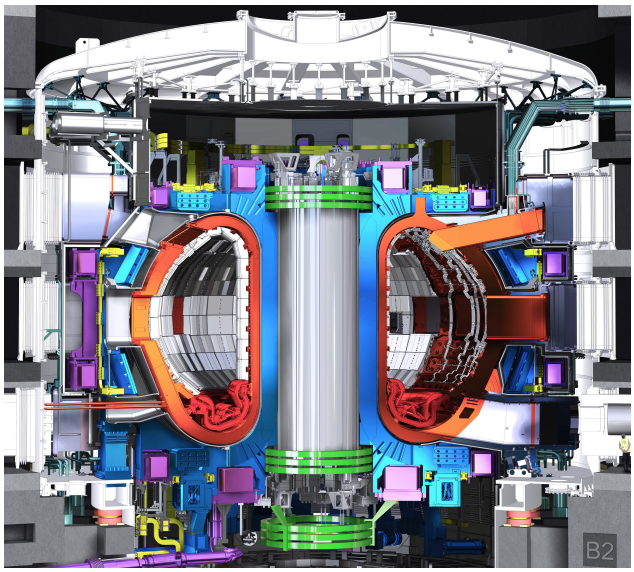

Figure 1.4: 3D illustration of the ITER device. Notable elements include the cryostat (white), toroidal field coils (orange), poloidal field coils (purple) and divertor (red). Image taken from https://www.iter.org/album/media/.

Optical diagnostics play a key role in the plasma diagnosis and control of a tokamak, since they can be generally positioned under less extreme conditions far from the plasma and recessed from PFCs. Mirrors relay the emission from the plasma to the optical diagnostics, such as in JET in the form of endoscopes, to study the impurity sources in the divertor [48]. Mirrors can also be used to guide laser light from diagnostics into the plasma in order to determine basic plasma parameters such as e.g. electron density and temperature via Thomson Scattering. Thus, the quality of the mirrors is a crucial factor in the performance of optical diagnostics and has to be preserved over a long operational time. Shutters can deliver some protection, but must function at high magnetic field, neutron and heat flux, which itself is a challenge.

One important class of optical diagnostic systems is the Wide Angle Viewing System (WAVS) operating in the visible and infrared (VisIR) part of the emission spectrum of the plasma. WAVSs play a key role in the safety of operation of the tokamak: on the one hand, infrared radiation of the divertor and first wall surfaces allow measurement of the surface temperature, which must be kept at a reasonable level to prevent surface melting and internal stresses [36], and is thus critical for the protection of the tokamak. On the other hand, the wide angle visible imaging can be used for qualitative monitoring of the integrity of PFCs, as well as visual

confirmation of plasma shape and strike point position. Events such as disruptions and Edge-Localized Modes (ELMs) can also be detected by observing the plasma edge region. WAVSs are installed in JET [4] for observation of the PFCs, detection of ELMs and monitoring impurity transport. WAVSs are planned to be installed in ITER in four locations in the Equatorial Port Plug (EPP) [16, 92] and in five locations of the Upper Port Plugs (UPP) [73] in the diagnostic first wall (DFW). The different systems provide Lines-of-Sight (LoSs) to regions of interest in the plasma edge and on the first wall and divertor.

1.5 Scope of this Work

Simulations are a crucial aspect of modern physics: they are performed to validate theoretical work and to deepen the insight into experimental results by reproducing them. When a code and the models behind have been validated, predictive modelling can be performed to extrapolate to future devices. The complexity of systems that can be described by numerical codes rises steadily. However, a fusion device is an extremely complex system, covering scales from the long-range transport of particles throug the massive devices to processes on the atomic scale when the particles collide with a surface, leading to erosion and deposition. Additionally, a variety of particle sources and sinks is present in a fusion device, e.g. on the one hand helium ash originating from fusion processes, impurity particles from sputtering of PFCs or additional fuel particles from gas injections; on the other hand, particles can be e.g. deposited or implanted in the wall or pumped from the plasma volume by cryopump systems. The different particles cover an energy range reaching up to several ten thousand kilo-electron volts, and a multitude of atomic or molecular species. Thus, a variety of interaction processes, transport mechanisms and reactions in the plasma is present, which each needs specific treatment. This results in the fact that no single code yet can describe the plasma, the transport, and the plasma-wall interaction in a full fusion device in sufficient detail, and an interplay between a variety of highly specialised codes is necessary to treat the full system in a qualitatively satisfying manner.
For the optical diagnostics planned in ITER, crucial questions considering the performance of the mirrors in a long-pulse, high power plasma are yet unanswered. It is unclear if the incoming particle fluxes will lead to potentially harmful erosion of the mirror surfaces, or if incoming impurity fluxes lead to significant deposition. These processes can severely degrade the optical performance of the mirror. Currently, the estimates for the extent of the degradation are based on extrapolation from experimental results in short-pulsed plasmas in JET. Additionally, the geometry

of the mirror systems planned for ITER is significantly more complex than the mock-up ITER-like mirror test assembly (ILMTA) used in JET, since the systems are integrated into the protective wall against high-energy neutrons from fusion reactions. This makes the extrapolations even harder to justify. It remains unclear if the mirrors will need cleaning, protection by shutters or even replacement to guarantee their performance over the ITER lifetime.

In this work, the erosion and deposition on mirrors used for optical diagnostics in fusion devices is assessed based on simulations using the established ERO2.0 code [103]. The code simulates erosion by plasma and impurity particles, as well as particle transport in a kinetic formulation and uses a Monte-Carlo technique. It is fully 3D to allow the evaluation of complex geometries, making it an ideal choice for the application here. However, the code is not optimized for simulations in recessed areas, where the quality of the Monte-Carlo approach is limited by the amount of simulated particles, i.e. computing power.

The first aim of this work is to enhance the ERO2.0 code for the application in recessed areas to ensure the quality of the results of this work. In simplified studies, key parameters for the simulation workflow are identified. When the workflow is fully defined, a significant study of erosion and deposition in a mirror assembly that was installed in the JET tokamak is performed, for which an experimental analysis was conducted [105]. After the simulations of the JET mirror assembly are benchmarked with the experimental results, predictive modelling for two diagnostic first mirrors in ITER is performed for a multitude of plasma scenarios. Additional studies using alternative assumptions about the wall composition and properties are executed to ensure the significance of the results and to show how the variation of these properties affects the mirrors. It should be noted that the simulations presented in this work focus on the mirrors from the perspective of materials – the potential deposition and erosion of the mirror surfaces is evaluated. This serves as an input to potential further detailed modelling focussing on the optical performance of the mirrors, which can not be simulated with ERO2.0 and is out of the scope of this work.

The outline of the thesis is the following: in chapter 2, the physics background of plasma-wall interactions is outlined, which is necessary for the further understanding of the work. Numerous interactions are possible, but the explanations in this chapter focus on the two mechanisms most relevant for this work – erosion and deposition of impurity particles.

Afterwards in chapter 3, the numerical codes used in this work are described, with a focus on the ERO2.0 code that was used for most of the simulations in this work. The codes are introduced in the state they were in at the beginning of this work.

The optimizations and improvements to the ERO2.0 code performed within this work are introduced in chapter 4. The focus of the optimizations is on a more efficient and accurate application of the guiding-centre approximation tracing methods recently introduced in ERO2.0. These optimizations allow the simulation of larger amounts of particles in global simulations, so that statistics problems can be minimized. Only with these optimizations, the simulations in this work are made possible.
To further improve the quality of the simulations in the volume where optical diagnostics are located, a multi-stage workflow for the simulation of recessed areas is introduced in chapter 5. Because the information on plasma parameters in and fluxes into these areas is generally limited, special processing of the available information is required. The plasma parameter extrapolation and particle sampling processes are explained in detail.
The main simulations performed in this work are presented in chapter 6, where the setup of the multi-stage simulation workflow is explained for the JET and ITER devices. For JET, the simulation results are compared to experimental results from an existing study. Afterwards, predictive ITER modelling is performed for the Be/W material mix. Additional ITER studies are performed to assess the significance of the main results and to highlight differences in further scenarios relevant for ITER operation.
Finally, in chapter 7 the results and main conclusions of this work are summarized, while an outlook to further possible improvements and applications of the workflow is given in chapter 8.

Chapter 2

Plasma-Wall Interactions

2.1 Overview of Processes

The plasma-facing components (PFCs) in a fusion device are subject to bombardment by plasma fuel and impurity particles, which can potentially erode wall material. In modern tokamak designs, the divertor regions of the device typically are the PFCs subject to the highest impinging fluxes. Ions from the scrape-off layer (SOL) are steered away from the first wall (FW) to the divertor by the magnetic field geometry, with the intention to exhaust the power and particle fluxes to the PFCs on wall regions far from the core plasma. Thus, the hot fusion plasma is protected better from eroded divertor material, which represents a main source of impurities. Additionally, the fusion product, He ash, is neutralised at the divertor target plates and pumped from the volume, since it is not relevant to further fusion processes.

However, even the FW is subject to particle bombardment: transport processes perpendicular to the magnetic field lines degrade the magnetic confinement of ions, e.g. anomalous diffusion and drift effects. In addition, neutral particles are not confined by the magnetic field and can reach all PFC regions with direct line-of-sight to the plasma unhindered. Neutral particles in fusion devices mainly originate from recombination of ions in colder plasma regions or at the wall, or from charge-exchange (CX) reactions.

The interaction between plasma fuel or impurity particles and the wall is therefore of critical importance to the operation of fusion devices in magnetic confinement fusion. A variety of processes take place when a particle impacts on the wall, depicted schematically in Figure 2.1. Upon impact, two main categories of mechanisms need to be considered: (i) the further trajectory of the impacting projectile and (ii) the response of the surface to the impacting projectile. The most important plasma

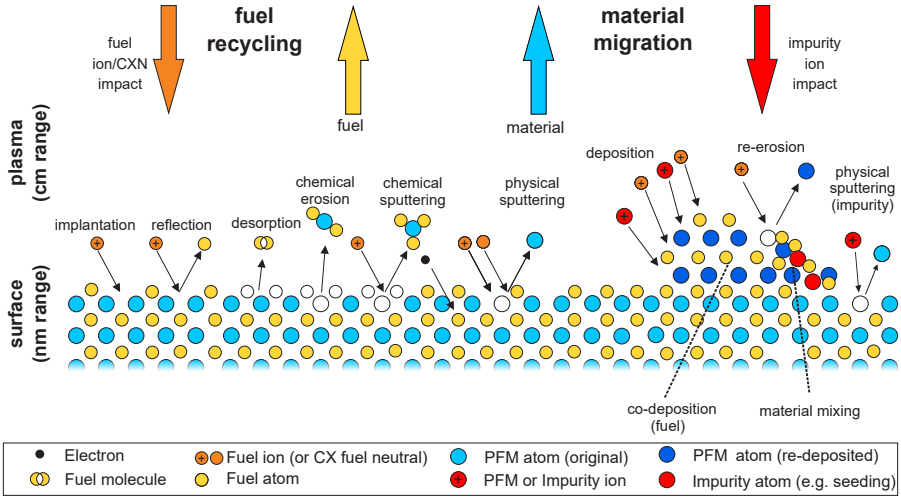

Figure 2.1: Overview of different processes possible during the interaction of impinging fuel or impurity particles with the plasma-facing material (PFM) of wall components.

wall interaction are outlined in the following sections, but for a more thorough explanation the reader is referred to e.g. Ref. [112]. The processes are introduced here individually, but it should be noted, that the different processes take place at the same time in a fusion device and the local balance should be considered.

2.2 Erosion

Energetic particle fluxes that impinge on the wall, e.g. fuel ions, charge exchange neutrals (CXN) or impurity particles, can induce bound particles from the wall material to leave the surface. There are different internal mechanisms possible as a cause.

Firstly, the kinetic energy of the impinging projectile can be transferred to a bound wall particle in an elastic collision, causing it to overcome the surface binding energy E_{SB} and leave the surface. This process is known as *physical sputtering* and commonly takes place in the form of a collision cascade. In this cascade, the projectile energy is transferred in multiple collisions to the wall atoms, which can themselves induce secondary collision chains. The erosion or sputtering rate of this process depends strongly on the impact energy of the incoming particle, the mass ratio of projectile and target element, the impact angle, and the internal structure of the target (e.g. crystalline orientation) [7, 95]. For each combination of projectile and target element, there is a threshold energy E_{T} below which no sputtering occurs. This energy generally is higher for projectiles of low atomic

mass and targets of high atomic mass, and can be estimated by taking into account the maximum energy transfer in a hard-sphere collision and the surface binding energy E_{SB}, which results in

$$E_T \simeq \frac{E_{SB}}{\gamma(1-\gamma)} \tag{2.1}$$

where γ is defined as

$$\gamma = \frac{4m_1m_2}{(m_1+m_2)^2} \tag{2.2}$$

with the projectile mass m_1 and target mass m_2 ([112, p.118], where the full derivation can be found). However, fitted values are preferred for the threshold energy, since Equation 2.1 does not describe self-sputtering where $\gamma = 1$. In the JET-ILW, the Be and W PFCs interact with the hydrogenic fuel, typical threshold energies are $E_T^{\mathrm{D}\rightarrow\mathrm{Be}} \simeq 9\,\mathrm{eV}$, $E_T^{\mathrm{D}\rightarrow\mathrm{W}} \simeq 220\,\mathrm{eV}$ and $E_T^{\mathrm{Be}\rightarrow\mathrm{Be}} \simeq 25\,\mathrm{eV}$[1] (fitted values taken from [112, p.120]). When the sputtered material ionizes, it is likely to impact on and erode the PFC due to transport along the magnetic field line, which is referred to as *self-sputtering* for identical projectile and target element.
Secondly, especially thermal fuel material (e.g. deuterium) can form chemical bonds with wall atoms, resulting in a molecule leaving the surface. This process is labelled *chemical erosion*.
Finally, a combination of the aforementioned effects is possible, in which the kinetic energy of the impinging particle additionally enhances the erosion of a newly formed molecule. This process is known as *chemical sputtering* or *chemically assisted physical sputtering* (CAPS) and was first described in the analysis of beryllium migration in the JET-ILW [13].
Both chemical erosion and CAPS depend strongly on the content of hydrogenic elements in the surface, which itself is affected by the choice of surface material, the plasma parameters at the PFC, and the temperature of the PFC. The chemical processes can take place at projectile energies lower than the threshold energies for physical sputtering, which leads to erosion where the impact energy of the hydrogenic fuel would otherwise be too low for physical sputtering. This mechanism has been observed especially for carbon (C) walls in a hydrogenic plasma, because the threshold energy for physical sputtering ($E_T^{\mathrm{D}\rightarrow\mathrm{C}} \simeq 30\,\mathrm{eV}$) lies above typical plasma temperatures at the wall, so that erosion is dominantly caused by

[1] In this work, the notation $X \rightarrow Y$ is used for sputtering yields, where the first element (X) indicates the projectile and the second element (Y) indicates the target. Therefore, sputtered material consists of species Y.

CAPS [37]. The effect has also been observed for beryllium [25], leading to an increase in sputtering yield by up to 50% compared to physical sputtering [13]. For Be surfaces, CAPS vanishes at a surface temperature of around 520 °C due to the decreasing hydrogenic content of the surface with increasing temperature.
The effect of all erosion mechanisms should be generally minimized in fusion devices, so that the safety and operability of the device can be sustained over years of operation. Especially the choice of the wall material plays a significant role, because the magnitude of the different erosion processes varies considerably between materials. Currently, materials based on tungsten (W) are favoured, since the threshold energy for physical sputtering by deuterium is far above typical plasma temperatures at the PFCs. Since CAPS and chemical erosion are negligible for W PFCs [14], erosion in steady-state conditions can only be caused by energetic CXN particles or impurities. However, a good inhibition of erosion is crucial in fusion devices with W PFCs. W impurity accumulation in the plasma results in high radiated power and cooling of the plasma core, since W is not fully ionized in a fusion plasma due to its high full ionization energy ($\sim 80.7\,\mathrm{keV}$ [65]). Sputtered W is likely to promptly re-deposit (see section 2.3) due to its low first ionization energy ($\sim 7.9\,\mathrm{eV}$ [65]), high mass and resulting gyration radius, which is beneficial in view of the reduced plasma contamination.
Apart from the wall material, another consideration for the minimization of PFC erosion is the magnetic field geometry. Physical sputtering yields depend strongly on the impact angle of the projectiles, and ionized particles generally follow the magnetic field lines, which means that the magnetic field angles on the PFCs can be optimized to reduce the physical erosion. However, it should be noted that gyration effects can cause the particle's impact angle to differ from the magnetic field angle. The engineering of toroidally shaped wall elements (e.g. the divertor tiles in JET, see Figure 1.3) should take into account the magnetic geometry. Leading edges protruding into the plasma should be avoided, because the significantly steeper impact angle leads to enhanced erosion [17].
Furthermore, the plasma shape and design affect erosion significantly, since plasma ions generally thermalize to local plasma background temperatures through collisions. Low plasma temperatures at the wall are thus critical for the long-term operation of a fusion device. In theory, this way the largest part of the impinging particle population can be kept below the sputtering threshold energy of the wall material, so that physical sputtering can be minimized. However, sheath effects must be considered for an accurate physical description of erosion of PFCs. Due to the difference in mass and mobility of the negatively and positively charged particles in a plasma (light, fast electrons and heavy, slower nuclei), electrons reach

the wall faster than positively charged nuclei. This leads to a build-up of negative charges close to the wall surface – the so-called sheath region. As a result, positively charged particles are accelerated to the wall according to the electric force when close to the wall, and the kinetic energy of the particle increases proportionally to its charge. Especially for highly charged particles, this can lead to a significant increase in impact energy. The increase in energy due to the sheath potential is around

$$\Delta E \simeq 3 k_B Z T_e \tag{2.3}$$

in hydrogenic plasmas, where Z is the charge state of the projectile [112, p.79].

2.3 Reflection, Deposition, and Implantation

Several processes are possible for the projectile after a particle-wall collision. On the one hand, a *reflection* of the particle at the wall surface can take place – either in an elastic collision at the first wall atom it hits, but more likely as a result of a collision cascade introduced in the previous section. Small angle changes in each collision can accumulate to reverse the particle's momentum and eject it from the surface again. In metallic surfaces, free electrons are available, so that all reflected particles leave the surface as neutrals.
However, it is also possible that the projectile remains in the surface. This process is called *implantation*, when the particles penetrate into the matrix of the surface material, or *deposition*, when the particles accumulate on top of the surface and form layers. Closed layers are only formed if enough particles are deposited to cover the surface with at least one monolayer of atoms ($\sim$ Å), otherwise local deposits are formed. Gaseous projectiles that hit the wall fill up gaps between the wall atoms or can accumulate in surface defects, which is called *trapping* of the fuel. The particles can enter deeper regions of the wall by diffusive processes. The diffusion can also lead the gaseous particle out of the wall again, which is called *desorption*. Depending on the surface temperature, fuel particles desorb as molecules or atoms [15]. If plasma fuel particles escape from the surface and enter the main plasma volume again, one speaks of *recycling*.
Impurity particles that were previously eroded from the wall are subject to transport effects in the plasma (e.g. collisions and diffusive processes) and to the magnetic field structure after ionization, which potentially leads them back to the wall where they can be *(re-)deposited*. Typically, three types of (re-)deposition are distinguished by the distance between erosion location and deposition: prompt,

local, and global (re-)deposition.

The shortest scale is labelled as *prompt (re-)deposition*. Several definitions for the range exist, but commonly it is defined as re-deposition within the time duration of one gyration. This process is most likely for elements with a low first ionization energy and large Larmor radius, thus especially for particles with a high atomic number like tungsten. The plasma parameters close to the wall can significantly affect prompt re-deposition, since the gyration only begins as soon as the particle ionizes. Higher plasma densities and temperatures at the wall increase the prompt re-deposition fraction due to the shorter mean free path for ionization of sputtered material. In simulations, prompt re-deposition of more than 90% of sputtered W flux has been found [57] in plasma edge conditions comparable to ITER ($T_e = 20\,\mathrm{eV}$, $n_e = 6 \times 10^{19}\,\frac{1}{\mathrm{m}^3}$).

If a wall particle travels further but still re-deposits close to its erosion location, e.g. on the same divertor tile, *local re-deposition* takes place; if it travels even further, e.g. entering the confined plasma and exiting at a different toroidal or poloidal location, one speaks of *global re-deposition* or simply deposition after impurity transport.

When there are PFCs made of multiple elements present in a fusion device, deposition can lead to material mixing in the wall in the so-called *surface interaction layer* – the top layer of the *bulk material* beneath. The thickness of this interaction layer depends on the impact energy of incoming projectiles, but is under normal circumstances not higher than $\sim$100 nm, because the impact energies are typically low by plasma design. Still, deposited material can accumulate on top of the surface in net deposition zones, leading to an increase in wall thickness much larger than the surface interaction layer. For example, in the JET-ILW, where the plasma transport in the SOL is directed towards the inner divertor legs [67], Be from the first wall has been observed accumulate on inner divertor W tiles with a thickness of several micrometres [13]. Since wall material is made from heavier elements than the fuel, the impact of sputtered impurity particles on the wall can lead to erosion in places where it would otherwise be negligible if only fuel particles were impinging, e.g. sputtering of the W divertor by Be particles in the JET-ILW.

Finally, additional plasma fuel ions can be deposited into the wall by *co-deposition* with impurity ions under deposition conditions [112, p.126].

2.4 Role of Charge-Exchange Neutrals (CXN)

In this work, optical diagnostics installed in recessed volumes of the fusion devices are the focus of interest. The ion fluxes into these regions far from the core plasma are minimized by the plasma design and magnetic geometry inside the tokamak. However, the magnetic field does not confine neutral particles. Recombination processes of the positive ions with the free electrons in the plasma are possible, but re-ionizations in the hot plasma are very likely so that only recombination neutrals from low-temperature edge regions of the plasma are likely to hit the wall.
However, another neutralization process can result in unconfined particles with high energy: charge-exchange neutralization. This interaction can take place when one interaction partner is an ion, and the other is a neutral particle, e.g.:

$$D^+ + T^0 \;\rightarrow\; D^0 + T^+$$

During the interaction, the electron from the originally neutral particle (here T) is transferred to the interaction partner – the charge between the two particles is exchanged in the reaction, hence the name. If the original ion is a confined, highly energetic plasma ion before the reaction, the interaction results in a highly energetic charge-exchange neutral (CXN), which is now unconfined. Thus, the particle can easily reach areas that are otherwise protected from the energetic plasma ions. Therefore, in recessed areas, the main erosion mechanism is expected to be bombardment by CXN. In this work, special emphasis was put on the inclusion of CXN in the simulation of erosion and deposition.
Considering the expected energy of CXN particles, the SOL is the main source of CXN impinging on the wall elements, since particles from further inside the plasma are more likely to re-ionize on their trajectory due to the higher plasma densities inside the core. However, since ionization is a statistical process, CXN particles from the confined region – in H-mode plasma scenarios the so-called pedestal region – can still reach the wall, which leads to large sputtering due to the CXN high-energy tail.

Chapter 3

Overview of Codes and Databases

ERO2.0 [103], a Monte-Carlo code with full 3D treatment, is the main impurity transport and plasma-wall interaction code used in this work. Figure 3.1 shows the workflow for a typical ERO2.0 simulation, featuring main input by plasma code packages (SOLPS-4.3/OEDGE [18, 71] and EDGE2D-EIRENE [38] in this work), and the neutrals transport code (EIRENE [94]). Databases for atomic processes in the plasma (ADAS [116]) and plasma-wall interaction processes at the plasma-facing material, generated by SDTrimSP [81], are queried. Each code is specialized in different areas. The main partitioning of the particle species to the transport codes is the following:

- SOLPS-4.3/OEDGE and EDGE2D-EIRENE are combined plasma-fluid transport and impurity particle codes, which treat ionized fuel gas species in the plasma boundary layer, thus, around the separatrix and in the scrape-off layer – in this work mostly D ions. Seeding impurities, the helium ash and other impurities can also be treated, but are not considered here. These codes are 2D and optimised for tokamaks.

- EIRENE treats neutral fuel particles originating from charge-exchange, molecular or recycling processes in the main chamber or gas injections fully three-dimensional – in this work mostly D neutrals.

- ERO2.0 treats sputtered impurity particles from plasma-facing components (PFCs) in the scrape-off layer and all transport into recessed areas in full 3D – in this work mostly Be particles and later additionally energetic D atoms and Fe ions in recessed areas.

The simulation domains of the codes can be seen in Figure 3.2 in the 2D R-z-plane for the example of an ITER simulation in diverted configuration. ERO2.0 covers the largest volume, up to the wall components and potentially even into

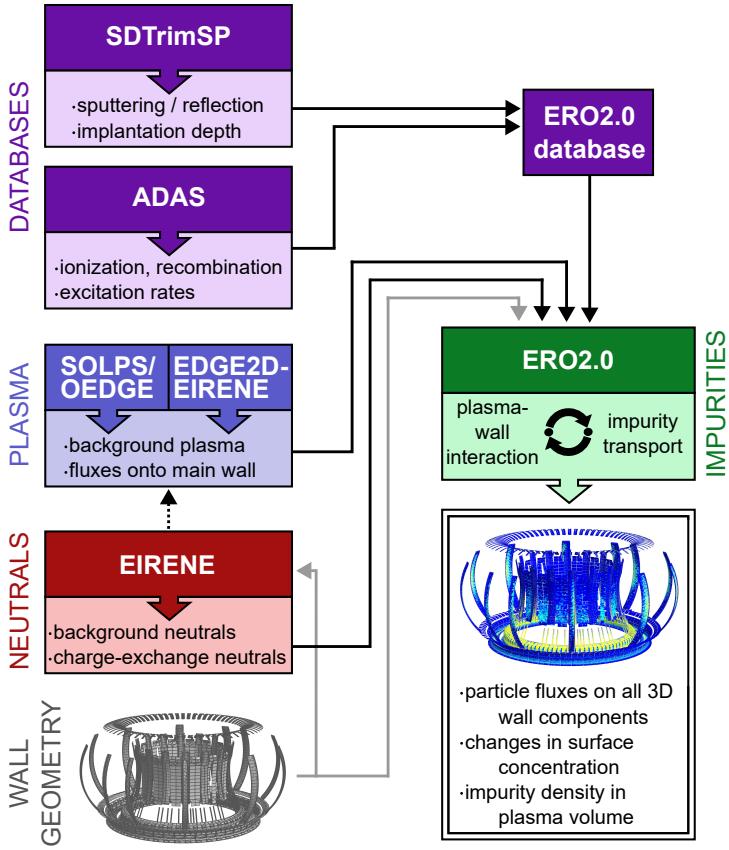

Figure 3.1: Overview of the main codes used in this work, the connections (dotted arrow), their output (coloured arrows) and the workflow for ERO2.0 simulations (black arrows). The wall geometry has to be provided as input to both the ERO2.0 and EIRENE codes (grey arrows). A detailed view of the ERO2.0 main loop is presented in Figure 3.3.

toroidal/poloidal gaps in 3D, therefore extrapolation methods are needed to extend the plasma background information to the full simulation volume. More details on the extrapolation methods applied in this work can be found in sections 3.1.1 and 5.2.

In the remainder of this chapter, the different codes, their application in this work

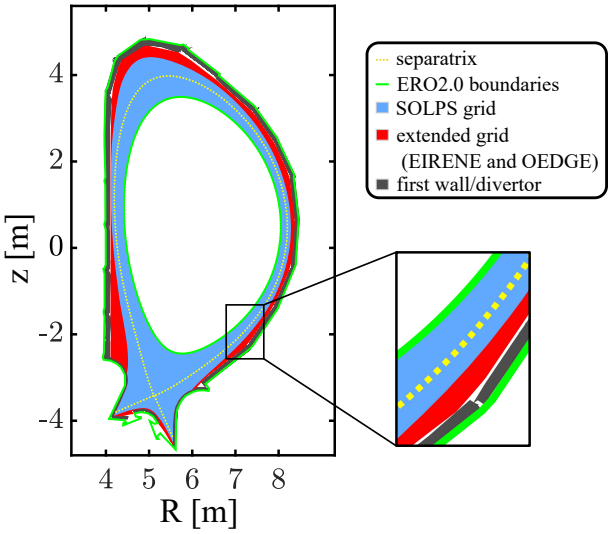

Figure 3.2: Simulation domains of ERO2.0 (green bounds), SOLPS-4.3 (blue area) and OEDGE+EIRENE (blue and red area combined) in a typical global ITER simulation in the R-z-plane. A poloidal projection of the apex of the shaped wall is shown in grey. Notes: ERO2.0 and EIRENE are 3D codes, while SOLPS-4.3 is a 2D code. Figure adapted from [100].

and their output are described in detail, providing an introductory picture of the workflow necessary for ERO2.0 simulations. ERO2.0 code updates developed in this thesis are described subsequently in chapter 4, and the advanced multi-stage simulation workflow utilizing all introduced codes is described in chapter 5, enabling sophisticated simulations of PFCs in recessed areas.

3.1 Monte Carlo-Code ERO2.0

The ERO code is a 3D Monte-Carlo impurity transport and plasma-wall interaction (PWI) code for fusion devices. It operates under the test particle approximation, in which the interaction amongst traced impurity particles is neglected. The code assumes a static plasma background provided as input by a plasma code. Under the test particle approximation, changes to the plasma background due to the impurity

densities are neglected. The simulation volume is limited to comparably small local volumes, e.g. one divertor leg or one test limiter in a tokamak [58, 59, 61]. The main output of ERO is the eroded and deposited flux density [particles/m²s] on the cells of the discretized wall geometry. In the following, flux densities will always be referred to as fluxes for brevity. ERO has a successful history, dating back to the 1990s [82] and has been applied to a multitude of fusion devices [2, 10, 60, 62].

In a massive code update in recent years, the ERO code has been completely rewritten in C++, resulting in the ERO2.0 code [103], which is the code version exclusively used in this work. The code keeps the main features of ERO (3D Monte-Carlo approach, test particle approximation), but in contrast to its predecessor, the ERO2.0 code is capable of simulating volumes covering the entirety of the PFCs of fusion devices, e.g. more than $90\,\mathrm{m}^3$ in the JET tokamak[1]. This significant increase in simulated volume (from cm^3 to m^3), surface area and performance is achieved by code optimizations and by the massive parallelization implemented in ERO2.0. This enables the efficient use of parallel processes on High-Performance Computing (HPC) hardware, like it is available on the JURECA [55] and MARCONI [52] supercomputers employed in this work. From a physics point of view, the vastly increased simulation volume permits a self-consistent simulation – in the predecessor ERO, impinging fluxes serving as boundary conditions have to be set by user-input at the bounds of the small simulation volume. ERO2.0 in contrast treats the transport in the global simulation volume, including all PFCs in a fusion device. Therefore, all impurity fluxes impinging on the PFCs originate from a source within the simulation volume, primarily from erosion of PFCs or by forced injection of seeding species. Due to the adaptability of the code, it has been applied in a wide variety of fusion devices, e.g. the tokamaks WEST [35], JET [99], KSTAR [84] and ITER [101], the stellarators LHD [108] and W7-X [104], or linear plasma devices like PSI-2 [28].

The ERO2.0 code features a loop between two main modules (Figure 3.3): in the PWI module, the impurity source term determined by the erosion of PFCs owing to the plasma particles is first calculated for each surface cell of the discretized 3D wall geometry. Subsequently, a finite number of test particles are initialized on the whole surface geometry as atoms. Test particles serve as a discretized approximation of the released impurity atoms by erosion. Each test particle carries a certain *Monte-Carlo weight* [atoms/s], determining the amount of real particle flux it represents. In the following, test particles are commonly referred to simply as 'particles'.

[1] https://euro-fusion.org/devices/jet

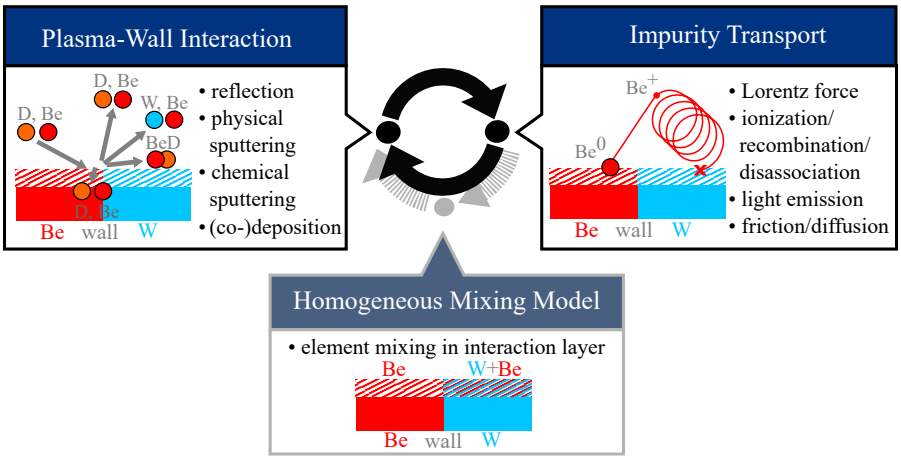

Figure 3.3: Overview of the ERO2.0 main loop, which consists of two essential modules – *Plasma-Wall Interaction* and *Impurity Transport*. The optional module *Homogeneous Mixing Model* can be enabled to recalculate surface concentrations in each loop.

Upon release of the sputtered particles, the impurity transport module is executed. The particles are traced in a kinetic description applying full-orbit resolution after ionisation by electron impact, i.e. resolving the gyrating particle motion in the magnetic field geometry. Far away from PFCs, an alternative tracing method utilizing the guiding-centre approximation can be optionally applied for ionized particles [96], in which the gyration is effectively averaged out and the particle's guiding centre is traced (see section 3.1.2). During the transport in the plasma, the particles are subject to a wide range of physical effects, e.g. basic motion in static electromagnetic fields including drifts, collisions with the plasma background, ionization excitation, recombination processes, or anomalous diffusion.
The impurity test particles are traced in 3D until they collide with a cell of the surface geometry, where their impact energy and angle are fully resolved. Based on this information, reflection of particles is calculated using a probability database generated by the SDTrimSP code (see section 3.3). During a reflection, all particles are neutralised. Additionally, the impinging particles can induce a further source term in the next iteration of the PWI module, because the impinging fluxes lead to sputtering of neutral atoms from the PFCs. Physical sputtering yields are calculated based on SDTrimSP data (see section 3.3). A simulation of steady-state erosion and deposition fluxes on the PFCs can be achieved by looping the two main modules of the ERO2.0 code, as the additionally sputtered wall fluxes iteratively converge against their steady-state values [103].
Optionally, the time evolution of the local surface concentration of impurities can be

simulated by a Homogeneous Mixing Model (HMM), detailed in section 3.1.5. The final output of the ERO2.0 code includes information about sputtering, incoming, eroded and deposited flux [particles/m²s] on all surface cells of the 3D PFC geometry, as well as density maps of the impurity particles in the simulation volume among others.
ERO2.0 requires input by other codes – importantly, the plasma background information is one such input (unless simplified plasma profiles or constant plasma backgrounds are assumed). The plasma background is usually generated by coupled plasma transport and neutrals codes like SOLPS-4.3, EDGE2D-EIRENE (see section 3.4) or EMC3-EIRENE. ERO2.0 operates under the test particle approximation, which means that any of the traced particles' effects on the plasma itself (e.g. electron density and electromagnetic fields resulting from the motion of charged particles) are neglected, i.e. the background plasma is assumed to be unperturbed by the impurities generated in the PWI processes. This assumption has been tested for low impurity concentrations in the plasma and remains valid unless strong impurity sources (e.g. external puffing) are considered [121, 122].
A selection of ERO2.0 capabilities that are relevant for and existed prior to this work are described in sections 3.1.1 to 3.1.5. The updates, enhancements, and optimizations to the ERO2.0 code performed in this work are detailed in chapter 4.

3.1.1 ERO2.0 grid and 3D simulation domain

ERO2.0 is a full 3D numerical code, therefore its simulation domain, depicted in Figure 3.4, typically covers the complete first wall (FW), divertor and recessed wall components in a fusion device. Still, boundaries of the simulation domain need to be defined, which are given as 2D contours in toroidally symmetric devices like tokamaks. Plasma-wall interaction is the focus of the code, thus the simulation domain is usually confined inwards to a region around the scrape-off layer (SOL) of the plasma. Outwards, a boundary lying behind the FW and divertor catches particles entering gaps between toroidally shaped wall elements.
Within the impurity transport module of ERO2.0, the R-z-projection of a particle's position is compared to these boundaries at the end of each tracing time step. The outer simulation boundary acts as a particle sink, i.e. the particle is assumed not to re-enter the simulation domain, whether it is permanently deposited or pumped outside the main plasma volume. The inner boundary excludes the core volume of the plasma from ERO2.0 simulations, since scrape-off layer (SOL) plasma codes like SOLPS-4.3 do not cover the core either (see Figure 3.2), so that no further assumptions about the core plasma are required in ERO2.0. This also

drastically reduces the computation time in ERO2.0 simulations, because particles entering the core volume usually stay inside this region for a long time. The PWI results of ERO2.0 are not significantly affected by the exclusion of the core volume at the inner simulation boundary [102]. If a particle crosses this inner boundary, reflecting or teleporting boundary conditions can be applied in the ERO2.0 simulation. The former is a reflection of the particle in place, while the latter includes a "teleportation" of the particle to a random point on the inner boundary, approximating the long-range transport and collisions inside the core volume in a stochastic approach. Typical boundaries for an ERO2.0 simulation in ITER are shown in Figure 3.4, reaching from a closed flux surface at radial flux coordinate[2] $\rho = 0.9$ to a contour around 2 cm recessed behind all included wall geometry.

Plasma information from SOL-plasma codes like SOLPS-4.3/OEDGE is stored on the ERO2.0 grid, which is generated in a pre-processing step before the actual ERO2.0 simulation. A rectangular grid is used with a fixed, predefined cell size of usually around 1 cm (see Figure 3.4c). The ERO2.0 simulation domain extends

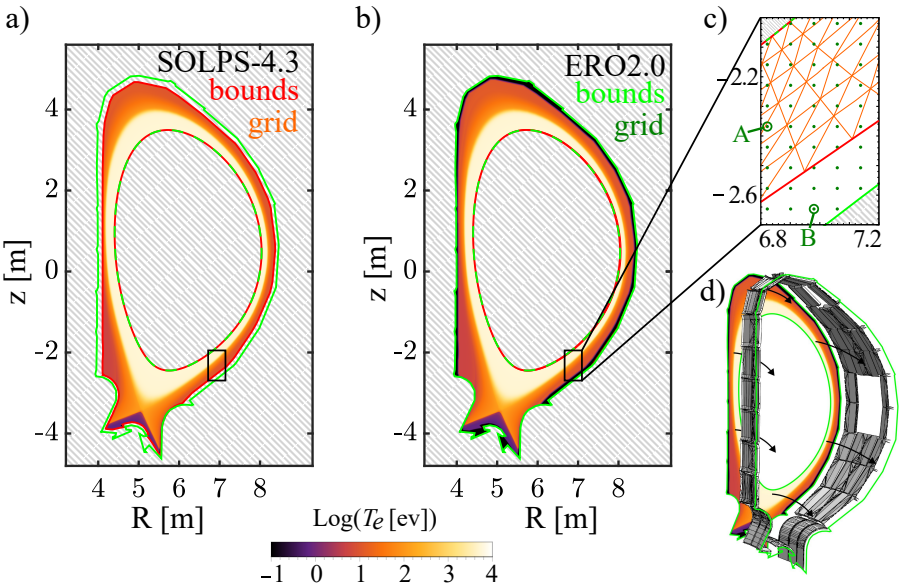

Figure 3.4: a)+b): Electron temperature T_e in the simulation domain of SOLPS-4.3 and ERO2.0, respectively. c) Schematic comparison of the simulation grids of the two codes in a zoomed-in region of the simulation domains. d) 2D plasma background information is used in the 3D simulation domain of ERO2.0 under assumption of toroidal symmetry.

[2]The radial flux coordinate ρ is used in plasma physics to label the nested flux surfaces in the plasma's confined region, where $\rho = 0$ denotes the magnetic axis and $\rho = 1$ denotes the last closed flux surface (LCFS).

further than that of the SOL-plasma codes, which commonly use grids aligned to the magnetic field. Therefore, ERO2.0 grid nodes lie either inside the plasma code simulation domain, like point A in Figure 3.4c), or outside of it, like point B. Using these two points as examples for the two possible cases, the plasma background information of the SOL-plasma codes is interpolated to point A, but extrapolation of the plasma parameters is necessary to point B. The extrapolation is commonly performed assuming an exponential decay of temperature and density of electrons and ions. The extrapolation profiles assumed in this work are detailed in section 5.2.
It should be noted that ERO2.0 is strictly a 3D code, while the plasma background provided by the SOL-plasma codes is in most cases two-dimensional. 3D SOL-plasma codes are available, like the EMC3-EIRENE code [32], but have not been applied to the plasma scenarios studied in this work. ERO2.0 is fully compatible with 3D background plasma information, in which case the ERO2.0 grid is extended to a third dimension in toroidal direction. In case only 2D information is provided, toroidal symmetry is assumed for all plasma parameters (see Figure 3.4d).
In an ERO2.0 simulation, the plasma parameters are queried at various locations, e.g. the plasma temperature at PFC surfaces is necessary to calculate erosion, or the plasma density at a traced particle's location to calculate collision rates. Interpolation from the surrounding ERO2.0 grid nodes is necessary, since these query locations are not restricted to the ERO2.0 grid. Bilinear interpolation is performed in case a 2D plasma background is used, while trilinear interpolation is performed for 3D plasma backgrounds. The interpolation scheme is further discussed in section 4.3.

3.1.2 Particle Transport, Full-Orbit Resolution (FO) and Guiding-Centre Approximation (GCA)

A main feature of ERO2.0 is the ability to trace complete particle trajectories in *Full-Orbit (FO) resolution*, which means that the gyrating motion of particles around magnetic field lines is fully resolved. FO tracing methods are a physically accurate description of a charged particle's motion in static electromagnetic fields, which is subject to the Lorentz force:

$$\mathbf{F}_L(\mathbf{r},t) = q \cdot (\mathbf{E}(\mathbf{r},t) + \mathbf{v}(t) \times \mathbf{B}(\mathbf{r},t)) \tag{3.1}$$

where q is the particle's charge, and $\mathbf{E}$ and $\mathbf{B}$ the electric and magnetic field vectors, respectively, at the particle's location $\mathbf{r}$ with velocity $\mathbf{v}$ at time t.

In the case of no electric field, the Lorentz force acts as a centrifugal force and the Larmor radius r_L (the radius of the circular motion perpendicular to the magnetic field) can be derived from the force balance in the plane perpendicular to $\mathbf{B}$:

$$\begin{aligned} |\mathbf{F}_L| &= |\mathbf{F}_{\text{centrifugal}}| \\ |q| \cdot v_\perp \cdot B &= \frac{m v_\perp^2}{r} \\ \Leftrightarrow r &= \frac{m v_\perp}{|q| B} := r_L \end{aligned} \tag{3.2}$$

with the particle's mass m and velocity $v_\perp$ perpendicular to the magnetic field. The Larmor frequency ω_L can be derived via the relation $\omega = \frac{v}{r}$:

$$\omega_L = \frac{|q| B}{m} \tag{3.3}$$

to which the gyration time $T_L = 2\pi/\omega_L$ is related.
For the numerical simulation of particle movement under influence of the Lorentz force, a well-known and efficient algorithm is available: the Boris-algorithm. This algorithm has significant positive traits: it is fully energy conserving in the absence of electric fields (unlike many other explicit algorithms), reversible in time and less computationally intensive than implicit algorithms. Because of these advantages, it is commonly used in a wide range of codes, ranging from PIC codes like VLPL [90] to Monte-Carlo transport codes like ERO2.0 [103].
However, FO resolution is not ideal in all situations, although it is the most physically accurate description of particle motion in electromagnetic fields. The gyration is a very fast process, leading to strongly curved trajectories. The Larmor radius and frequency define the length scale and the timescale of the gyration, respectively. In a numerical transport simulation that includes the full gyration, these scales have to be resolved. Since particle motion in ERO2.0 is not limited to a discrete grid, no particular problem arises from the length scale. However, the tracing time step Δt chosen for the discrete integration of the equations of motion is limited by the gyration time T_L. For light impurities (e.g. Be) in a typical tokamak magnetic field ($\sim$4 T in JET), T_L can become as low as 30 ns and even lower in stronger magnetic fields, so that numerical time steps in FO resolution are limited to some nanoseconds.
Guiding-Centre Approximation (GCA) is a common method to circumvent this numerical limit. In this approximation, the particle's guiding centre $\mathbf{R}$ is traced, which can be thought of as the average position over one gyration. The trajectories

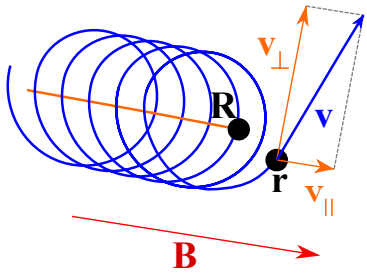

Figure 3.5: Sketch of a trajectory $\mathbf{r}(t)$ described in full orbit (FO) resolution (blue) and under application of guiding-centre approximation (GCA) $\mathbf{R}(t)$ (orange) in a constant magnetic field B (red). In GCA, the particle's true velocity $\mathbf{v}$ is split into its components parallel and perpendicular to the local magnetic field.

in GCA are much smoother, because the fast gyrating motion is effectively averaged out, which enables larger time steps for the tracing. The equations of motion for the phase space spanned by the guiding centre position $\mathbf{R}$, the velocity parallel to the magnetic field $v_\parallel$, the magnetic moment $\mu = \frac{mv_\perp^2}{2B}$ and the gyration angle φ then read:

$$\frac{d\mathbf{R}}{dt} = v_\parallel \frac{\mathbf{B}}{B} + \frac{\mathbf{E}\times\mathbf{B}}{B^2} + \left(\frac{\mu}{q} + \frac{v_\parallel^2}{\omega_L}\right)\frac{\mathbf{B}\times\boldsymbol{\nabla}B}{B^2} \tag{3.4}$$

$$\frac{dv_\parallel}{dt} = \frac{q}{m}\mathbf{E}\cdot\frac{\mathbf{B}}{B} - \frac{\mu}{m}\frac{\mathbf{B}}{B}\cdot\boldsymbol{\nabla}B \tag{3.5}$$

$$\frac{d\mu}{dt} = 0 \tag{3.6}$$

$$\frac{d\varphi}{dt} = \omega_L \tag{3.7}$$

where the right-hand side of Equation 3.4 is defined as the guiding centre velocity $\mathbf{v}_{GC}$. It consists of parallel motion along the magnetic field line and three drift terms: (i) the $\mathbf{E}\times\mathbf{B}$-drift, arising from electric fields perpendicular to the magnetic field; (ii) the $\boldsymbol{\nabla}B$-drift, arising from local changes in magnetic field strength; and (iii) the curvature drift, arising from the curvature of magnetic field lines. The parallel velocity $v_\parallel$ (Equation 3.5) varies due to parallel electric fields and due to the magnetic mirror effect, where particles can be reflected in regions of higher magnetic field strength. The magnetic moment μ (Equation 3.6) is a constant of motion, which makes it a prominent choice as a phase space coordinate in GCA compared to the perpendicular velocity $v_\perp$. The gyration angle and its constant change in time due to the Larmor frequency (Equation 3.7) are usually omitted when describing particle trajectories in GCA, because they only describe the gyration

in detail, which is intended to be smoothed out in this approximation. Thus, transport simulations applying GCA tracing methods are commonly performed in the five-dimensional phase space spanned by $\mathbf{R}$, $v_\parallel$ and μ.
The original implementation of particle tracing in ERO2.0 solely featured FO tracing methods in the full simulation domain, labelled *pure FO* simulation mode in the following. GCA tracing methods have recently been implemented into the ERO2.0 code [96] as an alternative to the FO tracing methods. However, the correct resolution of the impact angle is necessary for an accurate evaluation of surface processes like sputtering and reflection of particles (compare section 3.3), but is not given in GCA. Moreover, complex geometry is analysed in this work, so the impact locations of particles have to be resolved on the scale of some millimetres, while the guiding centre location in GCA approximates the real location only with an uncertainty of the Larmor radius. Due to these criteria, the *adaptive GCA* (AGCA, see Figure 3.6) simulation mode of ERO2.0 is applied in this work. This hybrid approach was additionally developed during the implementation of pure GCA tracing methods in ERO2.0 and combines the positive traits of both GCA and FO tracing methods. In the AGCA simulation mode, GCA is applied for the largest part of a particle's trajectory – as long as the particle is located far from the wall, the correct angle resolution of the FO tracing method is not necessary. Once a particle comes close to the wall, a random gyration angle is sampled and the particle tracing is further performed using FO tracing methods, so that correct angle resolution at the impact location is provided. If no wall collision takes place, the particle can adaptively switch back to GCA tracing methods. The AGCA simulation mode is further discussed in section 4.2, while a full derivation and overview of the AGCA development can be found in References [96, 97].

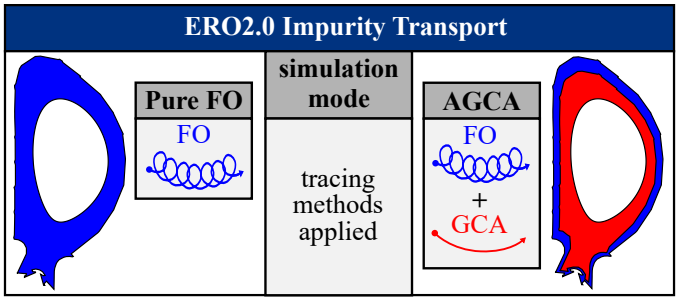

Figure 3.6: Two simulation modes for impurity transport are implemented in ERO2.0. In *pure FO* simulation mode, the FO tracing method is applied throughout the full simulation volume. In *AGCA* (adaptive GCA) simulation mode, GCA tracing methods are used far from the wall, while the FO method is applied only in a thin region close to the wall (region width exaggerated here for better visibility).

3.1.3 Collisions with Background Particles

Three main types of collisions between particles are considered in the ERO2.0 impurity transport module and treated separately: (i) ion-ion collisions, (ii) collisions with neutral background particles, and (iii) collisions between traced neutrals and the charged plasma background. The latter is considered via a friction force [5], while the first two types are discussed in the following. Collisions amongst traced particles are not simulated in the ERO2.0 code, as it operates under the test particle approximation and thus the probability of collisions amongst test particles is considered negligible.

The first type of collisions takes place between two ions, i.e. between a charged test particle and the plasma background in the ERO2.0 impurity transport module. The collision arises from the electrical potential originating from the positive, and thus repelling charges of the two particles. This type of collisions can be described by a Fokker-Planck term:

$$\frac{\partial f}{\partial t} = -\boldsymbol{\nabla} \cdot \left(\mathbf{K}\ f - \frac{1}{2} \boldsymbol{\nabla} \cdot (\mathbf{D}\ f) \right) \tag{3.8}$$

where f is the probability density distribution. $f(\mathbf{r}, \mathbf{v})\, d\mathbf{r}\, d\mathbf{v}$ then defines the probability to find a particle in the infinitesimal phase space volume $d\mathbf{r}\, d\mathbf{v}$ at position $\mathbf{r}$ with velocity $\mathbf{v}$. $\mathbf{K}$ is called the drift vector and $\mathbf{D}$ is the diffusion tensor. $\boldsymbol{\nabla}$ denotes the differential nabla operator.

For the implementation in ERO2.0, the plasma background is assumed to be Maxwellian, an assumption necessary to derive a closed form for the operators. A Monte-Carlo approach for the solution of this equation in discrete time steps of length Δt is known [93], and this approach has been evaluated for both FO and GCA phase spaces so that a consistent simulation is possible even in the AGCA simulation mode. Random numbers are used in the description, so that a total simulated particle ensemble correctly thermalize to a Maxwellian velocity distribution, fulfilling the Fokker-Planck relation (Equation 3.8).

The second type of collisions describes the interaction of traced ions or neutrals with the neutral part of the plasma background. In contrast to the ion-ion collisions, this interaction is on a much shorter scale, since the long-ranging electric force is absent. Therefore, the collision is described by a hard sphere collision process in ERO2.0. The van-der-Waals radii r_{vdW} of both collision partners – projectile and background neutral particles – are considered to determine a cross-section σ_n of

the collision process:

$$\sigma_n = \pi(r_{\mathrm{vdW,proj}} + r_{\mathrm{vdW,bg}})^2 \tag{3.9}$$

The van-der-Waals radius can be thought of as the radius of closest approach between two atoms [9] and can be measured experimentally [6], e.g. for deuterium the radius measures around 120 pm. More advanced estimates of the cross-section of the neutral background collisions in dependence of the projectile energy are available e.g. in [69], but are on the same scale as the simple estimate ($\sigma_n \simeq 10^{-19}\,\mathrm{m}^2$) and show only a variance of a factor of 2 over a large energy range, so the simpler model in Equation 3.9 is used in ERO2.0.
Using the cross-section σ_n, the collision rate of the test particle is calculated from the particle's relative velocity to the neutral particle background and the local neutral particle density. From this collision rate, the probability of the test particle to collide with a background particle in the current time step is calculated, and a random number is chosen to check if a collision takes place. If this is the case, ERO2.0 uses a simple model for the collision process, where only the velocity direction changes isotropically and the magnitude and thus energy of the particle remains constant.
The relative importance of these two main collision processes can be estimated by calculating the mean free path λ_{mfp}. For the ion-ion collisions, the collision time can be derived from basic assumptions about the plasma (e.g. [128, p.69] and [34]):

$$\tau_{ii} = \frac{12\pi^{3/2}\epsilon_0^2 m_i^{1/2} T_i^{3/2}}{n_i Z^4 e^4 \log(\Lambda)} \tag{3.10}$$

where ϵ_0 is the vacuum permittivity, m_i the mass of the plasma species, T_i the plasma ion temperature, n_i the plasma ion density, Z the mean charge state of the plasma, e the elementary charge, and $\log(\Lambda)$ the Coulomb-logarithm [128, p.725]. For a test particle with velocity v_{proj}, the mean free path $\lambda_{\mathrm{mfp},ii}$ can be calculated as

$$\lambda_{\mathrm{mfp},ii} = v_{\mathrm{proj}}\,\tau_{ii} \tag{3.11}$$

Considering the collisions of particles with the background neutrals, the cross-section of the collision σ_n and the local neutral particle density n_n determine the mean free path:

$$\lambda_{\mathrm{mfp},n} = \frac{1}{\sigma_n n_n} \tag{3.12}$$

The mean free path of particles in typical conditions used in this work is evaluated in section 5.2, where the plasma scenarios are introduced.

3.1.4 Implementation of Plasma-Wall Interactions in ERO2.0

Plasma fuel and impurities can interact in different ways with the plasma-facing materials in magnetically confined devices (see chapter 2), and each process needs unique treatment and implementation in a plasma transport and PWI code like ERO2.0. The two main distinctions in the PWI module of ERO2.0 are interactions (a) between the traced impurity particles and the wall, and (b) between the background plasma (usually D or H fuel) and the wall.

The first case takes place after a traced particle hits a PFC in the ERO2.0 impurity transport module. Three main effects are handled: (i) reflection of the impinging particle, (ii) deposition/implantation of the impinging particle, and (iii) sputtering of the wall material – see chapter 2 for a description of the underlying physics. Reflection takes place instantly in the runtime of the impurity tracing module of the ERO2.0 main loop (see Figure 3.3), while sputtering and deposition are calculated once per loop in the ERO2.0 PWI module, integrated over all particle-wall collisions that took place in the tracing module.

Physical sputtering of the wall material by energetic projectiles is calculated using a sputtering yield. The sputtering yield $Y(E, \theta)$ is the ratio of released target particles to impinging projectile particles and depends strongly on the atomic masses of the target and projectile, as well as the impact energy and angle of the projectile on the target. In ERO2.0, all this information is available for the traced particles, since the traced particle's species and velocity are known at all times, and the impact angle and target mass can be evaluated at each collision. It should be mentioned that both the pure FO and the hybrid AGCA simulation modes (see section 3.1.2) resolve the impact angle.

A pre-calculated database of SDTrimSP calculations (see section 3.3) for a wide range of projectile-target combinations is available for ERO2.0. For all database combinations used in this work, pure and smooth surfaces were assumed. However, impure surfaces can also be present in the ERO2.0 code (arising due to the homogeneous mixing model, see section 3.1.5) – for these, a linear interpolation of the sputtering yields, scaled by the surface concentrations of all surface elements is performed. For example for the impact of D particles on a surface with surface composition $\{c_i\} = \{70\%\ \text{Mo},\ 20\%\ \text{Be},\ 10\%\ \text{Fe}\}$, the effective sputtering yield is

calculated as

$$Y_{\text{tot}} = \sum_i c_i \; Y_{D\to i} \tag{3.13}$$

$$= 0.7Y_{D\to Mo} + 0.2Y_{D\to Be} + 0.1Y_{D\to Fe}$$

This serves as a simple estimate, as the sputtering yield is known not to scale linearly with surface concentration and no layer effects are considered [111]. SDTrimSP can reproduce this non-linear behaviour, as mixed surfaces can also be simulated in the code. For use in ERO2.0, a full scan of the concentration space would be needed, since the homogeneous mixing model can create surfaces with arbitrary concentrations depending on the fluxes present. The database would scale exponentially in size with the amount of materials possible in the surface. Another option to use this data would be a dynamic coupling of ERO2.0 with the SDTrimSP code, as it was implemented in the predecessor ERO (called ERO-SDTrimSP [24]). Since both of these options are not feasible in ERO2.0 at the moment, the linear approximation in Equation 3.13 is presently used. To calculate the velocity of the sputtered particles, a cosine distribution for the azimuthal angle and a Thompson-distribution [119] for the energy are assumed. Other possibilities for the choice of angular distribution implemented in ERO2.0 include the so-called butterfly distributions [28, 30, 72] or sampling of angles gathered from additional SDTrimSP simulations, but these options are not applied in this work. More details on the implementation of the distributions can be found in [103]).

Reflection of particles is also handled by the SDTrimSP database, as the SDTrimSP code analyses this effect and calculates a reflection probability $R_N(E, \theta)$ between 0 and 1. In ERO2.0, this is taken into account instantly when a particle collides with the wall. The reflection probability R_N is calculated, and the particle leaves the surface again as a neutral with its Monte-Carlo weight multiplied by R_N, since one test particle represents a large amount of real atoms. For mixed surfaces, linear interpolation is performed for R_N, similar to Equation 3.13. For the velocity of reflected particles, in this work the energy is set by an energy reflection coefficient provided by SDTrimSP, the azimuthal angle follows a cosine distribution and the poloidal angle is chosen uniformly.

The fraction $1 - R_N$ of the particle's Monte-Carlo weight that was not reflected in the wall collision remains in the surface, unless the traced particle is of a gaseous species (e.g. H, He), in which case the remaining fraction is assumed to instantly recycle and is not traced further. In ERO2.0, there is no internal distinction between implantation and deposition, so all particles remaining in the wall are

treated in the same way, independently of their impact energy. This covers the three main effects – reflection, deposition/implantation and sputtering – taken into account for interaction of traced particles with PFCs in ERO2.0.

For the background plasma interaction with the wall, the treatment is less direct, since the plasma itself is not simulated by ERO2.0. The main sputtering mechanism by plasma relevant for this work is physical sputtering, but chemical erosion or chemically-assisted physical sputtering (CAPS) can also be simulated. The implementation of the two latter processes are not described here further, because they are not used in this work. To determine the physical sputtering by the plasma background, the impact angle, the impact energy, the ionization level and the particle fluxes are required, but further calculations or assumptions are needed to determine these values.

For the impinging plasma fluxes, there are several options. On the one hand, 3D plasma codes like EMC3-EIRENE [32] can provide the fluxes directly on each cell of the discretized PFC geometry, which can be used directly in ERO2.0 in case the geometry is identical. However, most plasma codes assume toroidal symmetry and operate in the 2D R-z-plane. If such a 2D code (e.g. EDGE2D-EIRENE or SOLPS-4.3/OEDGE, see section 3.4) delivers a poloidal flux profile, ERO2.0 can map the fluxes to the 3D wall components assuming nearest neighbour extrapolation. If none of these options are possible, ERO2.0 can internally calculate the plasma fluxes onto each surface cell of the 3D wall geometry by taking into account the local plasma parameters and the magnetic geometry. 3D effects (e.g. toroidal or poloidal shaping of the wall elements) need to be taken into account due to magnetic shadowing – an effect that arises due to the majority of transport being parallel to magnetic field lines, which severely reduces the flux into magnetically shadowed areas. Therefore, ERO2.0 can perform magnetic field line tracing to calculate the magnetic connection length on each surface cell[3]. ERO2.0 commonly uses a simple model where a surface is assumed to be completely shadowed if its connection length is less than a threshold value, e.g. in this work 6.0 m for ITER and 2.7 m for JET.

Based on the flux information calculated on all surface cells, the ERO2.0 code then calculates the sputtering of the PFC. For the impact angle of the impinging background plasma particles on the wall, distributions can be used for the calculation of sputtering, but usually a constant impact angle is assumed, which also decreases the computation time noticeably. This is a simplification, but it has been

[3]The local magnetic connection length is defined as the distance between PFCs along the magnetic field lines and can thus be locally calculated by following the field line originating from a PFC.

found from kinetic simulations [20] that impact angle distributions of fuel ions are sharply peaked around 60° as long as the magnetic angle is sufficiently shallow ($\lessapprox 10°$), taking into account the gyrating particle motion in the magnetic field and $E \times B$-drift effects in the sheath. Therefore, 60° is assumed as the impact angle throughout this work for sputtering of PFCs by the plasma background particles. For the impact energy of plasma background particles, the value

$$E = 2k_B T_i + 3k_B Z T_e \tag{3.14}$$

is assumed [112], where $T_{i/e}$ is the local background temperature of ions/electrons at the surface cell, respectively, and Z is the effective charge state of the plasma. The first term describes the incoming heat flux by the one-way random flux density of the Maxwellian background plasma [112, p.92]. The second term describes the acceleration of background particles by the sheath potential (compare Equation 2.3) and is valid for hydrogenic plasmas with $Z = 1$, which are used exclusively in this work. For hydrogenic plasmas. However, especially when seeding gases are used in the plasma, higher effective charge states of the plasma background are possible. For the plasma background interaction with the PFCs, sputtering is the only mechanism considered. Implantation or deposition of the background plasma particles is not traced in the present ERO2.0 code, and all gases are assumed to recycle instantly.

3.1.5 Homogeneous Mixing Model (HMM)

Deposition and erosion processes on the wall can change the chemical surface composition of wall components after plasma operation. Material mixing is common especially in devices where multiple elements can be found among PFCs, as for example in the JET-ILW consisting of a Be first wall and a W divertor. For tracking these changes in ERO2.0, a Homogeneous Mixing Model (HMM) is implemented [83].

Once per main loop execution (see Figure 3.3), the HMM module can optionally be called in ERO2.0. For each surface cell of the 3D geometry, the following process is executed (see Figures 3.7 and 3.8 for a simplified visual representation): first, the volume V_{cell} of the cell is determined by the product of its surface area A and a surface interaction layer thickness d. d is defined by user input, which is further discussed below. At the start of the simulation, the cell volume is filled by a user-defined initial surface composition $\{c_{\text{init},i}\}$ of elements, where c_i is the surface concentration of element i and $\sum_i c_i = 1$. Each element occupies an initial

volume $V_{\text{init},i} = c_{\text{init},i} \cdot V_{\text{cell}}$. Underneath the cell, the bulk material lies with a fixed composition $\{c_{\text{bulk},i}\}$.
Afterwards, the total volume V_{dep} of particles deposited in the cell and the total volume V_{ero} of particles eroded from the cell are calculated as

$$V_{\text{ero/dep}} = A \cdot \Delta t_{\text{PWI}} \sum_i \frac{\Gamma_{\text{ero/dep},i}}{\rho_{N,i}} \tag{3.15}$$

with the cell surface A [m²], a user-defined plasma-wall interaction time Δt_{PWI} [s], and the element's number density ρ_N [atoms/m³]. $\Gamma_{\text{dep},i}$ and $\Gamma_{\text{ero},i}$ [atoms/m²s] are determined in the PWI module of ERO2.0 for each cell of the PFCs (see section 3.1.4). $V_{\text{ero}} > V_{\text{dep}}$ implies that more material is eroded than deposited, and the cell volume V_{cell} is not filled anymore. The missing volume V_{miss} is replenished by the bulk material, which is assumed to serve as an infinite reservoir underneath the interaction layer. The bulk concentration is taken into account to replenish volume of each element present in the bulk to fill up the missing volume:

$$\sum_i V_{\text{rep},i} = \sum_i (c_{\text{bulk},i} \cdot V_{\text{miss}}) = V_{\text{miss}} \tag{3.16}$$

If $V_{\text{ero}} < V_{\text{dep}}$, more material is deposited than eroded, and the total added volume V_{add} is taken into account for the concentration calculation. The new surface concentrations after the HMM are then calculated as the volumetric fraction that each element takes of the (potentially extended) cell volume:

$$c_{\text{new},i} = \frac{V_{\text{init},i} + V_{\text{dep},i} - V_{\text{ero},i} + V_{\text{rep},i}}{V_{\text{cell}} + V_{\text{add}}} \tag{3.17}$$

If erosion equals deposition ($V_{\text{dep}} = V_{\text{ero}}$) for species i, no material is replenished from the bulk ($V_{\text{rep}} = 0$) nor added to the surface ($V_{\text{add}} = 0$) and Equation 3.17 reads:

$$c_{\text{new}} = \frac{V_{\text{init}} + 0 + 0}{V_{\text{cell}} + 0} = \frac{V_{\text{init}}}{V_{\text{cell}}} = c_{\text{init}}$$

so the concentration is conserved as expected. In the next iteration of the ERO2.0 loop, the concentrations c_{new} are taken as the initial concentration of the cell.

As mentioned above, the HMM requires two parameters defined by user-input: the surface interaction layer thickness d and the plasma-wall interaction time Δt_{PWI} (not to be confused with the impurity tracing time step Δt), which both impact the volumes defined in Equation 3.17. ERO2.0 is usually used for evaluation of steady-state scenarios, in which the choice of d does not influence the final surface

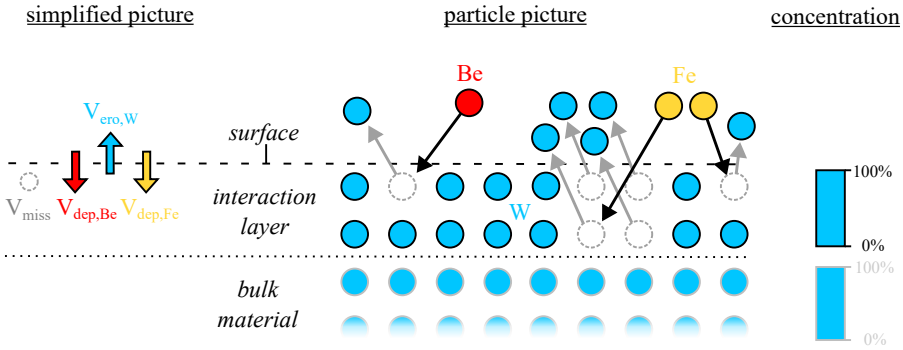

Figure 3.7: Sketch of the HMM (1): impinging particle fluxes erode material V_{ero} from the interaction layer of a surface cell, which can leave a gap V_{miss} in the cell volume. Some impinging particles are deposited (V_{dep}). At the start of the simulation, the concentration (right) in the interaction layer is identical to that of the bulk material below, unless set otherwise. The bulk material (solid grey outlined objects) serves as an infinite reservoir and does not interact with the particles or change in any way. Notes: a) the grid is only for illustration purposes; ERO2.0 does not perform any simulation of inter-surface processes and only calculates changes in the concentration. b) For simplicity, all elements are shown with the same size. ERO2.0 accounts for the density of each element to calculate the occupied volume.

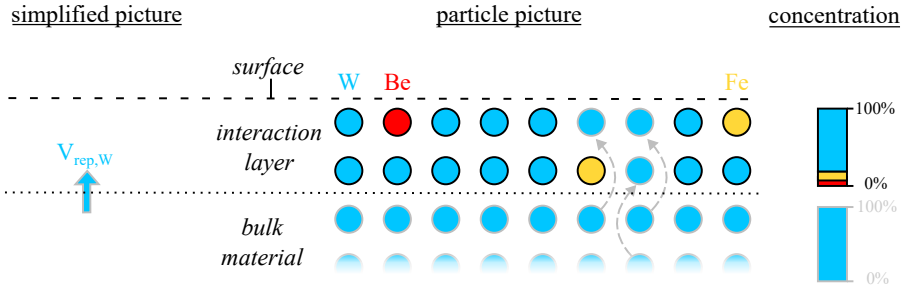

Figure 3.8: Sketch of the HMM (2): the deposited particles are integrated into the interaction layer and missing atoms are replenished from the bulk material (V_{rep}). The concentration of elements in the interaction layer (top right) changes, the bulk material stays unaffected. Since ERO2.0 only takes into account the concentration, the material is assumed to spread homogeneously in the interaction layer.

composition. The two parameters Δt_{PWI} and d can then be chosen rather arbitrarily as long as the time integration performs smoothly, because they affect how quickly the integration converges to steady state values. In this work, however, specified time periods corresponding to experimental campaign times (see section 6.2.1 and section 6.1.1 for more details) are simulated, so Δt_{PWI} is fixed. This implies that d also cannot be chosen arbitrarily any more. For this work, additional SDTrimSP calculations (see section 3.3) were performed to estimate d, using test ERO2.0 simulations in the specific mirror geometries as an input for the impact energy distribution. d generally scales with the energy of the impacting particles, so smaller values of d are used in more recessed areas, where the mean impact energy is lower due to earlier collisions with particles and wall elements. A study on the effect of the chosen layer thickness on the final results on the mirrors is described in section 6.3.1.

3.2 EIRENE

The EIRENE code is a three-dimensional kinetic neutral gas transport code utilizing Monte-Carlo methods. It was originally developed in the 1980s at Forschungszentrum Jülich for application in the TEXTOR tokamak [94], but has since become the de-facto neutral gas transport code in magnetic confinement fusion. It is applied in many devices and strong coupling is integrated in a wide range of plasma simulation code packages like SOLPS-4.3/OEDGE [71], EDGE2D-EIRENE [39] or EMC3-EIRENE [32].

EIRENE uses a kinetic description of the neutrals, and treats the real atoms by discretized test particles, similarly to the ERO2.0 code. Multiple species of neutral atoms and molecules of the fuel can be described and are treated by linear kinetic transport equations (Boltzmann equations) [94]. The EIRENE code solves them in a stochastic fashion under the test particle approximation (see section 3.1). EIRENE performs this calculation on a grid that extends up to the contour of the wall, further than the grids used in the plasma fluid boundary codes (see Figure 3.2).

EIRENE is commonly used in an iterative method with these plasma fluid boundary codes to provide the source terms for particles, parallel momentum, and energy for electrons and ions in the plasma fluid equations solved by the plasma boundary codes. Especially for high density divertor conditions, the kinetic treatment of neutral particles is essential, as a simplified fluid description of the neutral particles becomes incorrect under these plasma conditions. Based on the plasma density, temperature, and flow velocity information provided by the fluid plasma codes,

EIRENE takes into account volumetric sources of neutrals, e.g. volumetric recombination and charge-exchange processes of fuel ions, to sample particles which are traced throughout the simulation volume. Additionally, the fluxes of plasma ions onto the wall lead to a surface source term of neutral particles by recombination of the ions at the wall, as well as sputtering of wall material. Finally, point sources of neutrals can be defined, which is commonly applied to simulate gas puffing in fusion devices.
EIRENE is used in two distinct applications in this work: on the one hand, ERO2.0 modelling requires input by interpretative plasma boundary layer simulations, which employ code packages integrating EIRENE: the EDGE2D-EIRENE code package for the JET tokamak [38], and the SOLPS-4.3/OEDGE code package for predictive ITER plasma boundary layer simulations (see section 3.4). The toroidally symmetric plasma background information that these code packages provide in the R-z-plane is post-processed to the ERO2.0 grid and 3D simulation volume, as described in section 3.1.1.
On the other hand, EIRENE post-processing is performed as part of stage 1 of the multi-stage simulation workflow developed in this work (chapter 5), using the converged 2D plasma backgrounds as an initial condition. The stand-alone EIRENE simulation then determines the angular and energy distribution of impinging fuel neutral and CXN particles at specific poloidal locations in the recessed areas. The amount of particle trajectories simulated in this post-processing step is increased by around 4 orders of magnitude compared to the EIRENE simulations used for the interpretive plasma boundary layer modelling, massively increasing the statistics in recessed volumes.
The EIRENE energy and angular distributions of potentially highly energetic CXN used in this work were explicitly generated by EIRENE experts on request for this study, providing important input to the further ERO2.0 modelling in the multi-stage simulation workflow. CXN are especially important in this work, because in contrast to energetic plasma particles, the CXN are not confined by the magnetic field and can thus penetrate deep into magnetically shadowed regions and to recessed areas distant from the last closed flux surface (LCFS). The ratio of CXN neutrals to plasma ions reaching the first wall is dependent on the so-called wall clearance, defined as the distance between the LCFS and the wall contour. Present day devices like JET operate with small wall clearance of a few centimetres, thus, the ion flux contribution dominates over the CXN contribution by orders of magnitude. In the case of ITER and reactors, the distance is tens of centimetres. Thus, the role of energetic CXN is much more prominent, although the total flux to the wall is very low in the main chamber in comparison to ion fluxes at the divertor

with direct intersection of the separatrix at the target plates. Therefore, the EIRENE post-processing is critical for this work, providing accurate information about the CXN entering the recessed volumes.

3.3 SDTrimSP

SDTrimSP [81] is a surface interaction code for mono-energetic projectiles operating under the binary collision approximation (BCA) and is based on its predecessor Trim ("Transport of Ions in Matter"). SDTrimSP simulates the impact of an energetic projectile on a target surface and the resulting collision cascade (see section 2.2) in the target material, assuming a fixed projectile energy E and impact angle θ relative to the surface normal. The collision cascade is described by binary collisions between the particles, illustrated in Figure 3.9. All moving particles

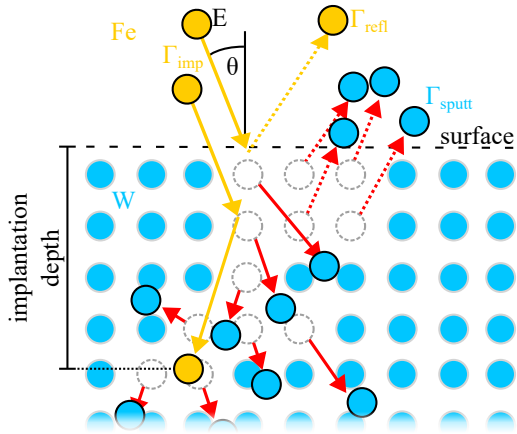

Figure 3.9: Sketch of an SDTrimSP simulation, shown here for Fe projectiles (yellow) and a W target (blue): collision cascade (red arrows) of impinging particles with flux Γ_{imp}, energy E, and impact angle θ. The trajectories of target and projectile atoms define the target sputtering Γ_{sputt} (red dashed arrows), the projectile reflection (yellow dashed arrows, Γ_{refl}), or projectile implantation, which gives an estimate of the average implantation depth.

are traced until they either leave the surface or until their energy is dissipated in elastic collisions with target electrons in the material. Only neutral projectiles are considered, thus no transport effects by electric or magnetic fields are considered. SDTrimSP can be performed in two modes: (i) static mode, in which the target is reset to its initial state after each particle impact, or (ii) dynamic mode, in which target damage and surface composition changes accumulate. Static mode simulations of SDTrimSP are performed in the scheme of this work to generate

the ERO2.0 database of impurity- and plasma-wall interactions, providing crucial information: the physical sputtering yield Y and corresponding threshold energy E_T, the reflection probability R_N and the implantation depth (see section 3.1.4 for an explanation of these values). Y and R_N can be calculated from SDTrimSP simulations as the ratio of target flux or projectile species flux leaving the surface, respectively, to the impinging projectile flux (compare Figure 3.9):

$$Y = \frac{\Gamma_{\text{sputt}}}{\Gamma_{\text{imp}}}$$

$$R_N = \frac{\Gamma_{\text{refl}}}{\Gamma_{\text{imp}}}$$

In the ERO2.0 database, a set of SDTrimSP calculations in the (E,θ) parameter space is performed for each projectile-target combination. For this work, an array of SDTrimSP simulations assuming 28 energies in the range from 1 eV to 12 500 eV and 20 angles from 0° to 89° was generated. For each of 20 elemental combinations that originally were not available in the database, a total of 560 SDTrimSP calculations were therefore performed. Present combinations in the database were used where available, which used a reduced grid size of 500 points covering energies up to 5000 eV. Since particle impact energies are expected to remain below 2000 eV in this work, all SDTrimSP datasets have effectively identical resolution. It should be noted that the surfaces are assumed to be clean, flat surfaces for the SDTrimSP calculations used in this work, which is in line with the total sputtering yield approximation for mixed surfaces in ERO2.0 (Equation 3.13).

Visualizations of the D → Be dataset can be seen in Figures 3.10 and 3.11. Between

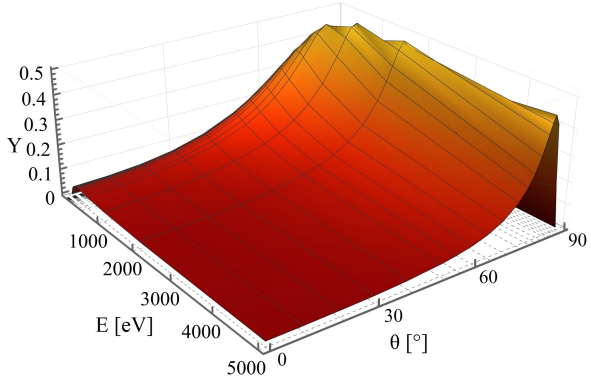

Figure 3.10: Sputtering yield Y of a pure Be surface bombarded by D particles in the parameter space of impact energy E and impact angle θ.

the data points, bilinear interpolation is used, as in the ERO2.0 simulation.
Finally, two more important parameters can be estimated by the SDTrimSP code and find use in the ERO2.0 simulation workflow: on the one hand, the threshold energy E_T for physical sputtering of a given projectile-target combination can be estimated, which reflects the projectile energy required to release a target atom from the bulk material matrix. E_T is defined in this work as the lowest energy at which a non-zero sputtering yield Y is found at any impact angle in the SDTrimSP simulations.
On the other hand, the SDTrimSP code calculates the average implantation depth of particles into the target surface, which is used in this work to estimate the surface interaction layer thickness d (see section 3.1.5) for use in the HMM module of ERO2.0. Specific combinations of projectile and target material were simulated with SDTrimSP to obtain estimates for d in the conditions required for this thesis, such as highly energetic D CXN impinging on a Mo mirror surface, so that a concise time integration of the surface mixing can be performed.

3.4 Other Codes and Databases

With the impurity transport, neutral transport and plasma-wall interaction covered by the codes introduced before, two gaps are left in the main workflow (Figure 3.1): plasma background generation and databases for atomic processes.
The plasma backgrounds used in this thesis were generated by two 2D plasma-boundary code packages. For JET, EDGE2D-EIRENE was used. EDGE2D-EIRENE is a code package for estimating plasma parameters (e.g. temperatures, densities, and flow velocities of electrons, ions, and neutrals) in the 2D scrape-off layer and near-separatrix region of fusion devices. It consists of a coupling of EIRENE [39] (see section 3.2) and the fluid edge code EDGE2D in an iterative scheme. EDGE2D solves the 2D Braginskii fluid equations [11, 110] for multiple species. Anomalous cross-field diffusion and thermal force effects are included in the code. For this work, the plasma backgrounds provided were calculated without additional cross-field drift effects like the $E \times B$-drift.
The equivalent plasma code package for ITER is SOLPS-4.3 [18], consisting of the 2D multi-fluid transport code B2 and the neutral particle transport code EIRENE [129]. B2 solves the 2D Braginskii equations [11, 120] and can include drift effects, which can in general be applied for high fidelity simulations for ITER and other machines with focus on e.g. divertor conditions, but were not required here with focus on the first wall interaction. Inside the SOLPS-4.3 package, the neutrals description is performed by EIRENE in an iterative coupling scheme with

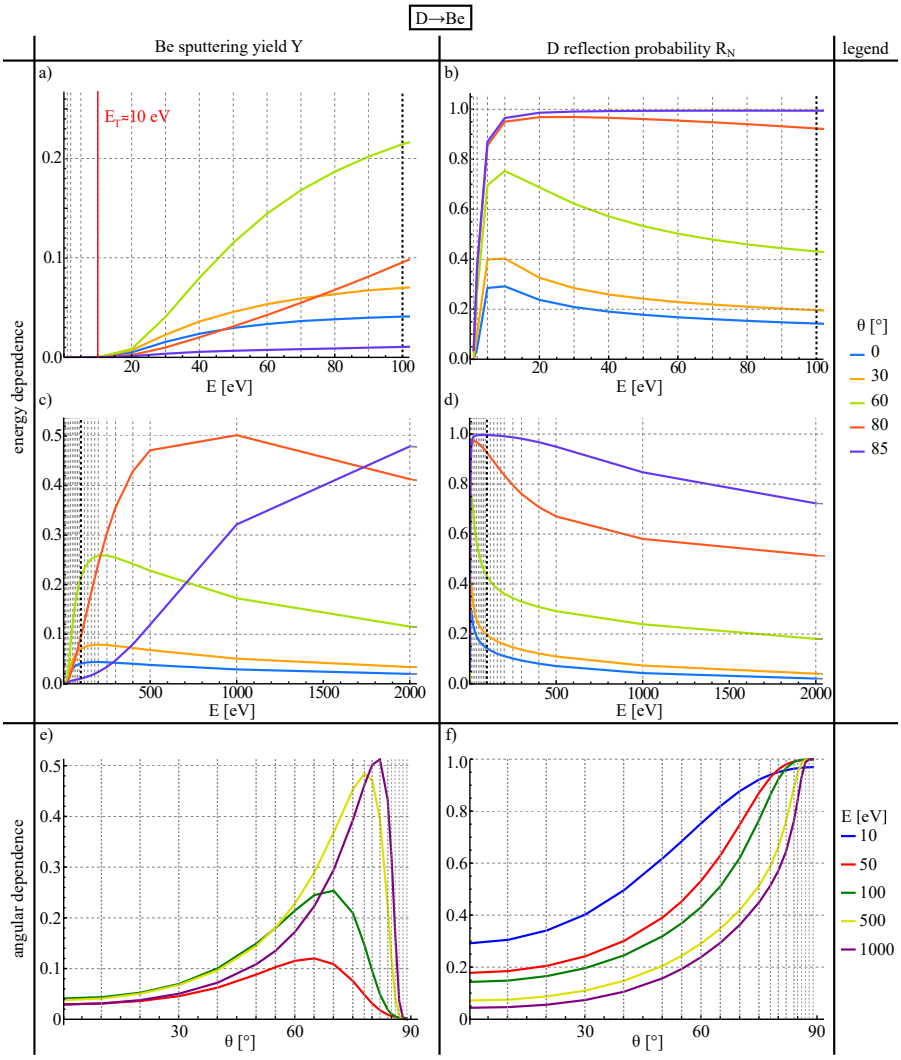

Figure 3.11: Results of SDTrimSP simulations of a pure Be surface bombarded by D particles with energy E under impact angle θ. a), c), e): Sputtering yield of Be target. b), d), f): Reflection probability of D projectiles. a)-d) show energy dependence at fixed impact angle, e)-f) show angular dependence at fixed impact energy. The sputtering threshold energy E_T is marked in a). The vertical grey lines mark points in the ERO2.0 database of SDTrimSP simulations.

B2. The plasma background is simulated on the B2 grid around the separatrix and in the divertor (as shown in Figure 3.2). With the OEDGE suit of codes, the 2D plasma background calculated by SOLPS-4.3 can be extended up to the 2D apex contour of the potentially toroidally shaped first wall. Onion-skin modelling and EIRENE are applied to solve 1D Braginskii equations [114] along the magnetic flux tubes in the far-SOL. This extension of the grid and the plasma solution to the first wall apex reduces the required extrapolation of plasma conditions necessary in ERO2.0. However, the 3D ERO2.0 simulation extends up to all first wall surfaces, which includes toroidally shaped elements lying behind the apex. Therefore, extrapolations or sound physical assumptions are necessary to fill the gap of the plasma background information by OEDGE to the real 3D wall elements. Studies about extrapolations with exponential decay or constant plasma conditions are described in [100]. Note, that EIRENE also simulates in full 3D up to the apex of shaped wall elements, but the EIRENE and ERO2.0 simulation volumes are not identical, since ERO2.0 takes even toroidal gaps into account (see Figure 3.2).
Finally, only the atomic processes remain to be covered from the main workflow of ERO2.0. The ADAS [116, 117] database is chosen, providing data on the ionization and recombination rates of ionized and neutral particles in a plasma background. Electron excitation rates are can be queried for the optional simulation of synthetic diagnostics in ERO2.0, providing a technique to benchmark simulations with measurements [103]. The ADAS database provides the reaction rates and population coefficients of electron energy levels in dependence on plasma background electron temperature and density. The underlying calculations are based on self-consistent collisional-radiative modelling (CRM) [41]. A visualization of the ionization rate of neutral beryllium originating from the ADAS database is shown in Figure 3.12. The ionization rate strongly depends on the plasma temperature and density, and can thus significantly affect impurity transport.
For completeness, it should be mentioned that in select simulation cases, additional atomic and molecular data is needed for ERO2.0 and queried from other databases. One such example is the simulation of chemical erosion, in which molecules are eroded from the surface (see section 2.2). The accurate simulation of molecule transport requires dissociation rates, which are taken from Ref. [53] for hydrogenic species.

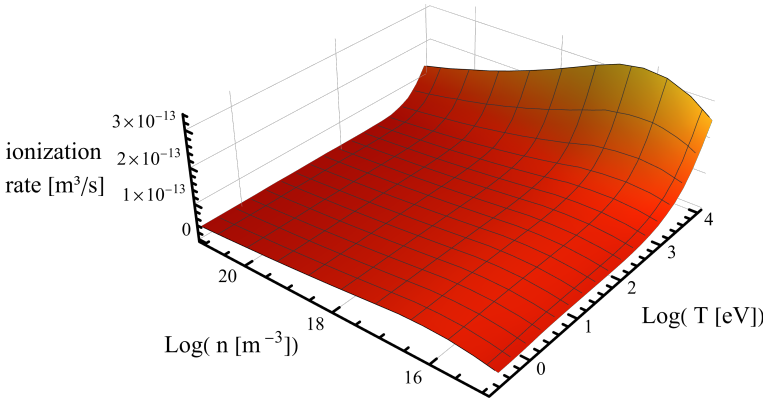

Figure 3.12: Ionization rate of Be^0 in dependence of plasma temperature and density (both shown here with logarithmic scale) taken from the ADAS database [116]. In this work, especially the region of low density ($<10^{16}\,m^{-3}$) and low temperature ($<1\,eV$) is relevant for the simulation of recessed areas.

Chapter 4

ERO2.0 Code Optimization

Monte-Carlo transport codes like ERO2.0 have the intrinsic drawback, that areas in which low fluxes are expected suffer by definition from statistics issues: simulated test particles ideally correctly follow physical laws and thus low-flux regions are reached only by a low amount of test particles. The recessed volumes analysed in this work lie far outside the core plasma, where especially the fluxes of ions are expected to be very low, since the magnetic field confines charged particles. Energetic CXN particles are in contrast not confined and may enter the recessed regions largely unperturbed. However, the fluxes of both of these sources, as well as (re-)eroded material fluxes from the plasma-facing components (PFCs) need to be resolved correctly to decrease the uncertainty in deposition and erosion on the recessed wall components and mirrors, which requires a large amount of test particles per surface cell.

One possibility to circumvent this problem is to trim the simulation volume to a small, local volume around the low-flux area of interest so that all simulated particles by definition traverse this volume and deliver relevant information, as it was commonly done in ERO [56], the predecessor version of ERO2.0. However, this approach does not lead to a self-consistent simulation – fluxes entering the local simulation volume need to be estimated beforehand to set the boundary conditions at the edges of the simulation volume, leading to potentially large uncertainties. ERO2.0 was introduced with the premise of massive code speed-ups and parallelization so that global, and thus, self-consistent transport simulations are possible. However, more and more particle trajectories need to be simulated to allow the self-consistent simulation approach to reach into the distant areas relevant for this work. Due to limited computing power and time, additional code optimizations are needed to significantly increase the amount of simulated particles required to provide statistically relevant results.

In a recent development, particle tracing methods applying Guiding-Centre Ap-

proximation (GCA) were introduced into the ERO2.0 code [96], providing an alternative to the Full-Orbit (FO) tracing method that ERO2.0 usually applies in simulations. The respective equations of motion and Fokker-Planck collision terms can thus be solved in either tracing method. Additionally, a hybrid simulation mode called *adaptive GCA* (AGCA) was introduced, in which GCA tracing methods are applied for the largest part of the particle trajectory far away from PFCs. A switch to the FO tracing method is performed whenever the particle is close to a PFC, where the higher accuracy and angular information of the FO tracing method is necessary. The implementation of GCA in ERO2.0, described in Ref. [96], focussed on the verification and validation of the implementation, which made direct comparisons to other transport codes applying GCA possible, e.g. ASCOT [45] or DIVIMP [107]. However, the performance of the AGCA simulation mode was unsatisfactory regarding computation speed compared to corresponding simulations in the pure FO simulation mode, which includes a higher level of sophistication in physical accuracy. The validation of the implementation revealed that the length of the tracing time step Δt_{GCA} was severely limited, because significant energy loss and numerical drifts took place at larger time steps [96]. Smaller time steps were required, leading to the comparative lack of computation speed in the AGCA simulation mode. Therefore, the updates to the ERO2.0 code performed in this thesis focus on optimizations to the AGCA simulation mode, with focus on the GCA tracing methods. A significant gain in code performance is intended, which in turn is necessary for increased statistics in the low-flux recessed regions. In the following sections, the implementation of the optimizations is described and verified, using test cases to determine the effect on numerical stability and computation speed.

4.1 Higher-Order GCA Algorithms

In the original implementation of the GCA tracing method into ERO2.0 [96], the simplest numerical scheme was used to solve the equations of motion in GCA – the explicit first-order Euler scheme [89]. For the five-dimensional phase space consisting of guiding centre location $\mathbf{R}$, parallel velocity $v_{\parallel}$ and magnetic moment μ, the equations of motion (see Equations 3.4-3.6) can be discretized to advance from time step t_n to t_{n+1} with time step length Δt in the Euler scheme, which

gives:

$$\mathbf{R}_{n+1} = \mathbf{R}_n + \mathbf{v}_{\mathrm{GC},n}\,\Delta t \tag{4.1}$$

$$v_{\parallel,n+1} = v_{\parallel,n} + a_{\parallel,n}\,\Delta t \tag{4.2}$$

$$\mu_{n+1} = \mu_n \tag{4.3}$$

A full derivation of the steps can be found in Ref. [96]. The magnetic moment stays constant, while the other two variables change according to the guiding-centre velocity $\mathbf{v}_{\mathrm{GC}}$ and the parallel acceleration $a_\parallel$, respectively, which are defined as:

$$\mathbf{v}_{\mathrm{GC},n} = v_{\parallel,n}\mathbf{b}_n + \frac{\mathbf{E}_n \times \mathbf{b}_n}{B_n} + \left(\frac{\mu_n}{q} + \frac{v_{\parallel,n}^2}{\omega_L}\right)\frac{\mathbf{b}_n \times (\boldsymbol{\nabla} B)_n}{B_n} \tag{4.4}$$

$$a_{\parallel,n} = \frac{q}{m}\mathbf{E_n}\cdot\mathbf{b}_n - \frac{\mu_n}{m}\mathbf{b}_n \cdot (\boldsymbol{\nabla} B)_n \tag{4.5}$$

$$\mathbf{b}_n = \frac{\mathbf{B}_n}{B_n} \tag{4.6}$$

The particle with electric charge q, mass m and Larmor frequency $\omega_L = \frac{qB}{m}$ is affected by the total electric field $\mathbf{E}$ and the magnetic field $\mathbf{B}$ with magnitude B and direction $\mathbf{b}_n$. $\boldsymbol{\nabla}$ denotes the differential nabla operator, and defines the magnetic field gradient $\boldsymbol{\nabla} B$. The index n denotes that the quantity should be evaluated at time step t_n at location $\mathbf{R}(t_n)$. The Euler scheme is explicit, therefore only evaluations of parameters at time step t_n are needed to calculate the next iteration of the phase space coordinates.

In order to enhance the numerical stability of GCA tracing methods in ERO2.0 and potentially enable larger time steps, two higher-order integration algorithms are implemented in this work: (i) Heun's method, a second order algorithm, and (ii) a fourth order Runge-Kutta (RK4) algorithm. Both are standard numerical integration schemes and are described in detail e.g. in Ref. [89]. Since multiple definitions of higher-order algorithms by different weights of the intermediate steps are possible, the three algorithms implemented in ERO2.0 are represented by exactly the following Butcher tableaus – for the Euler algorithm:

$$\begin{array}{c|c} 0 & \\ \hline & 1 \end{array}$$

For the Heun algorithm:

$$\begin{array}{c|cc} 0 & & \\ 1 & 1 & \\ \hline & \frac{1}{2} & \frac{1}{2} \end{array}$$

And for the RK4 algorithm:

$$\begin{array}{c|cccc} 0 & & & & \\ \frac{1}{2} & \frac{1}{2} & & & \\ \frac{1}{2} & 0 & \frac{1}{2} & & \\ 1 & 0 & 0 & 1 & \\ \hline & \frac{1}{6} & \frac{1}{3} & \frac{1}{3} & \frac{1}{6} \end{array}$$

As a first verification of the implementation, a test simulation in JET magnetic geometry is performed. Collisions with background particles, anomalous diffusion, ionization, and recombination are disabled for the test, so that a purely deterministic simulation with ideally full energy conservation of the traced particles is provided. The energy conservation and computation time across 20 simulation cases is compared: five discretization time steps of increasing length ($\Delta t \in \{1, 5, 25, 125, 625\}$ ns) are analysed for each of the four tracing methods – FO tracing, and GCA tracing with the three implemented numerical algorithms: Euler, Heun and RK4. Ten beryllium (Be) particles are injected at the outer mid-plane at $\mathbf{r} = (3.7, 0.0, 0.33)$ m with energies in the range 25–500 eV and varying ratios of parallel and perpendicular energy relative to the magnetic field. The starting conditions are identical across all simulation cases and the particles are traced for 0.1 s, a typical dwelling time of particles found in transport modelling of JET limiter plasmas [96]. The simulation case using the FO tracing method with the smallest time step is defined as the reference case.

A depiction of the trajectories from all 20 simulation cases is presented in Figure 4.1. The Euler scheme, which originally was the only numerical scheme present for the GCA tracing method in ERO2.0, fails to accurately simulate the Be particles at time steps larger than 25 ns, since a significant drift of the particles in outward direction is clearly visible. In all other simulation cases, the trajectories of banana- and passing orbits remain closed over the full tracing time. There is some broadening of the trajectories visible in the simulation using the FO tracing method with the highest time step ($\Delta t = 625$ ns). Since the gyration time of the particles ($T_L \sim 150$ ns) cannot be resolved by the chosen time step, the Larmor radius is overestimated, causing the broader width of the trajectory. In contrast,

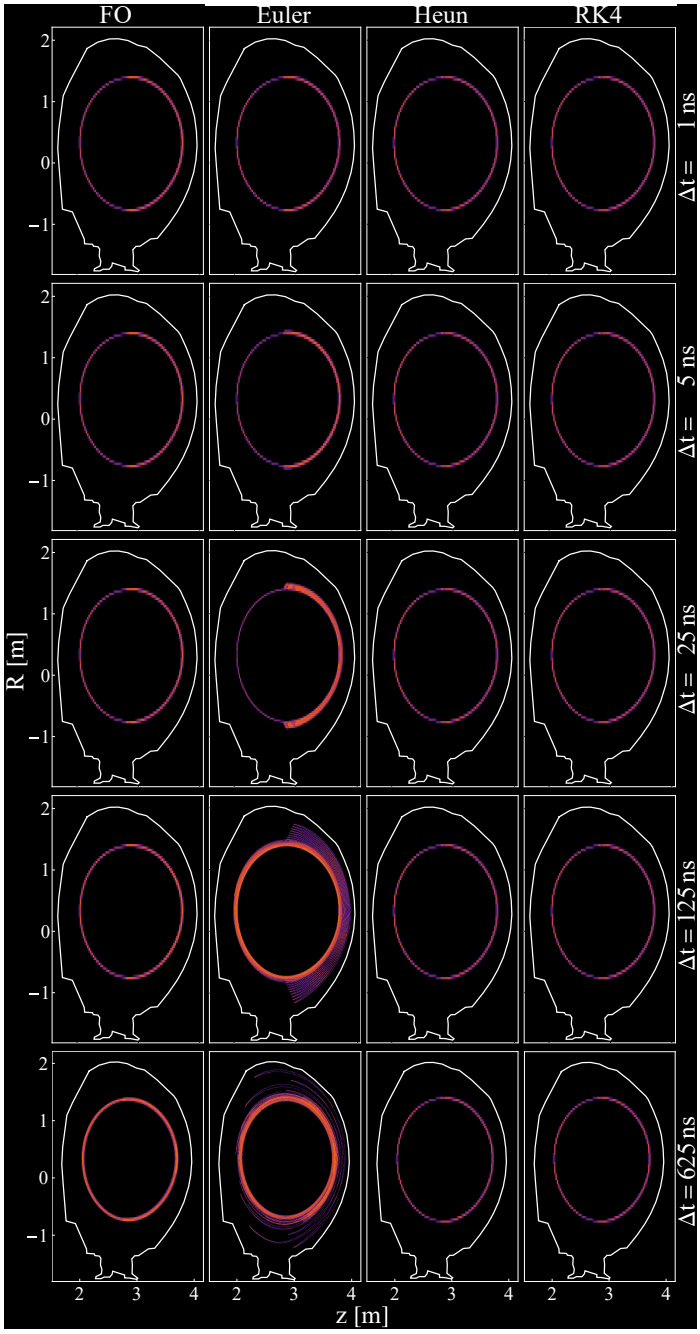

Figure 4.1: 2D traces of 10 Be particles injected in the outer mid-plane with energy between 25 and 500 eV. The tracing methods (FO and three numerical integration algorithms applied during GCA) are compared with different discretization time step Δt. The JET wall contour is shown in white.

the simulations using the newly implemented higher-order GCA tracing algorithms (Heun and RK4) show a generally thinner width of the trajectories, since the gyration is not included in the approximation. Even at the largest time steps, both of the newly introduced algorithms show no visible discrepancy to the reference case.

Full energy conservation is expected in the chosen simulation case, which is tested by determining the particle's energy at the start and end of its trajectory. The maximum relative energy loss over the ten traced particles is shown in Figure 4.2a) for all cases. The FO tracing method applies the energy-conserving Boris-algorithm, so the energy loss is in the range of numerical accuracy ($<10^{-10}$ %) for all time steps as expected. The relative error in simulations using the GCA tracing method with the Euler algorithm measures up to 40 % at the highest time step analysed. In contrast, both higher-order numerical algorithms show significantly enhanced numerical stability, with a relative error smaller than 0.01 % for all cases apart from the largest time step. The numerical error is within 2% between the Heun

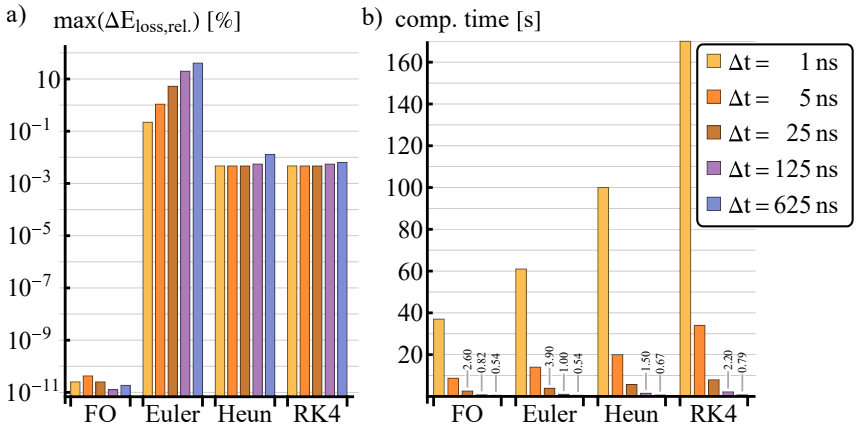

Figure 4.2: a) Maximum relative Be particle energy loss (logarithmic scale) measured in twenty simulation cases using four different tracing methods and five increasing time steps. b) Computation time of the simulations.

and RK4 numerical schemes at identical time step apart from the largest time step, where the RK4 algorithm shows 71% less energy loss compared to the Heun algorithm. This implies that the RK4 algorithm is superior to the Heun algorithm at even larger time steps than tested here, but at smaller time steps the Heun algorithm is sufficient. The higher-order RK4 algorithm comes at a cost, since the additional steps in the RK4 algorithm need further calculations, which increases the computation time (see Figure 4.2b). The Euler method takes on average 1.39x as long as the simulation using the FO tracing method at identical time step, the

Heun algorithm 2.05x and the RK4 algorithm 4.17x, respectively. In practice, the Heun algorithm has proven to show sufficient for the needed accuracy in energy conservation and trajectory resolution in all tested scenarios, while executing the computation around twice as fast as the RK4 algorithm. Therefore, the Heun algorithm is used whenever GCA tracing methods are executed in the remainder of this work, unless specified otherwise.

4.2 Handling of Wall Collisions in GCA

With the improved stability of the higher-order GCA tracing algorithms introduced in section 4.1, much larger time steps are possible for discretizing the particle trajectories. However, GCA tracing methods are not desirable throughout the full simulation volume – wall collisions in GCA should be avoided, because the impact angle is not correctly resolved in this tracing method. The sputtering yield and reflection probability of particles depend strongly on the impact angle (see section 3.3 and Ref. [26]), therefore the FO tracing method is necessary near the wall. The FO resolution of the ERO2.0 code is therefore a large advantage of the code over impurity transport and PWI codes based on GCA (e.g. the 2D Monte-Carlo transport code DIVIMP [113]) when considering the physical accuracy of wall collisions, and thus any plasma-wall interaction process. Additionally, geometric features of plasma-facing components on the scale of the gyration radius (e.g. toroidal gaps and leading edges on castellated divertor and first wall components) require the resolution of the gyration for accurate modelling, as PIC modelling has shown [40].

The hybrid simulation mode *adaptive GCA* (AGCA) in ERO2.0 [96] aims to retain the accuracy of the FO tracing methods for an accurate description PWI. In AGCA, the distance of the particle to the PFCs is continuously determined whenever, to ensure that the particle is not close to the wall and the GCA tracing method can be safely applied. In GCA however, the particle's true location is only known with an uncertainty of the particle's current Larmor radius, in contrast to the FO tracing method where the particle's true location is known at all times. To make sure that no particle collides with the wall while GCA tracing methods are applied, the FO tracing method is mandated as soon as a particle enters a region close to the wall, labelled here as *Mandatory Full-Orbit* (MFO) region. The width of this region, is defined by the distance $\eta \cdot r_L$ (see Figure 4.3) and takes into account the uncertainty of location in GCA. The distance buffer factor η defines a buffer distance so that the traced particle has enough space to execute its FO trajectory before hitting the wall when the tracing method is switched. η is defined by user

input, and a value of around 2.5 has proven to avoid collisions in GCA with the comparably small time steps used in the original GCA implementation. However, the number η shall be chosen as small as reasonable so that GCA can be executed as long as possible to reap the benefits of the faster computation.

The possibility of overstepping the MFO region completely is significantly increased

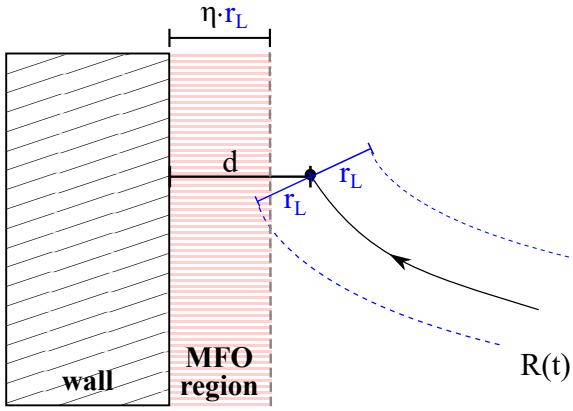

Figure 4.3: In adaptive GCA tracing mode, a particle is not allowed to execute GCA if its distance d to the nearest wall segment minus the uncertainty in position of r_L is smaller than a user-defined number η (typically $\sim 2.5 - 5$) times their current Larmor radius r_L. In the light red area ("mandatory full-orbit"-region), only FO tracing is allowed.

for particles with the computationally stable GCA tracing methods introduced in this thesis, since larger time steps are enabled. As an example, in the simulation presented in section 4.1, $\Delta t = 625\,\text{ns}$ was used as maximum time step, which leads to a step distance of up to 6.44 cm for a Be particle with 500 eV energy. In theory, the distance buffer factor η can be manually adjusted to larger values so that the MFO region is large enough to catch all particles. However, the exact value is hard to judge beforehand and an increase of η comes at the cost of performance, because the volume in which GCA tracing methods are executed becomes smaller the wider the MFO region is chosen. Additionally, even a particle ensemble thermalized to a Maxwellian velocity distribution has a high-energy tail, so that there is always a remaining probability for particles to become fast enough to overstep the region and cause an incorrect wall interaction process.

As a countermeasure, a more proactive approach was added in the scope of this work: a fallback mechanism was implemented (see Figure 4.4). When a particle hits the wall while it is simulated with GCA tracing methods, the collision is discarded. Instead, the particle's location, velocity, and charge state are reverted to its state before the last tracing step and the FO tracing method is mandated for at

least three gyrations. If the particle was moving towards the wall, it is likely that it reaches the MFO region, therefore further applying the FO tracing method and resolving the wall collision correctly. If the MFO region is not reached, the particle will switch back to GCA tracing and the fallback method will trigger again if it repeatedly collides with the wall during the GCA tracing method. Infinite loops of this mechanism can be excluded, as three full gyrations of the FO tracing method is mandated each time a fallback step is executed. This way, a user-independent precaution was implemented for the AGCA simulation mode, so that all collisions are correctly treated in the FO tracing method.

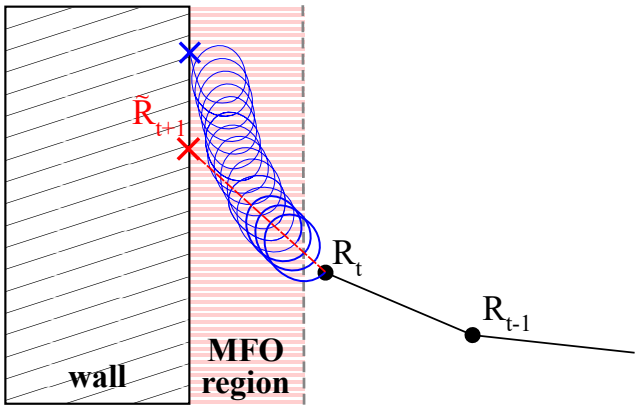

Figure 4.4: Sketch of fallback mechanism: in the hybrid AGCA simulation mode, a particles collides with the wall while in GCA at $\tilde{R}_{t+1}$ because the discretization time step is large enough to overstep the region of mandatory FO tracing (MFO region, light red area). Collisions in GCA are unphysical, therefore the last time step is reverted, the particle is set back to R_t and the FO tracing method (blue line) is mandated for at least three gyrations (thick blue line). The MFO region is reached and the subsequent wall collision (blue cross) is resolved correctly.

4.3 Accelerated Gradient Calculation

In a typical ERO2.0 simulation, more than 90% of the computation time is spent in the impurity transport module [103, p. 129]. Within this module, the interpolation of plasma parameters to the particle's current position in the 3D simulation volume takes up around 7.5% of the computation time. The interpolation of 3D plasma background data is performed with a trilinear method, for which the plasma parameters at all eight nodes of the current ERO2.0 grid cell are queried. If a 2D plasma background is used, toroidal symmetry is assumed and the neighbouring four nodes in the R-z-plane are queried for a bilinear interpolation of the plasma

parameters at the desired location.

In a simulation using the FO tracing method, the interpolation of the plasma

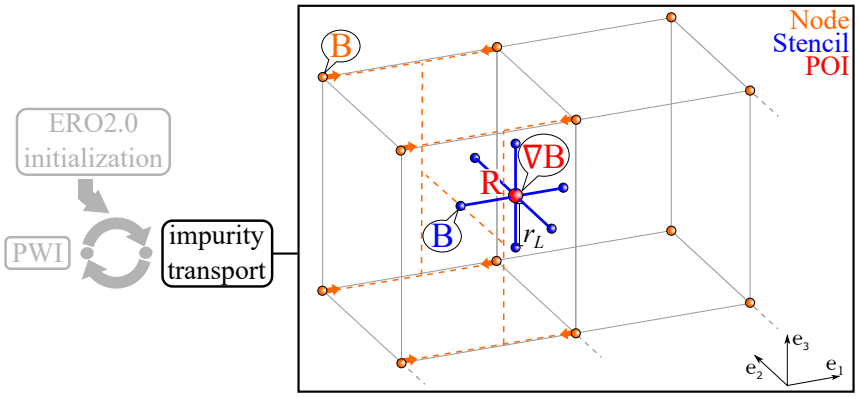

Figure 4.5: Sketch of the original method to estimate the gradient at a point of interest – here a particle's guiding centre **R** – during the impurity transport module of ERO2.0. First, trilinear interpolation from the ERO2.0 grid nodes (orange) to each of six additional stencil points (blue) is applied. $\nabla B(\mathbf{R})$ is then calculated as the finite difference (blue line) of B at the stencil points. Illustration adapted from [96].

parameters to the particle's location is ideally only needed once per tracing time step, because only the local plasma parameters are used in the tracing algorithm. In GCA tracing methods, the situation is different, since GCA is effectively a motion averaged over the particle's gyro-orbit. Even in first order approximation, gradient effects take place, leading to the well known ∇B-drift, curvature drift and magnetic mirror effects (see Equation 4.4). This however requires additional calculations, because information about the plasma parameters – specifically the magnetic field strength – in the *vicinity* of the particle's location are required to estimate the local gradients. Two additional stencil points are queried along each axis of the rectangular ERO2.0 grid, on which the provided 2D or 3D plasma background information is stored (see section 3.1.1), depicted in Figure 4.5). The stencil points lie in a distance s, chosen here as the particle's Larmor radius r_L. Thus, in every single particle tracing step, six additional stencil points with trilinear interpolation (3D) or four additional stencil points with bilinear interpolation (2D) are queried. From these stencil points, the derivative is estimated as the finite difference along each axis to calculate the desired vector ∇B. This time-consuming procedure was defined as a major source for the comparative lack of computational speed of the GCA tracing method compared to the FO tracing method.

In this work, a new two-step scheme for accelerated gradient calculation is implemented into the ERO2.0 code. At the start of the simulation (Figure 4.6),

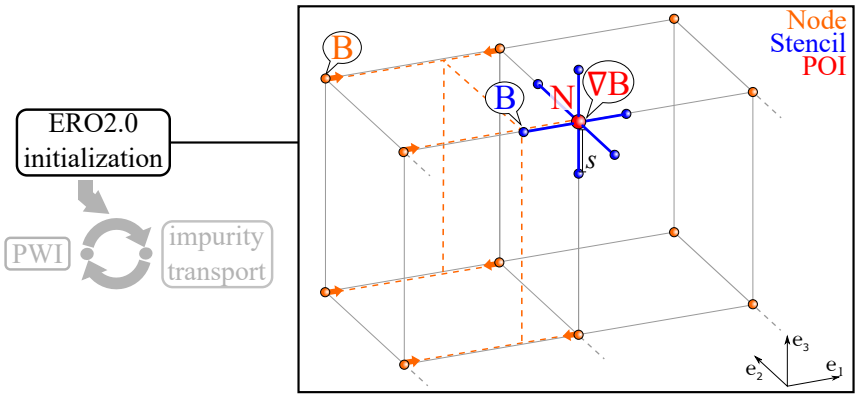

Figure 4.6: Sketch of the accelerated gradient calculation method. Step 1, during the initialization of the ERO2.0 simulation: the original gradient calculation method (see Figure 4.5) is applied once to each node N of the ERO2.0 grid, storing the ∇B information for later use. Note: the stencil points can span over multiple cells depending on the resolution of the ERO2.0 grid and the choice of the stencil length s. Neighbouring cells are shown here for simplicity.

the original gradient calculation method using stencil points is first applied to all ERO2.0 grid nodes N, storing the vector at each node. During the impurity transport module (Figure 4.7), the magnetic field gradient information is then available on the full ERO2.0 grid, and requires just one trilinear interpolation to the specific particle location like all other plasma parameters, e.g. the magnetic field and its direction. This avoids the former need for computationally expensive additional interpolations at stencil points in the impurity transport module, which were performed exclusively for the GCA tracing methods.

The accelerated gradient scheme is automatically initialized at the start of an ERO2.0 simulation, therefore the stencil length s must now be chosen beforehand and should roughly be on the order of the expected Larmor radii of the particles in the simulation. By default, $s = 1\,\mathrm{cm}$ is chosen, which was defined as an upper limit of Larmor radii to be expected in typical ERO2.0 simulations and roughly corresponds to the Larmor radius of high energy, singly ionized tungsten impurity particles in a typical magnetic field used in fusion application ($r_L = 1.09\,\mathrm{cm}$ for $E = 500\,\mathrm{eV}$, $B = 4\,\mathrm{T}$, $q = 1$, Equation 3.2). The role of the stencil length s was assessed to confirm that it has no significant impact on the trajectories. It was found that a more local calculation of the gradient, i.e. a shorter stencil lengths of $s = 0.1\,\mathrm{cm}$ and $s = 0.01\,\mathrm{cm}$, led to results within 0.3 % concerning the energy conservation of particles compared to $s = 1\,\mathrm{cm}$. This can also be attributed to the fact that the typical ERO2.0 grid resolution for plasma background information is on the order of 1 cm, so smaller features are not resolved by this grid either.

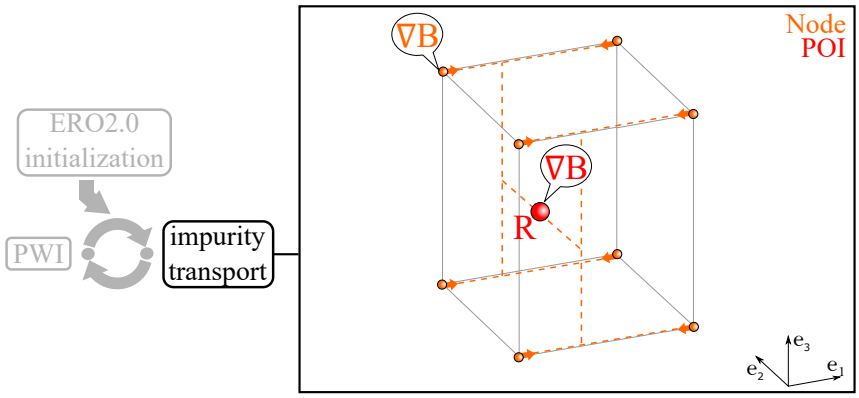

Figure 4.7: Sketch of the accelerated gradient calculation method. Step 2, during the impurity transport module in the ERO2.0 main loop: trilinear interpolation from all surrounding cell nodes (orange) is performed to directly estimate the gradient at a point of interest, e.g. a particle location **R** (red), without the need of stencil points.

Therefore, the stencil length should not be chosen smaller than the ERO2.0 grid resolution.

To put the relevance of the accelerated gradient calculation scheme into perspective, in a typical ERO2.0 simulation in JET geometry, around 10^6 particles are simulated with dwelling times of around 0.1 s. The GCA tracing method is executed for more than 95% of simulated steps of the trajectories [96, p. 56] in the AGCA simulation mode. With a typical tracing time step of 50 ns, a total of about $95\% \times 10^6 \times 0.1\,\mathrm{s}/50\,\mathrm{ns} \simeq 1.9 \times 10^{12}$ steps are performed using the GCA tracing method. With the original gradient calculation method, the six stencil points lead to $1.2 \cdot 10^{13}$ additional interpolations for gradient calculations. In contrast, the accelerated gradient calculation scheme reduces this number to 9×10^8 magnetic field interpolations performed at the beginning of the simulation, assuming a typical ERO2.0 grid size of $1000 \times 500 \times 300 = 1.5 \times 10^8$ cells for a 3D plasma background[1]. All gradient calculations during the impurity tracing module of the ERO2.0 simulation afterwards are much simpler using the direct trilinear interpolation, which results in total in a shorter computation time.

To verify the implementation and desired speed-up of the code, the test case from section 4.1 is repeated with the accelerated gradient calculation enabled and otherwise identical settings and hardware. The results can be seen in Figure 4.8. The computation is significantly faster than without the accelerated gradient calculation (compare Figure 4.2): on average, the simulations using the accelerated

[1] A 2D plasma background needs around two orders of magnitude less initial interpolations due to reduction in dimension by assuming toroidal symmetry.

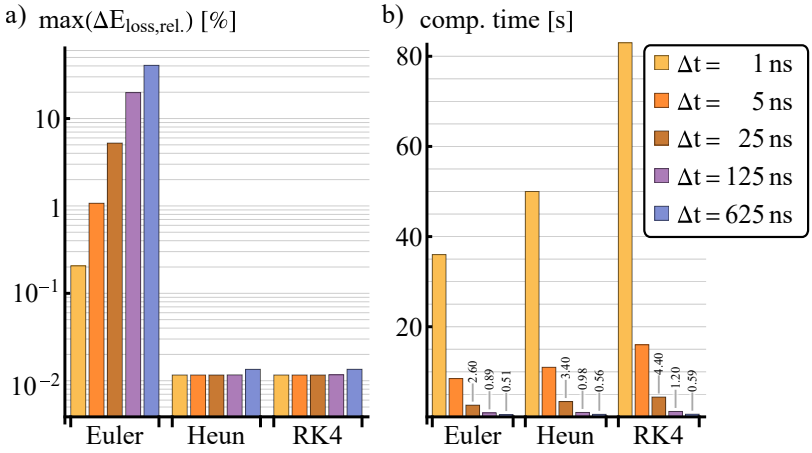

Figure 4.8: Evaluation of the JET test case using the accelerated gradient calculation scheme. a) Maximum relative Be particle energy loss (logarithmic scale) and b) computation time of the simulations across fifteen simulation cases using three different GCA tracing algorithms and five increasing time steps. See Figure 4.2 for the results without accelerated gradient calculation.

gradient calculation require 38.3% less computation time, leading to a code speed-up of a factor of 1.62x. The pre-initialization of the gradient data on the ERO2.0 grid took 0.06 s on average, which is negligible in any realistic applications of ERO2.0. The relative errors (Figure 4.2a) in the energy conservation are found to be larger than in the simulations without pre-initialization of the gradient by an average factor of 2.1x. While this is not ideal, the relative energy loss using the Heun and RK4 algorithms still remains below 0.015% in all observed cases. This is deemed as an acceptable compromise for the significantly accelerated computation speed gained by the accelerated gradient calculations implemented in this work. In 3D plasma backgrounds, where 50% more interpolations are necessary for the calculation of the gradient compared to the 2D plasma background tested here, the speed-up is expected to be even more significant. However, since all further simulation cases analysed in this work use 2D plasma background information, the test is concluded here.

In total, the accelerated gradient scheme significantly reduces the computation time needed for simulations applying the GCA tracing method. This assists the higher-order numerical integration schemes implemented to enhance the AGCA hybrid simulation mode in ERO2.0, making it advantageous compared to the pure FO simulation mode.

4.4 Verification and Validation of Code Optimizations

The ERO2.0 code updates described in sections 4.1, 4.2, and 4.3 focussed on increasing the accuracy and stability of the transport algorithm using the GCA tracing method so that larger time steps can be used. Together with optimizations of gradient calculations, the updates lead to a significant speed-up and performance enhancement of the ERO2.0 code. The upgraded ERO2.0 code is now in turn better capable of simulating larger amounts of particles, which increases the statistics in recessed regions like the ITER diagnostic first wall ports analysed in this thesis. Additionally, full-3D simulations of complete devices (e.g. full-torus simulations of the W7-X advanced stellarator) are possible in more reasonable computation time.
In an ERO2.0 simulation, the interaction between the two main modules, the plasma-wall interaction (PWI) module and the impurity transport module (see Figure 3.3), is of high importance. Since the impurity transport module was heavily modified in this thesis by the code optimizations to the GCA tracing methods, a full simulation verification and validation has been carried out in a JET case. ERO2.0 simulations using the pure full-orbit (FO) simulation mode have been benchmarked successfully against experiments in the past [102, 104], therefore an inner-code validation of the updated ERO2.0 code with optimized GCA tracing methods in the AGCA hybrid simulation mode is sufficient for the validation at this stage. This allows for direct comparisons between the two simulation modes, and permits a quantitative assessment of the code optimisation regarding the runtime performance in realistic scenarios. Simplified test cases were analysed in sections 4.1 and 4.3 to verify the implementation and measure first code speed-ups, but a full benchmarking is necessary to show the relevance of the optimizations in realistic applications. A broad selection of relevant characteristics is taken into account to verify the updated GCA tracing methods. The physical results are validated by analysing the impact angle distribution of particles on PFCs and the resulting erosion for the PWI module, and the impurity density profiles in the poloidal plane for the impurity transport module.
The primary focus of the validation is on comparing the physical results between the two simulation modes: (i) *pure full-orbit* (pure FO) simulation mode, in which FO tracing methods with a fixed time step are used throughout the entire simulation volume, and (ii) *adaptive guiding-centre approximation* (AGCA) simulation mode, in which the updated GCA tracing methods introduced in the preceding sections are applied far from the PFCs, and FO tracing methods are executed near the PFCs. Additionally, a variation of the impurity tracing time step Δt is

Table 4.1: Definition of impurity tracing time steps Δt used in the six simulation cases for verification and validation of the updated ERO2.0 code. In the pure FO simulation mode (cases A-C), only FO tracing is applied, while in the AGCA simulation mode (cases D-F), a hybrid approach between FO and the updated GCA tracing methods is applied.

simulation case	simulation mode	Δt_{FO} [ns]	Δt_{GCA} [ns]
A	pure FO	2	—
B	pure FO	10	—
C	pure FO	50	—
D	AGCA	2	50
E	AGCA	2	100
F	AGCA	2	500

performed for both simulation modes to test the limits of the applicability of each simulation mode and analyse computation performance gains of the updated GCA tracing algorithms. The indices FO and GCA are used to denote the time step used whenever FO/GCA tracing methods are used, respectively. Six simulation cases are analysed, denoted by letters A-F. The impurity transport time step Δt_{FO} in the pure FO simulations (cases A-C) is varied between 2–50 ns. Case A is chosen as the reference case, since the FO tracing methods applied throughout this case includes a more complete physics description than the simulations in AGCA simulation mode and case A uses the smallest numerical time step among the pure FO simulation cases. For the simulations in AGCA simulation mode (D-F), a fixed FO tracing time step $\Delta t_{\mathrm{FO}} = 2\,\mathrm{ns}$ is chosen to retain the highest resolution of PWI processes, while the GCA tracing time step Δt_{GCA} is varied between 50–500 ns. An overview of the choice of time step for each case is presented in Table 4.1).

The plasma background in the simulation case chosen for the verification and validation corresponds to the magnetic field configuration of a JET limiter plasma (JET Pulse Number #80319 at $t = 10\,\mathrm{s}$) in deuterium (D). The 2D distribution of plasma parameters was calculated based on the JET EFIT equilibrium reconstruction and experimentally measured profiles, as described in Ref. [79], and subsequently interpolated to the rectangular grid ERO2.0 grid with a resolution of $1.2\,\mathrm{cm} \times 1.3\,\mathrm{cm}$. Figure 4.9a) and b) show the 2D profiles of electron density and temperature, respectively.

For the simulations performed for the validation and verification, a wide range of JET-ILW (ITER-like wall) plasma-facing or wall components is included in the simulation. The geometry consists of Outer Poloidal Limiters (OPL), Inner Wall Guard Limiters (IWGL), the Upper Dump Plate (UDP), Inner Wall Cladding (IWC) and the Inner Wall Protection Bars (IWPB). The 3D models with a total

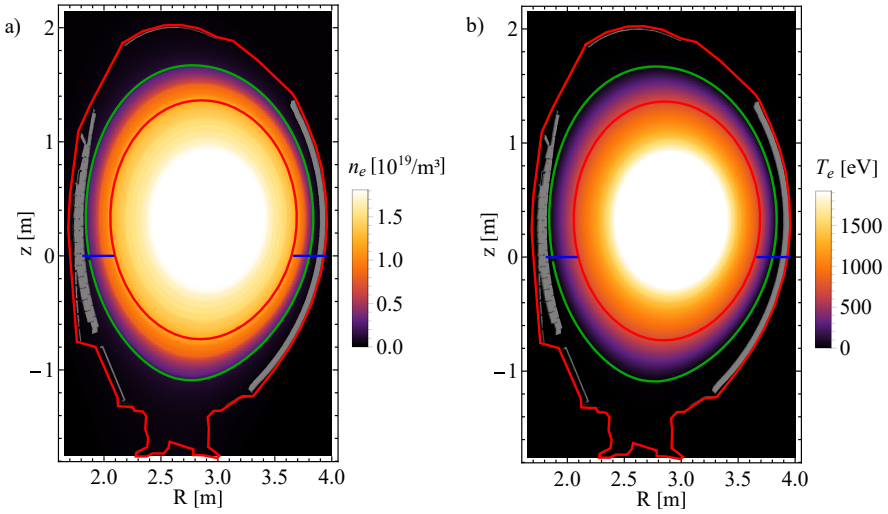

Figure 4.9: a) Electron density and b) electron temperature in the R-z-plane of the JET 2D plasma background used in the verification and validation of the updated ERO2.0 code. Additionally: 2D projections of JET PFCs used in the simulation (grey), inner and outer bounds of the ERO2.0 simulation volume (red), last closed flux surface (green) and locations of mid-plane profiles used in the later analysis (blue).

area of 37.52 m^2 are discretized to a mean polygon area of around 0.44 cm^2, leading to a total of 8.1×10^5 polygons. An overview of the location of the components in the JET device can be seen in Figure 4.10, where each component is colour-coded by its main material composition: bulk Be, W-coated Carbon Fibre Composites (CFC), Be-coated Inconel or bulk W. In the ERO2.0 simulation, only the topmost layer, i.e. Be or W, is included. No material mixing is performed in this validation of the code updates, since the HMM implemented in ERO2.0 was not altered. The divertor geometry is omitted in the simulations, because a plasma background in limited configuration is used.

A first look at typical erosion patterns on the JET first wall elements can be seen in Figure 4.11, depicting the erosion rate induced by impinging Be impurity particles on each cell of the 3D wall geometry in the reference simulation case A. Note that the erosion by the D plasma background is not included in this depiction, because it is identical across all six simulation cases. In the limiter configuration case studied here, the largest erosion rates in JET can be found on the IWGL (eroded flux $\sim 10^{21} \frac{1}{\mathrm{m^2\,s}}$), where erosion patterns can be seen (compare Figure 4.12). The second zones of significant erosion by Be are the OPL (eroded flux $\sim 10^{19} \frac{1}{\mathrm{m^2\,s}}$).

Figure 4.12 shows a closer look at the erosion rates on one IWGL as a comparison between the six simulation cases A-F. One notices that the pattern observed on

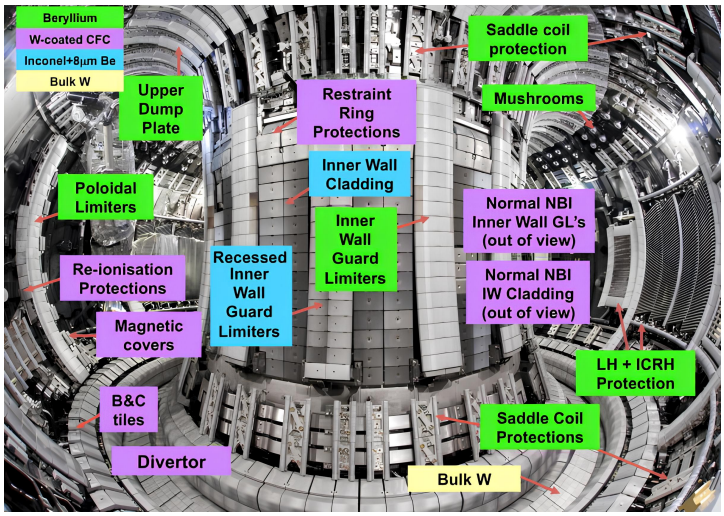

Figure 4.10: Overview of the JET ITER-like wall (ILW) with colour-coded materials of the first wall and divertor components. (Outer) Poloidal Limiters (OPL), Inner Wall Guard Limiters (IWGL), the Upper Dump Plate (UDP), Inner Wall Cladding (IWC) and the lower Inner Wall Protection Bars (IWPB, "Saddle Coil Protections" in the image) are included in the simulation for validation and verification of the updated ERO2.0 code. Image taken from Ref. [46].

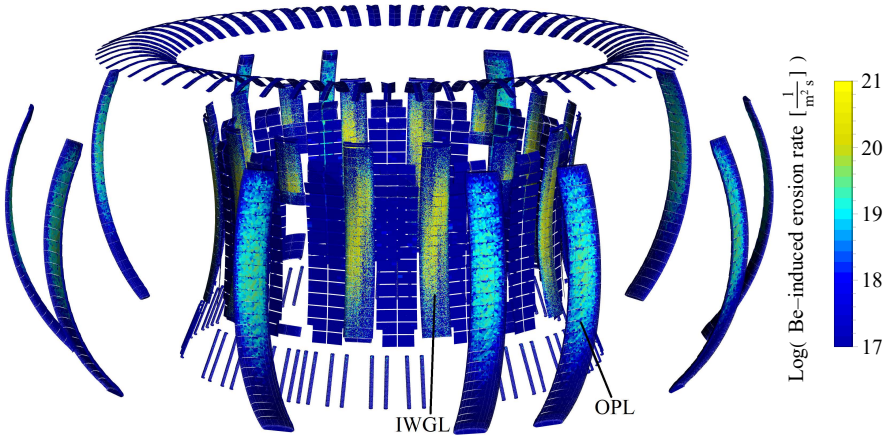

Figure 4.11: Erosion rate induced by impinging Be impurity particles on the wall tiles of JET with logarithmic colour scaling. Data from the reference case A (pure FO simulation mode, $\Delta t_{\mathrm{FO}} = 2\,\mathrm{ns}$) is shown. The regions showing the highest erosion rate are highlighted: the Inner Wall Guard Limiters (IWGL) and the Outer Poloidal Limiters (OPL). A detailed look comparing the IWGL erosion rates across simulation cases A-F is presented in Figure 4.12.

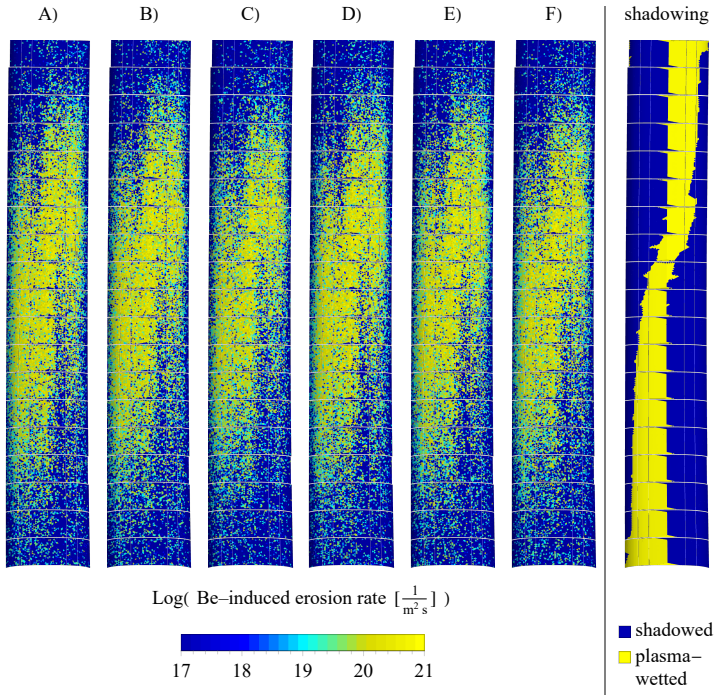

Figure 4.12: A)-F): Erosion rate induced by impinging Be impurity particles on one inner wall guard limiter (IWGL, highlighted in Figure 4.11) across the six simulation cases. The rightmost picture shows the shadowing pattern on the IWGL as calculated by the ERO2.0 code.

the IWGL roughly follows the pattern of the magnetic shadowing, described in section 3.1.4. The magnetic shadowing does not directly influence the erosion by impurity particles, but only the erosion due to plasma fluxes impinging on the wall, which are excluded in this depiction. However, transported Be impurity particles largely follow the magnetic field lines within the plasma, and therefore regions of the IWGL with long magnetic connection lengths (i.e. plasma-wetted areas) are also exposed to larger fluxes from impurities, causing higher erosion. The longer flux tube along the magnetic field line accumulates a larger amount of particles, resulting in larger erosion compared to magnetically shadowed areas. Diffusive and cross-field transport processes however spread the impurity flux even into magnetically shadowed regions, so that the magnetic shadowing pattern does not directly match the pattern of erosion. Between the six simulation cases, no significant differences in the erosion pattern is present.

To quantify the differences between simulation cases A-F, Table 4.2 shows a comparison of integrated erosion values over the two regions showing the highest erosion – IWGL and OPL. Notably, the discrepancy to the reference case A is higher, the larger the time step is chosen for both simulation modes. However, simulations applying the AGCA simulation mode have much more accurate results at the same time step size – case C (pure FO) and case D (AGCA) use the same particle tracing time step far from the wall ($\Delta t_{\mathrm{FO/GCA}} = 50\,\mathrm{ns}$), but case C disagrees by at least 25.3 %, while case D differs by at most by 3.1 %. Even the results from case F, in which a time step 250x as long as in the reference case far from the wall is used, the results agree within 12.7 %. Note that all simulations in AGCA simulation mode (cases D-F) use $\Delta t_{\mathrm{FO}} = 2\,\mathrm{ns}$ close to the wall, where FO tracing methods are used in the hybrid approach. Therefore, a higher quality of the results is retained even at much larger time steps far from the wall.

The erosion of PFCs is influenced by the impact angles of particles impinging on

Table 4.2: Evaluation of discrepancy between the integrated erosion rates in JET on the inner wall guard limiter (IWGL) and outer poloidal limiter (OPL) for all six simulation cases (see Table 4.1). For the reference case A, the absolute value of erosion flux is shown, while the rest of the cases denote the relative difference to this value.

simulation case	IWGL	OPL
A (ref.)	2.8×10^{20} /s	3.9×10^{19} /s
B	-1.2%	+1.5%
C	-25.3%	-26.1%
D	-3.1%	-0.1%
E	-4.0%	-3.2%
F	-11.1%	-11.7%

the wall, which affect the sputtering yield [27] (see Figure 3.11). Figure 4.13 reveals that the angular distributions of impurity particles impinging on the PFCs in the hybrid AGCA simulation mode are in very good agreement to pure FO simulations, even though GCA tracing methods are used for the largest part of the trajectories. The impact angle distributions are nearly unperturbed in cases D-F, which use the

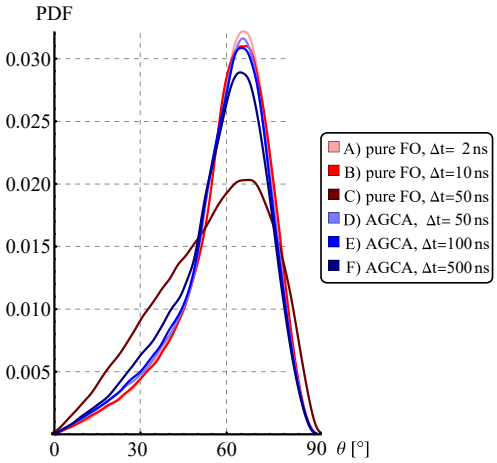

Figure 4.13: Probability density function of the impact angle of impurity particles impinging on all PFCs in simulation cases A-F. An evaluation of the discrepancies between the curves is shown in Table 4.3.

AGCA simulation mode, and are far less affected by increasing the time step size. In contrast, case C (pure FO, $\Delta t_{\mathrm{FO}} = 50\,\mathrm{ns}$) shows significant discrepancy to the reference case A ($\Delta t_{\mathrm{FO}} = 2\,\mathrm{ns}$), while even case F using AGCA simulation mode ($\Delta t_{\mathrm{GCA}} = 500\,\mathrm{ns}$) shows acceptable agreement. This can be attributed to the fact that in AGCA simulations, the time step size is chosen very small, here 2 ns, as soon as the particle enters the mandatory-FO region (see Figure 4.3) close to the wall. To quantify the similarity of the distributions, the normalized mean absolute error (NMAE) is calculated, defined by

$$\mathrm{NMAE}_k = \frac{\frac{1}{N}\sum_{i=1}^{N} |f_{\mathrm{ref.},i} - f_{k,i}|}{\max\left(f_{\mathrm{ref.},j} \mid 1 \leq j \leq N\right)} \tag{4.7}$$

where f_k is the data (here: angular distribution) of simulation case k. The distribution is discretized into $N = 90$ equidistant query points, each representing a bin of 1° width. The normalization of the NMAE is chosen to estimate the relative magnitude of the mean absolute error compared to a typical value in the reference case. The reference case has a NMAE of zero by definition.
The evaluation of the NMAE for the angular distributions is shown in Table 4.3.

Table 4.3: Evaluation of discrepancy between the angular distributions (see Figure 4.13) of Be impurity particles impinging on the PFCS for the six simulation cases.

simulation case	NMAE
A (ref.)	(0.0%)
B	1.6%
C	13.2%
D	1.3%
E	1.8%
F	4.3%

Matching the observations stated before, case C shows the highest discrepancy and is the only simulation case with a NMAE of over 10 %. At the same time step size, case D using the AGCA simulation mode has a NMAE one order of magnitude smaller. Therefore, the AGCA simulation mode allows an accurate description of the PWI processes even when larger time steps far from the PFCs are used.

As a last physical observable for the validation of the ERO2.0 code updates, the impurity particle density in the mid-plane of JET ($z = 0$, blue line in Figure 4.9) is analysed, which indicates the impurity transport in the ERO2.0 code and importantly is also used for synthetic diagnostics (see e.g. Ref. [103]). Because 2D and 3D density plots are hard to compare quantitatively, Figure 4.14 shows the beryllium impurity density as a 1D profile along the mid-plane for the six analysed simulation cases[2]. The data is averaged over the toroidal angle, integrated over the simulation time and summed over all Be charge states from 0 to +4.

The impurity density in the confined plasma is underestimated by up to 11 % in the simulation cases at larger time steps compared to the reference case A. This effect starts being significant at the largest time steps analysed in this benchmark, in cases C (pure FO) and F (AGCA). However, the simulations performed in AGCA simulation mode allow larger time steps than simulations in pure FO simulation mode: case C (pure FO, $\Delta t_{\mathrm{FO}} = 50\,\mathrm{ns}$) shows noticeable discrepancies to the reference case A, while the curve for the AGCA simulation using the same time step (case D) overlaps nearly perfectly with the reference curve. The AGCA simulation case with the largest time step (case F, $\Delta t_{\mathrm{GCA}} = 500\,\mathrm{ns}$) instead roughly matches the results from case C.

The quantitative discrepancy of the simulation cases to the reference case is evaluated using the NMAE (Equation 4.7) as before. The results are described in

[2]The simulations are limited to the plasma boundary layer around the last closed flux surface (LCFS), thus the region between $R = 2.13\,\mathrm{m}$ and $R = 3.67\,\mathrm{m}$ is excluded from the simulation volume and the profiles (see Figure 4.9), and reflecting boundary conditions are applied in the simulation as described in section 3.1.1.

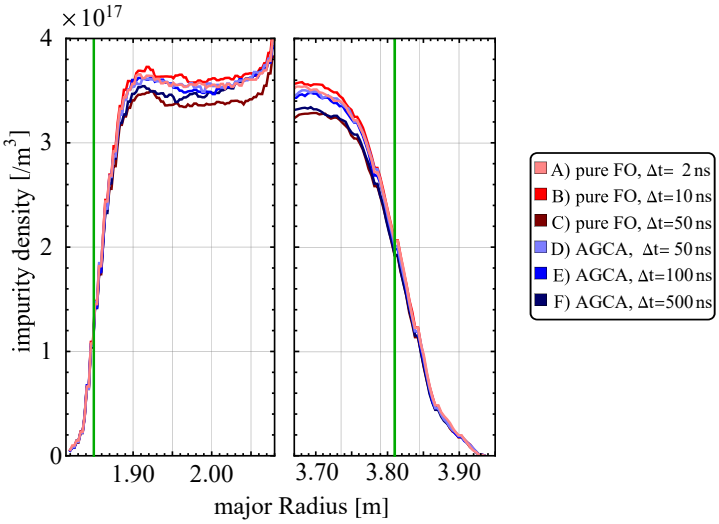

Figure 4.14: Beryllium impurity density in the inner mid-plane (left)/outer mid-plane (right) for the six simulation cases A-F. Green: Position of last closed flux surface (LCFS). Figure 4.9 shows the location of the profiles. An evaluation of the discrepancies between the curves is shown in Table 4.4.

Table 4.4, using $N = 100$ query points along the profiles in radial direction. The errors increase as expected with larger time steps, because the finite time step leads to discretization errors. Noticeably, the NMAEs of simulation cases E and F using AGCA simulation mode are very comparable to cases B and C, respectively, which use pure FO simulation mode, but one order of magnitude smaller time steps.

The validation of the updated ERO2.0 code with optimized GCA tracing methods is concluded here with success. The results between simulations using the hybrid AGCA simulation mode and the original pure FO simulation mode are overall in good agreement. Two of the analysed cases are discarded assuming a threshold

Table 4.4: Evaluation of discrepancy between the beryllium impurity density profiles (see Figure 4.14)in the mid-plane for the six simulation cases.

	NMAE	
simulation case	inner mid-plane	outer mid-plane
A (ref.)	(0.0%)	(0.0%)
B	1.3%	0.9%
C	4.2%	3.7%
D	0.6%	0.6%
E	1.3%	1.5%
F	2.1%	3.3%

of 10 % maximum discrepancy to the reference case A. Case C using pure FO simulation mode ($\Delta t_{\mathrm{FO}} = 50\,\mathrm{ns}$) shows discrepancies of up to 26 % in integrated impurity erosion rates and angular distribution, and case F using AGCA simulation mode ($\Delta t_{\mathrm{GCA}} = 500\,\mathrm{ns}$) differs by 11.7 % in integrated erosion rates. Thus, in the realistic test scenario studied here, it was determined that the AGCA simulation mode with a time step of 100 ns leads to qualitatively good results in all analysed physical quantities, which is significantly larger than the 10 ns time step size that was determined as maximum for simulations applying the pure FO simulation mode. The rather weak dependence of AGCA simulation results on the time step size suggests that reasonable simulations results can be obtained at even larger time steps than 100 ns.

With the accuracy of the ERO2.0 optimizations confirmed, the computation time of the simulations should be considered. All simulations in the verification and validation were conducted on 2304 CPU cores of the supercomputer MARCONI [52], thus a direct comparison is justified. Figure 4.15 shows that ERO2.0 simulations with large time steps using the AGCA simulation mode lead to significantly shorter computation times in comparison to simulations using the pure FO simulation mode. Discarding simulation cases C and F as discussed before, the fastest simulation using pure FO simulation mode, case B, finished in 127 minutes. The fastest AGCA simulation with preserved quality, case E, finished in just 14 minutes. Consequently, a code speed-up of a factor of x9.1 is achieved by the AGCA simulation mode comparing to a simulation using pure FO simulation mode, which is achieved by the optimizations introduced in this work. Comparing case E to the pure FO simulation with identical particle tracing time step near the wall (case A, $\Delta t_{\mathrm{FO}} = 2\,\mathrm{ns}$), a speed-up of x44.1 is achieved with an agreement within 4.0 % in all analysed quantities in the validation.

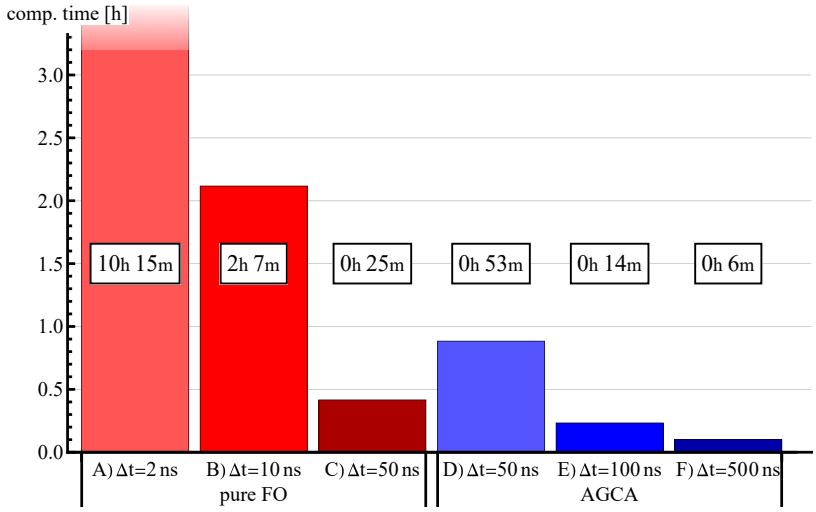

Figure 4.15: Computation time of simulations cases A-F on the MARCONI supercomputer [52], using 2304 CPU cores each. Identical conditions apart from the simulation mode and associated numerical impurity tracing time step are used (see Table 4.1).

Chapter 5

Multi-Stage Simulation Workflow

5.1 Overview

ERO2.0 is programmed in a way, that enables large volume simulations by using an efficient parallelization. The massive amount of processed particles mitigates the statistics problems common to Monte-Carlo transport codes. In the core and edge regions of the plasma, where particles are usually ionized and far away from the wall, the full benefit of the GCA optimizations introduced in chapter 4 comes into play and enables simulations with even larger amounts of particle trajectories. In fusion devices, excellent confinement of the plasma is necessary to minimize the heat loads on plasma-facing components (PFCs), so that the particle fluxes onto the PFCs are comparably low. However, the operational time of a reactor is in the range of multiple years, thus, the low fluxes accumulate and reach significant fluence, which can cause critical damage. Therefore, lifetime predictions of the PFCs require accurate modelling of even the low-flux regions, which is a significant challenge for codes based on the statistical Monte-Carlo approach.
In this study, recessed volumes are the ultimate focus of interest – in the scope of this work, estimates will be shown proving that only roughly 1 of 10^8 simulated test particles from a global ERO2.0 simulation would hit recessed components or objects like mirrors on which a result is desired (see section 6.2.3). The performance of mirrors inside assemblies far behind the main wall of ITER over years of operation and multiple erosion and deposition processes is investigated. In an ERO2.0 simulation, thousands of particle impacts are necessary on these mirrors to accurately estimate the fluxes, and the evolution of surface concentration changes requires multiple loops of the impurity transport and plasma-wall interaction modules (see Figure 3.3). Even with the massive speed improvements of the newly optimized ERO2.0 code, the simulation of this enormous amount of particles is not

feasible on modern High-Performance Computing (HPC) hardware – new ideas are required.

A novel approach for ERO2.0 simulations is introduced here: a multi-stage simulation workflow. Instead of a single ERO2.0 simulation, that encompasses all tokamak wall components including the first wall and divertor, the recessed mirror assembly, and finally the mirrors themselves, the simulation itself is split into successive stages using the ERO2.0 and EIRENE codes. These successive stages cover volumes closer and closer to the mirrors. Each stage delivers information about the test particles, representing the real atoms, impinging on the interface to the simulation volume covered in the subsequent stage. The interface surfaces are labelled *catcher* planes in this work, which are further discussed in section 5.3. At the start of the subsequent stage, a large number of test particles are injected on the catcher plane, upsampling the amount to increase the statistics while retaining the physical details of the incoming particles, e.g. total flux and energy distribution. This modular approach in multiple stages also simplifies studies with different mirror geometries or material assumptions, because results from earlier stages can be reused. In the different simulation stages, a multitude of particle species needs to be simulated: impurity particles sputtered from the tokamak's first wall like beryllium (Be), hydrogenic neutral particles from the fuel like deuterium (D), and sputtered particles from the mirror assembly and mirrors themselves like iron (Fe) and molybdenum (Mo), respectively. The multi-stage approach is outlined in general in Figure 5.1. In the flowchart, the increase in particle species that needs to be considered along the multi-stage simulation workflow is illustrated.

The multi-stage approach can best be explained with a defined simulation case, therefore it is demonstrated with the example of an ITER simulation, which is later analysed in detail in chapter 6 (case #1). The 2D plasma background information for this simulation, further detailed in section 6.2.1, was provided by the ITER Organization and generated by SOLPS-4.3/OEDGE plasma modelling of a baseline H-mode burning plasma scenario with a power amplification factor $Q = 10$.

The application of the multi-stage simulation workflow to the ITER geometry of this case is presented in Figure 5.2, from (1) the global simulation volume, to (2) the diagnostic first wall (DFW), and finally (3) the mirror system deep inside the DFW. The volume containing the mirror system, treated in simulation stage 3, is referred to as *mirror box* in this work. Stages 1 and 2 provide the particle ensemble distributions at the interfaces between simulation volumes (catcher planes C1 and C2) closer and closer to the mirror box, while stage 3 delivers the results on the first mirror (FM) and second mirror (SM). A two-stage approach was tested in this geometry, but did not deliver satisfying results on the mirrors, and provided

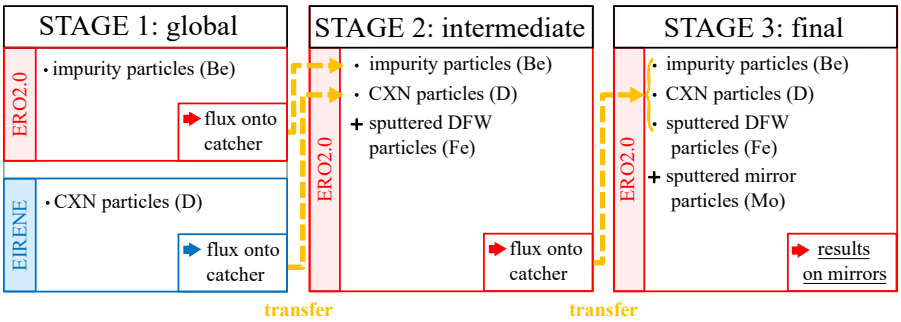

Figure 5.1: Outline of the modelling workflow for the multi-stage simulation approach, with simulations in three successive stages using the ERO2.0 and EIRENE Monte-Carlo transport codes. Information about incoming fluxes is collected on several catcher surfaces closer and closer to the mirrors. Yellow dashed arrows indicate data transfer and upsampling of fluxes on the catcher surfaces, which serve as interfaces between the simulation stages. Four simulations and three transfers are necessary. The listed elemental species are examples for the particle category.

less flexibility for additional studies, so that a three-stage approach is justified. Within this work, the stages will be referred to either by their number (stage 1, stage 2, and stage 3) or their ordering (global, intermediate, and final stage). The consecutive simulations should be performed as consistently as achievable. The four simulations in the three-stage approach are described in the following, while the required workflows for the plasma background and for the upsampling of test particles at the interfaces are discussed separately in sections 5.2 and 5.3.

Stage 1 (ERO2.0)

The first simulation performed in stage 1 is a standard ERO2.0 full-device simulation. The simulation volume contains the main tokamak volume, covering the first wall and divertor, but also includes the entrance to the DFW. A three-dimensional catcher plane C1 is defined, covering the entrance into the DFW leak-tight. In ITER, the first simulation stage is conducted using periodic boundary conditions to take advantage of the toroidal symmetry of the tokamak device. Thus, a 20° sector of the torus is chosen, which covers the width of the cut-outs of the DFW in the upper port plug (UPP) and equatorial port plug (EPP). Sputtering of the first wall (FW) by three sources is considered: (i) energetic plasma ions according to local plasma conditions, (ii) incoming charge exchange neutrals (CXN) of the plasma species, and (iii) impinging impurity particles simulated in the ERO2.0 impurity transport module. The sputtered particles are traced throughout the whole simulation volume. The main output of this stage is information about impurity atoms and

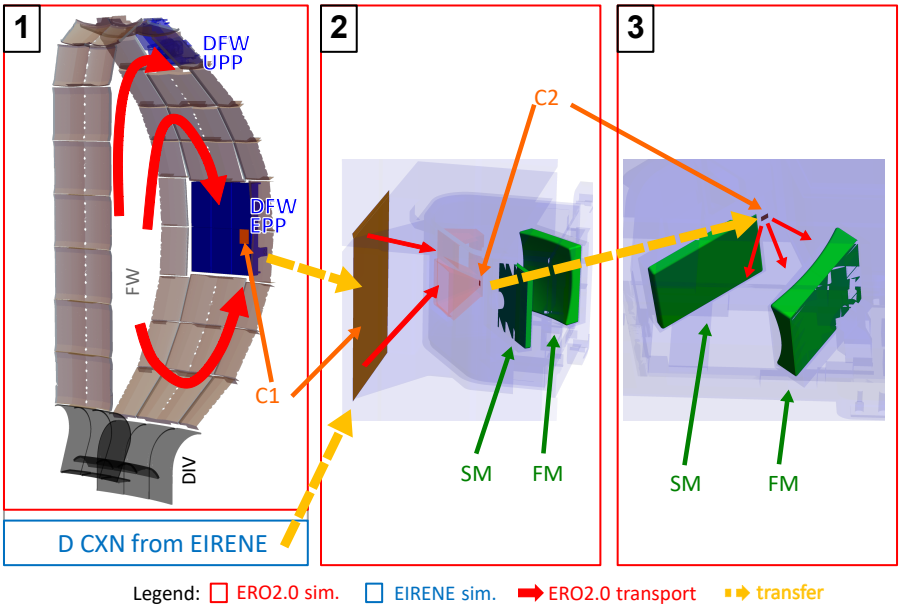

Figure 5.2: Illustration of the multi-stage simulation workflow applied to one ITER diagnostic first wall (DFW) port, with simulations in three successive stages: (1) global, (2) intermediate, and (3) final. The equatorial port plug (EPP) in the DFW contains a first and second mirror (FM/SM). The global simulation stage can also be used as input to simulations of the upper port plug (UPP), which are performed later in this work section 6.2. Red arrows schematically indicate ERO2.0 particle trajectories simulated during each stage. Yellow dashed arrows indicate data transfer between simulation stages via the catcher planes C1 and C2, respectively, whose position is identical in all stages, as well as the additional information about CXN from EIRENE post-processing runs.

ions entering the DFW: test particles from this global simulation, representing the impurities, are collected on the C1 catcher plane. The gathered statistics are used in stage 2 to sample impurity particles at the entrance to the DFW. The collection of data and subsequent upsampling for the stage 2 simulation are described in section 5.3a).

Stage 1 (EIRENE)

Parallel to the ERO2.0 simulation, a stand-alone EIRENE simulation is conducted, which ideally uses the same plasma background and wall geometry. Although EIRENE is included in both plasma code packages used for plasma background modelling in this work (EDGE2D-EIRENE for JET, SOLPS-4.3/OEDGE for ITER), a post-processing with EIRENE using these plasma solutions as input is necessary, as discussed in section 3.2. In the post-processing, EIRENE traces a large number of neutral fuel particles throughout the simulation volume, in this work commonly deuterium (D). A catcher surface E is defined in the simulation volume, which lies at or close to the entrance into the DFW, depicted in Figure 5.3 in the R-z plane. Although conceptually similar to the three-dimensional C1 catcher plane used in the ERO2.0 simulation, the catcher surface E is defined by a line segment in the R-z plane in EIRENE, from which a toroidally symmetric collection ring is generated inside the 3D EIRENE simulation volume[1]. On this catcher E, the main output of the stage 1 EIRENE simulation in the multi-stage simulation scheme is gathered: the total flux, as well as distributions of impact angle and energy of impinging neutral particles. The collection of the distributions and subsequent mapping onto the C1 catcher plane for stage 2 are described in section 5.3.

Stage 2

The second simulation stage is performed entirely in ERO2.0 and covers the recessed volume between the entrance of the DFW cut-out up to the narrow aperture hole, which leads to the mirror box (see Figure 5.2). The two separate stage 1 simulations define the incoming source of particles injected at the start of this stage. The statistics from both stage 1 simulations are used to generate a large ensemble of test particles at the entrance into the DFW, representing the impurity and fuel neutral transport inside the DFW. The upsampling is described in section 5.3. Sputtered DFW wall material acts as a third species treated in the multi-stage

[1]Although EIRENE has capabilities to work with toroidally shaped or confined 3D wall elements, typically toroidally symmetric geometries are used to remain consistent with 2D plasma modelling.

simulation workflow. The three particle species are traced up to the aperture hole, which is covered leak-tight by a three-dimensional catcher plane C2. The Homogeneous Mixing Model (HMM) in ERO2.0 is applied to simulate resulting changes in surface composition in the DFW due to deposition and (re-)erosion of impurity and DFW material. All test particles impinging on the C2 catcher plane are collected, thus providing information about all impurity, fuel and sputtered DFW particles that enter the mirror box as input to the stage 3 simulation.

Stage 3

The third simulation stage finally delivers the desired results on the diagnostic mirrors in full 3D resolution. The simulation starts at the aperture hole and covers the mirror box directly around the first and second mirror. The particles gathered on C2 in the stage 2 simulation are injected into the simulation volume, upsampling the number of test particles by particle splitting of typically factor 10–100 as described in section 5.3. Sputtering of the DFW and mirrors inside the mirror box is taken into account. Particles sputtered from the molybdenum (Mo) mirror represent a fourth species in the multi-stage simulation workflow. The surface composition of the mirrors and DFW changes over time due to the deposition of impurity or sputtered DFW material, as well as erosion of the mirror by the impinging particles, especially energetic CXN. The evolution of the surface composition is simulated using the HMM implemented in ERO2.0 and discussed before in section 3.1.5.

5.2 Extrapolation of the Plasma Background

Stage 1

For the first simulation stage, the plasma background in both the ERO2.0 and EIRENE simulations is provided by a plasma code package – the SOLPS-4.3/OEDGE code package for all ITER plasmas and the EDGE2D-EIRENE code package for all JET plasmas (see chapter 3 for brief descriptions of the codes). These plasma boundary layer codes provide 2D information in the R-z plane about the magnetic field strength and direction, the electron and ion density and temperature, and the plasma flow velocity parallel to the magnetic field. No electric fields outside sheath regions are considered in this work, and all 2D plasma background information is used with the assumption of toroidal symmetry of all plasma parameters throughout the 3D simulation volume in the stage 1 simulations. In the global ERO2.0 simulation (stage 1), the plasma background information is used directly where

available as described in section 3.1.1.
The two plasma code packages however do not cover the full volume investigated in this work, but only cover the scrape-off layer (SOL) around the separatrix or last closed flux surface (LCFS) of the plasma. The magnetic geometry and different simulation boundaries for the specific case investigated in this section are depicted in Figure 5.3a). The profiles of electron temperature and density along the outer mid-plane are shown in Figure 5.3b) and c), while the values at key radial positions are listed in Table 5.1. The 3D shaping of the wall leads to a gap in the plasma background information even in a global ERO2.0 simulation, as in stage 1 of the multi-stage simulation workflow. For example in the case of ITER, the OEDGE plasma background reaches up to the apex of the wall components, defined as the inner contour of their R-z projection. The gap in the plasma background information in this case measures up to 3 cm to shaped FW elements and up to 18 cm to the outer boundary of the ERO2.0 simulation volume at the DFW.
Extrapolation is necessary to fill this gap pf the plasma background information. During the stage 1 ERO2.0 simulations performed in this work, the plasma background is extended by nearest-neighbour extrapolation, i.e. constant extrapolation, to the OEDGE grid (ITER) or EDGE2D-EIRENE grid (JET), respectively. This is the most conservative estimate of plasma parameters in the far SOL (see orange extrapolation profile in Figure 5.3) and thus sputtering of the first wall. In Ref. [100], Romazanov et al. investigated different approaches to the extrapolation and performed a sensitivity study with different extrapolation profiles up to the wall, concluding that a decay length of around 1 cm leads to realistic conditions at the first wall and divertor of ITER.
The plasma parameters affect not only the sputtering of the PFCs, but also the transport of traced particles in the ERO2.0 simulation. In the global simulation stage, particles are subject to a wide range of physical effects, including ionization, recombination, and charged-particle collisions, all of which strongly depend on the local plasma parameters. Anomalous cross-field diffusion of traced ions is performed in the global stage 1 ERO2.0 simulation of this work, assuming a constant diffusion coefficient of value of $D_\perp = 1.0\,\frac{\mathrm{m}^2}{\mathrm{s}}$.

Stage 2 and Stage 3

In the local ERO2.0 simulations of the multi-stage simulation work flow (stages 2 and 3), the plasma parameters in the remote region inside the DFW are unknown: the recessed volume is not covered by the plasma boundary layer simulations, requiring further extrapolation of the plasma parameters from the main plasma

Table 5.1: Plasma background parameters at key locations in the outer mid-plane, ordered radially outwards. The parameters inside the DFW are extrapolated from the value at the OEDGE grid boundary.

location	T_e [eV]	n_e [10^{19}/m^3]
inner core boundary	5000	7.5
separatrix	200	3.0
SOLPS-4.3 boundary	15	1.2
OEDGE boundary	10	0.2
DFW centre	2×10^{-7}	3×10^{-9}

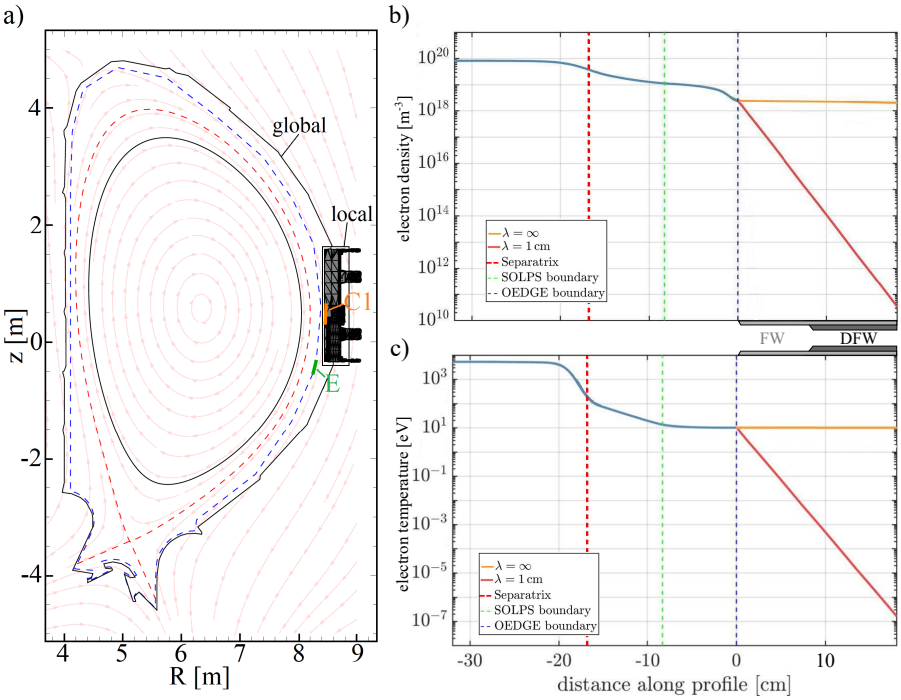

Figure 5.3: a) 2D overview of the location of the diagnostic first wall (DFW, grey) in the ITER EPP with catcher plane C1 used in ERO2.0 (orange), catcher surface E used in EIRENE (green), the ERO2.0 simulation volumes (black solid lines), separatrix (red dashed line), the outer border of the OEDGE grid (dashed blue line) and the magnetic field direction (light red arrows). b)+c): 1D profiles of electron density and temperature at $z = 0.3$ m in the outer mid mid-plane with code grid boundaries and wall indicated, as well as extrapolation profiles assumed in this work. The extrapolation distance from the last OEDGE grid point, which lies at the first wall (FW) apex, to the centre of the local simulation volume, which lies inside the DFW, measures 18 cm.

background described in the preceding section. Here, an exponential decay with $\lambda = 1.0\,\mathrm{cm}$ of plasma density and temperature for the gap region between the last plasma grid point and the centre of the recessed volume is assumed, shown as the red extrapolation profile in Figure 5.3. The distance from the centre of the DFW to the main plasma volume is on the order of tens of centimetres, therefore the parameters inside the DFW correspond almost to vacuum conditions (here: $n_e \sim 10^{10}\,\frac{1}{\mathrm{m}^3}$, $T_e \sim 10^{-7}\,\mathrm{eV}$). These extrapolated values in the centre of the DFW are used to generate a constant plasma background inside the local simulation volume and stages 2 and 3 are handled by one plasma background in ERO2.0 due to the near-vacuum conditions. The DFW does not erode by impact of plasma ions in the region of the DFW due to the low plasma temperature. The magnetic field strength inside the DFW is calculated using the $1/R$-relation of magnetic field strength in toroidal geometry, and the parallel flow velocity of the background plasma is assumed to be zero due to the extremely short extent of the volumes inside the DFW along the magnetic field lines.

Concerning the transport of traced particles in the extrapolated near-vacuum plasma conditions in the local simulation volume, ionization is far less likely due to the low plasma temperature present, and anomalous diffusion of ions is assumed to be absent due to the low plasma density. Collisions of traced particle with a neutral particle background depend on the local neutral gas pressure, density, and temperature of the fuelling gas, which were determined in the local simulation volume as part of the EIRENE stage 1 simulation, e.g. in this case the neutral density is $n_n = 1.4 \times 10^{16}\,\frac{1}{\mathrm{m}^3}$.

The plasma parameters and neutral gas density can be used to estimate the relevance of collisions for particle transport in the recessed volumes. Table 5.2 shows calculations of the mean free path for ion-ion collisions and collisions with neutrals, as introduced in section 3.1.3. Three situations are assessed: the transport of a D ion originating from the far-SOL region into recessed volumes in JET and ITER, respectively, is compared to a thermalized ion in typical conditions in a scrape-off layer (SOL) plasma. The values listed for the recessed regions correspond to plasma scenarios examined in the main analysis (section 6.1 for JET and section 6.2 for ITER). In the SOL plasma, ion-ion particle collisions are dominant over collisions with background neutrals. In the recessed regions, the density, and temperature of background ions is significantly lower, while the neutral particle density is comparable, since the magnetic field does not confine the neutral particles. Still, the mean free path for neutral collisions is larger than the ion-ion collisional mean free path. Both types of collisions can however be considered negligible in the recessed regions, because the optical path distance from

Table 5.2: Estimates of mean free path λ_{mfp} for ion-ion collisions and collisions with neutral particles (see Equations 3.11 and 3.12) with plasma parameters and projectile energies E_{proj} relevant in different tokamak regions considered in this work.

	SOL plasma	JET recessed region	ITER recessed region
E_{proj} [eV]	50	10	10
n_i [/m^3]	1.0×10^{19}	3.0×10^{14}	1.0×10^{10}
T_i [eV]	50	0.7	1.0×10^{-3}
n_n [/m^3]	5.0×10^{16}	2.0×10^{16}	1.4×10^{16}
$\lambda_{\mathrm{mfp},ii}$ [m]	5.0	122.1	339.7
$\lambda_{\mathrm{mfp},n}$ [m]	110.5	276.3	386.5

the entrance of the DFW to the first mirrors investigated in this work measures only $\sim$ 20–50 cm in both tokamaks. Additionally, the low background temperature and density of the plasma makes ionization of neutral particles unlikely, which further decreases the importance of ion-ion collisions. Particles reflected or sputtered from surfaces are in neutral charge state as well. Therefore, the majority of particles inside the recessed regions are neutrals and the transport in this volume is largely ballistic, like treated in the 3D-GAPS code [76].

5.3 Catcher Planes and Sampling of Test Particles

The multi-stage simulation approach developed in this work requires the definition of the transition of test particles between successive simulation stages. Test particles act as discretized representations of a large amount of real atoms in Monte-Carlo simulation codes like ERO2.0 and EIRENE. The *Monte-Carlo weight* (MC weight) of a test particle determines the amount of real atoms that it represents, and in ERO2.0 holds the unit [atoms/s][2]. Test particles are labelled in the following simply as "particles".

The *catcher planes* are crucial for the multi-stage simulation approach, serving as leak-tight interfaces between the simulation stages. The location of the catcher planes defines the stages and can thus be chosen arbitrarily, but should ideally lie in tight spaces compared to the preceding simulation volume, since the catcher planes act as absorbing surfaces in all simulations. Particles are terminated as soon as they hit the catcher plane and their current parameters (e.g. position and velocity) are collected. The termination of the particles implies that all fluxes through the catcher plane are assumed to be one-way in the multi-stage approach,

[2]Thus, strictly speaking the MC weight in ERO2.0 defines a physical flux.

as the stages are successive and no two-way coupling via a feedback loop takes place. By defining the catcher planes in tight spaces, e.g. the aperture hole in front of the mirror box, it is justified to assume the fluxes in the return direction to be negligible. This assumption is considered a worthy trade-off against the drastically increased statistics introduced by the approach. A close-up view of the two catcher planes for the ITER EPP DFW can be seen in Figure 5.4, located inside the DFW opening (C1, between simulation stages 1 and 2) and in the aperture hole in front of the mirror box volume (C2, between simulation stages 2 and 3). Simple planar geometry is chosen for the catcher planes, so that the impact angle information can be easily transferred.

Upsampling techniques are applied between the simulation stages to increase the

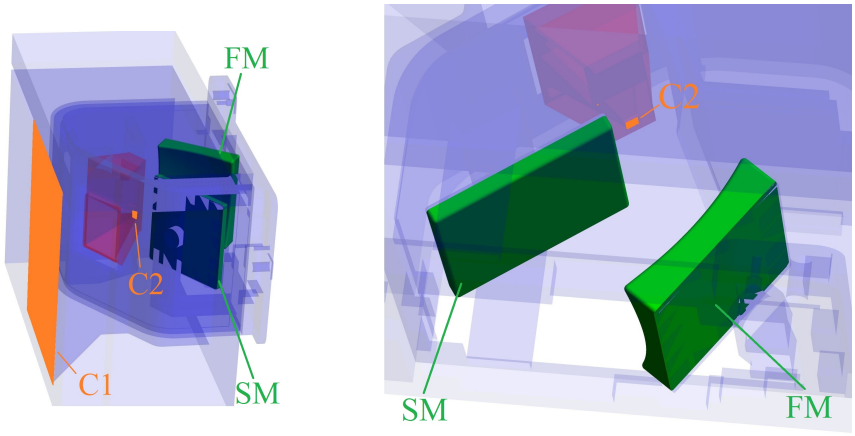

Figure 5.4: Close-up view of the stage 2 and stage 3 simulation volumes in the ITER equatorial port plug (EPP), showing the view from the plasma-facing side (left) and the mirror box (right) – see Figure 5.2 for a view of the EPP in the global ITER volume. Transparent: the EPP diagnostic first wall (blue) and the cone-shaped cut-out (red) that leads to the mirror box. Solid: first mirror (FM) and second mirror (SM) (green) and catcher planes (orange) C1 at the entrance to the DFW and C2 in the aperture hole in front of the mirror box.

statistics in the increasingly recessed regions. In the following, *collected particles* refers to particles impinging on a catcher plane at the end of one simulation stage, e.g. on the C1 catcher plane at the end of simulation stage 1. A large amount of *sampled particles* is then generated and injected into the next simulation stage in a self-consistent approach by applying the caught particles' statistics – position, velocity (magnitude and direction), charge state and MC weight. Importantly, the total MC weight of the sampled particles is identical to the total MC weight of the collected particles, so that no real atoms are artificially injected in the upsampling. Three transitions of particles are present in the multi-stage simulation approach

(see Figure 5.1), and each of these requires a distinct approach explained in the following.

a) Stage 1 (ERO2.0) → Stage 2

The global ERO2.0 stage 1 simulation collects the impinging impurity particles entering the mirror assembly, i.e. impinging on the catcher plane C1. The transition of these impurity particles from stage 1 to stage 2 (conducted completely in ERO2.0) is rather simple, since the code remains the same and the C1 catcher plane is identically present in both stages: statistics of the collected impurity particles on catcher plane C1 are gathered and subsequently sampled to generate a large amount of particles entering the stage 2 simulation (see Figure 5.5). In detail, the following steps are applied to consistently generate the particles for the stage 2 simulation:

From the stage 1 ERO2.0 simulation with k iterations of the main loop (see Figure 3.3), the collected particle ensemble consists of M particles that hit the C1 catcher plane. The statistics of the impact angle θ relative to the C1 catcher surface normal $\hat{n}$, impact position and energy, as well as charge state and MC weight of the particles are collected. Figure 5.7a)-d) show the distributions for the ITER EPP case demonstrated in this chapter.

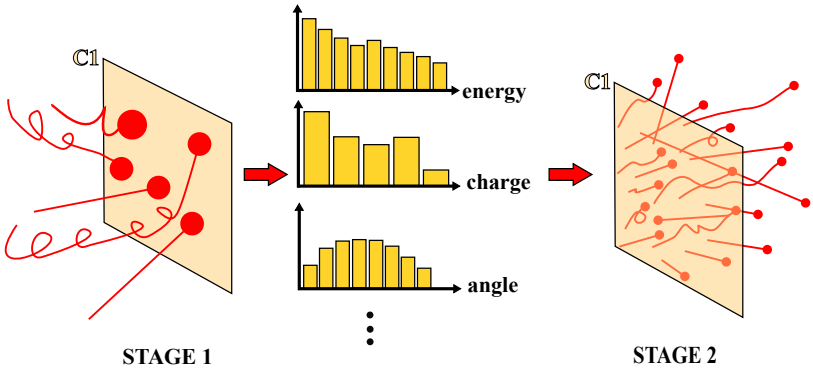

Figure 5.5: Sketch of the transition from ERO2.0 stage 1 to ERO2.0 stage 2 – statistics of impurity particles on the catcher plane C1 are gathered and used to generate a large amount of start particles for the second stage.

The $N \gg M$ particles entering the stage 2 simulation are then sampled from the gathered distributions. For each of the N sampled particles, the triplet of impact angle θ, energy, and charge state is kept consistent with one of the M collected particles, chosen randomly. This keeps potential correlations intact, e.g. (arbitrary): highly charged particles only impinging under steep angles or high

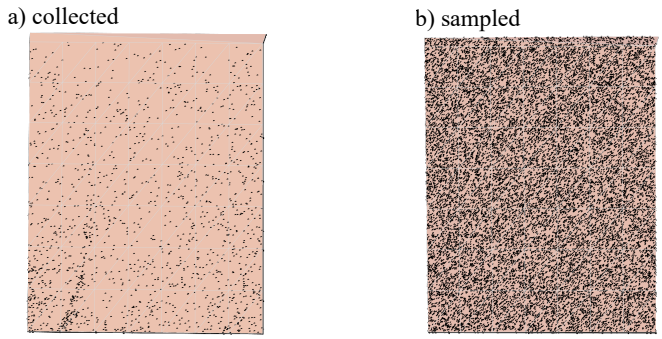

Figure 5.6: Left: impact locations of the Be impurity particles that hit the ITER EPP C1 catcher plane in the ERO2.0 stage 1 simulation – no strong pattern is observable. Right: randomly distributed starting locations of particles in stage 2, upsampled in number of test particles.

energy particles always having a certain charge state.

The velocity magnitude is calculated from the chosen energy. Concerning the direction of the velocity, two rotations are performed, which are visualised in Figure 5.8. First, the C1 normal vector $\hat{n}$, which points into the stage 2 simulation volume, is rotated in the R-z-plane by the impact angle θ. The 3D velocity is not uniquely defined by θ, so an additional random poloidal rotation by an angle φ between 0° and 360° in the plane of the catcher plane is performed. This rotation keeps the impact angle intact, thus a 3D velocity vector following the collected statistics and pointing into the stage 2 simulation volume is achieved. A final test (step 3 and 4 of Figure 5.8) is performed for charged sampled particles, since it is known that the particles *departed* the stage 1 simulation volume at catcher plane C1 and followed the magnetic field line due to their charge. Therefore, it is checked if the sampled particle's velocity component $v_\parallel$ parallel to the magnetic field points *into* the stage 2 simulation volume. $v_\parallel < 0$ is possible due to the random φ-rotation, in which case the particle's 3D velocity is mirrored at its injection location. Although the 3D velocity then points out of the stage 2 simulation volume, the parallel component correctly points into the new simulation volume. Thus, the charged particle will enter the simulation volume as intended, while the correct impact angle is retained along the gyration. For neutral particles, this test is not necessary, since their trajectories are straight until collision or ionization.

The MC weight carried by each sampled particle is also kept consistent with the triplet of energy, impact angle and charge state. However, it is scaled down per particle by the total amount of sampled particles N and the number of performed stage 1 ERO2.0 iterations k, so that the total MC weight of the N sampled particles correctly reproduces the total MC weight of the M collected particles per ERO2.0

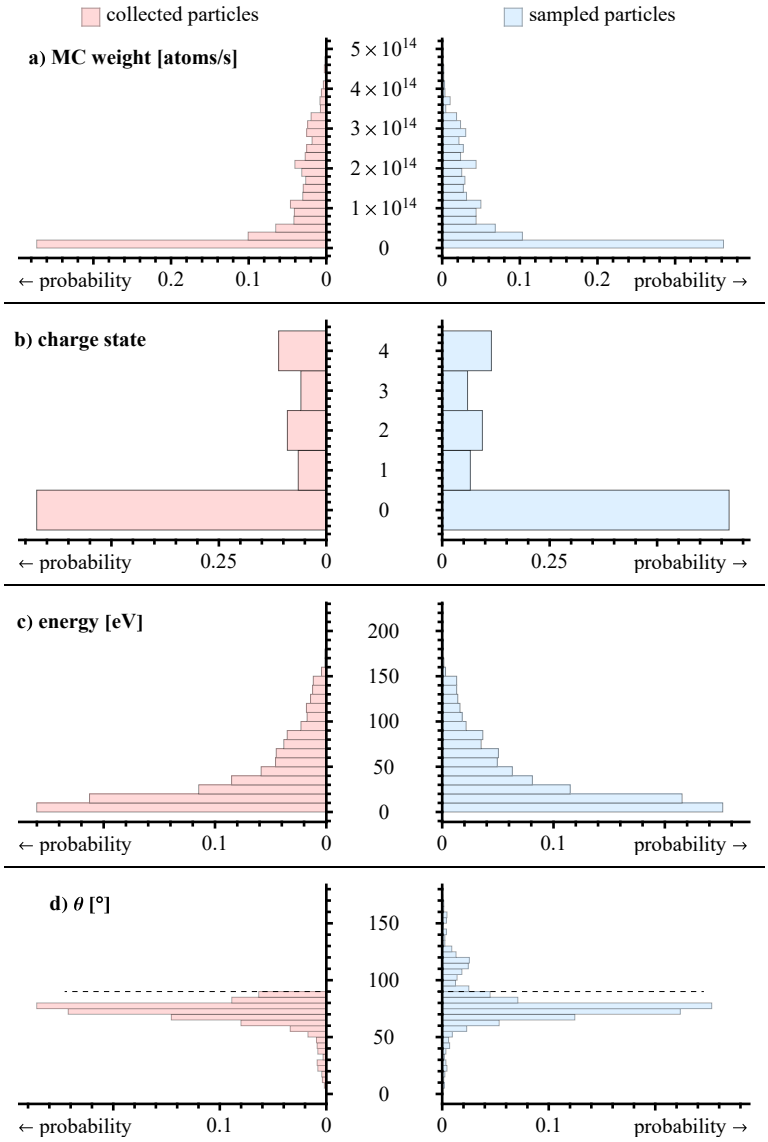

Figure 5.7: Histograms of collected (left, $M = 1622$) and sampled (right, $N = 2 \times 10^6$) particle ensembles in the transition from stage 1 to stage 2, for (a) MC weight, i.e. flux, (b) charge state, (c) energy and (d) impact angle. The respective quantity is shown along the y-axis, the probability is shown outwards. Notes: (i) the MC weight of sampled particles has been scaled for this graphics so that the axes match – in the simulation, the sum of MC weights is identical for the M collected particles and N sampled particles. (ii) The particles with $\theta > 90°$ are sampled charged particles that had their velocity inverted to ensure they move into the local simulation volume (see full text for more detail), which mirrors their angle at 90° (dashed line) from θ to $180° - \theta$. The distributions are otherwise identical.

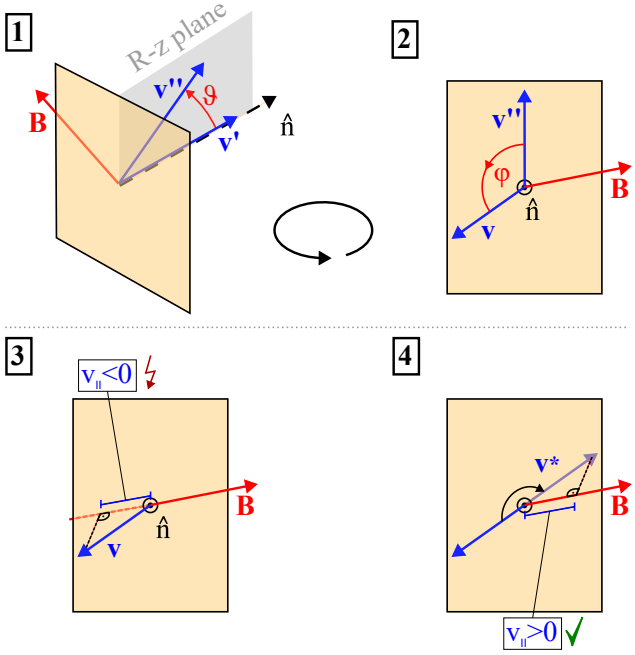

Figure 5.8: Geometry for the rotations necessary to generate the 3D velocity vector $\mathbf{v}$ in the stage 1 (ERO) $\rightarrow$ stage 2 transition via intermediate vectors $\mathbf{v}'$ and $\mathbf{v}''$. $\hat{n}$ is the normal vector of the C1 catcher plane (orange), pointing into the local simulation volume. For neutral particles, only the first two steps are performed. For charged particles, the velocity $v_{\parallel}$ parallel to the magnetic field $\mathbf{B}$ is determined afterwards. Only if $v_{\parallel}$ is negative, the velocity is mirrored at the injection point to generate the starting velocity $\mathbf{v}^*$.

iteration.
Finally, for the position, a random starting point on the C1 catcher plane is chosen, since no strong patterns in the impact locations of impurities in the stage 1 ERO2.0 simulation were found in any of the simulated cases, as seen in Figure 5.6.
The statistics and starting locations of the sampled particle ensemble consisting of 2×10^6 particles can be seen on the right side of Figures 5.7 and 5.6, using the described methods and correctly reproducing the input statistics in the scope desired.

b) Stage 1 (EIRENE) → Stage 2

In the global stage 1 EIRENE simulation, neutral hydrogenic atoms are treated – deuterium (D) or hydrogen (H) depending on the used plasma background. The particles are collected at the catcher plane E, resulting in information about the flux of these neutrals into the recessed mirror assembly. Figure 5.3 shows the location of the E catcher plane, and D is assumed as the neutral species for the explanation in this section. The transition of these neutral particles into the stage 2 ERO2.0 simulation is similar to the transition discussed in section a), but slightly more complicated, since different catcher planes are used in the two codes. In general, the statistics (angular and energy distribution) of the neutral particles on catcher plane E are collected, mapped to catcher plane C1 and sampled to generate a large amount of neutral D particles entering the stage 2 simulation, as depicted in Figure 5.9.

In detail, the output of the EIRENE stage 1 simulation is the total flux measured on

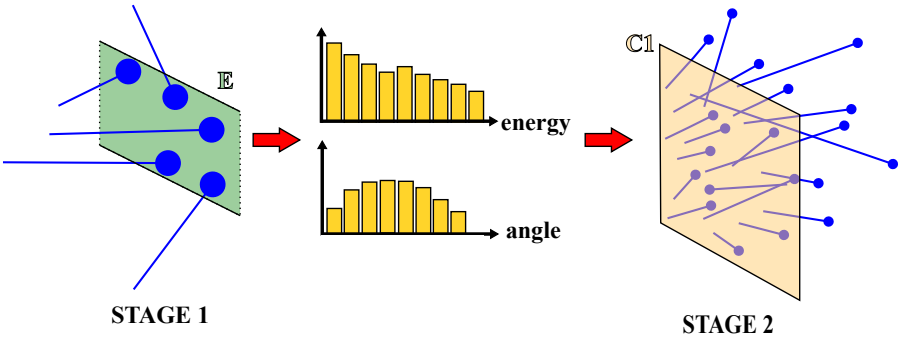

Figure 5.9: Sketch of the transition from EIRENE stage 1 to ERO2.0 stage 2 – statistics of fuel atoms (D/H) on the toroidally symmetric catcher plane E are gathered, and used to generate a large amount of start particles for the second stage. The particles are mapped onto the C1 catcher plane covering the entrance to the mirror assembly.

the toroidally symmetric E catcher plane, an energy distribution and a distribution

Table 5.3: Binning parameters for the collection of energy and angular distributions in EIRENE stage 1 simulations.

	energy distribution		angular distribution
device	dE_{bin} [eV]	$E_{\mathrm{bin,max}}$ [eV]	$d\cos(\alpha)_{\mathrm{bin}}$
JET	5.0	2000	0.022
ITER	0.15	1500	0.002

of the cosine of the impact angle $\cos(\alpha)$ of the impacting neutral D particles. The two distributions, depicted in Figure 5.10, are considered to be independent, which is a simplification of the model. In reality, the impact angle of highly energetic charge exchange neutrals originating from the core plasma region may vary from the impact angle of those neutrals originating from refuelling, but such correlations are not considered in the approach of EIRENE simulations performed as input to this work.

The distributions of the energy and the cosine of the impact angle relative to the catcher surface normal $\hat{n}$ are collected using a binning method with equidistant bins to reduce the computational memory needed for the data acquisition. Upon impact of a particle on the catcher plane E, the flux $\Gamma_{\mathrm{D}}^{\mathrm{in}}$ of the impinging particle is added to the bin b_i matching its energy/impact angle, defined by the binning width $dE_{\mathrm{bin}}/d\cos(\alpha)_{\mathrm{bin}}$, respectively. For example, for the energy spectrum the bin b_1 collects flux from particles with energy within the interval $[0, dE_{\mathrm{bin}})$, b_2 within the interval $[dE_{\mathrm{bin}}, 2dE_{\mathrm{bin}})$ and so forth. The binning parameters are defined ahead of the simulation, see Table 5.3 for the parameters applied in this work.

For the angular spectrum, the possible values for the cosine of the impact angle are bound from both sides – impact angles between 0° and +90° are possible, corresponding to cosine values between 0 and +1. For the energy distribution however, an upper bound $E_{\mathrm{bin,max}}$ has to be set in addition to the binning width dE_{bin}, so that a finite amount of bins b_i can be defined in EIRENE, because the energy of particles is theoretically unbound. The energy spectrum is resolved up to $E_{\mathrm{bin,max}}$, while the flux from all particles with higher energy is collected in one bin b_{max} with the collection interval $[E_{\mathrm{bin,max}}, \infty)$.

Figure 5.10 depicts the energy and angular distribution for the H-mode ITER plasma case covered in this chapter. In the energy spectrum, it is evident that the fluxes at higher energies are far lower than at low energies. However, a significant high-energy tail is present in the distribution, showing increased highly energetic fluxes in comparison to a particle distribution following of a Maxwell-Boltzmann statistics (red dashed line). Impinging high-energy particles in general have a higher physical sputtering yield Y than low-energy particles (compare section 3.3),

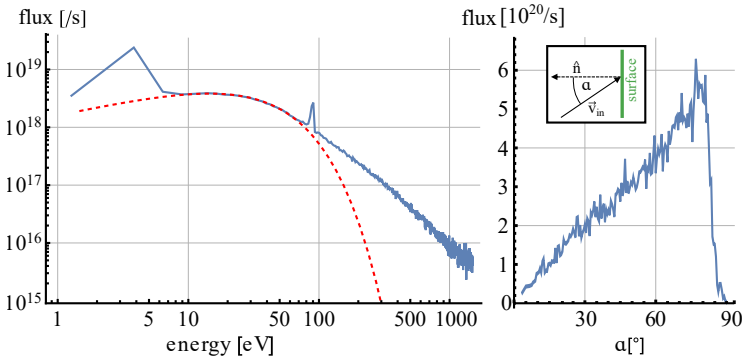

Figure 5.10: Energy spectrum (left, double logarithmic scale) and angular distribution (right, linear scale) from the stage 1 EIRENE simulation of a high-density H-mode plasma. α is defined as the angle between the surface normal and the impact velocity, depicted in the box. The red dashed line shows a Maxwellian energy distribution fitted to the energy range below 90 eV. For a discussion of the plots, see the main analysis in sections 6.1.1 and 6.2.1.

but the energy distribution above $E_{\text{bin,max}}$ is unresolved. However, the validity of the choice of $E_{\text{bin,max}}$ can be checked 'post-mortem' under simplified conditions by estimating the physical sputtering given an energy distribution. Here, the DFW material's main component iron (Fe) is assumed as surface material, with a fixed impact angle of 60° for the D neutral projectiles. The energy distribution is transformed to a distribution showing the relevance of each bin to the total expected sputtering, using the following definition:

$$\begin{aligned} \Gamma_{\text{Fe}}^{\text{sputt}}(E_i) &= \Gamma_{\text{D}}^{\text{in}}(E_i) \cdot Y_{D\to Fe}(E_i) \\ \Gamma_{\text{Fe,tot}}^{\text{sputt}} &= \sum_i \Gamma_{\text{Fe}}^{\text{sputt}}(E_i) \\ \gamma_{\text{rel}}^{\text{sputt}}(E_i) &= \frac{\Gamma_{\text{Fe}}^{\text{sputt}}(E_i)}{\Gamma_{\text{Fe,tot}}^{\text{sputt}}} \end{aligned} \tag{5.1}$$

where $\Gamma_{\text{D}}^{\text{in}}$ is the D neutral flux collected in bin b_i with mean collection interval energy E_i, and Y is the physical sputtering yield. $\gamma_{\text{rel}}^{\text{sputt}}(E_i)$ is visualized in Figure 5.11 for the energy spectrum shown before in Figure 5.10. 95% of the sputtered flux is attributed to incoming D neutral fluxes below 1124 eV. The curve of the accumulated sputtering contributions flattens significantly at higher energies, which means that the higher energy bins are less and less relevant to the total sputtering. While the energy distribution above the upper energy bound remains unknown, this gives confidence in the chosen upper binning energy $E_{\text{bin,max}}$.

A large number N of D neutral particles is then sampled from the collected

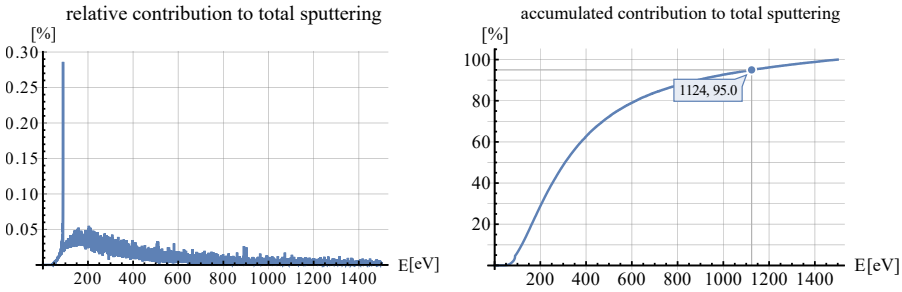

Figure 5.11: Left: Relative contributions $\gamma_{\text{rel}}^{\text{sputt}}$ (see Equation 5.1) to the total sputtering flux $\Gamma_{\text{Fe,tot}}^{\text{sputt}}$ of Fe for the energy spectrum shown in Figure 5.10. A 60° impact angle of D projectiles and a pure iron surface as a representative of the steel DFW are assumed. Right: Accumulated view of $\gamma_{\text{rel}}^{\text{sputt}}$.

EIRENE energy and angular distributions at the start of the stage 2 ERO2.0 simulation. The energy of each starting neutral D particle is chosen statistically from the energy distribution provided by EIRENE. The velocity magnitude is calculated from the energy. The direction of the velocity is determined by the impact angle α, requiring two rotations that are visualized in Figure 5.12. The rotations start with the 3D surface normal $\hat{n}$, which is first generated at the impact location, pointing outward into the volume of the stage 2 simulation. The $\cos(\alpha)$-distribution is sampled and converted into an impact angle α, which gives the first angle of rotation. Two options exist for the interpretation of the angle α: 2D mapping and 3D mapping. For the main analysis of this work, 2D mapping of the angle α was performed. The impact angle α is interpreted in 2D in the R-z-plane as the angle between R-z-projection of the impact velocity and the 2D normal of the catcher plane E, which itself is defined by a two-dimensional sequence of line segments in the R-z-plane. In this case, an angle β between +90° and -90° is chosen randomly as the second rotation angle for the velocity rotation. To generate the velocity, $\hat{n}$ is rotated by β in the plane spanned by $\hat{n}$ and $\hat{n} \times \hat{z}$ where $\hat{z}$ is the z-axis. The resulting vector is then rotated by $\pm\alpha$ in the R-z-plane, which keeps the sampled distribution of α intact. In the later parts of this work, 3D mapping of α is performed, since it was found that the 2D mapping did not accurately represent the 3D impact distribution measured in EIRENE. In this case, α is interpreted as the angle between the 3D velocity vector at impact and the 3D surface normal $\hat{n}$. For the generation of the velocity vector, $\hat{n}$ is first rotated by α in the R-z-plane, keeping the 3D angle statistics intact. Afterwards, the second rotation is performed in the plane perpendicular to $\hat{n}$, using a random poloidal angle φ between 0 and 2π. The 3D mapping leads to up to 60% higher D fluxes onto catcher plane C2 at the end of the stage 2 ERO2.0 simulation compared to

the 2D mapping. The increase in flux at the C2 catcher plane is caused by the fact that the 3D angle mapping attributes a wider range of the angle distribution to velocities pointing along the normal, i.e. into the direction of the C2 catcher plane and mirrors. This results in higher erosion on the mirrors due to impacting energetic D CXN particles, but the effect depends strongly on the 3D geometry of the mirror assembly – for details see the main analysis in section 6.3.2.

For the position of sampled particles, a random starting point on the C1 catcher

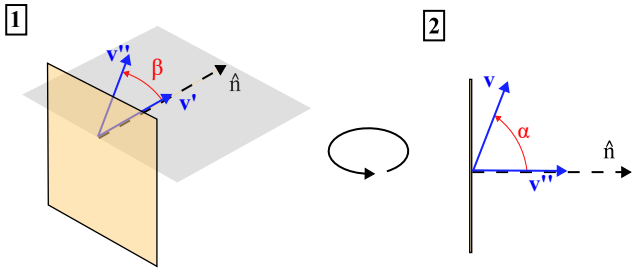

Figure 5.12: Rotations for generating the 3D velocity vector $\mathbf{v}$ in the stage 1 (EIRENE) $\rightarrow$ stage 2 transition with 2D-mapping of the angle α, via intermediate vectors $\mathbf{v}'$ and $\mathbf{v}''$. $\hat{n}$ is the normal vector of the C1 catcher plane (orange), pointing into the local simulation volume. For 3D mapping of α, the generation is equivalent to the ERO2.0 case (Figure 5.8) with $\theta = \alpha$.

plane is chosen, keeping it consistent to the transition described in the previous section a). As only neutrals are considered in EIRENE, the charge state of all D particles generated from the EIRENE stage 1 distributions is defined as zero.

Finally, the MC weight of the sampled particles in the stage 2 ERO2.0 simulation is defined by the total D neutral flux measured in the EIRENE simulation on catcher plane E. EIRENE collects the D neutral particles on the toroidally symmetric catcher plane E with much larger area, therefore the MC weight is multiplied by the ratio of the surface areas of catcher plane C1 to catcher plane E. This total flux is then spread evenly as MC weight across all N sampled particles.

c) Stage 2 $\rightarrow$ Stage 3

Stage 2 is performed entirely in ERO2.0, so a consistent approach for all sampled particles can be chosen for the transition from stage 2 to stage 3 at the catcher plane C2. It differs from the transition discussed in section a) due to two facts: on the one hand, a large correlation between impact location and impact direction was found on the catcher plane C2 in all observed cases, which is attributed to the cone-shaped aperture applied in the DFWs analysed in this work (see Figure 5.4). On the other hand, the number of collected particles in stage 2 is much larger than

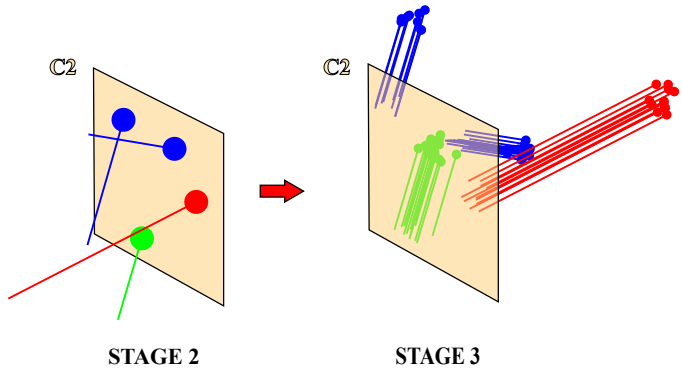

Figure 5.13: Sketch of the transition from ERO2.0 stage 2 to ERO2.0 stage 3 – fuel (blue), impurity (red) and sputtered DFW particles (green) on the catcher plane C2 are collected, and particle splitting is applied to generate the starting particles for stage 3. The split particles are all subject to unique Monte-Carlo behaviour in stage 3. Note: the starting position is identical for each split particle, the small offsets in the right picture are only for visualisation.

in stage 1, because the simulated volume is much smaller.

Therefore, a "cloning" approach is used here for the transition of the particles into the stage 3 simulation (see Figure 5.13) and no dedicated sampling is performed: position, velocity vector and charge state for all generated particles are kept consistent with collected particles. The MC weight of each collected particle is spread over all its "cloned" particles, i.e. one particle from the stage 2 simulation splits into N particles with identical parameters, but the MC weight carried by each is multiplied by $1/N$. Consequently, patterns and correlations are kept entirely intact, but the statistics and resolution in the final simulation stage is still improved, as the clones are all subject to unique Monte-Carlo behaviour inside stage 3 due to collisions with background neutrals, wall components and mirrors.

Chapter 6

Main Analysis and Discussion

The following definitions are used in this work:

- *gross deposition fluence* [atoms/cm^2]: all particle fluxes impinging on a surface (not counting reflected particles), normalized by the surface area, integrated over simulation time;
- *gross erosion fluence* [atoms/cm^2]: all particle fluxes eroded from a surface, normalized by surface area, integrated over simulation time;
- *net fluence* [atoms/cm^2]: local balance of gross deposition and gross erosion – negative values show net erosion, positive values show net deposition zones. Scales with the exposition time of each case;
- *layer growth* [nm], *layer growth rate* [nm/s]: an estimate of the eroded/deposited thickness, calculated by dividing the net fluence by the element's number density;
- *concentration*: as described in section 3.1.5, the HMM in ERO2.0 calculates the surface concentration of elements within the surface interaction layer of thickness d, i.e. the volumetric concentration in this interaction volume;
- *(surface) composition*: triplet of all elements' concentrations in the surface. In the main analysis, a graphical overview of the surface composition on the mirrors will be shown, where clean Mo mirrors are represented by pure blue colour, impurities from the main plasma (Be, B) add red to the colour and sputtered wall material (Ni, Fe) adds green. These colours are also used throughout the whole analysis for these elements, unless specified otherwise. Hydrogenic particles are shown in orange, but do not add to surface composition, as they are assumed to leave the surface instantly.

Further details and a visual guide for the composition plots are presented in Appendix A;

- *mean values* of the quantities above are defined as the average value measured over the respective mirror's front surface, unless specified otherwise. Numeric cell sizes of the discretized 3D mirror models are taken into account.

In the full simulation workflow of the recessed areas analysed in this work, charge-exchange neutrals play a significant role. Therefore, it was deemed necessary that energy spectra of fuel neutrals entering the relevant recessed areas are available for JET and ITER. As mentioned in chapter 3, the generation of these spectra was not part of this work, thus the resulting spectra are only presented and discussed in the following analysis, but the specific setup for the EIRENE simulations is not further detailed. General information about EIRENE and how the data is used in this work can be found in section 3.2 and section 5.3. The ERO2.0 simulations for both tokamaks, JET and ITER, share some settings which are summarised here, while differences in the modelling will be explained in the respective section:
Inside the plasma volume, the traced ERO2.0 test particles – impurity particles in stage 1, additionally D CXN and sputtered DFW particles in stages 2 and 3 – are subject to the Lorentz force and collisions with neutral background particles, while charged test particles are additionally subject to collisions with the charged plasma background as described in section 3.1.3. Ionization and recombination of test particles are calculated with the rates depending on the plasma background parameters. Anomalous diffusion of charged test particles is assumed only in the global stage of each case with a diffusion constant of $D_\perp = 1.0\,\mathrm{m}^2/\mathrm{s}$, and disabled in the intermediate and final stages as discussed in section 5.2. Electric fields outside the sheath region as well as thermal force effects are not considered in this work as outlined in section 3.4. All particle tracing is performed in the AGCA simulation mode, using the optimizations to the GCA tracing methods introduced in chapter 4 for ionized particles.

6.1 JET

6.1.1 Setup

Geometry and multi-stage definition

For the JET simulations, an ITER-Like Mirror Test Assembly (ILMTA) – in the following denoted as mirror assembly (MA) – is studied. This MA was built for testing different cone-like apertures designed for application in ITER [123], using an ITER-like optical path arrangement. The system was installed inside the JET tokamak at the outer mid-plane as illustrated in Figure 6.1. In the operation campaigns between 2014 and 2017, significant time of plasma operation was accumulated in order to test mirrors inside under realistic plasma load and high magnetic field.
Six mirror samples made of Molybdenum (Mo) were installed inside the MA during the ILW-3 campaign taking place between 2015 and 2016. The mirrors were exposed in JET to 8 h of H-mode plasma discharges and 15.3 h of L-mode plasma discharges in deuterium [105]. These exposure times were taken as simulation times for the ERO2.0 simulations performed in this work. After extraction of the MA from JET, specific post-mortem analysis and surface characterisation took place to assess the mirrors' properties. This post-mortem analysis, described in detail in Ref. [105], included measurements of diffuse and total reflectivity, optical and scanning electron microscopy, x-ray spectroscopy and ion beam analysis for elemental composition of deposits and implantations.
Figures 6.1, 6.2 and 6.5 show different 3D and 2D views of the relevant geometry used in the modelling and the elemental composition assumed in this work. The geometry consists of the mirror assembly (MA), the divertor (DIV), and the first wall (FW) components: inner-wall guard limiter (IWGL), inner-wall protection bars (IWPB), inner-wall cladding (IWC), upper dump plate (UDP), and outer poloidal limiters (OPL). The elemental composition of the JET FW and DIV components assumed in the ERO2.0 simulations is shown in Figure 6.1, matching the surface layer of the composition present in the JET-ILW (see Figure 4.10). The MA is located radially recessed behind the OPL to protect it from significant plasma exposure. The MA has three entrances and is made of Inconel alloy, of which the main component[1] nickel (Ni) is used in the simulations as a proxy. Two of the entrances (labelled A and B) have a cone-like structure in front of them. All three entrances are used as test diagnostic cut-outs for planned ITER mirror systems [105] and lead to the same closed volume inside the assembly. The enclosed

[1] https://www.alloywire.com/alloys/inconel-600/

volume is labelled *mirror box* in this work, and contains three mirrors. Each entrance only has a direct line-of-sight to its respective mirror and not to the other two mirrors. Figure 6.2a)-c) show the MA and its interior with the three entrances A-C, the two cones A and B and the three mirrors M_A-M_C. It should be noted that the geometries used as mirrors in the simulation correspond to the mirror holders, because no specific models for the mirrors themselves were available. In the experiment, two Mo mirrors were placed on each mirror holder. The simulation results on the mirror holders are expected to be nearly identical to the mirrors, because the actual mirror surfaces are parallel to the holders, although a slightly larger surface is considered. From this point on, the mirror holder geometries in JET will be simply referred to as mirrors A, B and C (M_A, M_B, M_C).
For the location of the first set $C1_i$ of catcher planes used in the multi-stage simulation approach, the cone A and cone B entrance as well as the MA entrance C were chosen (see Figure 6.2c). For the second set $C2_i$ of catcher planes, the aperture holes in cone A and B, as well as a passage behind entrance C were chosen, leading to a leak-tight volume between the three sets of catcher planes. The third simulation stage is the mirror box behind the C2 catcher planes. Due to the open design of the mirror box containing the three mirrors, sputtered material from one mirror can potentially deposit on the other mirrors. The multi-stage simulation workflow applied to JET is illustrated in Figure 6.3.

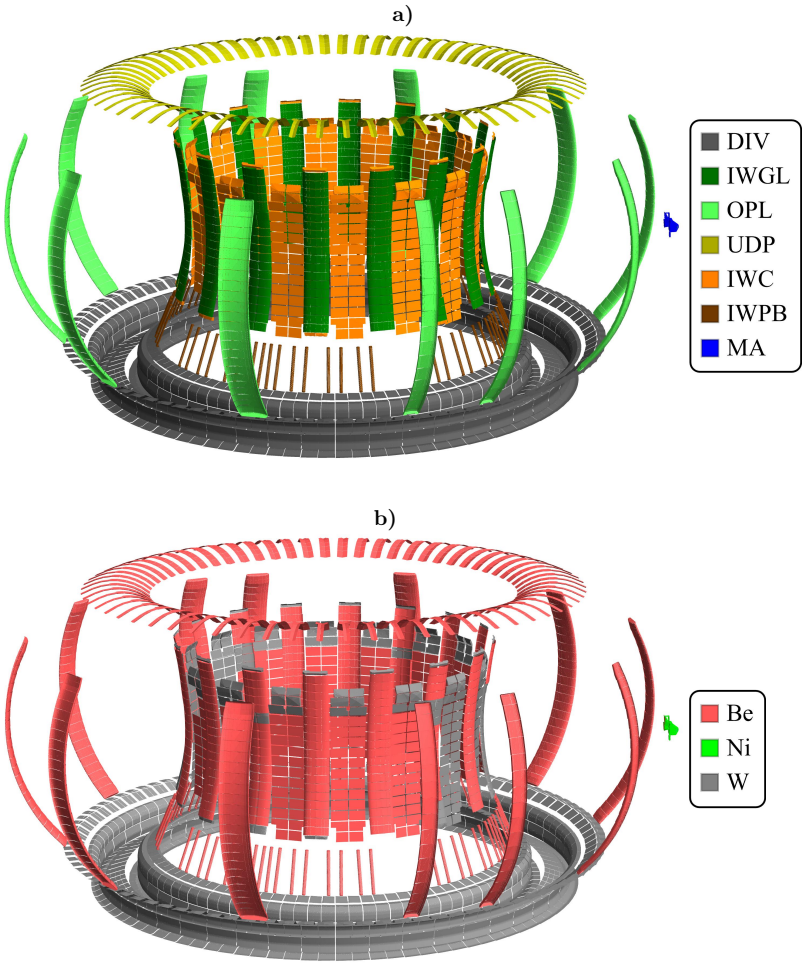

Figure 6.1: Geometry used in the JET global simulation stage. a) Definition of the geometry. The mirror assembly (MA) is shown in blue on the right. b) Same geometry colour-coded by material used in all ERO2.0 simulations for JET.

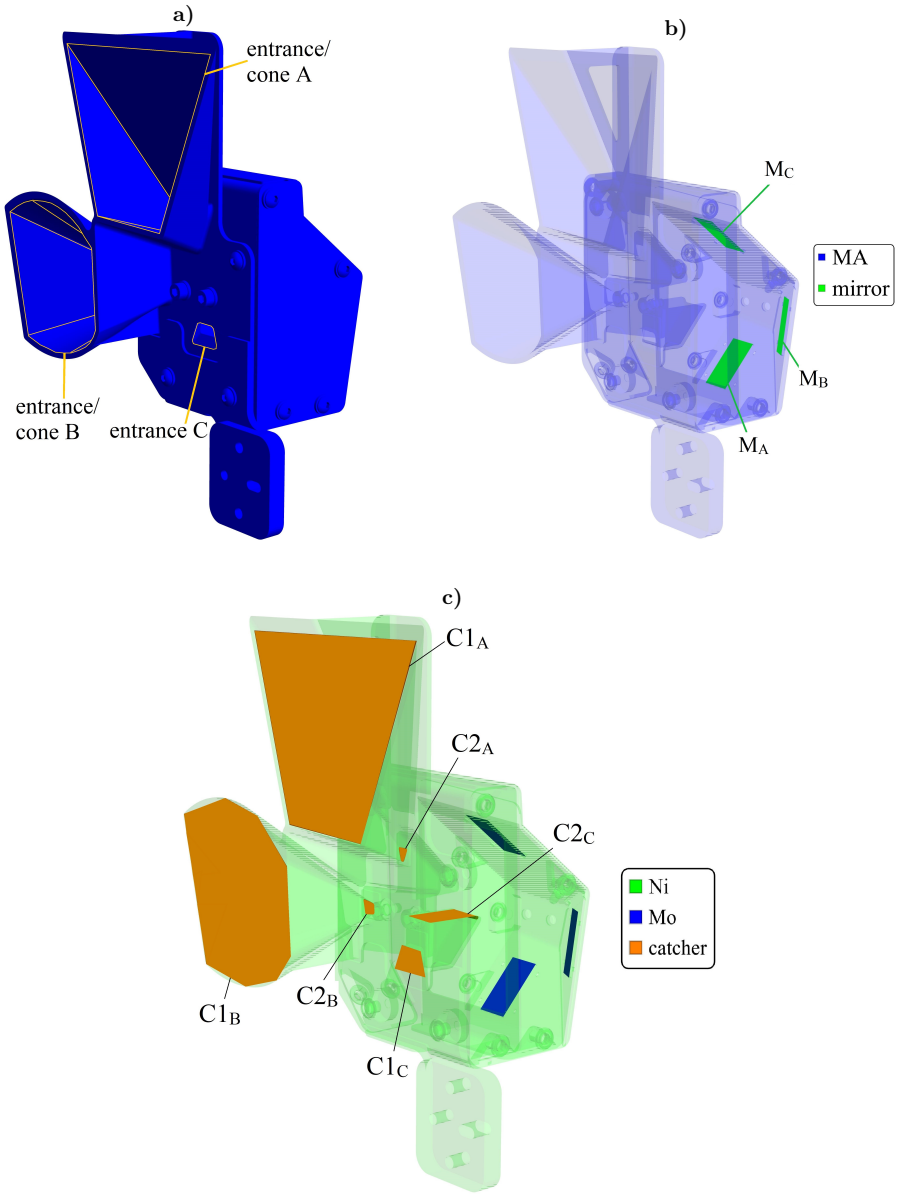

Figure 6.2: Geometry used in the JET simulations inside the Mirror Assembly (MA), which contains the three mirror holders M_i. a) Front view of the MA with two cones and one cone-less entrance. b) Locations of the three mirrors M_i inside the mirror box. c) Geometry colour-coded by material assumed in all ERO2.0 JET simulations, together with locations of the catcher planes $C1_i$ and $C2_i$.

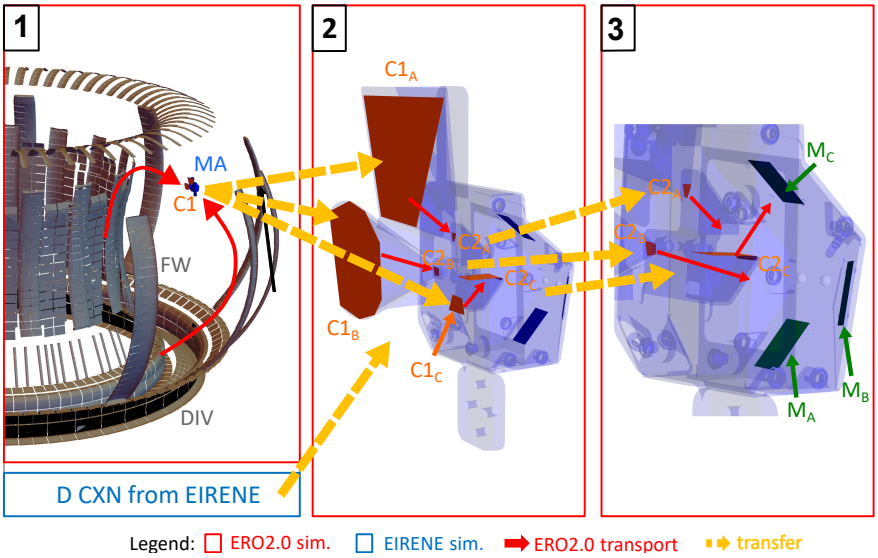

Figure 6.3: Illustration of the multi-stage modelling workflow applied to JET geometry in three stages: global (1), intermediate (2) and final (3). The global simulation contains the first wall (FW) components, divertor (DIV), and first catcher planes (C1) leading into the mirror assembly (MA). The MA has three optical paths (A, B and C) leading to three mirrors M_i. Only entrances A and B are equipped with entrance cones. Red arrows schematically indicate ERO2.0 particle trajectories simulated during each stage. Yellow dashed arrows indicate data transfer between simulation stages via the sets of three catcher planes $C1_i$ and $C2_i$, respectively, whose position is identical in all stages.

Plasma scenarios

Two plasma scenarios are analysed in the JET modelling of this work, one case in High-Confinement mode (H-mode) and one case in Low-Confinement mode[2] (L-mode). Key parameters of the plasma scenarios are outlined in Table 6.1. For the plasma background data, existing EDGE2D-EIRENE solutions for L-mode and low-power H-mode at $I_p = 2.0\,\mathrm{MA}$, $B_t = 2.0\,\mathrm{T}$ based on earlier studies were used [102]. The plasma background is summarised in the following, and more information on the EDGE2D-EIRENE plasma modelling can be found in Ref. [38].

The magnetic field is in semi-horizontal divertor configuration – so-called V5

Table 6.1: Definition of JET plasma cases for ERO2.0 simulations in this work.

plasma case	$n_{\mathrm{e,sep,omp}}$ [/m^3]	$P_{\mathrm{core,E2D}}$ [MW]	Fuel	ERO2.0 sim. time [s]
H-mode	3.0×10^{19}	4.8	D	3.0×10^4
L-mode	1.4×10^{19}	2.2	D	5.5×10^4

configuration – with the inner strike-line on the vertical target and the outer strike line on the bulk-W divertor target tile 5. The simulated H-mode plasma is close to the campaign-averaged H-mode plasma in this first phase of JET-ILW exploitation. In the plasma modelling, EDGE2D-EIRENE assumes a radial profile for the anomalous diffusion coefficient of fuel ions with values close to $1.0\,\mathrm{m}^2/\mathrm{s}$. ERO2.0 uses a constant value of $1.0\,\mathrm{m}^2/\mathrm{s}$ throughout the whole volume for simplicity.

An overview of the plasma parameters in the R-z-plane can be seen in Figure 6.4 for all considered scenarios. The plasma parameters provided by EDGE2D-EIRENE as 2D maps were considered toroidally symmetric throughout the ERO2.0 simulation volume in the first stage of the simulation. The simulation volume includes the full 360° model of JET, as due to the irregular pattern of the discrete poloidal limiters in JET, no periodic boundary conditions can be used in contrast to ITER. For the total simulated time, values were chosen that correspond to the exposure time of mirrors in the experimental campaigns performed at JET [105] (see section 6.1.3). Plasma background parameters in the region of the mirror assembly, thus far away from the separatrix in the SOL-layer, were extrapolated as described in section 5.2. Due to the recessed location of the assembly, $R - R_{\mathrm{sep}} = 16\,\mathrm{cm}$ far away from the separatrix, the resulting plasma temperatures are well below 1 eV and density below $10^{15}\,\frac{1}{\mathrm{m}^3}$. The extrapolated values for both plasma scenarios can be found in Table 6.2.

[2]H-mode and L-mode are operational regimes of fusion devices. Low and high refer to the energy confinement time τ_E, which "approximately doubles in magnitude" [112] in H-mode compared to L-mode. The transition from L-mode to H-mode operation was found to scale with the auxiliary heating power [125], requiring a threshold power that "is known to depend on the plasma density, magnetic field and plasma size" [74].

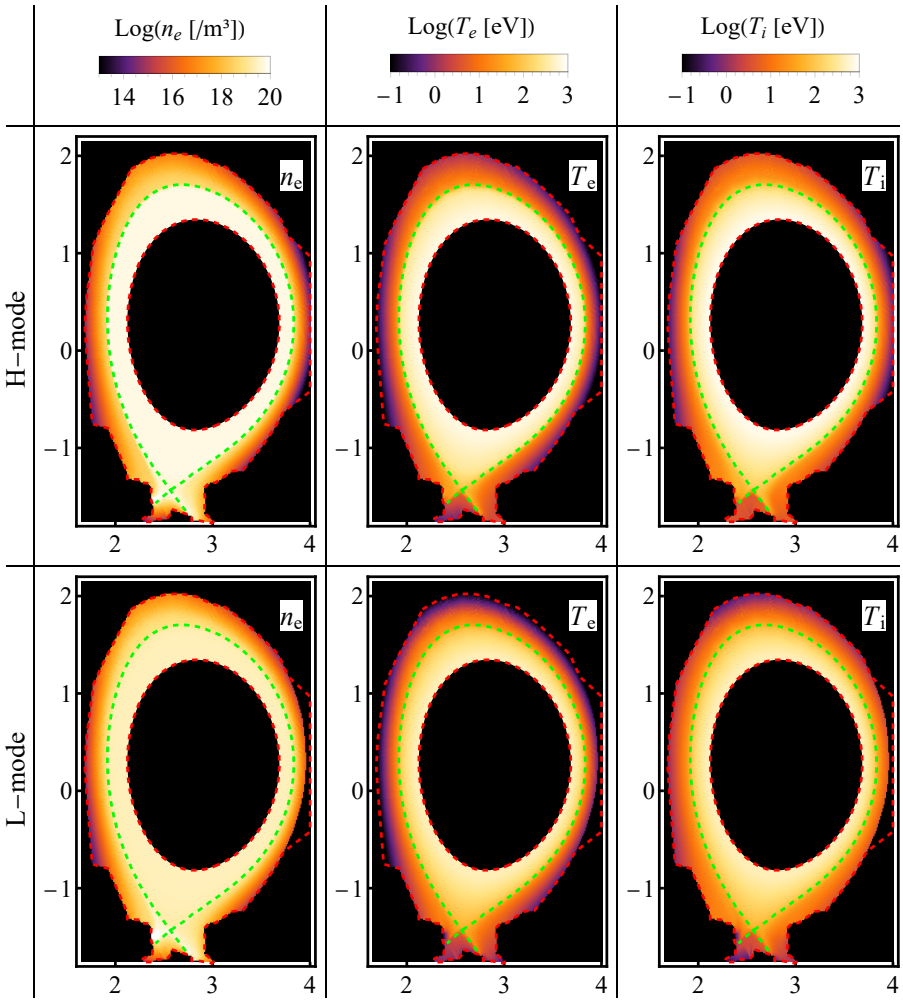

Figure 6.4: Overview of the plasma scenarios assumed for the JET simulations in this work: electron density, electron temperature and ion temperature as 2D maps in the R-z-plane (all coordinates in units of metres). Also shown: inner and outer ERO2.0 simulation boundaries (red dashed line) and separatrix (green dashed line).

Table 6.2: Extrapolated plasma parameters at the JET mirror assembly local plasma volume. These constant plasma parameters for JET L-mode and H-mode plasma cases, respectively, are used in stages 2 and 3.

plasma case	B [T]	T_e [eV]	T_i [eV]	n_e [/m³]
H-mode	1.51	0.13	0.65	3.10×10^{14}
L-mode	1.51	0.03	0.18	1.59×10^{13}

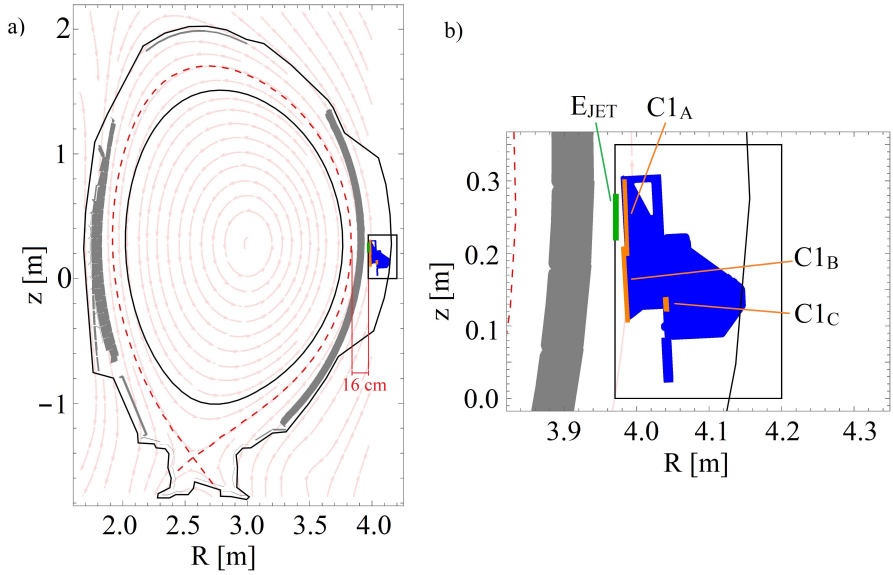

Figure 6.5: ERO2.0 simulation volumes (solid black lines) in the JET simulation workflow in the R-z-plane with projection of the relevant geometry (grey: FW/DIV, blue: mirror assembly), catcher planes used in ERO2.0 stage 1 ($C1_i$, orange), E_{JET} catcher plane used in EIRENE stage 1 (green), and magnetic geometry (red dashed: separatrix, light red arrows: field lines). a) Full volume used in stage 1. b) Zoom of local plasma volume used in stages 2 and 3.

CXN spectra

The deuterium neutral spectra were generated by post-processing of the EDGE2D-EIRENE plasma solutions presented with EIRENE. The impact energy and angular distributions are shown in Figure 6.6. The high-energy tail of the energy distribution is clearly present in both plasma cases. In general, the distributions look similar in H- and L-mode, especially in the case of the angular distribution. In Table 6.3, the mean energy of the distributions and the total flux onto the catcher plane is summarised. The flux entering the recessed volume in H-mode operation is lower than in L-mode as expected due to the better plasma confinement, but consists of more highly energetic particles.

Table 6.3: Integrated neutral hydrogenic fluxes entering the JET mirror assembly and their mean energies, generated by EIRENE (see Figure 6.6 for spectra).

D neutrals	flux [1/s]	mean energy [eV]
H-mode	3.0e18	66.4
L-mode	6.5e18	52.2

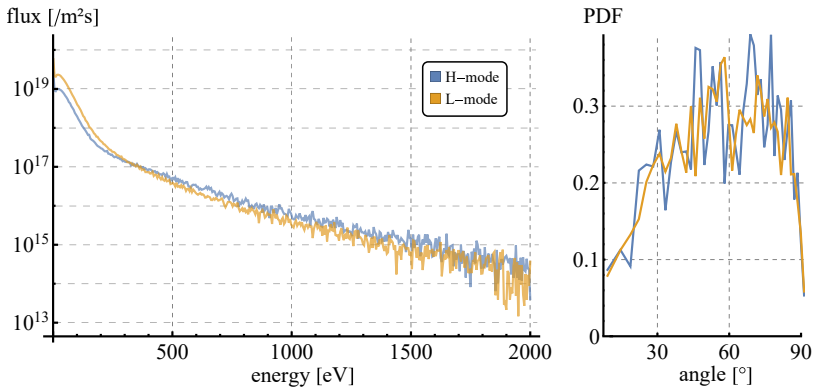

Figure 6.6: Impact energy (left) and angular (right) distribution of impinging hydrogenic fuel neutrals entering the JET mirror assembly region, generated by EIRENE as part of the stage 1 simulations. Note, that a logarithmic scale is applied for the energy distribution to emphasize the high energy tail.

Energy and angular distribution of impinging particles on the mirror

To discern a reasonable choice for the surface interaction layer thickness d for the Homogeneous Mixing Model (HMM, see section 3.1.5) used in ERO2.0, the multi-stage simulation workflow was first performed as introduced until the end of stage 2. In a test simulation of stage 3, particle impact statistics on the mirrors

were then evaluated. Figure 6.7 shows the energy distribution of particles impinging on the mirror and is resolved by elements. Thereby, deuterium particles reach up to the highest energies (∼1 keV) due to the high-energy tail of the incoming CXN energy spectrum as indicated in compare Figure 6.6a) and c). However, these high-energetic neutral particles can sputter Be and Ni inside the assembly, therefore a fraction of Be and Ni particles is present at high energies, although their mean energies are far lower than of D. The highest mean impact energy at around 33 eV is reached by D in the H-mode plasma case, while the other elements mean impact energy onto the Mo mirror lays below 11 eV. The mean energies in the L-mode case are slightly lower.
Impact angle statistics are shown in Figure 6.7b) and d) and line up with considerations of the geometry: D, Ni and Be mostly originate from outside the mirror volume, therefore their impact angle spectra show generally the same trend, while Mo – which can only originate from the other mirrors – follows a visibly different distribution. The two peaks in the Mo angular distributions could be attributed to the two other mirror locations in the assembly.

With this information, sample SDTrimSP calculations were performed to estimate a physically reasonable value for the surface interaction layer thickness d, using the mean energies from the H-mode case due to the higher values, and corresponding inpact angles. From the four combinations (i) Ni $\rightarrow$ Mo, 8 eV, 30°, (ii) Be $\rightarrow$ Mo, 11 eV, 30°, (iii) D $\rightarrow$ Mo, 33 eV, 30°, (iv) Mo $\rightarrow$ Mo, 11 eV, 25°, the D impact showed the highest average implantation depth of 1.5 nm into Mo, while the other elements showed depths much lower than 1 nm. For this reason, the surface interaction layer is assumed with the thickness $d = 1$ nm in all JET stage 3 simulations, so that the surface concentration values on the mirrors in the analysis should be as realistic as possible within the framework of the HMM. In simulation stages 1 and 2, where impact energies are significantly higher, the ERO2.0 standard value of 100 nm is used for all geometry.

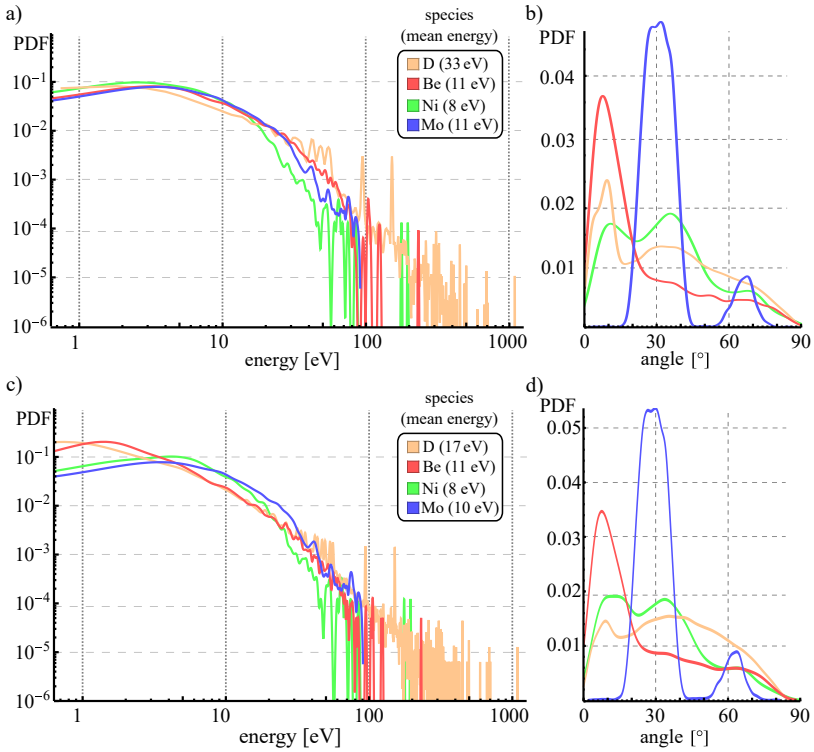

Figure 6.7: Impact energy (a+c) and angular (b+d) distribution of impinging particles on JET mirror A in the ERO2.0 stage 3 simulation for the H-mode (top) and L-mode (bottom) plasma case. The mean energy is marked in the legend for each case, respectively.

6.1.2 Simulation Results

A graphical overview of the mirror surfaces at the end of the simulation time of both plasma scenarios can be seen in Figure 6.8 for mirror A. Mirror A is discussed here in detail as it accumulated the highest Be deposition on the surface, while corresponding overview graphics for mirror B and C can be found in Figure 6.10 and Figure 6.11, respectively.

Figure 6.8 shows the front side of mirror A in the H-mode and L-mode cases after 3.0×10^4 s and 5.5×10^4 s of plasma operation, respectively. The accumulated Be, Ni, and Mo net fluences (a-c) at the end of the simulation are depicted with net deposition in blue and net erosion marked in red. Be, originating from the main chamber and re-erosion from the mirror assembly, and Ni, sputtered from the mirror assembly itself, are deposited nearly homogeneously in small quantities of less than 0.5 nm thickness everywhere on the mirror surface. The deposition of Ni is around one order of magnitude higher than Be deposition in the H-mode case, and around twice as high as Be in the L-mode case. Still, even for Ni, barely one atomic monolayer ($\sim$0.35 nm [44]) is deposited on average on the mirror. Although technically a layer thickness can be defined, it should be noted that the extremely low values of less than one atomic monolayer averaged over the mirror surface should be interpreted as local deposition of the elements and not as a distinct homogeneous layer. The mirror material Mo is slightly net eroded with a mean value over the mirror surface of 0.003 nm thickness in H-mode and 0.004 nm in L-mode. A similarly homogeneous distribution on the surface can be seen in the simulation, which as before should be interpreted as local erosion.

The surface composition of mirror A at the end of the simulation time is visualised in Figure 6.8d). A non-negligible concentration of Ni ($\sim$27% on average) can be found on the Mo mirror in the L-mode case, while the H-mode case shows slightly lower Ni concentration ($\sim$13%). It should be noted, that this surface concentration is determined in the interaction layer with only 1 nm thickness. Still, even after the full exposure time of more than 10^4 s in the simulation, mirror A retains a mean Mo concentration of more than 60% in L-mode and 85% in H-mode. The higher Be and Ni fluences and surface concentrations in L-mode can partially be attributed to the approximately twice as long exposure time in L-mode compared to H-mode, which has been chosen to match experimental data from Ref. [105]. Additionally, the fluxes into the MA are higher in L-mode – especially the around twice as high CXN fluxes (Table 6.3) result in more sputtered Ni from the mirror assembly.

The impinging and eroded fluence on mirror A is summarised in Tables 6.4 and 6.5

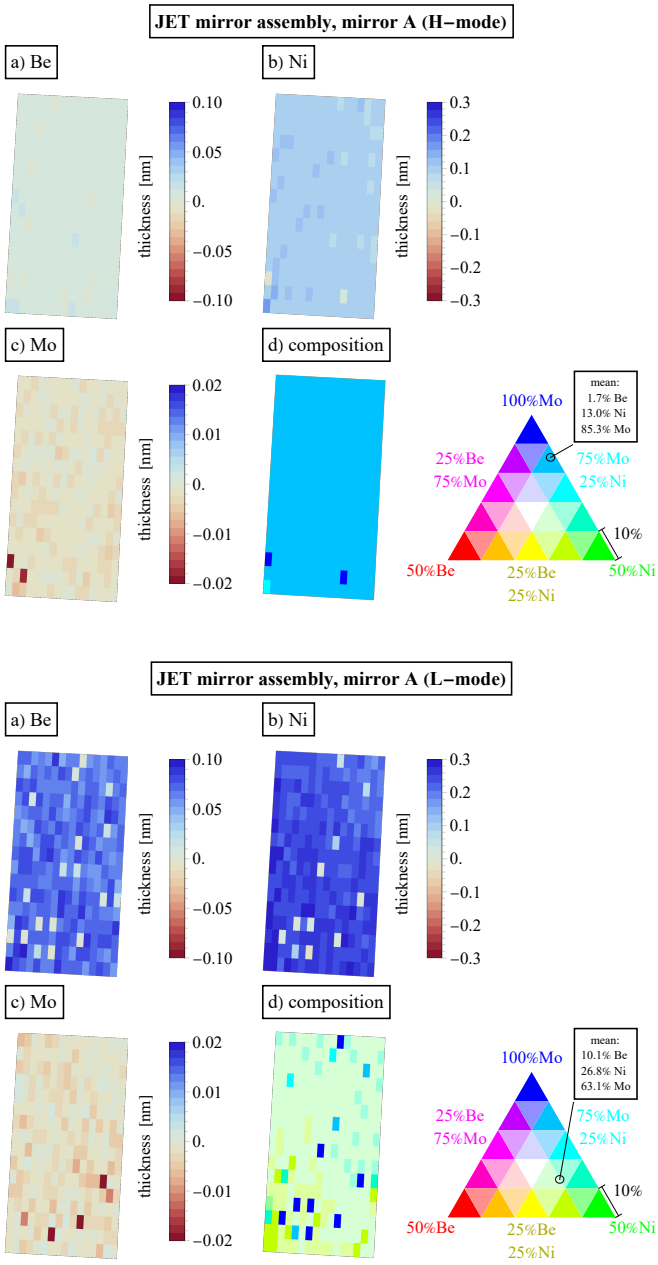

Figure 6.8: Mirror A in the JET H-mode (top)/L-mode (bottom) simulation case: a)-c) net fluences of Be, Ni, and Mo with the net erosion shown in red and net deposition in blue. d) Surface composition in a 1 nm surface layer. Each coloured triangle corresponds to a range of 10% in concentration. The mean surface composition is marked and amounts to 1.7% Be, 12.9% Ni, and 85.4% Mo in H-mode and 10.1% Be, 26.8% Ni, and 63.1% Mo in L-mode.

Table 6.4: Simulated net, gross deposition, and gross erosion fluences integrated over the H-mode plasma exposure time and averaged over mirror A (first block). The coloured block shows the contribution of the different projectiles to the sputtering of each element on the mirror surface.

JET mirror assembly mirror A (H–mode)	net fluence [at./cm²]	gross deposition fluence [at./cm²]	gross erosion fluence [at./cm²]	...by D [%]	...by Be [%]	...by Ni [%]	...by Mo [%]
D	2.09×10^{17}	2.09×10^{17}	0.00	––	––	––	––
Be	1.22×10^{14}	1.64×10^{14}	4.19×10^{13}	99.96	0.04	3.3×10^{-3}	1.29×10^{-5}
Ni	9.08×10^{14}	9.38×10^{14}	2.96×10^{13}	99.53	0.25	0.21	4.97×10^{-3}
Mo	-2.06×10^{13}	1.29×10^{13}	3.35×10^{13}	99.00	0.31	0.66	0.02

Table 6.5: Equivalent of Table 6.4 for the JET L-mode plasma case.

JET mirror assembly mirror A (L–mode)	net fluence [at./cm²]	gross deposition fluence [at./cm²]	gross erosion fluence [at./cm²]	...by D [%]	...by Be [%]	...by Ni [%]	...by Mo [%]
D	9.03×10^{17}	9.03×10^{17}	0.00	––	––	––	––
Be	8.35×10^{14}	1.79×10^{15}	9.56×10^{14}	99.88	0.12	7.69×10^{-4}	1.29×10^{-7}
Ni	2.20×10^{15}	2.39×10^{15}	1.85×10^{14}	99.39	0.52	0.09	3.63×10^{-4}
Mo	-1.28×10^{14}	1.56×10^{13}	1.44×10^{14}	99.59	0.29	0.12	5.15×10^{-4}

for H-mode and L-mode, respectively, resolved by element. More than 99% of the sputtering of all materials is caused by impinging D particles (orange column), while the other elements contribute at most 0.5% to the erosion, as summarised in Table 6.4. Be and Ni are deposition dominated in the balance, since the reflection probability of these elements on the Mo surface is low at the low impact energies (compare Figure 6.7), and thus the elements stick and deposit. However, some minor re-erosion of these elements takes place, as 25% of the impinging Ni flux, and 12.5% of the impinging Be flux is sputtered again. Additionally, although Mo is in balance net eroded from the Mo surface, Mo deposition also occurs on the mirror. This is caused by the open design of the mirror box, in which sputtered material from one mirror can reach the other mirrors.

Figure 6.9a) shows that the surface composition changes nearly linearly in time, which falls in line with the aforementioned domination of deposition and only slight re-erosion. The behaviour is similar in the L-mode case depicted in Figure 6.9b). The D fluxes impinging on the mirrors are assumed to leave the surface instantly and do not accumulate in the interaction layer.

The general results for the other two mirrors in the mirror assembly are similar to mirror A and are shown in Figure 6.10 (mirror B) and Figure 6.11 (mirror C), respectively. An overview of the simulation results for all mirrors in both plasma cases can be found in Table 6.6, where the mean values over the respective mirror surface are summarised, thus, averaging over the spatial distribution of the surface is applied. Since the erosion and deposition is rather homogeneous in all cases,

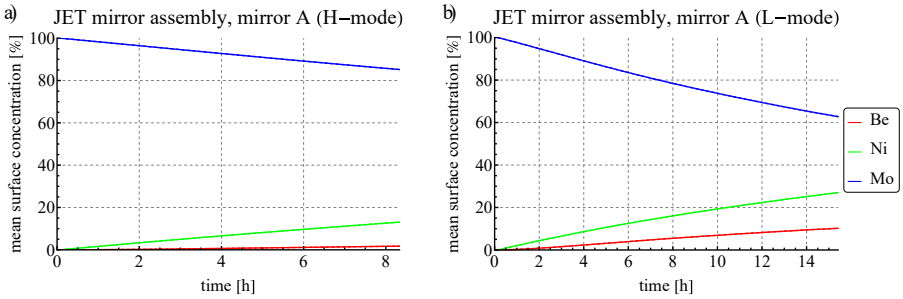

Figure 6.9: Evolution of mean surface composition over the simulated time on mirror A in the a) H-mode and b) L-mode simulation, each performed in 100 discrete time steps with the HMM. The values are averaged over the mirror front surface.

these values can be compared well and are representative of the 3D depiction.

Overall, the results for mirror A and B are extremely similar. This falls in line with

Table 6.6: Overview of average Be and Ni deposition and Mo erosion on the front of the mirror surfaces at the end of the simulation time in the JET H-mode and L-mode simulation, respectively. Fluxes simulated by ERO2.0 were integrated over time and mirror front surface, and converted to a layer thickness using the element's density. Negative values imply net erosion.

		Be layer [nm]	Ni layer [nm]	Mo layer [nm]
Mirror A	H−mode	9.97×10^{-3}	0.10	-3.21×10^{-3}
	L−mode	0.07	0.24	−0.02
Mirror B	H−mode	8.27×10^{-3}	0.11	−0.02
	L−mode	0.06	0.27	-3.58×10^{-3}
Mirror C	H−mode	2.17×10^{-3}	0.41	−0.19
	L−mode	0.02	0.97	−0.33

the fact, that mirror A and B have cone-like apertures in front of their respective entrance into the mirror assembly. The results for mirror C differ slightly: while the Be deposition is lower on mirror C than on mirrors A and B, around four times as much Ni is deposited on mirror C than on the other mirrors. The Mo erosion values are one order of magnitude higher than the respective maximum erosion on mirrors A and B in the L- and H-mode plasmas. These simulation results imply that the cones in front of entrances A and B provide some protection for the mirrors. It should however be noted, that the deuterium fluxes, which are coming into the entrance C of the assembly and are responsible for the dominant fraction of Ni sputtering, were likely overestimated in this simulation setup. The total CXN flux into the assembly simulated by EIRENE was spread over the surfaces of the first set of catcher planes covering the cone entrances, scaled by their respective area. Entrance C does not have a cone structure, but only a hole in the assembly, and

importantly lies further outside than the two cone entrances of entrance A and B (see Figures 6.2 and 6.5). In a more refined approach of the particle sampling, the distance to the plasma would also be taken into account, which is different only for entrance C. Due to this simplification, the simulation results for mirrors A and B are potentially more realistic than the simulations for mirror C.
Furthermore, in all 3D depictions of the mirrors, it is apparent that no specific geometric influence or pattern is found on the mirror. At a glance, one could think this might be caused by the rather low resolution of the mirror models, with 256 cells covering the 6.5 cm^2 models. However, this phenomenon and the generally very low fluence on the mirrors can be reasonably explained by the geometry of the apertures leading to the mirror box (see Figure 6.2): the apertures are shaped in a way so that no particle eroded or reflected from the cone can directly reach the mirror by straight line-of-sight transport because of their opening angles, i.e. nearly all particles that hit them in stage 2 of the simulation miss the mirror by line-of-sight transport later in the simulation. Since the aperture hole is significantly smaller than the cone, the impinging particle fluence is reduced, although reflections from other surfaces and collisions with the thin plasma and neutral particle background can still contribute to additional fluence onto the mirrors. Particles that do not impinge on the apertures see the respective mirror without obstruction, which explains the mostly homogeneous deposition and erosion found on the mirrors.

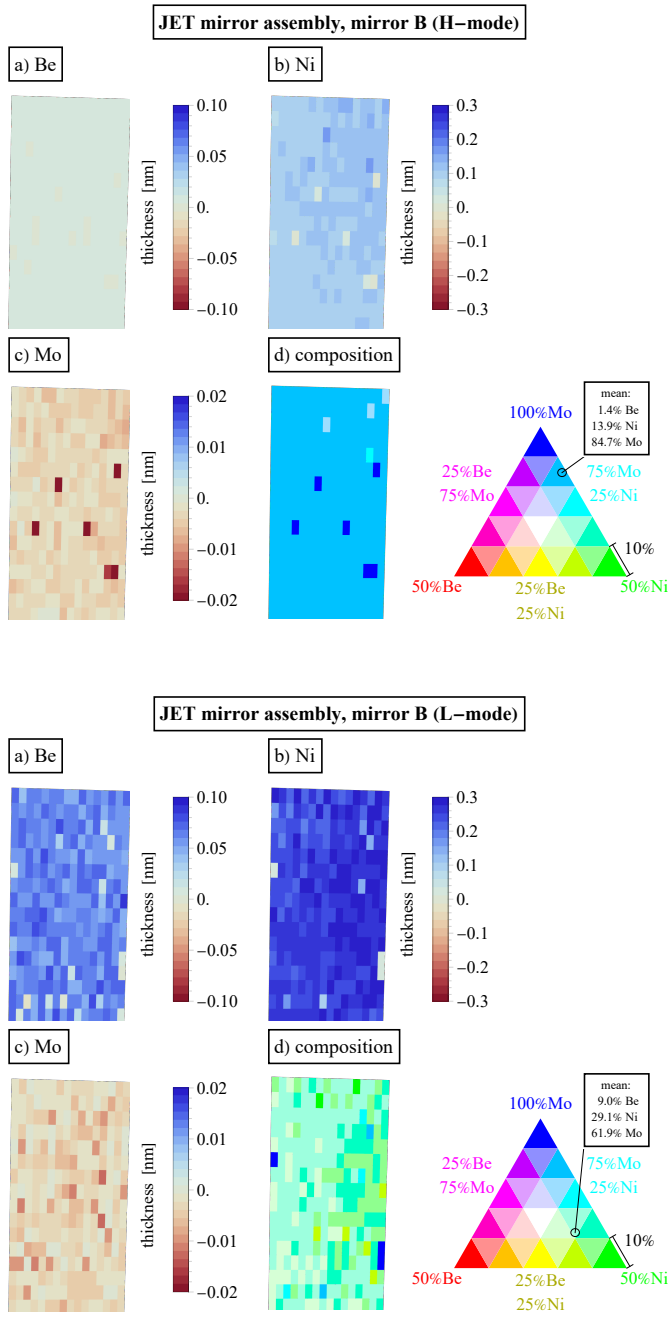

Figure 6.10: JET mirror B front surface at the end of the simulations in H-mode plasma (top) and L-mode plasma (bottom). a)-c) Accumulated fluence of Be, Ni, and Mo. d) Surface composition in a 1 nm thick interaction layer. Each coloured triangle corresponds to a range of 10% in concentration.

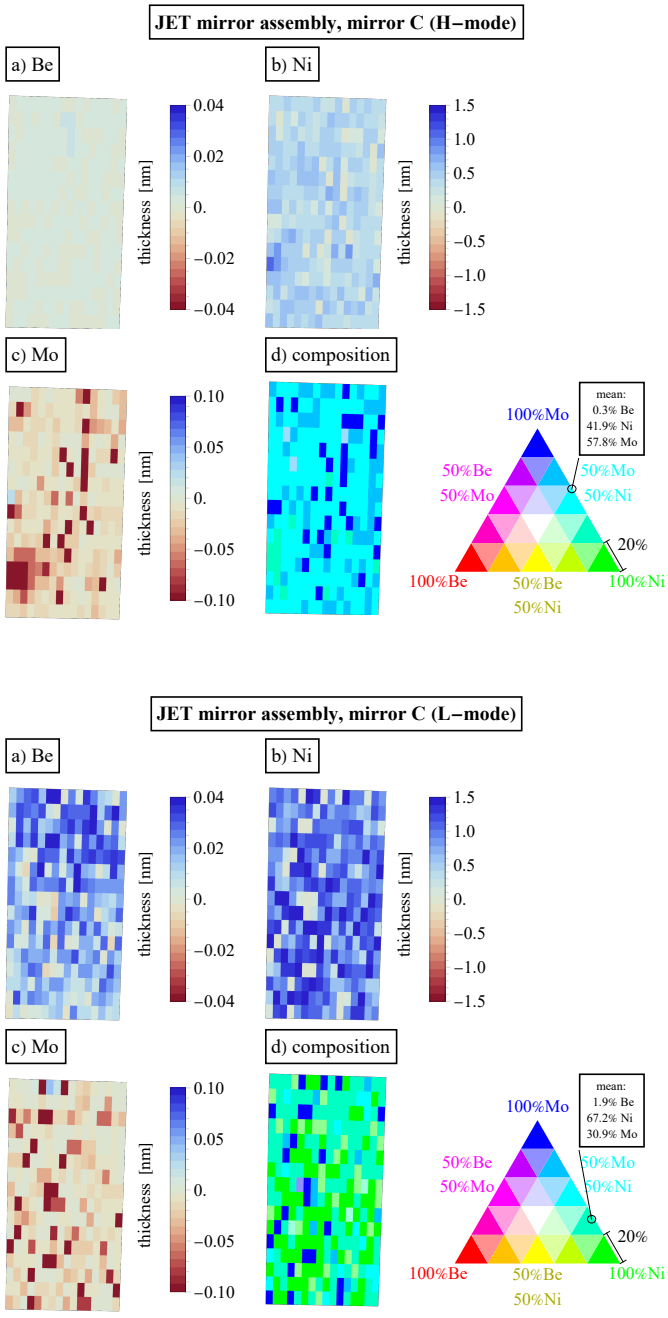

Figure 6.11: JET mirror C front surface at the end of the simulations in H-mode plasma (top) and L-mode plasma (bottom). a)-c) Accumulated fluence of Be, Ni, and Mo. d) Surface composition in a 1 nm thick interaction layer. Each coloured triangle corresponds to a range of 20% in concentration.

6.1.3 ERO2.0 Benchmark with Experiment

The experimental analysis performed on the mirror samples placed in the JET mirror assembly is detailed by Rubel et al. in Ref. [105]. The main experimental findings about optical properties and material composition on the surface of the mirrors will be summarized in the following:
The post-mortem analysis revealed, that the mirrors did not suffer from a loss of total reflectivity relative to the initial measurements. In contrast, the analysis showed an improved total reflectivity on all mirror samples in the range of 0.6–7.7 %. Rubel et al. suggest the increase in total reflectivity is attributed "to at least partial removal of molybdenum surface oxides" [105, p.5] due to the increased surface temperature in the hot environment of the JET vacuum vessel, which operates at around 160–220°C [105, p.6]. The diffuse reflectivity however deteriorated, rising "from 1.5–2.0 % to 2.8–4.0 %" [105, p.6]. Most importantly for this work, Heavy Ion Elastic Recoil Detection Analysis (HIERDA) was applied to the mirror surfaces to measure the surface concentrations of several present elements implanted on the Mo mirror samples. The depth resolution of the technique is stated as 10–15 nm, and measurements probed up to 120 nm deep into the surface. The measured surface concentration can be directly compared to the simulation results from this work, permitting a benchmark between experiment and simulation. In Ref. [105], the surface concentration is given in units of atoms/cm², therefore this unit is adapted here for this section. For the comparison, the net fluences of the two separate ERO2.0 H-mode and L-mode simulations were added up to make a direct comparison with the campaign-integrated results of the experiment possible. However, the following caveats should be noted:
Firstly, the simulations in the two plasma cases were conducted separately and not in succession, and the mirror started with a pure Mo surface in both simulations. Secondly, as described in section 6.1.1, mirror holder geometries were used in the simulation. In the experiment, each holder holds two mirrors for a total of six mirrors. However, since atomic surface concentrations are compared, and since the holders are parallel to the mirror surfaces, this should not lead to significant differences compared to the experiment. Additionally, the simulation results showed a nearly homogeneous distribution of the fluences on the surfaces, so a smaller surface would still show nearly identical surface concentration. Finally, the plasma backgrounds for L-mode and H-mode simulation were assumed as constant, respectively, while the experimental results are campaign-averaged over the exposure time.
In the experimental analysis, multiple elements were found on the mirrors, with

the highest measured concentrations being the impurities carbon (C) and oxygen (O), with smaller amounts of Be, nitrogen (N) and metallic materials – nickel (Ni), chromium (Cr), and iron (Fe). In the presented ERO2.0 simulations, no C, O, Fe or Cr were considered, with the metallic components of Inconel being approximated by pure Ni. Rubel et al. discuss different possible sources for C and O, e.g. post-exposure oxidization before the analysis for O, and trace sources of diamond dust from polishing processes or residual impurity concentration in the plasma for C. The mirrors had been polished before the exposure to a surface roughness in the range of some nanometres. These processes were not included in the simulation, because they are not related to the actual exposure of the mirrors inside JET and thus, the comparison here focusses only on the Be and Ni data. Unfortunately, the experimental analysis using HIERDA is not able to measure eroded material. Therefore, the Mo erosion values from the simulation cannot be compared with experimental results, since no other techniques were applied before and after the exposure to determine erosion of the installed Mo mirrors.

The comparison is summarised in Table 6.7. In the experiment, Be densities of

Table 6.7: Comparison of accumulated surface density of beryllium and sputtered wall material between simulation (this work) and experiment [105]. Notes: two mirrors in each location in experiment, one mirror holder surface in simulation, the experimental values shown as Ni are combined values for all materials sputtered from the assembly (Ni+Cr+Fe), and the simulation values are added up from two separate simulations for the H- and L-mode phases with exposure times according to experiment (compare Table 6.1).

	Be deposition [10^{15} cm^{-2}]			Ni deposition [10^{15} cm^{-2}]		
	simulation	experiment		simulation	experiment	
position	mirror	mirror 1	mirror 2	mirror	mirror 1	mirror 2
A	0.96	<0.5	<0.5	3.11	2.5	3.0
B	0.86	4.8	<0.5	3.39	3.7	2.2
C	0.25	3.9	<0.5	12.42	1.5	1.6

4–5$\times 10^{15}$ $\frac{1}{\text{cm}^2}$ were measured on two mirrors located on holders B and C, with no Be found on the other mirror in position B and C and or any mirrors in position A. The simulated values between 0.25–1$\times 10^{15}$ $\frac{1}{\text{cm}^2}$ lie around the detection limit mentioned in the reference ($\sim$0.5 $\times$ 10^{15} $\frac{1}{\text{cm}^2}$), which is in line with the fact that on four of the six mirrors in the experiment, no Be was detected at all. The combined values are in fair agreement with the experimental values, where deposition was found, although experimentally the highest Be deposition was found on mirror C, where the simulation predicts the least Be. For Ni, the experimental analysis showed deposition on all six mirrors, in the range of 1.5–3.7 $\times$ 10^{15} $\frac{1}{\text{cm}^2}$. These results match the simulated results of 3.11–3.39 $\times$ 10^{15} $\frac{1}{\text{cm}^2}$ quite well for mirrors A and B, with the caveat that Rubel et al. list values for Ni, Cr, and Fe combined. Mirror C

simulation results differ significantly in the Ni deposition values compared to the experiment by a factor of 8. This likely indicates, that the remapping of hydrogenic CXN fluxes from EIRENE stage 1 into the different apertures might need a more detailed treatment than presented in this work, as discussed in section 6.1.2. The overestimation of the fluxes, as discussed before, led to increased sputtering of the assembly material in entrance C, which in turn deposited mostly on mirror C. However in general, the experimental benchmark of the simulations is successful, and the results align to a satisfactory degree with the experimental results, which gives confidence in the workflow developed in this work. Therefore, the transfer of the workflow to other facilities, conditions and geometries in a fully predictive manner is supported by this benchmark on JET.

6.2 ITER

6.2.1 Setup

Geometry and multi-stage definition

In ITER, mirror systems are planned to be installed in neutron shielding blocks of the diagnostic first wall (DFW). The multi-stage simulation workflow applied to the ITER geometry is illustrated in Figure 6.12. The first stage of the simulation setup is conducted in a 20° sector of ITER with periodic boundary conditions. For the main chamber in ITER, a beryllium (Be) first wall and a tungsten (W) divertor are assumed for the main simulations in this work. The presented material mix is analysed in this section, while a selection of other relevant material assumptions in the ITER device is analysed in section 6.3 and a summary of the structure of all ITER studies is presented in Appendix B. An overview of the ITER main geometry can be seen in Figure 6.13. The W divertor was not considered as a source for sputtered material in the multi-stage simulation workflow, since the transport from the W divertor up to the DFW entrances was found to be negligible in test simulations (see also section 6.3.3). Stages 2 and 3 of the multi-stage simulation workflow are handled in separate simulation branches for the two DFWs, embedded in the upper port plug (UPP, stages labelled 2U/3U, see Figure 6.14) and equatorial port plug (EPP, stages labelled 2E/3E, see Figure 6.15 (EPP)). The stages are defined by the positions of the catcher planes C1 and C2. The C1 catcher planes are defined covering the entrances into the two DFW ports, and the C2 catcher planes are located in the aperture hole leading to the mirror box in each DFW. The included 3D models in the simulations in each branch consist of the respective DFW (iron, Fe) and the mirror box containing the first mirror (FM, molybdenum (Mo)), the second mirror (SM, Mo) and their respective housing (Fe). It should be noted that pure iron was used as a material for the DFW ports and mirror housing in the simulations as a proxy for the ITER grade 316LN-IG steel[3], as it has the highest concentration and one of the lowest sputtering thresholds of the main metallic materials used in the steel.

In the further analysis, it became apparent that the FM front surfaces have specific geometric regions of interest, which are shown in a close-up view of the FMs in Figure 6.16. The FM front measures 201.7 cm^2 in the UPP and 174.2 cm^2 in the EPP. The EPP DFW itself consists of six modules, depicted in Figure 6.13b), of which only one contains the mirror system. The other five modules are not relevant

[3] https://www.cmmcalloy.com/sale-11244222-316ln-ig-stainless-steel-forgings-special-alloys-for-clean-energy-and-oceaneering.html

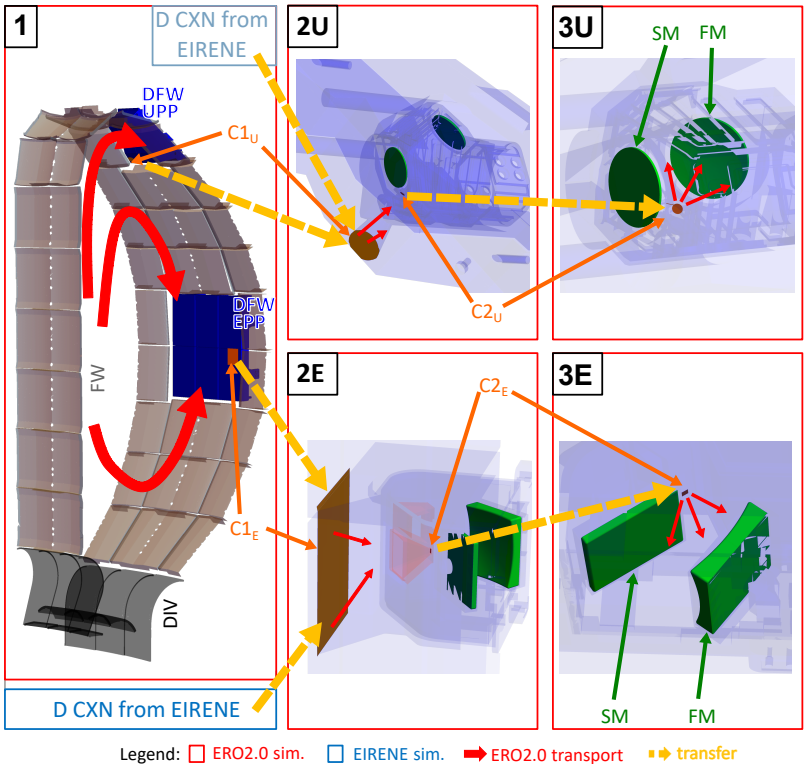

Figure 6.12: Illustration of the multi-stage simulation workflow applied to ITER geometry for five ERO2.0 simulations and one EIRENE simulation in three stages (global (1), intermediate (2) and final (3)). Stage 1 in both codes includes the first wall (FW) and divertor (DIV) and provides input to the two further simulation branches for the DFW in the upper port plug (UPP) and equatorial port plug (EPP). Both DFWs containing a first and second mirror (FM/SM) inside a mirror box (stage 3 simulation volume). Red arrows schematically indicate ERO2.0 particle trajectories simulated during each stage. Yellow dashed arrows indicate data transfer between simulation stages via the catcher planes $C1_{U/E}$ and $C2_{U/E}$, respectively, whose position is identical in all ERO2.0 simulations.

in this work, therefore only the module containing the mirror system is included in the simulations in the EPP simulation branch. The adjusted geometry is shown in Figure 6.15. In Figure 6.15d), red "seal" surfaces are shown. These artificial surfaces cover slits present in the 3D model, provided by the ITER Organization (IO), which were confirmed by IO not to act as channels to the mirror box in the real geometry, but do so in the 3D model. Therefore, the seal surfaces were inserted and act as particle sinks in the simulation without erosion. The fluxes into these slits were confirmed to be negligible compared to the fluxes onto the DFW.

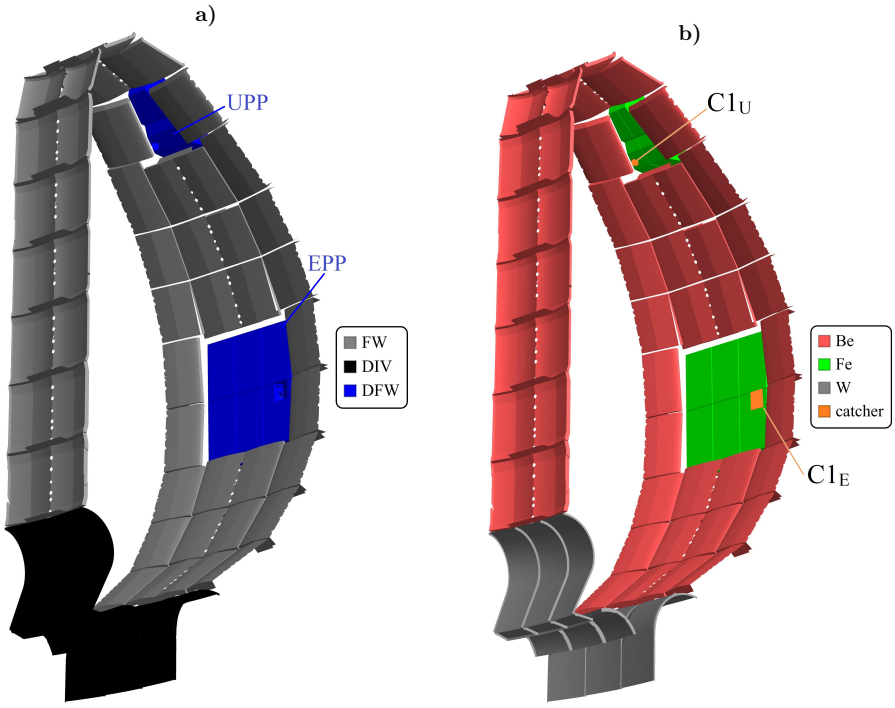

Figure 6.13: Geometry of one 20° ITER sector. a) First wall (FW), divertor (DIV) and diagnostic first wall ports (DFW). b) Colour-coded sector by material assumed in the simulation: Be (red), Fe (green), W (grey); C1 catcher planes leading to the two local simulation branches in the equatorial and upper port DFW are shown in orange.

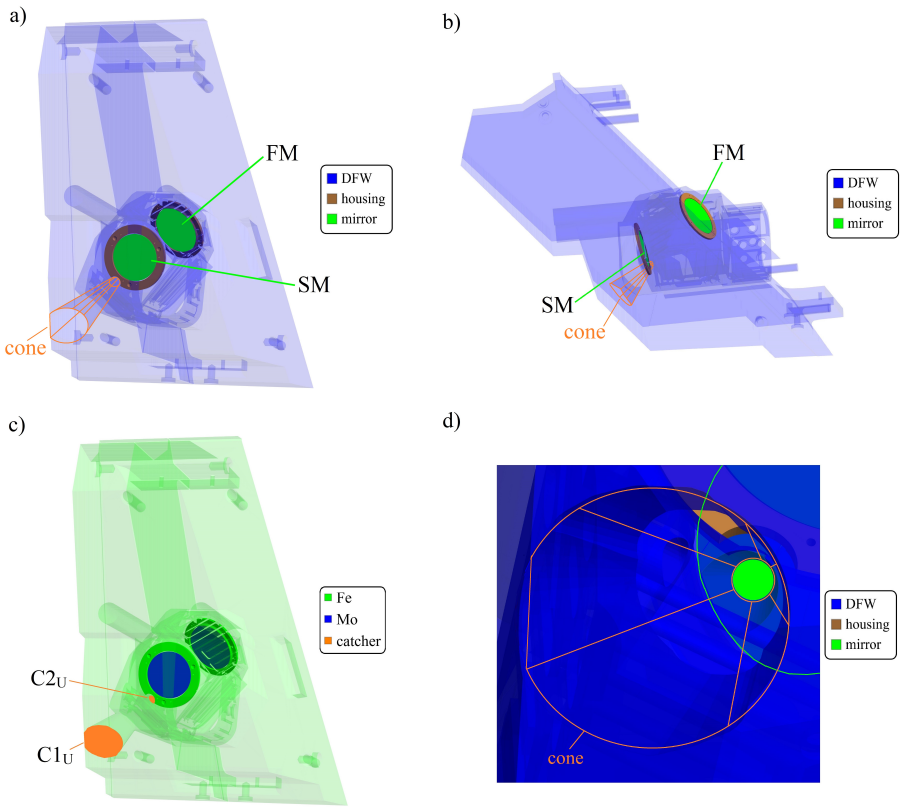

Figure 6.14: Geometry in the local ITER simulation UPP branch. a) + b) Front and rear view coloured by function, shown with the cone leading to the aperture hole highlighted in orange. c) Front view coloured by element, together with catcher planes in orange. d) Close-up view along the cone to the first mirror (outline in green) behind.

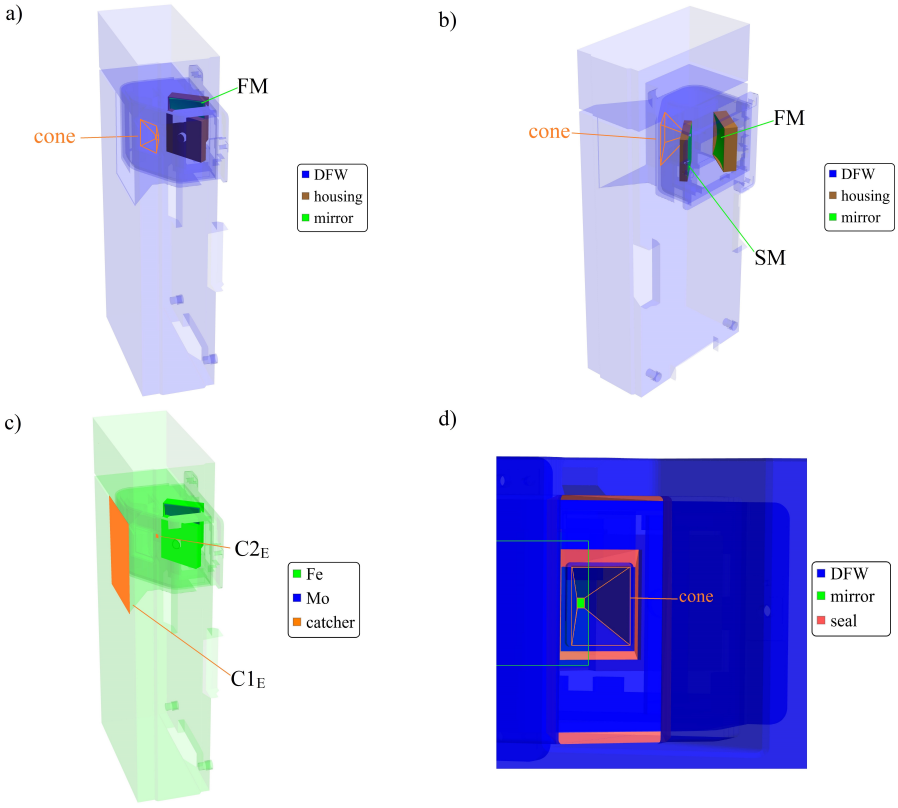

Figure 6.15: Geometry in the local ITER simulation EPP branch. a) + b) Front and rear view coloured by function, shown with the cone leading to the aperture hole highlighted in orange. c) Front view coloured by element, together with catcher planes in orange. d) Close-up view along the cone to the first mirror (outline in green) behind.

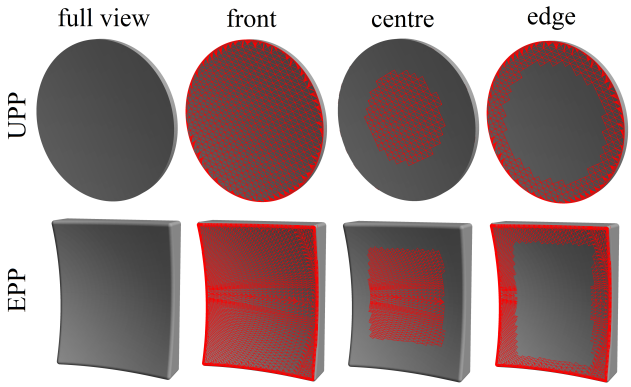

Figure 6.16: Close-up view of the UPP (top row) and EPP (bottom row) first mirror. The leftmost column shows the mirror models, while the three columns to the right highlight regions in red, serving as definition for later use in the analysis – mirror front surface, centre and edge. The mirror front measures 201.7 cm^2 in the UPP and 174.2 cm^2 in the EPP.

Plasma scenarios

Three ITER plasma scenarios were analysed in this work: two H-mode scenarios corresponding to deuterium-fuelled fusion-power operation (FPO) at different plasma edge densities (labelled "High" and "Low") and one L-mode scenario from pre-fusion-power operation (PFPO) with H fuel (see Table 6.8). The three plasma scenarios are labelled in the following as cases #1,#2, and #3. Global ITER first wall modelling using these ITER baseline scenarios [88] with ERO2.0 has been conducted in the past by Romazanov et al. ([101], see Table 6.8 for corresponding case numbers), but the focus was on the direct plasma-facing side and no dedicated analysis of the recessed regions has been performed prior to this work for these plasma scenarios. As Romazanov et al., the plasma backgrounds considered in the ERO2.0 simulations in this work assume a 100% deuterium concentration in the plasma in the H-mode cases to stay consistent with the SOLPS-4.3/OEDGE simulations modelling the plasma backgrounds. The plasma backgrounds assume a steady-state operation, so transient events like Edge-Localized Modes (ELMs) are not considered.

The 2D plasma boundary background from SOLPS-4.3 OEDGE (see section 3.4) modelling for each scenario is used assuming toroidal symmetry throughout the 3D ERO2.0 simulation volume, which consists of a 20° sector of ITER with periodic

Table 6.8: Definition of ITER plasma scenarios for ERO2.0 simulations in this work. P_{SOL} is the power flowing to the scrape-off layer (SOL). See Ref. [101] for more information on the SOLPS-4.3/OEDGE plasma modelling.

Label in this work	Description	Density	Fuel	ERO2.0 simulation time [s]
Case #1	Baseline $Q = 10$ H-mode burning plasma (nominal 15 MA, 5.3 T, $P_{SOL} = 100$ MW), high far-SOL density, zero imposed SOL flow. Case #1 in [101].	High	D	8×10^6
Case #2	Baseline $Q = 10$ H-mode burning plasma (nominal 15 MA, 5.3 T, $P_{SOL} = 100$ MW), low far-SOL density, zero imposed SOL flow. Case #3 in [101].	Low	D	8×10^6
Case #3	Baseline hydrogen L-mode, characteristic of basic divertor operation in low power, non-active phases (nominal 7.5 MA, 2.65 T, $P_{SOL} = 20$ MW), low far-SOL density, zero imposed SOL flow. Case #7 in [101].	Low	H	9×10^5

Table 6.9: Extrapolated plasma parameters to the EPP and UPP local plasma volumes for all ITER plasma cases. These plasma parameters are used in stages 2U and 3U and stages 2E and 3E, respectively. Note: a single extrapolated plasma background was used for case #1 and #2 (both H-mode) because the extrapolated values were in the same order of magnitude and nearly correspond to a vacuum.

	plasma case #1 and #2		plasma case #3	
parameter	UPP	EPP	UPP	EPP
B [T]	5.23	4.05	5.23	4.05
T_e [eV]	1×10^{-5}	1×10^{-7}	5×10^{-5}	1×10^{-6}
T_i [eV]	2×10^{-5}	1×10^{-7}	1×10^{-4}	2×10^{-7}
n_e [/m^3]	1×10^{12}	1×10^{10}	5×10^{9}	1×10^{8}

boundary conditions in toroidal direction. As described before, the OEDGE plasma boundary background does not reach toroidally shaped elements of the first wall and thus also not the region of the DFWs far outside the main plasma. Therefore, extrapolations were carried out to these recessed regions as described in detail in section 5.2. With a decay length of $\lambda = 1\,\text{cm}$, the values inside the mirror assemblies inside the DFWs correspond approximately to vacuum (e.g. for case #1: $T_e \sim 10^{-5}\,\text{eV}$, $n_e \sim 10^{12}\,\frac{1}{\text{m}^3}$) in both ports. Table 6.9 summarises all extrapolated values. In Ref. [100], a sensitivity study regarding the decay of the profiles was carried out, where 1 cm was concluded as a realistic value for the decay length.
SOLPS-4.3/OEDGE also provides information about the plasma fuel fluxes onto the first wall and divertor. These ion fluxes are used in the global (first) stage of the simulation and contribute there to sputtering of the PFCs. The surfaces of the recessed areas are assumed to be plasma-shadowed in ERO2.0, thus sputtering by the plasma ions is not performed in the intermediate and final stages of the multi-stage simulation approach.
In stage 1 of the multi-stage simulation workflow, the simulation volume covers the whole ITER first wall and divertor surfaces and extends in ERO2.0 inwards up to a closed flux surface at $\rho = 0.9$, where the core boundary was chosen as discussed in section 3.1. For the further simulation stages, the simulation volume is chosen tight around the respective DFW and thus includes all relevant geometry (see Figure 6.18).

Finally, the total simulation times – $8 \times 10^6\,\text{s}$ ($\sim$2200 h) for the H-mode plasma scenarios and $9 \times 10^5\,\text{s}$ (250 h) for the L-mode plasma scenario – correspond to the total expected plasma time of the three ITER operational phases described in the research plan [88] at the time this work was performed. The provided plasma backgrounds were assumed as constant over the full discharge time in the ERO2.0 simulations, so for the H-mode simulations a high-power plasma background was

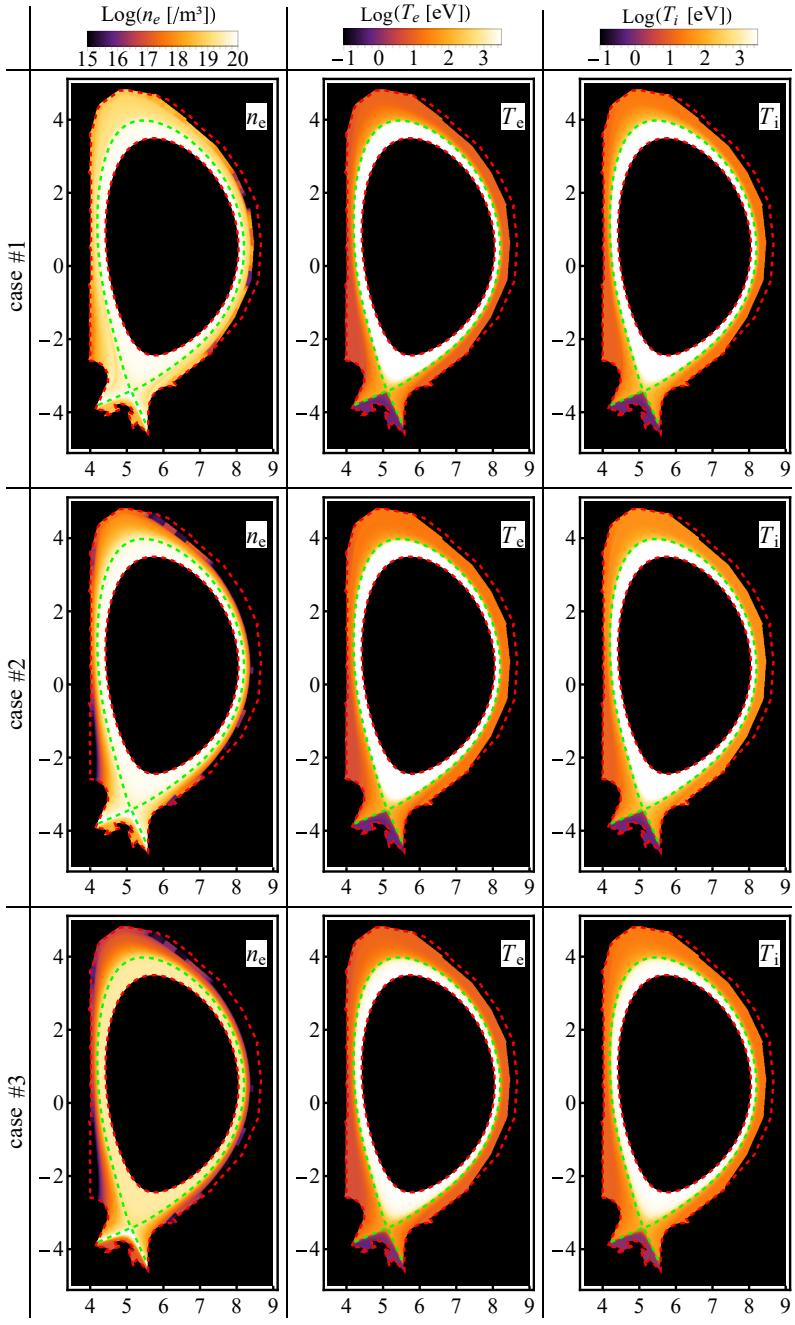

Figure 6.17: Overview of the plasma scenarios assumed for the ITER simulations in this work: electron density, electron temperature and ion temperature as 2D maps in the R-z-plane (all coordinates in units of metres). Also shown: inner and outer ERO2.0 simulation boundaries (red dashed line) and separatrix (green dashed line).

assumed throughout the whole simulation time, providing an upper limit of the plasma density and temperature. No limiter phase or other low power H-mode discharges are included in the modelling, so this can be seen as a conservative estimate.

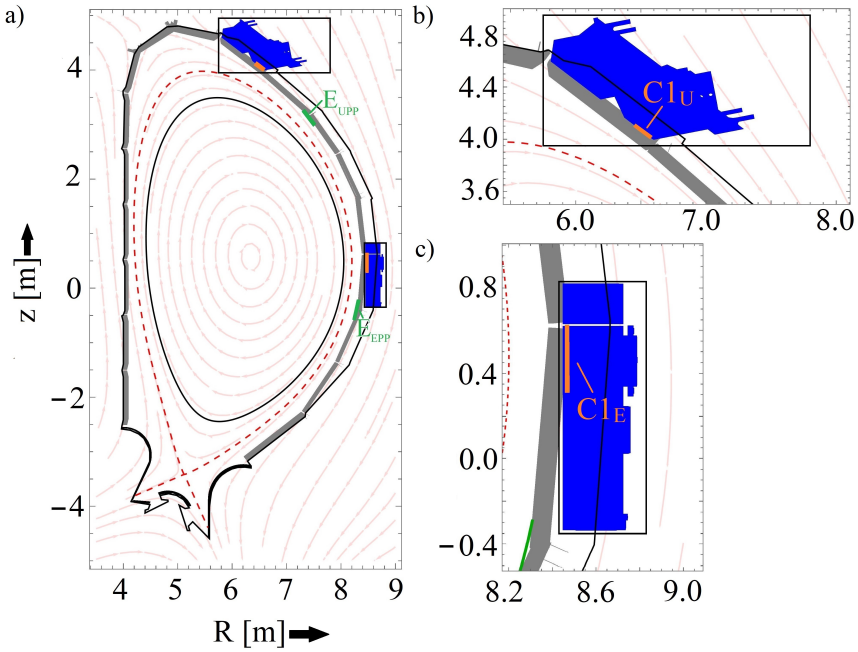

Figure 6.18: ERO2.0 simulation volumes (solid black lines) in the ITER simulation workflow shown in the R-z-plane with projection of the relevant geometry (grey: FW/DIV, blue: DFW, see Figure 6.13 for 3D view), C1 catcher planes used in ERO2.0 stage 1 (orange), E catcher planes used in EIRENE stage 1 (green), and magnetic geometry of case #1 global plasma (red dashed: separatrix, light red arrows: field lines). a): Full volume used in stage 1, b) zoom of UPP region used in stages 2U and 3U, c) zoom of EPP region used in stages 2E and 3E (compare Figure 6.12).

CXN spectra

The result of the stage 1 EIRENE post-processing of all SOLPS-4.3/OEDGE plasma backgrounds analysed in this work is illustrated in Figure 6.19. Note that case #3 has H fuel compared to the D fuel used in the other cases, as detailed in the preceding section (see Table 6.8). The particle statistics were collected on the EIRENE catcher planes E_{UPP} and E_{EPP} at two different poloidal locations reflecting the two simulation branches, which can be seen in Figure 6.18. This shall incorporate any differences in the spectra due to geometry effects. For technical

reasons, the E catcher planes are slightly displaced from the entrance to their respective DFW port. It is assumed that the collected hydrogenic particle spectra at these locations are identical at the respective DFW entrance. The binning for the spectra (described in detail in section 5.3) was performed with 10^4 equidistant bins up to 1500 eV for the energy distribution and with 500 bins for the angular distribution. Figure 6.19 confirms that the CXN spectra indeed show differences at the two analysed locations, although general trends can be observed between the plasma scenarios:

In the energy spectra, a peak at about an energy of 90 eV (plasma cases #1

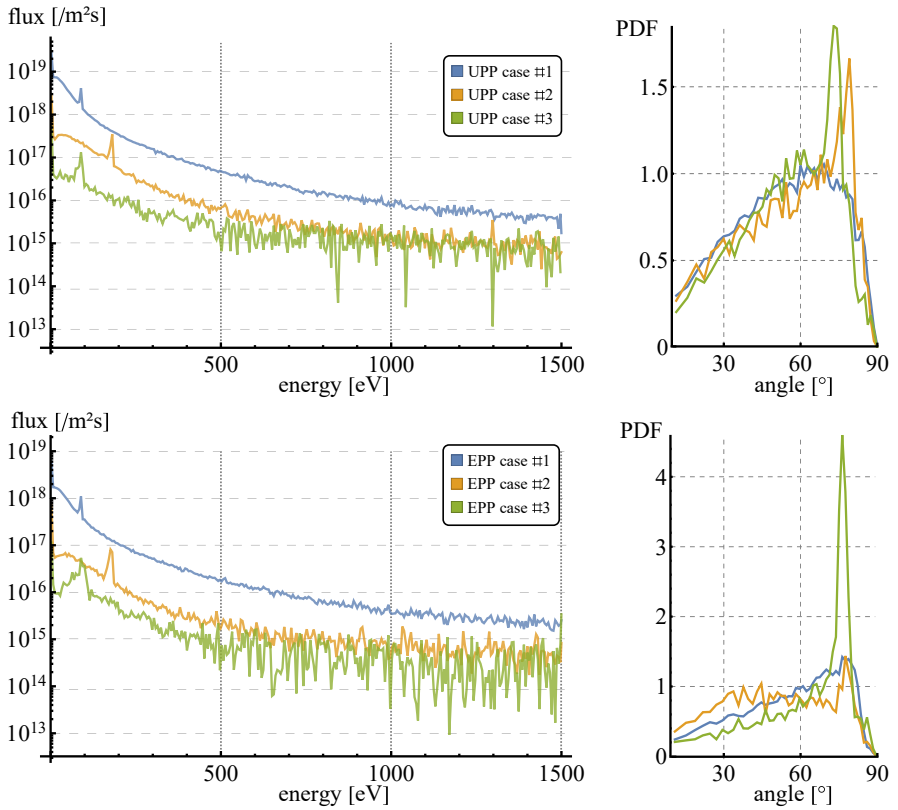

Figure 6.19: Impact energy (left column, logarithmic scaling) and angular distribution (right) of neutrals entering the DFW in the UPP (top row) and EPP (bottom), generated by EIRENE as part of the stage 1 simulations. See Table 6.8 for a definition of the plasma cases.

and #3)/170 eV (case #2) can be explained by the fact that this is approximately the ion temperature at the separatrix of the provided plasma backgrounds. The total fluxes (see also Table 6.10) are highest in case #1 (H-mode, high SOL-density)

Table 6.10: Integrated neutral hydrogenic fluxes entering the UPP and EPP entrances, and their mean energies, generated by EIRENE (see Figure 6.19 for spectra).

	UPP		EPP	
plasma (fuel)	flux [1/s]	energy [eV]	flux [1/s]	energy [eV]
case #1 (D)	1.80e18	72.6	2.53e18	94.3
case #2 (D)	1.93e17	108.2	3.23e17	138.4
case #3 (H)	3.53e16	186.5	7.32e16	193.9

and lowest in case #3 (L-mode), which matches expectations considering the lower power in the L-mode plasma scenario and the high SOL-density in the first analysed H-mode scenario. Fluxes into the EPP DFW are 40–90 % higher than the respective flux into the UPP. The mean energies follow the same pattern and are 4–30 % higher in the EPP. Among the H-mode cases, case #2 shows lower fluxes but higher mean energy than case #1.

Note, for the angular distribution of impinging particles, there was an error in the original data provided by the EIRENE simulations, in which particles hitting the backside of the catcher plane were miscounted. In Appendix C, the original spectra and corrected angular distributions are shown. The original distributions have a sharp, unphysical peak at $\alpha = 90°$, which includes 5% of the total flux in case #1, 40% of the flux in case #2 and 0.6% in case #3. The corrected results from an updated code version are shown here in Figure 6.19. This data was not available for the analysis presented in this section, but it was applied for the additional studies performed in sections 6.3.2 and 6.3.4, where the impact of the corrected spectra is discussed.

As mentioned before, pure D plasmas were used throughout this work for H-mode plasma scenarios, since the plasma boundary modelling, on which the ERO2.0 and EIRENE post-processing simulations are based, did not include tritium (T). In a realistic high-power fusion plasma, a 50/50-mix of D and T is used. Due to

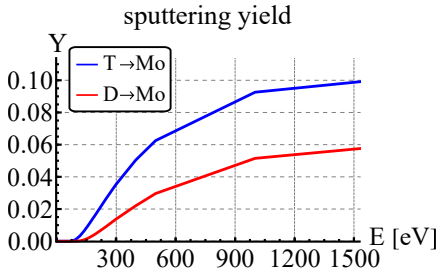

Figure 6.20: Physical sputtering yield of a pure Mo surface under bombardment of D (red) and T (blue), calculated by SDTrimSP and assuming an impact angle of 60°.

its higher mass, T has generally around a factor of 2-3x higher sputtering yields than D in the energy range relevant for CXN neutrals (Figure 6.20). Assuming 50/50-mix of D and T, around 1.5-2x higher sputtering of surfaces can be expected compared to the results presented in this work.

Energy and angular distribution of impinging particles on the mirror

As for the JET analysis, sample stage 3 simulations were performed to assess a reasonable choice of the parameter d, the surface interaction layer thickness on the mirrors. This was performed for the simulation with the highest particle fluxes at the end of stage 2, which is the EPP simulation branch in plasma scenario #1.
Figure 6.21 shows the energy spectrum of atoms impinging on the mirror resolved by element. Deuterium reaches the highest energies due to the high-energy tail of the incoming CX neutrals. Fe and deposited Be sputtered from the DFW by these high-energy neutrals can also be highly energetic, but their mean energies are far lower.
The corresponding angular distribution of the particle species is presented in Figure 6.21 on the right-hand side. The angular distributions for D, Be, and Fe agree rather well. These three species can originate from outside the mirror box, and are thus affected by the cone-like aperture in front of the mirrors. Mo from sputtering of the first and second mirror has a significantly different distribution as its source location differs from the other elements.
With the mean values of these distributions, sample SDTrimSP calculations were

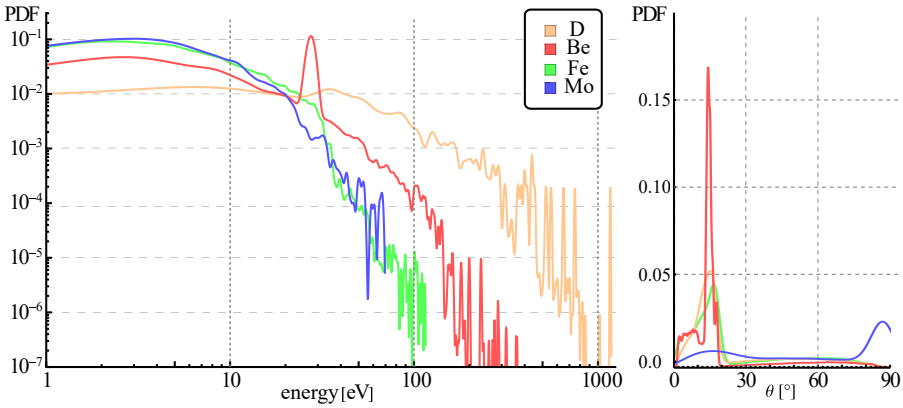

Figure 6.21: ERO2.0 energy spectrum (left) and impact angle distribution (right) of impinging particles on the upper port first mirror front surface by element for plasma case #1, split by element. The mean energies are D: 89 eV, Be: 20 eV, Fe: 9 eV, Mo: 9 eV.

performed as in the JET simulation cases before (see section 6.1.1). The highest

penetration depth of 3.6 nm was obtained for the bombardment of Mo by D atoms with 89 eV impact energy at an angle of 25°. The surface interaction layer thickness for the HMM implemented in ERO2.0 was therefore set to $d = 5$ nm in the ITER stage 3 simulations. A test case with a different choice of d is elaborated in further detail in section 6.3.1.

6.2.2 Simulation Results

a) ITER case #1: high density H-mode

From the three analysed plasma scenarios in ITER, case #1 shows the highest erosion and deposition fluxes onto the First Mirror (FM), which can be attributed to the highest impinging CXN fluxes (see Table 6.10). For this reason, case #1 is discussed in this section in detail, while an overview of the analysis in the other two plasma scenarios is given in section 6.2.2b).
Firstly, results for the UPP simulation branch are analysed: Figure 6.22 shows the

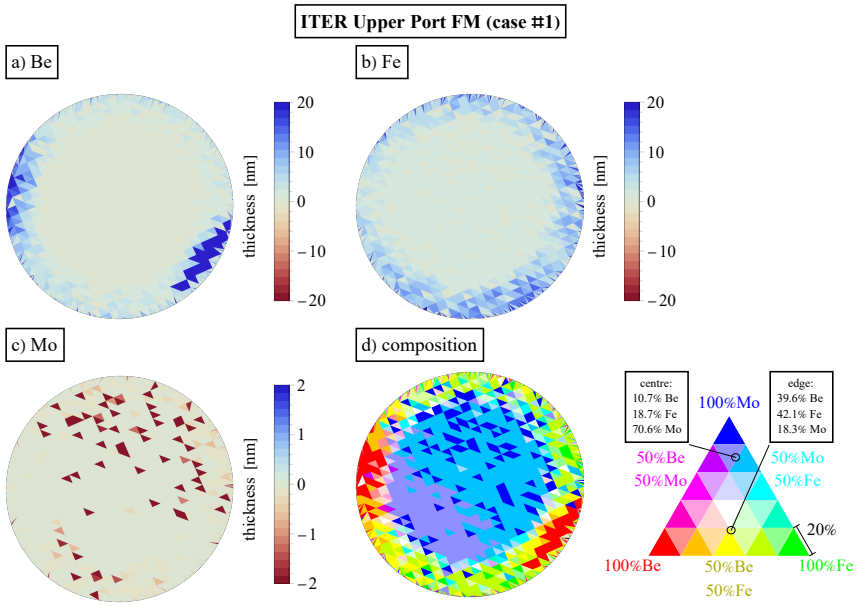

Figure 6.22: Net fluence of a) Be, b) Fe, and c) Mo on the ITER upper port first mirror (FM) – net erosion is shown in red, net deposition in blue. d) Surface composition in a 5 nm surface layer. Each coloured triangle in the legend represents a range of 20% in concentration.

UPP FM front surface at the end of the simulation time. The accumulated Be, Fe, and Mo net fluences (a-c) are depicted. Be, originating from the main chamber,

and Fe, sputtered from the DFW, are net deposited, which is depicted in blue. Mo, the mirror material, is net sputtered, which is depicted in red. A small amount of Mo is also deposited on the FM, originating from sputtering of the Second Mirror (SM) and subsequent transport in the mirror box. This contribution is included in the balance of the net fluence depicted on the FM. Figure 6.22d) shows the surface composition in the surface interaction layer with thickness $d = 5\,\text{nm}$. The centre of the FM, which is the area mainly used for the optical path of diagnostics, retains more than 70% Mo concentration. In contrast, the edges show significant amounts of Fe and Be, which lines up with the net fluence observations (a+b). The evolution of the mean surface composition over the full simulation time is shown in Figure 6.23. Even after 2200 h of plasma operation in this simulation, a steady-state surface composition is not reached, because the fluxes into the remote areas are so small.

Overall, a strong geometrical pattern can be observed on the UPP FM: the edge

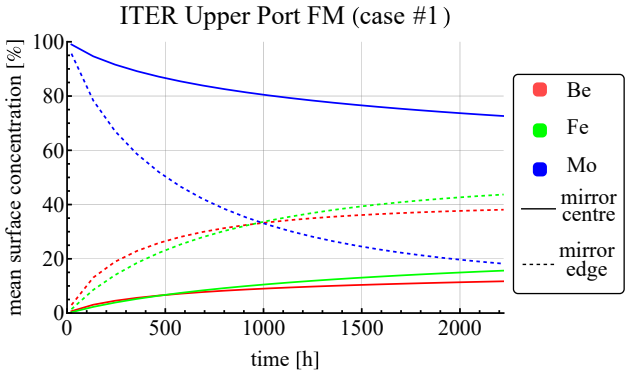

Figure 6.23: ITER UPP FM, case #1: evolution of surface concentrations over the simulated time, performed in 100 discrete time steps with the HMM in ERO2.0. Values are averaged according to the definitions in Figure 6.16 over the mirror centre (solid lines) or mirror edge (dashed lines), respectively, and resolved by element.

of the mirror shows much higher fluence values, whereas the mirror centre is nearly unaffected. The net values for Fe and Be deposition lie well below 1 nm in the central part, thus in the range of a monolayer, while values at the edge are on average 10 nm for Be deposition and 5.5 nm for Fe. This geometric pattern can be directly attributed to the applied geometry of the mirror assembly located in front of the mirror: a cone-like structure leads from the plasma-facing side to the mirror box, which is highlighted in Figure 6.14d). The transport of the particles inside the mirror assembly is mostly ballistic as analysed in section 5.2, since (i) most particles stay neutral throughout the simulation in the mirror assembly,

due of the low temperatures inside the volume and recombination upon contact with the PFCs and (ii) the background neutral atomic densities are low enough to barely affect the transport. This means that particles are transported mostly along line-of-sight. The particles reflected or sputtered from the cone structure 'see' only a part of the mirror, which is exactly the edge of the mirror. Therefore, the preferential deposition in the edge region can be explained by the line-of-sight transport in the recessed region and the applied geometry.

In Figure 6.22c), single cells of the geometry seen as dark red triangles are present,

Table 6.11: Net, gross deposition and gross erosion fluences averaged over the front surface of the ITER upper port first mirror and integrated over the ITER FPO time (first block) in plasma case #1. The coloured blocks show the contributions of the different projectiles to the sputtering of each element present in the surface, thus Be, Fe, and Mo.

ITER Upper Port FM (case #1)	net fluence [at./cm²]	gross deposition fluence [at./cm²]	gross erosion fluence [at./cm²]	...by D [%]	...by Be [%]	...by Fe [%]	...by Mo [%]
D	3.10×10^{18}	3.10×10^{18}	0.00	--	--	--	--
Be	5.43×10^{16}	7.79×10^{16}	2.36×10^{16}	98.29	1.71	3.09×10^{-3}	7.86×10^{-6}
Fe	2.52×10^{16}	3.16×10^{16}	6.41×10^{15}	97.76	2.16	0.08	3.28×10^{-4}
Mo	-7.74×10^{15}	6.25×10^{13}	7.80×10^{15}	99.65	0.33	0.02	$3.\times10^{-4}$

signifying very strong Mo erosion values. These values lie in the range of 5–40 nm outside the shown colour scale and can be attributed to single D CXN particles that passed all simulation stages without a collision. These particles carry a high energy in the range of keV and a large numerical Monte-Carlo weight, i.e. they represent a large amount of real particles. These two factors lead to a very high sputtering yield when the particles finally hit a surface, e.g. the mirror as here. Even with the three-stage approach used here, the resolution of the particle upsampling is not good enough to resolve these rare particles in sufficient quality. Therefore, the resolution of rare high-energy D CXN is an area of potential improvements in the future (see chapter 8). However, since these 'collision-free' particles in reality likely spread evenly over the mirror, and most sputtering is caused by D CXN particles (see Table 6.11), the area-averaged Mo erosion value over the mirror front surface of 1.2 nm is a more realistic interpretation of the FM erosion.

The rest of this section continues with the EPP branch of the simulation. Although the geometry in general and the shape of the mirrors are very different from the upper port, the results show the same general behaviour: Be and Fe are deposited in the order of up to 20 nm in the edge regions, while Mo is slightly eroded (Figure 6.24). The Mo erosion again shows strong single cells of up to 20–70 nm erosion due to aforementioned resolution problem of high-energy CXN. The area-averaged erosion value on the mirror front is 2.5 nm. The left edge of the

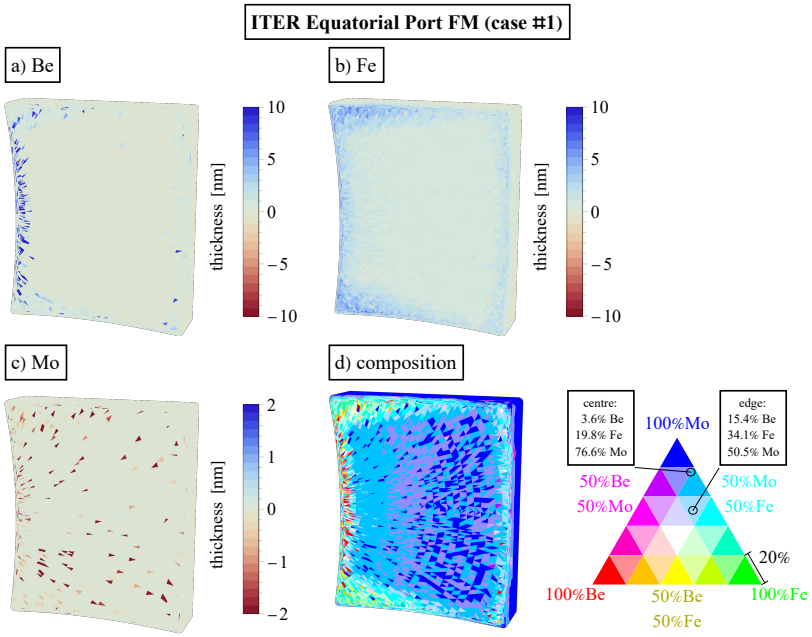

Figure 6.24: Net fluence of a) Be, b) Fe, and c) Mo on the ITER equatorial port first mirror (FM) – net erosion is shown in red, net deposition in blue. d) Surface composition in a 5 nm surface layer. Each coloured triangle in the legend represents a range of 20% in concentration.

mirror shows significant changes in surface composition, but the Mo concentration stays above 60% in nearly all regions of the mirror. Sputtering is caused nearly exclusively by D and re-erosion is insignificant (Table 6.12), but in the equatorial port, slightly more Fe than Be is deposited in total on the mirror.

The strong influence of the DFW geometry can also be observed clearly in the EPP DFW port. The rectangular shape of the mirror matches the rectangular shape of the cone-like aperture present in the EPP DFW. In Figure 6.15d), the view along the cone is illustrated and clearly shows that line-of-sight transport from the cone leads to preferential fluxes onto the mirror edges, which exactly matches the observations here. Figure 6.25d) shows that due to this effect, the centre of the FM stays above 85% Mo concentration over the whole ITER lifetime simulated in this work. The edge is more affected by the fluxes and drops to around 55% mean Mo concentration after 2200 h of plasma operation.

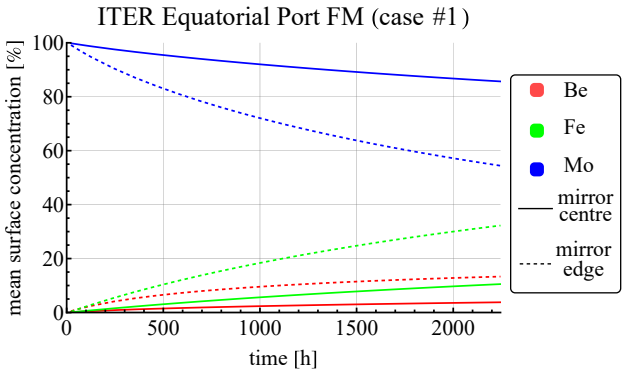

Figure 6.25: ITER EPP FM, case #1: evolution of surface concentrations over the simulated time, performed in 100 discrete time steps with the HMM in ERO2.0. Values are averaged according to the definitions in Figure 6.16 over the mirror centre (solid lines) or mirror edge (dashed lines), respectively, and resolved by element.

Table 6.12: Net, gross deposition and gross erosion fluences averaged over the front surface of the ITER equatorial port first mirror and integrated over the ITER FPO time (first block) in plasma case #1. The coloured blocks show the contributions of the different projectiles to the sputtering of each element present in the surface, thus Be, Fe, and Mo.

ITER Eq. Port FM (case #1)	net fluence [at./cm²]	gross deposition fluence [at./cm²]	gross erosion fluence [at./cm²]	...by D [%]	...by Be [%]	...by Fe [%]	...by Mo [%]
D	1.96×10^{18}	1.96×10^{18}	0.00	--	--	--	--
Be	8.27×10^{15}	1.20×10^{16}	3.75×10^{15}	98.02	1.97	5.65×10^{-3}	4.98×10^{-4}
Fe	1.12×10^{16}	1.27×10^{16}	1.44×10^{15}	98.37	1.29	0.32	0.03
Mo	-1.60×10^{16}	6.44×10^{14}	1.67×10^{16}	99.92	0.05	0.03	5.49×10^{-3}

b) Overview of results for other ITER plasma scenarios and SMs

The other two ITER plasma scenarios summarised in Table 6.8 (case #2: low density H-mode and case #3: hydrogen L-mode) were simulated using an identical approach. Table 6.13 summarises the results, showing the thickness of the deposited or eroded layer as an overview for the three elements in each simulation. Due to the strong geometric influence found in all cases, the mean values are shown separately for mirror edge and mirror centre in addition to the full mirror front surface.

The main findings are that (i) the erosion in the H-mode cases is quantitatively higher than in the L-mode, with the high-density H-mode scenario (case #1) showing the highest erosion. This is partially due to the longer operation time in H-mode (around 10x, compare Table 6.8), but also due to higher fluxes into the diagnostic first wall ports (compare Figure 6.19). (ii) General trends from the case #1 analysis (section 6.2.2a) can also be observed in the other two plasma scenarios. The deposition is always much stronger on the edge regions of the mirrors due to the 3D geometry of the cone-shaped cut-out leading up to it, but the magnitude of deposition and erosion strongly depends on the plasma scenario. Overall, only a few nanometres of molybdenum erosion are expected on average over the mirror front surfaces. The 3D illustrations for the two mirrors in both plasma cases are shown in Figures 6.26 and 6.27, respectively, where the geometric influence is clearly visible in all simulated cases. Note, the scales were chosen differently for each case due to strong differences in magnitude.

The analysis in this section focussed on the FM in each port. The Second Mirrors (SMs) in the UPP and EPP DFW (see Figure 6.12) are summarized in Table 6.14, showing the mean deposition values on the second mirrors, while the complete graphical results for the SMs are presented in Appendix D.

The SMs are in general reached by about 5–15 % of the fluxes impinging on the respective FM. A notable difference to the results on the FMs is, that Mo is moderately net deposited on the SMs in addition to Be and Fe. The Mo originates from sputtering of the FMs and reaches the SMs via transport in the simulation volume. In additional reflections before reaching the second mirror, the impinging energies of the particles are lowered and thus erosion is also significantly reduced. The deposition of all elements on the SMs is much more evenly spread out over the mirror front surface due to the additional reflections needed to reach the second mirror. No dominant surface pattern is observable, which is why no 3D results are shown here for the SMs. In conclusion, the change in mirror performance of the SMs due to incoming fluxes is expected to be negligible compared to the FMs.

	subsurface →	Be layer [nm]			Fe layer [nm]			Mo layer [nm]		
		front centre	front edge	front (all)	front centre	front edge	front (all)	front centre	front edge	front (all)
case #1	UPP	0.29	9.63	4.42	0.86	5.49	3.00	−1.14	−1.22	−1.21
	EPP	0.11	1.39	0.67	0.86	1.91	1.34	−2.46	−2.36	−2.50
case #2	UPP	0.13	2.61	1.26	0.11	0.46	0.27	−0.21	−0.17	−0.21
	EPP	0.01	0.14	0.07	0.10	0.28	0.18	−0.17	−0.19	−0.19
case #3	UPP	1.84×10^{-3}	0.04	0.02	7.05×10^{-3}	0.01	8.78×10^{-3}	-2.87×10^{-3}	-2.64×10^{-3}	-2.79×10^{-3}
	EPP	1.43×10^{-4}	2.12×10^{-3}	1.02×10^{-3}	4.24×10^{-3}	7.6×10^{-3}	5.78×10^{-3}	-2.31×10^{-3}	-1.56×10^{-3}	-1.69×10^{-3}

Table 6.13: First mirrors in ITER: overview of mean Mo erosion as well as Be and Fe deposition on the mirror surfaces at the end of the simulation time, averaged over the full mirror front surface, mirror front centre or mirror front edge, respectively. Figure 6.16 illustrates the corresponding area taken into account. The values for the mirror centre, the area most relevant for imaging optical diagnostics, are highlighted in yellow. The impinging fluxes simulated by ERO2.0 were integrated over time and the respective surface, and converted to a layer thickness using the element's density. Negative values imply net erosion.

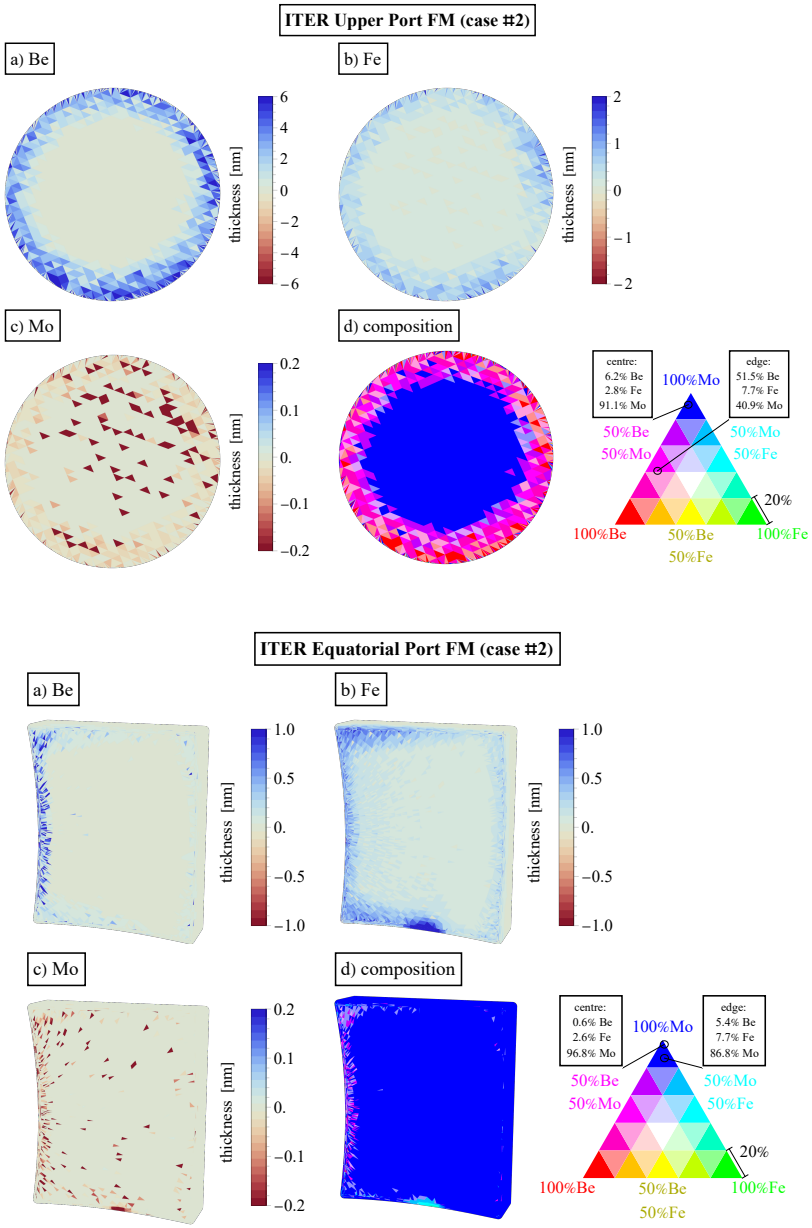

Figure 6.26: UPP (top) and EPP (bottom) first mirrors in the main analysis, plasma case #2: net fluences of Be, Fe, and Mo (a-c) and surface concentration in a 5 nm interaction layer on the mirror front surface (d), respectively. Each coloured triangle in the composition legend represents a range of 20% in concentration.

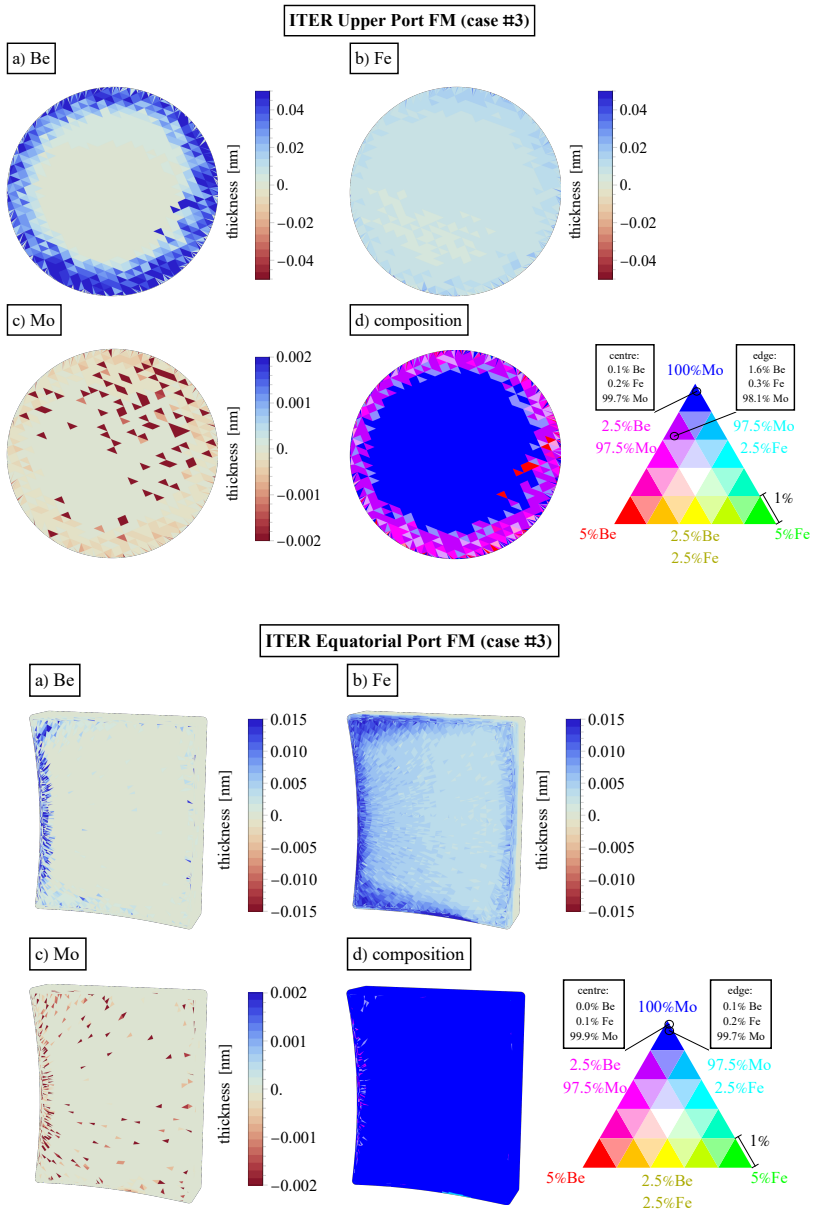

Figure 6.27: UPP (top) and EPP (bottom) first mirrors in the main analysis, plasma case #3: net fluences of Be, Fe, and Mo (a-c) and surface composition in a 5 nm interaction layer on the mirror front surface (d). Each coloured triangle in the composition legend represents a range of 1% in concentration, most polygons of the first mirrors retain over 99% Mo concentration.

Second Mirrors		Be layer		Fe layer		Mo layer	
		[nm]	rel. to FM	[nm]	rel. to FM	[nm]	rel. to FM
case #1	UPP	0.24	×0.05	0.35	×0.12	0.03	×(−0.02)
	EPP	0.03	×0.05	0.15	×0.11	0.14	×(−0.05)
case #2	UPP	0.07	×0.05	0.04	×0.15	5.63×10^{-3}	×(−0.03)
	EPP	3.81×10^{-3}	×0.05	0.02	×0.09	0.01	×(−0.06)
case #3	UPP	8.09×10^{-4}	×0.04	5.47×10^{-4}	×0.06	6.86×10^{-5}	×(−0.02)
	EPP	4.65×10^{-5}	×0.05	1.73×10^{-4}	×0.03	1.26×10^{-4}	×(−0.07)

Table 6.14: Equivalent of Table 6.13 for the second mirrors (SMs) planned in the ITER DFW ports. All elements are net deposited on the SMs, and mean values averaged over the full SM front surface are shown, as no geometrical dependence was observed. The second column under each element lists the ratio of the deposited layer thickness on the SM compared to the respective FM. The negative relative values for Mo are caused by the moderate net Mo erosion on the FMs, while the SMs are net Mo deposition zones.

6.2.3 Efficiency of the Multi-Stage Simulation Workflow

To judge the necessity of the multi-stage simulation workflow, the amount of test particles and integrated fluxes [atoms/s] carried by them at the start and end of the three simulations of the multi-stage workflow are evaluated. The evolution of these two values throughout the ITER EPP simulation branch in plasma case #1 are depicted in Figure 6.28 as an example for the evaluation. The integrated flux of the different atomic species throughout the multi-stage simulation approach diminishes strongly, the deeper the particles enter the DFW. For Be, which originates exclusively from sputtering of the ITER first wall, the initially eroded flux diminishes over 11 orders of magnitude during the transport simulation until it reaches EPP FM. Even from the entrance of the DFW port, where the catcher planes C1 and E were defined in the multi-stage simulation approach, only 1 in 10^6 real particles reaches the FM.
For the amount of test particles, the numbers are similar. For beryllium, it is shown that only 2.3×10^{-7}% (or 1 in 425 million) of globally eroded Be test particles reach the first mirror. Even from the entrance of the DFW, only 8×10^{-3}% (or 1 in 14.000) of all test particles are transported to the FM surface. To counteract this drastic decrease in test particles, the upsampling processes take place on the catcher planes serving as interfaces between the simulations in the DFW entrance and aperture hole. On the catcher planes, all particle species are upsampled to 2×10^8 test particles by applying the upsampling methods outlines in section 5.3, increasing the statistics in the recessed regions. Figure 6.28 clearly shows that the real fluxes represented by the test particles are kept constant during the upsampling process, so that the physical meaning of the test particles and thus particle balance is retained. For beryllium, one particle entering the DFW can theoretically split into up to 76 million test particles throughout the multi-stage simulation approach. However, this is only valid if all upsampled particles reach the next simulation stage, which is extremely unlikely, since only 1 in 14.000 particles on average reaches the mirror from the DFW entrance.

With the approach introduced in this work, around 1.5 billion trajectories were simulated in total with ERO2.0 in the EPP simulation branch for plasma scenario #1, with around 77 million trajectories impinging on the FM (equivalent to 1 in 20, or 5%) and thus delivering information directly relevant for the work. As it was proven that only 1 of 425 million Be test particles eroded from the FW would hit the FM by transport throughout the ITER global and DFW volume, a single stage ERO2.0 simulation would require the simulation of more than 3×10^{15} particles to gain the resolution achieved in this work. This number of simulated

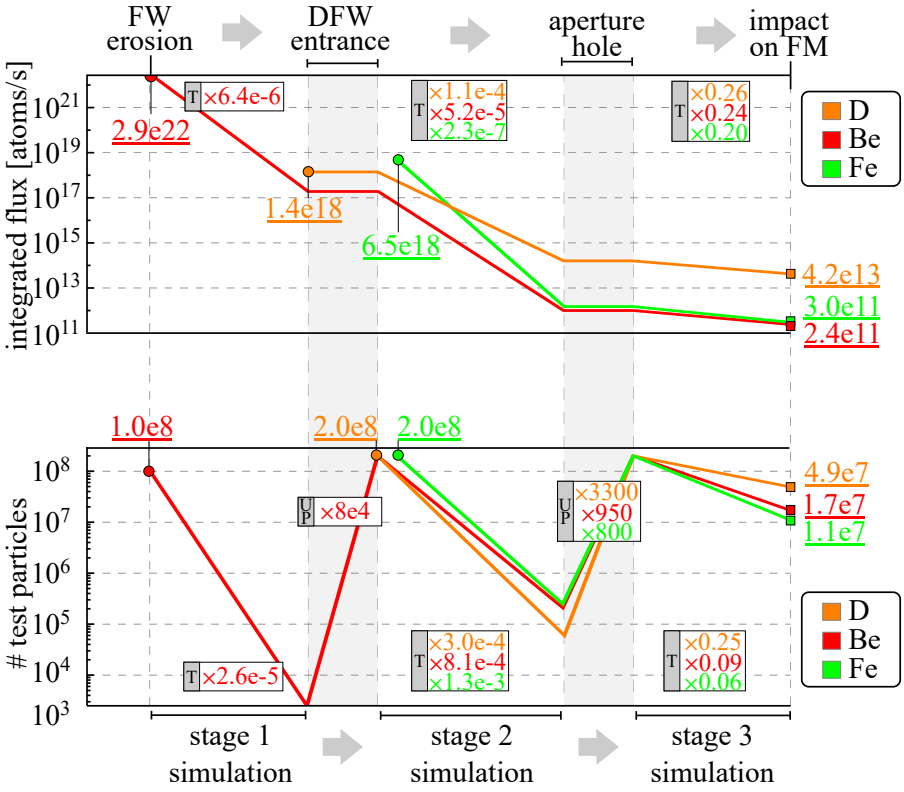

Figure 6.28: Integrated flux carried by test particles (top) and amount of test particles (bottom) throughout the ERO2.0 simulations performed in the ITER EPP case **#1** branch. The data is resolved by element and progresses from main chamber erosion (left) via the multi-stage approach to the first mirror surface (right). The boxes marked by the letter T show the ratio of the initial to remaining value at the end of the respective transport simulation in ERO2.0. The boxes marked by the letters UP show the upsampling factor. Note: D appears in ERO2.0 first in stage 2, originating from an EIRENE stage 1 simulation; Fe originates from sputtering of the DFW during stage 2.

trajectories is orders of magnitude above any number feasible on modern high-performance computing architecture, and proves that the multi-stage approach is around 7 orders of magnitude more efficient from the amount of simulated trajectories alone. This figure does not even take into account that the largest fraction of simulated trajectories in the multi-stage approach are much shorter than full trajectories in a single-stage approach, which further favours the multi-stage simulation approach. Thus, the significant computational advantage of the multi-stage approach compared to a standard single-stage ERO2.0 simulation is demonstrated, showing a strong capability of retaining the statistics even in volumes with significantly diminishing fluxes.

6.3 Variation of Material Properties and Composition

In the preceding section, the computational advantage of the multi-stage simulation workflow in ITER was established. The multi-stage approach, however, has another major advantage compared to a single-stage simulation approach: adaptability. This advantage is demonstrated in the following sections, in which additional material studies are performed, representing a selection of scenarios relevant for ITER operation or analysing the credence of the results presented in the main study (section 6.2). Importantly, only select stages of preceding studies need to be repeated in most of the additional studies, showcasing the modular approach of the simulations performed in this work. The modular approach to all ITER studies is further illustrated in Appendix B.

6.3.1 Surface Interaction Layer Thickness

As described in the section introducing the Homogeneous Mixing Model (HMM) implemented in ERO2.0 (section 3.1.5), the surface interaction layer thickness d is a parameter, that has to be set manually. The ERO2.0 code is most commonly applied for analysis of steady-state scenarios, in which d does not influence the final surface composition, but only how fast the numeric iteration converges. In this work, however, a time-integration in a fixed simulation time is performed to estimate the layer thickness of deposited and eroded material as shown in the main analysis in sections 6.1.2 and 6.2.2. For these simulations, the surface interaction layer thickness was estimated on the basis of the expected impact energies on the first mirrors, associated binary-collision calculations with the SDTrimSP code and consideration of the implantation depth for the atomic species in a Mo surface (sections 6.1.1 and 6.2.1) mimicking the Mo mirrors.
A test case is performed in this section to assess the validity of the results. A much thicker interaction layer ($d = 100\,\mathrm{nm}$) is applied on the mirrors in these test simulations to check if the main results are largely independent of the parameter as assumed. Otherwise, all parameters and simulation assumptions are kept identical to the main analysis with $d = 5\,\mathrm{nm}$. The test case is performed for all three ITER plasma scenarios and both geometries, EPP and UPP, by re-using the output of the stage 2 simulations of the main analysis and repeating the stage 3 simulations with the adjusted material assumptions. For brevity, only results for case #1 are shown in the upcoming figures and discussed in detail, while an overview of all cases is given afterwards. The deposition and erosion on the first mirrors

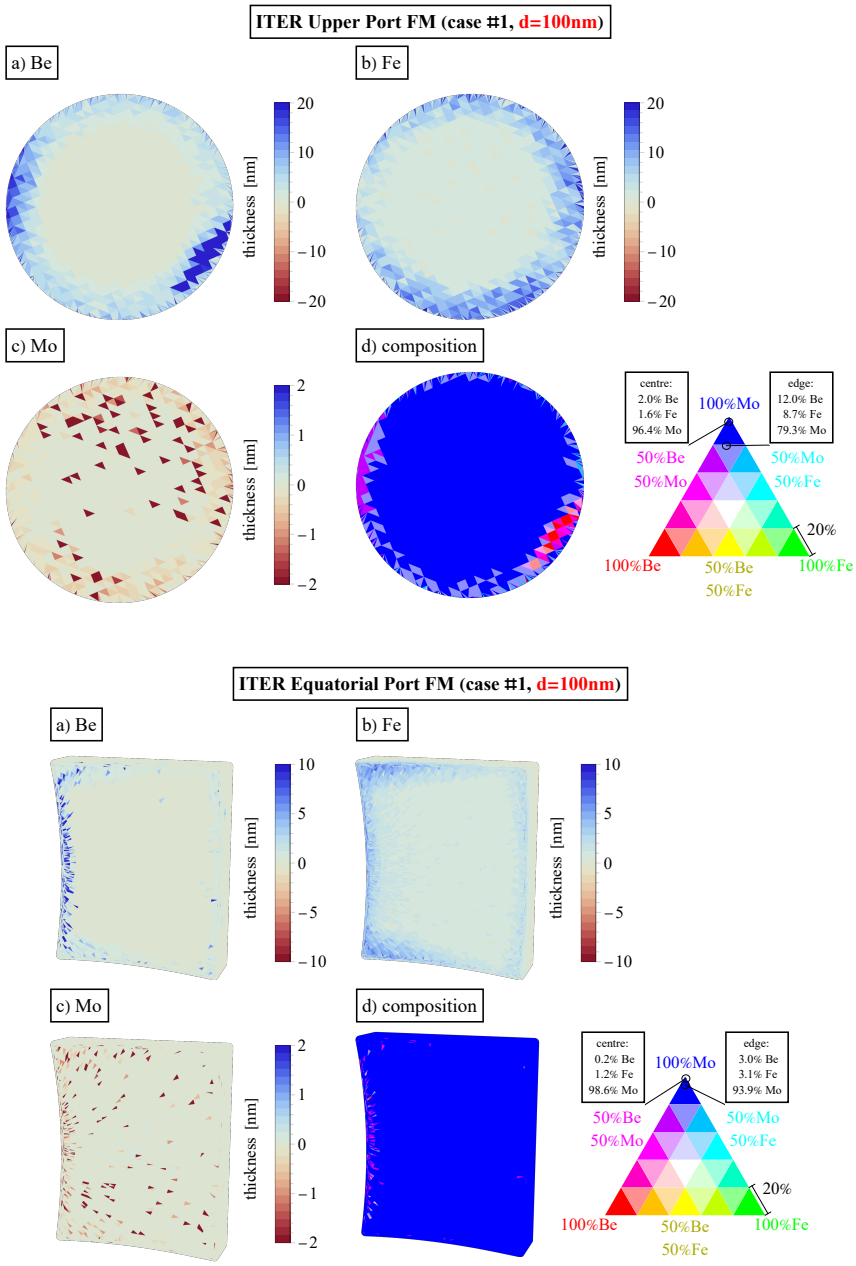

Figure 6.29: UPP (top) and EPP (bottom) first mirrors in the $d = 100\,\text{nm}$ study: Net fluences of Be, Fe, and Mo (a-c) on the upper port first mirror front surface – the difference to the main simulation (Figure 6.22) is that the HMM affects a 100 nm surface layer, of which the composition can be seen in Figs. d).

depicted in Figure 6.29 looks at a glance very similar to the main results depicted in Figures 6.22 and 6.24, even though they were simulated with the much lower interaction layer thickness. This is promising because it implies that the choice of d does not have a major impact on the results. The most noticeable difference in the graphical overview is the significantly different surface composition (Figs. d) compared to the original findings – in the test case with $d = 100\,\text{nm}$, the largest part of both FMs retains more than 95% Mo concentration (dark blue), and only a few comparatively small regions at the edge of the mirrors show significant beryllium concentration. As a reminder, in the original study, the whole front surface showed large changes in surface composition, with the edges of the FMs reaching more than 80% impurity concentration and the centre barely retaining 75% average Mo concentration. Here, the mirror centre essentially does not change in surface composition at all. The explanation for this phenomenon can be deduced from the information in Figure 6.30: the time-evolution of the surface composition takes place on a much slower timescale. This is due to the fact that the volume that is mixed in the HMM is 20 times as large in this test case compared to the main results, so the roughly constant impinging fluxes of particles take 20 times as much time to fill up the volume. This causes the significantly slower change in surface composition, although the total deposited material is nearly identical.

The mean values of net accumulated Be, Fe and eroded Mo layer thickness on

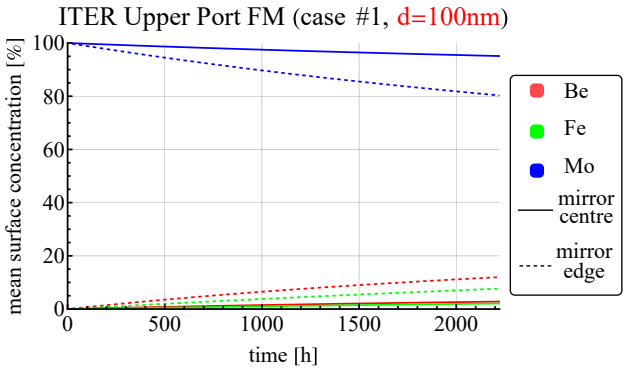

Figure 6.30: Evolution of surface concentration for the UPP first mirror in case #1 in the $d = 100\,\text{nm}$-study, in which a 20x larger value for d was assumed. Compared to the simulation with $d = 5\,\text{nm}$ (see Figure 6.23), the evolution of the surface concentration is much slower, because a 20x larger interaction volume is mixed.

the mirror front surface can be found in Table 6.15, where the results for all three plasma scenarios are detailed. It becomes apparent that in the assessed test case, the values for Mo erosion and Be and Fe deposition are generally very similar, but around 5–20 % higher compared to the main analysis. Only one deviation

Table 6.15: Overview of simulation results for the surface interaction layer thickness test case with $d = 100\,\text{nm}$: average Mo erosion and Be and Fe deposition on the front of the mirror surfaces at the end of the simulation time. The second column in each coloured block is the relative difference to the main results, which can be found in Table 6.13 and were calculated with a physically realistic value of $d = 5\,\text{nm}$ reflecting the expected implantation depth of atoms on the first mirrors.

d=100 nm test case		Be layer		Fe layer		Mo layer	
		[nm]	rel. to main	[nm]	rel. to main	[nm]	rel. to main
case #1	UPP	4.71	+6.53%	3.65	+21.78%	−1.30	+7.84%
	EPP	0.70	+4.16%	1.47	+10.01%	−2.51	+0.18%
case #2	UPP	1.29	+2.29%	0.30	+10.52%	−0.23	+10.47%
	EPP	0.07	+1.87%	0.19	+4.10%	−0.19	+1.17%
case #3	UPP	0.02	−0.02%	3.27×10^{-3}	−62.78%	-2.99×10^{-3}	+7.36%
	EPP	1.03×10^{-3}	+0.51%	2.36×10^{-3}	−59.19%	-1.87×10^{-3}	+11.12%

from this pattern is found for Fe deposition in case #3, where the strong relative difference in deposition is likely caused by the negligibly small absolute value. The overall slightly higher Be and Fe deposition can be explained by the fact, that sputtering of the surfaces takes place proportional to the concentration in the surface interaction layer in ERO2.0. The thin surface interaction layer assumed in the main analysis (compare Figure 6.23) quickly fills up with deposited Fe or Be, which can be re-eroded by impinging particles, especially highly energetic D particles. In this test case however, a much thicker interaction layer is assumed, which even after the full simulation time retains mostly over 95% Mo concentration. Thus, mostly Mo is sputtered from the mirror, while re-erosion of deposited Be and Fe is much less dominant because the Fe and Be concentrations stay very low. Altogether, the qualitative and quantitative results are very similar between this test case and the main analysis, which gives confidence in the overall results found on the first mirrors. The similarity between the results can be explained by the fact that the injected fluxes from stage 2, identical in both simulations, are net deposited since re-erosion is not significant. In these deposition-dominated areas, the choice of the surface interaction layer thickness d in the HMM does not play a significant role and the net fluences are largely independent of the assumed value of d, which explains the similar findings.

6.3.2 Beryllium Covered Diagnostic First Wall

Experiments in JET equipped with beryllium (Be) first wall and tungsten (W) divertor have demonstrated substantial material migration of Be in the vessel causing Be deposition at the wings of limiters and predominantly deposition on the W tiles of the inner divertor as reported by S. Brezinsek et al. [13]. Transferring this to the ITER case, Be will be eroded at the first wall and migrate in the vessel, with the possibility of transport of Be to the DFW and full coverage of the DFW with Be in multiple years of operation. Thus, a fully deposited Be coverage of the DFW represents the worst case possible of local Be source potentially impacting the mirror arrangement. Since Be has a lower sputtering threshold than Fe – used as proxy for the ITER steel, that the DFW surfaces are made of – local re-erosion and transport could lead to more impurity transport into the mirror box. Erosion of the molybdenum (Mo) mirrors by Be or deposition of Be on the mirror surface both have an impact on the optical properties of the mirror, potentially endangering the operation of the diagnostics. Thus, a specific worst-case study for ITER is performed here for plasma case `#1`, which showed the highest Be deposition values from all regular three-stage simulations in the main analysis, in which the full DFW is made of Fe. In this worst-case study, the DFW is assumed to be completely covered by an infinite Be layer up to the aperture hole right in front of the mirrors (see Figure 6.31). Therefore, the global stage 1 simulation results of the multi-stage simulation workflow can be retained, while in stage 2, Be is assumed as a material for the entrance cone of the DFW. In stage 3, the DFW's mirror box surrounding the Mo mirrors is still initially considered as a clean Fe surface.

The other simulation parameters were kept as consistent as possible with the main simulations, e.g. the surface interaction layer thickness is chosen as the physically reasonable $d = 5\,\mathrm{nm}$ in contrast to the test case studied in section 6.3.1. However, a difference lies in the applied angular distributions of the stage 1 EIRENE CX simulation of D atoms. The corrected EIRENE angular distributions were used here (see also section 6.2.1). These updated spectra of the angular distribution (shown in Appendix C) were generated with a newer EIRENE code version that fixed a miscounting of particles hitting the back side of the EIRENE catcher plane, which lead to peaks at 90° in the originally applied spectra, as this was the last bin queried. The corrected spectra show a smoother distribution that is mostly peaked between 70° and 80°, which means that a larger flux of D neutrals into the mirror volume is expected: a smaller angle means that the trajectory is more aligned with the surface normal, and thus points into the direction of the mirrors. From the further analysis of the cases, it was estimated that in the plasma scenario studied

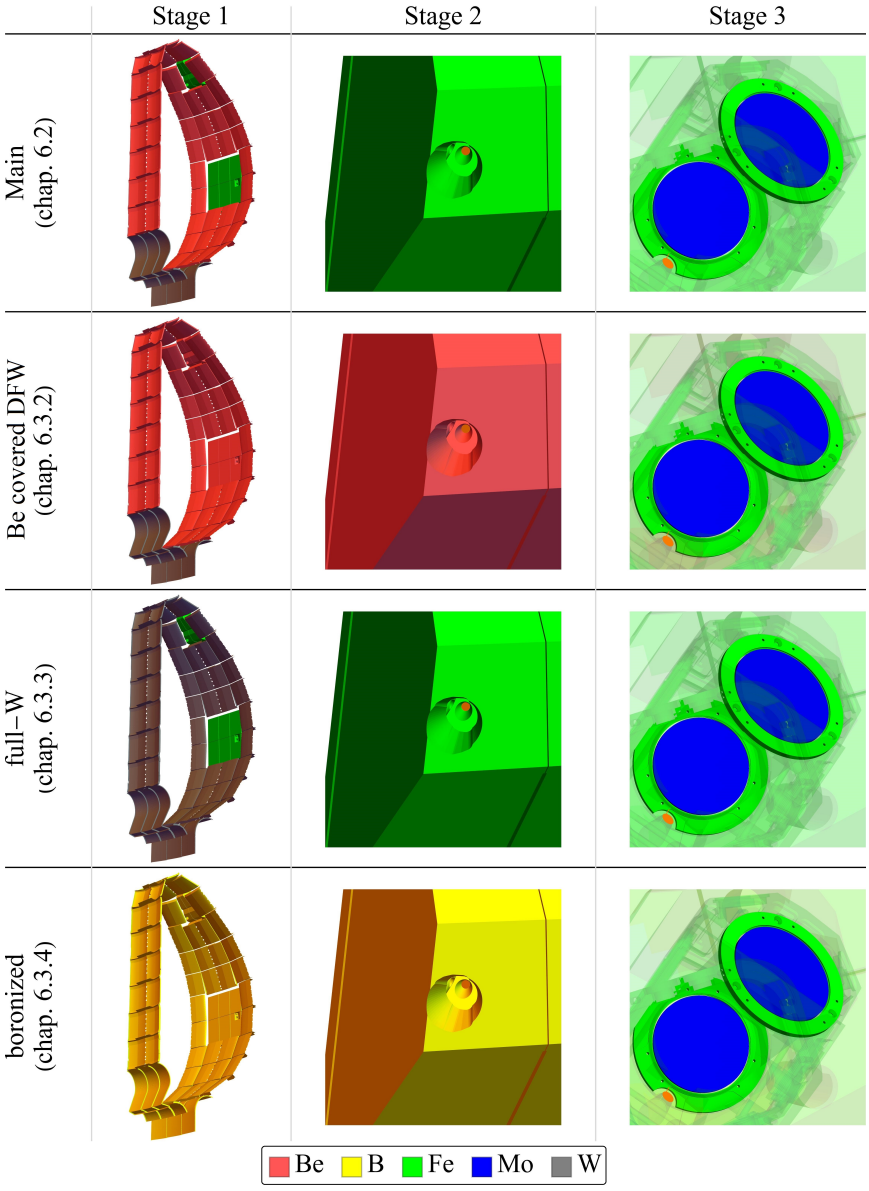

Figure 6.31: Overview of initial material compositions assumed in the three material variation studies ("Be covered DFW", "full-W ITER" and "boronized ITER") in all three simulation stages compared to the main analysis (top row). The EPP is handled equivalent to the UPP, but is not explicitly shown here. The mirror box behind the aperture hole (C2 catcher plane, orange) is assumed initially clean in all simulations, which is why stage 3 looks identical for all cases. The shown material composition is only valid at the start of the simulation, as the HMM in ERO2.0 simulates changes in surface composition over time.

here (case #1), the D flux at the aperture hole is around 2.8 times higher with the corrected EIRENE angular distributions compared to the originally available angular distributions. Since the assumed materials in the studies were different, this could also be caused to some degree by different reflection behaviour of Be surfaces compared to Fe surfaces used in the main analysis, although this effect is likely not dominant.

The results of the study are depicted in Figure 6.32 for both, the upper port plug (UPP) and the equatorial port plug (EPP) first mirror (FM). The geometric influence of the cone structures in front of the mirrors, that was found and discussed in the main analysis, is still present. The edges of the FM show significantly higher Be deposition than the centre in both geometries, respectively. However, this phenomenon cannot be observed for the deposited Fe in this study, for which a much more homogenous distribution on the mirror is found. The fact that Fe is only assumed here as a surface material in the 'clean' mirror box in stage 3 (compare Figure 6.31) explains the observation. Thus, the Fe transport is not influenced at all by the geometric effects of the cone structure located in front of the aperture hole. All Fe deposited on the FM originates from sputtering of the mirror box inside the DFW and mirror housing, and consequently is much more homogeneously spread on the FM front surface than in the main analysis (Figures 6.22 and 6.24).

The overall results of all mean deposition/erosion values on the first mirror front surfaces is summarised Table 6.16. More Be is found on the mirror surfaces compared to the main analysis, nearly 15x as much on the EPP front mirror. This is to be expected, because in this study, Be can continuously sputter from the DFW front surface from the start of the simulation. In contrast, in the main analysis, the Be has to accumulate on the Fe DFW front before it can re-erode from there to deeper regions of the DFW. All Be originates solely from simulation stage 1, thus global main chamber erosion.

Regarding the behaviour of Fe, two different processes come into play when

Table 6.16: Overview of simulation results for the study with complete and infinite Be coverage of the DFW front: average Mo erosion and Be and Fe deposition on the front of the first mirror surfaces at the end of the simulation time. The second column in each coloured block is the relative difference to the main results (Table 6.13), in which Fe was assumed as the DFW material throughout.

Be covered DFW study		Be layer		Fe layer		Mo layer	
		[nm]	rel. to main	[nm]	rel. to main	[nm]	rel. to main
case #1	UPP	7.54	+70.60%	2.29	−23.55%	−8.93	+638.99%
	EPP	9.93	+1373.51%	1.54	+15.35%	−7.84	+213.06%

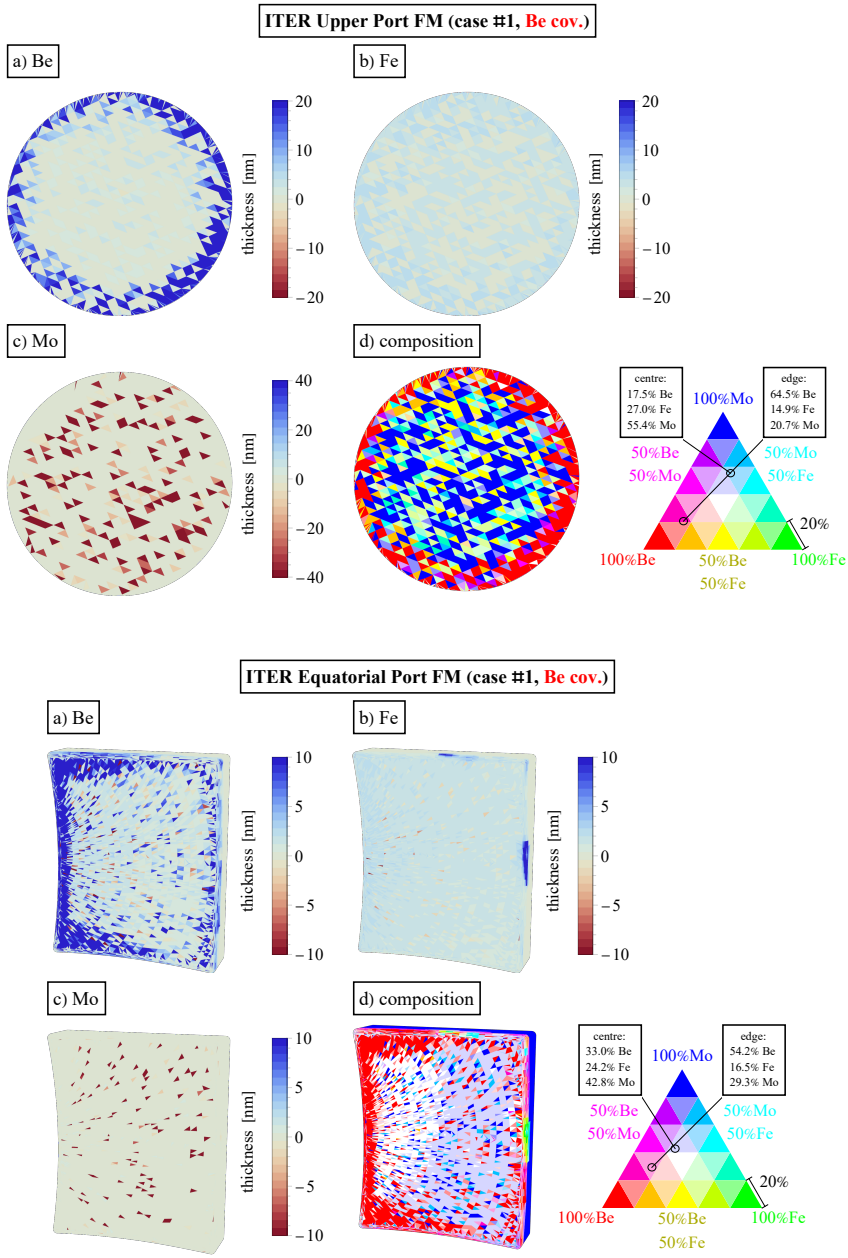

Figure 6.32: UPP (top) and EPP (bottom) first mirror front surface in the "Be covered DFW" study in plasma case #1, respectively. (a-c) Net fluences of Be, Fe, and Mo. (d) Surface composition in a 5 nm interaction layer. In this study, Be was assumed to cover the DFW up to the aperture hole.

comparing the "Be covered DFW" study to the main analysis: on the one hand, less Fe impinges on the mirrors, because only the mirror box inside the DFW acts as a Fe source. On the other hand, the corrected EIRENE angular distributions of the D CXN cause generally higher sputtering deep inside the DFW and more Fe is eroded from the mirror box inside the DFW. These two concurrent processes are different in relative scale in the two DFW geometries, EPP and UPP, as the EPP FM shows more Fe deposition than before, while the UPP FM shows less deposition in the "Be covered DFW" study.
Finally, the Mo erosion on the FMs is higher in general in this study, which can be partially attributed to the higher D CXN fluxes onto the mirror due to the corrected EIRENE angular distributions. Overall, the deposition values in this study are significantly higher than in the main analysis, but stay below 5 nm in the centre of the mirror in all cases.
In conclusion, a thin beryllium layer of less than 5 nm thickness would be deposited in the centre of the FMs at the end of the operation time. This assumes, that beryllium is covering the DFW completely and permanently with infinite source, which is an unlikely and hypothetical case.

6.3.3 Full-Tungsten ITER

The ITER organization has recently announced the change of the first wall (FW) material in ITER from beryllium (Be) to tungsten (W) to obtain a higher resilience against melting during disruption events and a reduced erosion and material migration of the FW material. The divertor remains equipped with actively cooled W plasma-facing components to withstand the high expected heat fluxes of $10\,\mathrm{MW/m^2}$ in steady-state [88]. A first study evaluating particle fluxes into the DFW in this so-called full-W ITER device is presented here for plasma case `#1`, which showed the strongest first mirror (FM) deposition in the Be/W ITER mix analysed in the main study. It should be noted that initial global ERO2.0 simulations in ITER with a hypothetical full-W wall have been performed before with a focus on FW results [29], demonstrating the reduction of the primary erosion source with W in comparison to Be as a FW material.
A first look at the results of the full-W study can be found in Figure 6.33, where the W net fluxes in the global simulation are illustrated. The W sputtering (integrated: $7.0 \times 10^{17}\,\frac{1}{\mathrm{s}}$ in the simulated 20° sector) is overall negligible on the largest parts of the first wall and divertor, with only some regions showing sputtering of up to $10^{17}\,\frac{1}{\mathrm{m^2\,s}}$ – around four orders of magnitude lower than Be sputtering in Be/W ITER. The sputtering is attributed by 84% to CXN deuterium, the other 16%

are by W self-sputtering. There is no impurity seeding acting as an additional sputtering mechanism in this type of proof-of-principle simulations considered, and ionized D plasma particles do not contribute to the sputtering either, since the sputtering threshold for D on W lies at around 250 eV, much higher than the plasma temperatures at the wall. This leaves CXN sputtering as the main sputtering channel, which is performed based on mean energy and flux values provided by the SOLPS-4.3/OEDGE-solution as poloidal profiles[4]. The sputtering source is therefore likely underestimated, since the high-energy tail of an incoming D CXN energy distribution would cause some physical sputtering even where the mean energy of the distribution is below the threshold energy.
The poloidally resolved mean energy of D CXN is shown on the right in Figure 6.33. The regions of highest mean energy of impinging D CXN align very well with the regions of net sputtering. The results match up reasonably well with the published full-W ITER results from Ref. [29], where the order of magnitude and general pattern of deposition and erosion are very similar.

However, the global simulation is not the focus in this work. As before, the

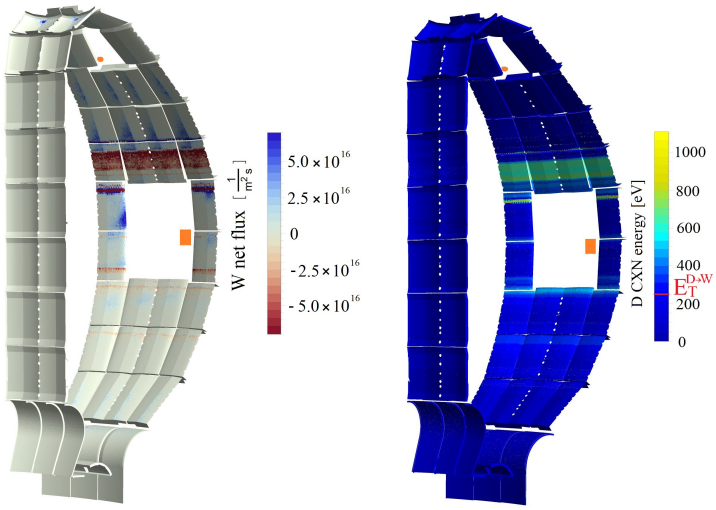

Figure 6.33: Net W flux (left) in the full-W ITER global simulation using plasma case #1. The peaks in mean D CXN energy (right) align with the main sputtering regions, since the sputtering by the ionized plasma background is negligible due to the high energy threshold for physical sputtering of D on W (∼250 eV, indicated in red in the energy scale on the right). Catcher planes covering the entrance to both DFW ports are shown in orange.

[4]The full CXN energy spectra generated for this work are only available at the locations of the EPP and UPP entrance, while a global simulation would require poloidally resolved around the full device. CXN energy distributions are therefore not included in global stage 1 simulations.

particle fluxes onto the catcher planes (orange in Figure 6.33) are acquired in the global simulation. The W particle fluxes entering the two ports are summarised in Table 6.17. Compared to the main results, where a Be/W wall was applied, the

Table 6.17: Fluxes of W onto the EPP and UPP C1 catcher planes in the full-W ITER study for plasma case #1. The fluxes are compared to Be fluxes from the main analysis (see section 6.2), in which a Be/W composition of ITER was assumed.

port	W flux (full-W) $[\frac{1}{\mathrm{m^2\,s}}]$	Be flux (main) $[\frac{1}{\mathrm{m^2\,s}}]$	ratio
EPP	2.9×10^{13}	1.9×10^{17}	1.6×10^{-4}
UPP	4.0×10^{10}	2.2×10^{16}	1.9×10^{-6}

fluxes of the eroded and transported wall material reaching the catcher planes are reduced by four orders of magnitude in the EPP, and even six orders of magnitude in the UPP. This is in line with the decrease by four orders of magnitude in total erosion found when going to a full-W wall [29], which reduces the total impurity source. The even more drastically reduced fluxes into the UPP can be explained by the fact that the erosion in full-W ITER is generally focussed more in regions closer to the EPP (see Figure 6.33) according to the poloidally resolved CXN energy distribution. For W, local or prompt redeposition is much more significant than for Be [57], since the Larmor radius of W particles is generally larger than for Be particles due to the significantly increased mass, and the ionization energy is lower. Therefore even fewer particles are transported to the UPP.

Altogether, an immense decrease in flux into both ports is measured compared to the results of stage 1 in the main analysis, where a Be/W material mix was assumed for ITER. In the main analysis, the multi-stage simulation workflow revealed, that the expected total fluence in the centre of the first mirrors accumulated to less than 5 nm deposition for the impurity Be. With at least four orders of magnitude less impurity fluxes into the DFW ports, the W impurity deposition on first mirrors in full-W ITER is expected to be entirely negligible. Although the sputtering yields for W potentially impacting on the Fe DFW and Mo mirror are higher than for Be projectiles (see Figure 6.34) due to the higher atomic mass of W, this is only around a factor 2-4 in the expected energy range, and thus is offset completely by the four orders of magnitude lower fluxes of the impurity. In the main analysis, more than 99% of the mirror surface sputtering was caused by impinging D neutrals (compare e.g. Table 6.11), which are basically unaffected by the change to a full-W device. Therefore, the results on the first mirrors in full-W ITER are expected to be very similar to the main results, but without any noticeable deposition of impurities from the main chamber on the mirror, i.e. only Fe deposition. Consequently, no further stages of the multi-stage simulation approach were performed for the full-W

ITER case study. The mirror performance in the two geometries analysed in this work, UPP and EPP DFW, is not expected to degrade by W deposition over the full ITER operation time in a full-W ITER device.

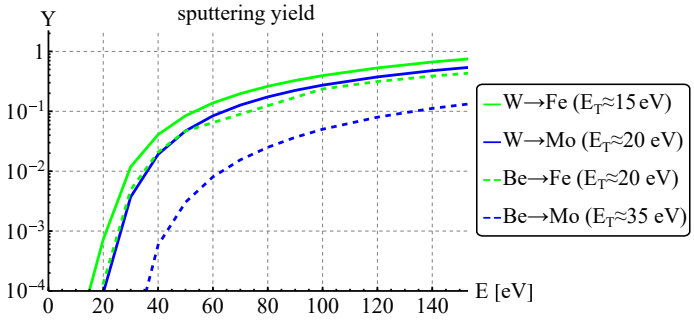

Figure 6.34: Physical sputtering yield of pure Fe (green) and Mo (blue) under bombardment with W (full lines) and Be (dashed lines) projectiles in the energy range up to 150 eV. Data is calculated by SDTrimSP and assumes projectile impact at 60° angle relative to the surface normal. The threshold energy of the projectile-target combination is indicated in the legend.

6.3.4 Infinitely boronized ITER

With the change of the ITER FW to a tungsten surface, boronization is becoming relevant for the device, because the positive oxygen-gettering capabilities of Be and the resulting positive impact on the plasma confinement are not present in a full-W device. Regular boronizations, i.e. artificial coating by deposition of boron (B) on all PFCs [130], can mitigate this effect and have been observed to increase the plasma performance [124]. However, since boronizations are usually performed in glow-discharges without a confining magnetic field, the boron is deposited even in recessed areas. During the boronization, the DFW mirror systems can be protected by shutter systems. However, B will likely still be deposited very close to the mirrors, up to the aperture hole where the shutters are located. B has different optical properties compared to Be [21] and a low sputtering threshold as well, therefore the mirror performance could potentially be negatively impacted by the boronization. Thus, as a final material variation in this work, a first study of the effect of boronizations on the erosion and deposition on ITER diagnostic first mirrors (FMs) is presented.

In the ERO2.0 simulations for this study, the ITER first wall, divertor and DFW front surfaces are assumed to be fully covered by a B layer, which acts as an infinite source of the material into the global and local plasma volumes. Only behind the DFW aperture hole, clean Fe (DFW, housing) and Mo (mirror) surfaces

are assumed – see Figure 6.31 for an overview of the assumed materials. The assumption of an infinite boron source in ITER is a simplification, since the B layer is expected to be around 50–100 nm in thickness directly after a boronization, so the total amount is limited in reality. Therefore, the results represent a very conservative set of assumptions and realistic values are likely lower, since the W under a potentially eroded B layer is much less affected by erosion, as shown in the "full-W ITER"-study (section 6.3.3). All other assumptions in the ERO2.0 simulations are consistent with the conceptually analogous "Be covered DFW"-study (see section 6.3.2). Importantly, again the corrected angular distributions of impinging D neutrals from improved EIRENE stage 1 simulations are used.

The analysis was performed for one H-mode scenario (case #1) and one L-mode scenario (case #3). The graphical 3D overview of the results can be seen in Figures 6.35 and 6.36. The results at first sight seem to be very similar to the "Be covered DFW"-study presented in section 6.3.2: the geometric influence of the cone structure on impurity particles originating from stages 1 and 2 can be observed clearly in the B deposition pattern, while Fe deposition is again rather uniform over the front surface. Mo is net eroded and shows large single outliers as in all observed cases before, so mean values of the erosion should again be taken as more accountable.

Table 6.18 lists the mean erosion/deposition over the mirror front surface resolved

Table 6.18: Overview of simulation results for the "boronized ITER"-study: average Mo erosion and Be and Fe deposition averaged over the full front of the first mirror surfaces at the end of the simulation time. The second and third column in each coloured block show the relative difference of this study (B FW, B DIV, B DFW front) to the main results (compare Table 6.13 – Be FW, W DIV, Fe DFW) and the "Be covered DFW"-study (compare Table 6.16 – Be FW, W DIV, Be DFW front). Note: in the final red column, B deposition is compared to Be deposition from the aforementioned study. Empty fields are left for cases not studied in the "Be covered DFW"-study.

boronized ITER study		B layer			Fe layer			Mo layer		
		[nm]	rel. to main	rel. to Be cov.	[nm]	rel. to main	rel. to Be cov.	[nm]	rel. to main	rel. to Be cov.
case #1	UPP	2.44	−44.87%	−67.69%	2.38	−20.57%	+3.90%	−9.18	+659.45%	+2.77%
	EPP	3.28	+386.80%	−66.96%	1.58	+18.15%	+2.43%	−7.91	+215.82%	+0.88%
case #3	UPP	0.007	−63.46%	−−	0.007	−18.26%	−−	−0.01	+425.44%	−−
	EPP	0.005	+339.37%	−−	0.002	−61.69%	−−	−0.005	+181.14%	−−

by element for all plasma scenarios analysed in this study. The results are shown in relation to the main study and to the "Be covered DFW"-study. The results for Mo erosion and Fe deposition in the "boronized ITER"-study are remarkably similar

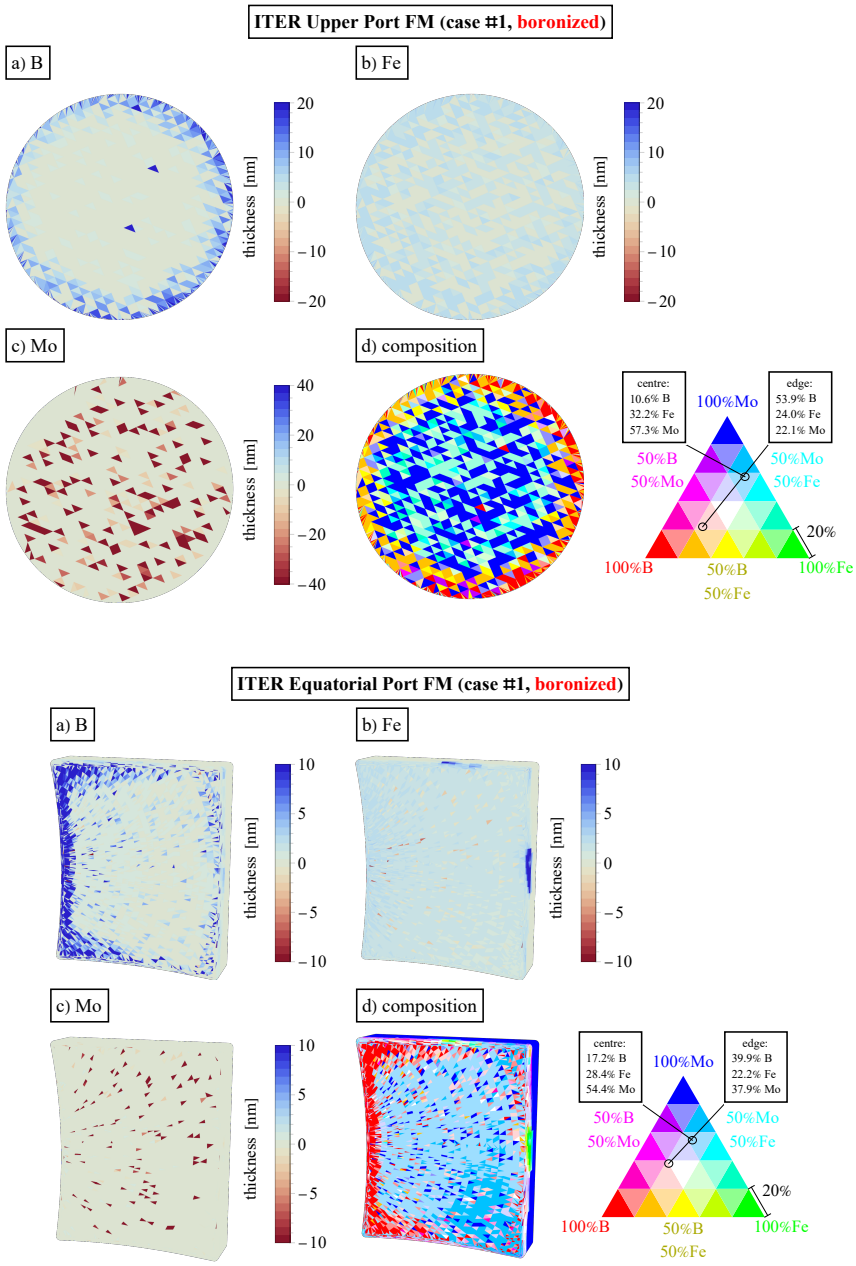

Figure 6.35: UPP (top) and EPP (bottom) first mirror front surface in the "boronized ITER"-study in plasma case #1, respectively. (a-c) Net fluences of B, Fe, and Mo. (d) Surface composition in a 5 nm interaction layer. In this study, B was assumed to cover the entire device up to the aperture hole in the DFWs.

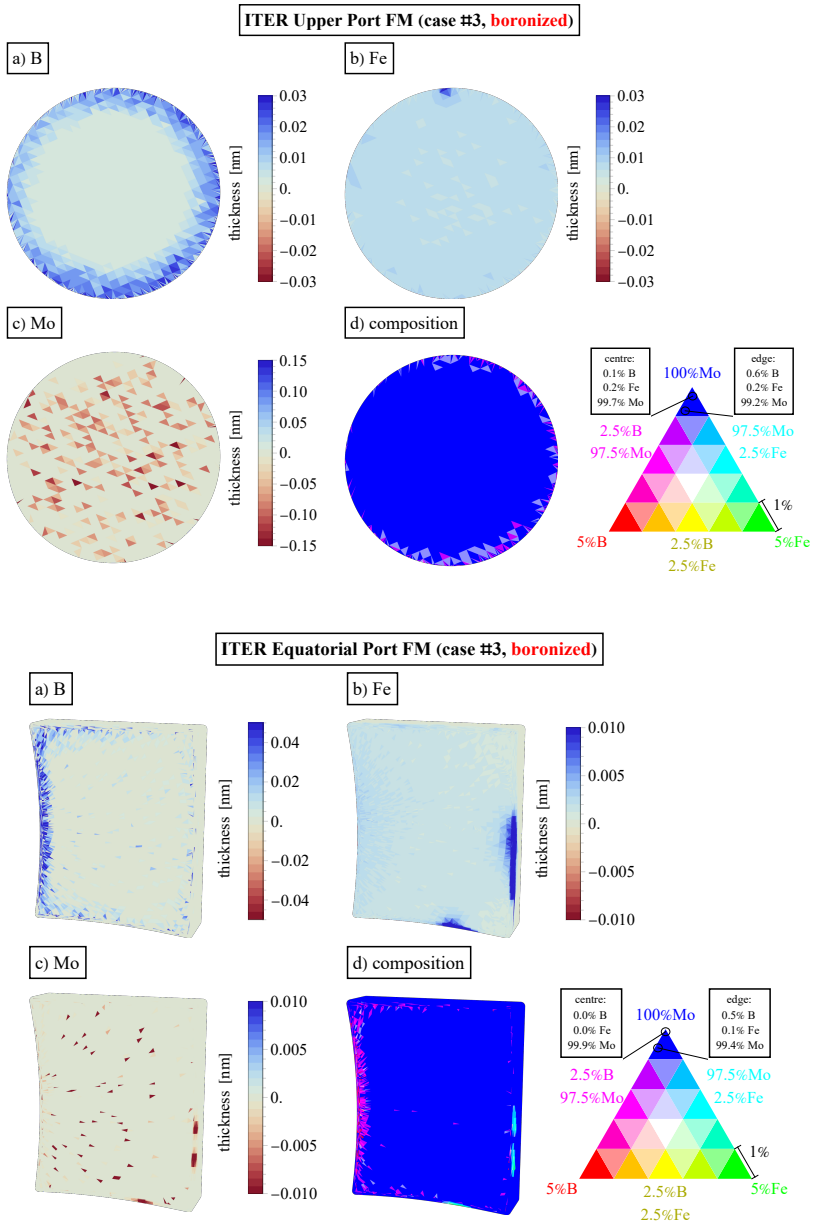

Figure 6.36: UPP (top) and EPP (bottom) first mirror front surface in the "boronized ITER"-study in plasma case **#3**, respectively. (a-c) Net fluences of B, Fe, and Mo. (d) Surface composition in a 5 nm interaction layer. In this study, B was assumed to cover the entire device up to the aperture hole in the DFWs. Note the decreased scale applied for the surface composition – nearly the whole surface retains more than 99% Mo content.

to the "Be covered DFW"-study, within 5% for all scenarios. The B deposition however is significantly lower with 67% thinner layers than the Be deposition in the former study. This reduction can be reasonably well explained by the decrease in physical sputtering yield of B compared to Be (see Figure 6.37): in the energy range of the impinging particle fluxes, the ratio of the sputtering yields of the two elements is between 0.2 and 0.5, i.e. a decrease between 50% and 80%. D was chosen as a projectile for this comparison, since it accounts for the by far dominant part of the erosion in all observed cases. Thus, the 67% decrease in B deposition on the mirror can be attributed to the decrease in B erosion in earlier stages of the simulation due to the reduced sputtering yield. However, it should be noted that other factors such as the higher density of B compared to Be, and slight changes in transport patterns due to different reflection behaviour of Be and B also affect the deposition on the mirror.

Furthermore, in Table 6.18 some general trends can be observed: L-mode

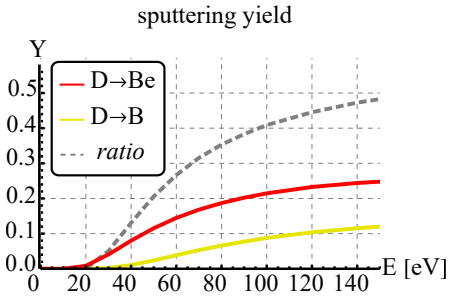

Figure 6.37: Sputtering yield of a pure B (yellow) and Be (red) surface in the range up to 150 eV, calculated by SDTrimSP and assuming D projectiles at 60° impact angle. The grey dashed line shows the ratio of the two yields.

deposition and erosion values are small compared to the H-mode results, as it was the case in the main analysis. The comparison also shows that the ratios between all studies' results are about the same between the different plasma cases, e.g. the B deposition on the respective FM is about 50% lower in the UPP and 400% higher in the EPP when comparing a boronized ITER device to a Be/W ITER, regardless of the plasma background. This also reveals that the two ports are significantly differently affected by the change in material at the DFW front. Due to the complex and substantially distinct geometry of the two DFW ports, it is however not possible to attribute this to one single parameter. In all analysed cases, the centre of the mirror stays comparably clean however, with at most around 2.0 nm mean impurity deposition in the UPP H-mode case.

6.3.5 First Assessment of Optical Performance

In sections 6.2.2-6.3.4, the erosion, deposition and resulting surface composition of the ITER diagnostic first mirrors (FMs) was assessed after the full ITER operational time, assuming a variety of material mixes for the PFCs in the device. The presented results focus on the mirror surfaces from a material perspective, because the ERO2.0 code is primarily an impurity transport and plasma-wall interaction simulation code, and does not consider optical properties of the surface. A detailed simulation of the optical performance of the mirror is outside the scope of ERO2.0 and this thesis.
However, as a first rough assessment of the mirror performance, a strongly simplified estimate is proposed in this chapter: the relative reflectivity R_{rel}, defined as the reflectivity averaged over the surface composition, relative to a pure Mo mirror:

$$R_{\mathrm{rel}} = \frac{\sum_i c_i R_i}{R_{\mathrm{Mo}}} = \sum_i c_i R_{\mathrm{rel},i} \tag{6.1}$$

In Equation 6.1, i enumerates the elements present in the mirror surface with local concentration c_i, and $R_{\mathrm{rel},i} = R_i/R_{\mathrm{Mo}}$ is the total reflectivity of a pure surface of element i compared to the total reflectivity of Mo. Due to the normalization by R_{Mo}, a value of $R_{\mathrm{rel}} = 100\,\%$ implies unperturbed mirror performance. A value $R_{\mathrm{rel}} < 100\,\%$ implies that a fraction $1 - R_{\mathrm{rel}}$ of an impinging light source is absorbed by the material mix compared to a pure Mo mirror. The impinging light source can for instance be a probing diagnostic laser beam or light emitted from the plasma and relayed to a diagnostic system. The total reflectivity of a surface is a quantity that depends on the wavelength λ and the angle of incidence θ of the reflected light [21], but for simplicity specific values are chosen here. A wavelength of $\lambda = 656\,\mathrm{nm}$ is selected, which corresponds to the wavelength of the H_α line, thus representing light emitted from the plasma and relayed to a Wide-Angle Viewing System (WAVS). Normal incidence of the light is assumed. The reflectivity values for pure surfaces used in the calculation of R_{rel} are shown in Table 6.19.

Depictions of R_{rel} on the FM front surfaces are shown in Figure 6.38 for the high

Table 6.19: Overview of total reflectivity values used for the calculation of R_{rel}, assuming a wavelength of $\lambda = 656\,\mathrm{nm}$ and normal incidence of the light.

element	total reflectivity R_i	rel. reflectivity $R_{\mathrm{rel},i}$	source
Be	0.54	83.1%	[91]
B	0.25	38.5%	[21]
Fe	0.53	81.5%	[54]
Mo	0.65	100.0%	[70]

Figure 6.38: Overview of relative reflectivity for three ITER material studies in the H-mode high density plasma scenario (case #1), which showed the highest deposition values of all scenarios analysed. The relative reflectivity is a strongly simplified estimate of the optical performance of the mirrors at the end of the ITER lifetime in the simulations performed in this work. See full text for details and caveats.

density H-mode plasma scenario in all three performed material studies. Case #1 is chosen for the comparison, since it showed the highest erosion and deposition in all studies. In the main study, in which a Be/W material mix in ITER is assumed, the optical performance is expected to stay well above 90% in the centre regions of both mirrors. The edge of the mirror, as well as the full mirror in the "Be covered DFW"-study show values of around 75–80 % relative reflectivity, i.e. the mirror performance degrades by around 20–25 % over the full ITER operational time. Only in the "boronized ITER" study, the relative reflectivity is expected to drop to lower than 70 % in the centre and to less than 50 % on the edges of the mirror. This is caused by the significantly worse optical properties of B compared to Mo, Fe, and Be as indicated in Table 6.19.

However, it should be stressed that R_{rel} is a strong simplification of the optical performance for several reasons: (i) the optically active layer of mirrors is usually thicker than the 5 nm considered for the material composition here [21]. In SDTrimSP studies performed in this work, assuming the impinging energy spectra on the FMs collected in ERO2.0 simulations, the implantation depth of impinging material was estimated to lie below 5 nm. The Mo mirror is therefore essentially unperturbed in a volume deeper than 5 nm from the surface. If this additional volume is also taken into account for the calculation of the relative reflectivity, the relative reflectivity values would be closer to that of a clean Mo surface. (ii) The material on the mirror will likely not be deposited in clean layers and porosity is known to negatively affect reflectivity [19], so the results here are on the other hand overestimates of the performance. (iii) Only one wavelength is considered, while WAVSs are often designed to take the full visible spectrum into account.

(iv) Potential modification of the surface morphology due to erosion of the Mo surface by energetic CXN is not taken into account. Due to these simplifications, additional studies are necessary to gauge the influence of the different effects on the optical performance, which are out of the scope of this work.

Chapter 7

Summary and Conclusions

This thesis explored the simulation of plasma and impurity transport in magnetically confined plasmas, and erosion and deposition processes of plasma-facing components (PFCs) in tokamaks, with a focus on diagnostic first mirrors (FMs) embedded in recessed regions. A multi-stage simulation workflow was developed to ensure the correct treatment of different particle species in the tokamak and to improve the statistics in the recessed regions. The workflow is based on the ERO2.0 impurity transport and PWI code, and the EIRENE neutral transport code. To prepare the ERO2.0 code for use in the multi-stage simulation workflow, significant code updates were performed. The multi-stage workflow was then first applied in simulations for the JET tokamak, where a mirror assembly was installed during the ILW-3 campaign (2015-2016). To validate the workflow, a benchmark against experimental measurements was performed, achieving satisfactory results. With the validated workflow, predictive modelling of the erosion and deposition on diagnostic first mirrors (FMs) planned for use in diagnostic Wide-Angle Viewing Systems (WAVSs) in the ITER experimental fusion device was performed, assuming several material mixes relevant for ITER operation.

The ERO2.0 code updates focussed on the improvement and speed-up of the guiding centre approximation (GCA) tracing methods, which is used in the AGCA (adaptive GCA) simulation mode [96, 97]. This hybrid simulation mode permits a switch between full-orbit (FO) and GCA tracing methods along a particle's trajectory, and originally featured a basic implementation without performance optimisation. In the frame of this thesis, the magnetic gradient calculations necessary for the application of GCA tracing methods were accelerated significantly by the pre-calculation of the gradient vectors on the ERO2.0 grid, so that far fewer interpolations of the background data are necessary during the runtime of the code. Additionally, higher-order numerical schemes were implemented for the solution of the equations of motion in GCA. While a single step in the higher-order

numerical schemes takes longer to compute than the original first-order algorithm, the far higher numerical stability of the improved schemes enables the choice of considerably larger discretization time steps in the transport simulation. Control mechanisms were implemented to prevent unphysical collisions of traced particles with the wall geometry during application of GCA, so that the correct resolution of impact angles achieved by pure FO tracing methods – one of ERO2.0's main features – is preserved.

The optimizations were verified by an inner-code benchmarking of a JET simulation in limiter configuration, directly comparing results between the pure FO simulation mode and the improved AGCA simulation mode with accelerated GCA tracing methods. The results showed that not only did the code optimizations preserve the quality of the physical results, e.g. physical sputtering rates, net deposition and erosion patterns as well as impact angles on the wall, but they reduced the computation time by a factor of at least 9. This significant increase in performance of the ERO2.0 code is not only relevant for this work, but can find application in future PWI and impurity transport simulations with ERO2.0. In the frame of this thesis, the optimizations are however especially important to improve the statistics, thus the resolution of the particle fluxes into the recessed volumes relevant for this work, which requires a vast amount of test particles to be simulated.

A multi-stage workflow utilizing the ERO2.0 and EIRENE codes and at least four simulations in three simulation stages was developed to further improve the statistics gathered. Both the EIRENE and ERO2.0 codes are based on the Monte-Carlo technique, which generally limits their quality of results in recessed regions that only few test particles enter. With the multi-stage approach, key locations in the 3D geometry of the specific recessed volume – a test mirror assembly in installed in JET and two mirror systems planned for ITER in the equatorial and upper port plug (EPP/UPP) of the diagnostic first wall (DFW) – were chosen as locations for so-called catcher planes. These artificial surfaces served as interfaces between successive simulations stages and cover the volume behind leak-tight. The statistics of any impinging test particles were collected on the catcher planes, i.e. velocity, impact location, carried flux and charge state. The gathered statistics then served as a source for upsampling the number of test particles in order to permit simulations of low fluxes into recessed volumes. The technique of upsampling is chosen according to the local requirements so that the gathered statistics are accurately represented in each simulation stage with increased statistics. Within the multi-stage workflow, firstly an ERO2.0 simulation for the impurity transport and an EIRENE simulation for the hydrogenic neutral transport are performed in the global tokamak volume, using plasma boundary codes like EDGE2D-EIRENE

as main background input regarding the plasma and its conditions. ERO2.0 delivers the impurity fluxes into the recessed regions, while EIRENE provides data on energetic charge-exchange neutrals (CXN), which are critical for erosion in the recessed areas. The gathered deuterium (D) CXN and beryllium (Be) impurity fluxes and energy distributions entering the relevant recessed regions are collected and injected into later stages, which focus more and more closely on the local volume around the mirrors.

The multi-stage simulation workflow was applied to JET, where an ITER-like mirror test assembly (ILMTA) was installed during the ILW-3 experimental campaign in the years 2015-2016, with a Be/W material mix of the JET PFCs. The simulation results showed less than 1 nm of net beryllium (Be) deposition on all three mirror locations in the ILMTA, with slightly more nickel (Ni, up to 1.5 nm) deposition. Ni originates from sputtering of the Inconel ILMTA, for which pure Ni was used as a proxy in ERO2.0. The resulting erosion was less than 0.1 nm averaged over the molybdenum (Mo) mirrors in each of the two plasma scenarios investigated, an H-mode and an L-mode plasma provided by the EDGE2D-EIRENE plasma boundary code package. The interpretative ERO2.0 simulation results of both plasma scenarios were combined to perform a benchmark with the experimental results from post-mortem analysis, with simulation times matching the exposure times from the experiment. In the experiment, the deposition on all mirrors was measured by Heavy Ion Elastic Recoil Detection Analysis (HIERDA) at the end of the operational campaign [105] and thus presents an integration over all applied plasma conditions during the experimental campaign. The benchmark showed very promising results, with the deposition being in the correct order of magnitude for all cases and matching the experimental values to 10% on some mirrors. Impurities from other sources than the PFCs measured on the Mo mirrors, mostly oxygen and carbon, were not included in the simulation since they are not part of the PWI processes in JET.

With the workflow benchmarked successfully against experimental results, predictive modelling for the ITER DFWs was performed for the whole expected ITER lifetime. Figure 7.1 shows an overview of results for all cases. From global ERO2.0 simulations of three ITER baseline plasma scenarios (high- and low density H-mode and a low-density L-mode plasma background from the SOLPS-4.3/OEDGE plasma boundary code package), two branches of local simulations in the UPP and EPP geometry were performed for each scenario, assuming a Be/W material mix in ITER. In all cases, strong geometrical patterns on the FMs were found, which are attributed to the cone-shaped structures in front of the aperture hole in the UPP and EPP, respectively. Unlike in the JET ILMTA, the models provided have direct

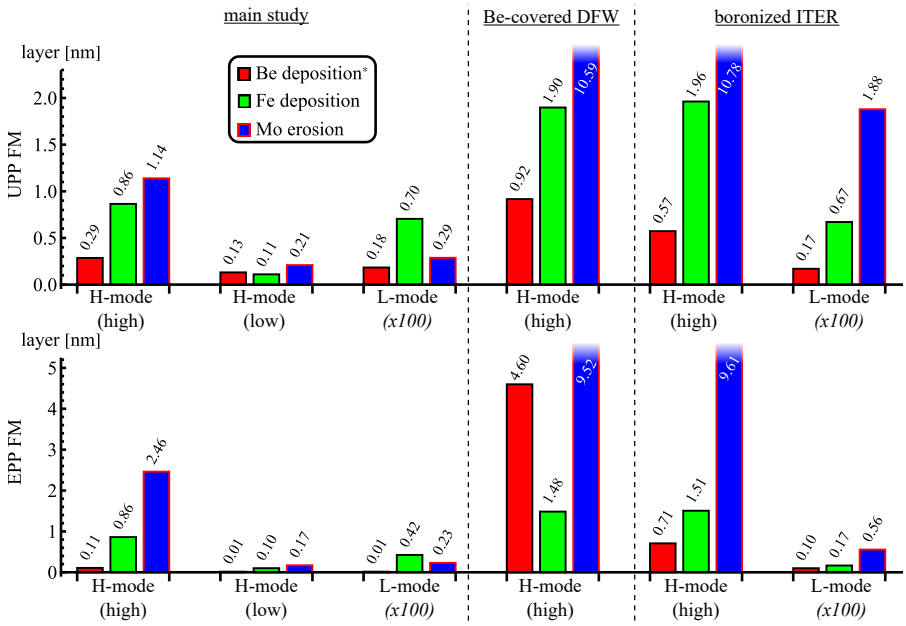

Figure 7.1: Overview of all ITER material studies: net deposited Be (red) and Fe (green) layer thickness and eroded Mo layer (blue) in the centre of the FM in the UPP (top) and EPP (bottom, shown with different scale). Notes: *in the "boronized ITER"-study, the red bar corresponds to boron (B) deposition, since it replaces Be as the main material in the ITER FW in this study. All results for L-mode were multiplied by a factor of 100 for this graph for better visibility.

line-of-sight from the cone surfaces to the edge regions of the FMs, which resulted in significantly higher fluxes onto the edges of the mirrors. In general, the source location of transported material was found to have a large impact on the deposition pattern on the mirrors. Beryllium (Be) originates from first wall sputtering and global transport, iron (Fe, used as proxy for ITER steel) originates from sputtering of the DFW surfaces, and molybdenum (Mo) originates solely from sputtering of the first and second mirrors. However, the centre regions of the FMs, for which the optical systems are optimized, are much less effected by the deposition, with a factor of 10–20 difference between mirror centre and edge for Be and a factor of 2–6 difference for Fe. Because the centres of all mirrors were found to accumulate only minimal deposition layers compared to the edge, we expect that cleaning of the mirrors is likely not needed under the given assumptions. A detailed simulation of the optical properties given the material mix resulting from this work is, however, outside of the scope of the present studies. Nevertheless, with the cone geometry in front of the aperture holes shown to facilitate impurity deposition on the edges of the mirrors, small adjustments to the cone geometry should be considered in ITER

to decrease the deposition on the FMs. In updated models, no direct line-of-sight from the cone surface to the mirror should be present. This is expected to lead to up to 97% lower net deposition on the edges of the FMs in EPP and UPP DFW, as it was observed in the simulation results in the centre of the FMs, respectively. Considering FM erosion, up to 2.5 nm averaged erosion over the mirror front surface was found in the main study, with more than 99% of the sputtering attributed to energetic D CXN particles. Even with the upscaling of the amount of test particles performed in the multi-stage simulation workflow, the CXN with the highest energy could not be perfectly resolved, leading to numerical artefacts of single surface cells with drastically higher erosion than surrounding cells. In reality, the erosion is expected to be more uniform over the mirror, since the highest erosion stems from completely unperturbed D CXN traversing the aperture without collision. Considering the second mirrors (SMs), the modifications of the front surface are significantly reduced compared to the FMs. Erosion is negligible, since no direct line-of-sight is given to the main plasma, where the energetic CXN originate from. The deposition of impurities is around one order of magnitude lower compared to the FMs. Geometrical effects are much less prominent on the SMs, which is caused by the additional reflections of particles necessary to reach the SMs.
Between the three different plasma scenarios, the high density H-mode (case #1) showed the strongest erosion and deposition values, which again is attributed to the D CXN fluxes which were highest in this case. While the low density H-mode (case #2) plasma resulted in ∼50% higher mean energies of the CXN, the 90% reduction in flux led to all around less PWI on the mirrors. The L-mode deposition and erosion (case #3) were all around negligible compared to the H-mode values, which can be attributed to the ∼99.8% lower CXN fluence compared to the high density H-mode plasma. For the H-mode scenarios shown in this work, pure D was assumed as discussed in section 6.2.1. Assuming a DT-plasma, the erosion of the first mirrors is expected to increase by a factor of 1.5-2 in all shown H-mode scenarios in this work. The deposition of impurities on the first mirrors is expected to increase by the same factor for species originating from sputtering by CXN, e.g. Fe in the main study.
In further studies, the modular approach of the multi-stage simulation workflow was exploited. First, the independence of the main study's results on the choice of the model parameter d, the surface interaction layer thickness, was established. The parameter was increased to $d = 100\,\text{nm}$ in this study. The variation of d showed a very good match with the main study, in which a value of $d = 100\,\text{nm}$ was assumed based on simulations of the implantation depth with SDTrimSP. This adds further credence to the results of the main study.

Moreover, the FM erosion and material deposition on it were examined in three material studies using different assumptions of the material mix of the first wall, divertor, and DFW in ITER. (i) Assuming a DFW covered by Be, the mean Be deposition on the FMs in ITER was identified to increase by a factor of 1.7–14 in the H-mode high density case, with the variation caused by the different 3D geometries of the two DFW ports. The Fe deposition showed similar results to the main study, but more uniformity over the mirror was found, since all Fe originated from the mirror box behind the cone-shaped aperture. (ii) Assuming a full-W ITER device, the impurity fluxes into the DFW ports in the global ITER simulations are found to decrease by at least four orders of magnitude due to the significantly lower erosion of W compared to Be from the first wall material. Local studies of the two DFW ports were not performed, as the already low impurity deposition on the FMs in a Be/W ITER device would equivalently be orders of magnitude lower and thus completely negligible in the case of a full-W ITER. (iii) Assuming an infinitely thick boronized ITER, the results show very strong similarity to the Be-covered case, but all around $\sim$70% lower impurity deposition due to the reduced physical sputtering yield of boron compared to beryllium under bombardment of D projectiles.

Finally, the necessity of the multi-stage simulation workflow was evaluated for a simulation in the ITER EPP simulation branch. In order to obtain the same statistics, thus, the same amount of test particles on the mirror, in a single-stage ERO2.0 simulation without the multi-stage simulation workflow, seven orders of magnitude more particles would be required. This number of simulated particles is not feasible on modern high-performance computing architecture. Additionally, the multi-stage simulation workflow allows focussing the computing power efficiently on the local simulations, where the trajectories are much shorter than in the large global plasma volume, thus saving computing power and resources.

Concluding the predictive ITER modelling, the energetic CXN have shown to be critical for the erosion and deposition processes in the recessed regions throughout all studies performed in this work. On the one hand, direct erosion of FMs is caused nearly exclusively by the CXN, which is caused by the direct line-of-sight to the main plasma necessary for the FMs. On the other hand, the DFW walls are sputtered by the CXN as well, releasing material that can deposit on the mirrors. In nearly all analysed plasma scenarios and geometries, the deposition of sputtered DFW material (Fe) exceeds the deposition of sputtered FW material (Be). For both species, the deposition on the mirror is significantly higher where a direct line-of-sight to cone surfaces in front of the aperture hole is given, i.e. on the mirror edges assuming the geometries investigated in this work. In contrast, the mirror

centres are nearly unaffected by deposition, but only by the slight erosion by CXN. High-density H-mode plasma scenarios show the strongest modifications of the FM surfaces, while the investigated L-mode scenario is negligible in comparison. Using a strongly simplified model of optical performance, the FMs are expected to retain more than 90% of their initial reflectivity over the whole ITER lifetime. Larger losses of the FM optical performance in this model are expected in case the DFW itself is covered by Be ($\sim$75%), or boronizations are performed in ITER ($<$70%). The SMs show negligible modifications in comparison to the FMs, as they are only negligibly affected by erosion due to the absence of direct line-of-sight to the main plasma, while the deposition of impurities is reduced by 85–97 %. Therefore, the SMs are not expected to suffer from loss of optical performance.

Chapter 8

Outlook

In this work, deposition and erosion on diagnostic first mirrors in JET and ITER were evaluated for a wide range of plasma scenarios and different assumptions on the wall material composition. With the codes used in this work, the results are explicitly from the material perspective – optical properties were not simulated in this work, which will in the end be relevant for the decision if and how often the ITER FMs will need cleaning as currently planned [106, 131]. Therefore, a next step would be to investigate the optical performance of the simulated layers deposited and eroded from the mirrors. For this, two approaches are possible: firstly, further simulation work using a different set of codes could be performed, e.g. applying transfer matrix methods [8]. Secondly, experimental studies and subsequent characterisation of optical properties could be envisaged, e.g. using linear plasma devices like PSI-2 [66] (Forschungszentrum Jülich, Germany) for the deposition of impurity material on sample mirrors and subsequent reflectometry [50] for analysis.

While the deposition results on the FMs were successfully benchmarked against experiments in JET, some uncertainties remain in the approach developed in this work: most significantly, the plasma solutions from validated plasma codes had to be extrapolated to generate a plasma background for the local ERO2.0 simulations. In some geometries, the extrapolation distance was up to 18 cm, which comes with a large uncertainty. The simulation of the plasma and neutral particle conditions in the complex 3D geometry inside the diagnostic first wall in ITER is not easily possible with the current modelling tools, but the availability of wide-grid solutions covering the volume up to first wall elements steadily increases. Current extrapolations imply that collisions of particles with the plasma and neutral background are negligible in the recessed volumes, with a mean free path of over 100 m for all types of assessed particle collisions. Wide-grid solutions would reduce the extrapolation gap to the recessed volumes analysed in this work significantly,

and thus improve the quality of the results.
From the perspective of the codes used in this work, more detailed physics models could be implemented into the main code ERO2.0. Especially for this work, surfaces with mixed elemental composition are important, since a multitude of components with different compositions is simulated. In ERO2.0, the simulation of the elemental composition is handled by a Homogeneous Mixing Model (HMM), which tracks the changes in surface composition assuming a homogeneous distribution of implanted material inside a fixed interaction volume. The sputtering of mixed surfaces is however handled in a simplified way, in which the sputtering for pure surfaces is scaled by the respective surface concentration of the elements. In a more sophisticated approach, the sputtering of the mixed surface would be described without falling back to pure surface data. This can be achieved in two ways: firstly, the ERO2.0 database of SDTrimSP calculations could be expanded to include mixed surface data, with further interpolations from these data points to the momentary surface composition present in the simulation. However, the size of the background database would grow roughly with $(1/\Delta c)^{n-1}$ if mixing of n elements is considered, where Δc is the desired resolution in the surface composition space. In the case of this work ($n = 3$, e.g. Be, Fe, Mo), with a resolution of $\Delta c = 10\%$, around 100 additional SDTrimSP scans (each sampling around 500 points in the parameter space of impact angle and energy) would need to be performed, instead of only three scans needed for the current approach. Additional work would be needed to manage this massive increase in background data.
The second approach would be a dynamic coupling of ERO2.0 with SDTrimSP, as it was possible in the predecessor ERO [22]. While this approach could handle arbitrary surface compositions without the need for a background database, it requires considerable implementation work in ERO2.0. Additionally, the dynamic coupling likely would cause a drastic increase in runtime of ERO2.0, as it has been observed for ERO before [23], which requires higher computing power.
Furthermore, as the computing power of high-performance computers increases, ERO2.0 simulations with even more test particles will also be viable and would increase the resolution and thus quality of the results, as even with the massive amount of test particles ($\simeq 1.5 \times 10^9$ per plasma scenario) that were traced in the presented simulations, rare high-energy CXN particles are still not resolved perfectly, resulting in local spikes of erosion in certain isolated locations in all presented ITER first mirror cases. Using more test particles would further spread the flux of these high-energy particles, leading to a more realistic result. Since it was shown in this work that in most cases more than 99% of the sputtering on the mirrors can be attributed to high-energy D CXN, more advanced particle

sampling methods could be considered to circumvent the need for a larger amount of simulated particles. For example, the number of sampled D particles could be weighted more heavily to the high-energy regions, increasing the statistics in the energy range most relevant for sputtering on the mirrors.
For future perspectives, the multi-stage simulation workflow developed for JET and ITER in this work offers unique versatility that cannot be achieved in a single-stage approach. Different material combinations in the DFW and mirror system can use preceding results from already performed simulations to make significant studies with small additional effort. For example, for a simulation of different mirror materials which are under consideration for mirror systems like rhodium (Rh) [77], all results up to the final stage of introduced simulation workflow could be re-used, significantly reducing the workload and computational power needed to achieve the desired results. Similarly, the proposed adjustments to the cone geometries in the ITER DFWs, which are expected to significantly decrease the impurity deposition on the edges of the FM, can be validated efficiently: a repeat of global stage 1 simulations is not necessary in this case, while adjustments in the DFW cone geometry require repeating only stage 2 and 3 and adjustments in the mirror geometry require solely new stage 3 simulations.
Furthermore, the multi-stage workflow developed in this work can be applied in other locations of JET and ITER, and other fusion devices. Firstly, the workflow could be evaluated and benchmarked further by simulating recessed areas that are part of experiments, e.g. JET mirror cassettes installed in the divertor regions [80]. Secondly, the applicability of the workflow could be demonstrated in more complex geometries, where the 3D capabilities and massive parallelization of ERO2.0 can provide unique results, e.g. in the H_α spectroscopy system installed in the Wendelstein 7-X stellarator [33, 43]. Thirdly, the predictive capabilities of the simulation workflow presented in this work can be applied to future devices, e.g. the EU-DEMO reactor planned as the bridge linking ITER to a fusion power plant [31] for which first plasma scenarios are in development [109].
Finally, the optimizations to the Guiding-Centre Approximation (GCA) tracing methods of ERO2.0 developed in this work, which are used in the adaptive GCA simulation mode, significantly improved the overall performance of the code. This gain in efficiency facilitates simulation cases where the performance of ERO2.0 was reaching its limits before, e.g. large-scale global DEMO and W-7X simulations, where the long dwelling times of the particles require a massive amount of time steps to be calculated. The adaptive GCA methods improved in this work are now integrated into the main code and will likely find application in most future ERO2.0 simulation work.

Appendices

Appendix A

Interpretation Guide for Surface Composition Plots

In the main analysis, the surface composition is analysed on the mirror surfaces in JET and ITER. The surface composition is defined here as the triplet $\{c_i\}$ of the surface concentration of mirror material, first wall material/impurity and DFW material. c_i denotes the respective element's surface concentration in the surface interaction layer with thickness d, as described in section 3.1.5, and can thus assume values between 0 and 1, or 0% and 100%. The sum of the three concentrations adds up to exactly 1 as long as no other species is implanted into the surface, which is not the case in any of the scenarios analysed in this work[1]. This fact implies that only two of the concentration values are independent, while the sum gives the third. Therefore, the possible values of the surface composition lie in a 2D plane. This can be used to construct an unambiguous colour mapping for the three values c_i that can still be visualized in a simple 2D graphic, shown in Figure A.1. The mapping and graphics are explained in this section for the example of a Be first wall, Fe DFW material and a Mo mirror, which is the material mix assumed in the main study for ITER in this work (section 6.2).
For determining the colour, the composition is converted to an RGB value where the FW material concentration (Be) determines the red component, the DFW material concentration (Fe) determines the green component and the mirror material concentration (Mo) determines the blue component. Thus, a clean mirror surface, as present at the start of each simulation, is depicted as blue. Impurity deposition adds red to the colour, while DFW material adds green to the colour, see Figure A.1a).

A binning method is used for the composition to reduce the total number of

[1] D is assumed to leave the surface instantly.

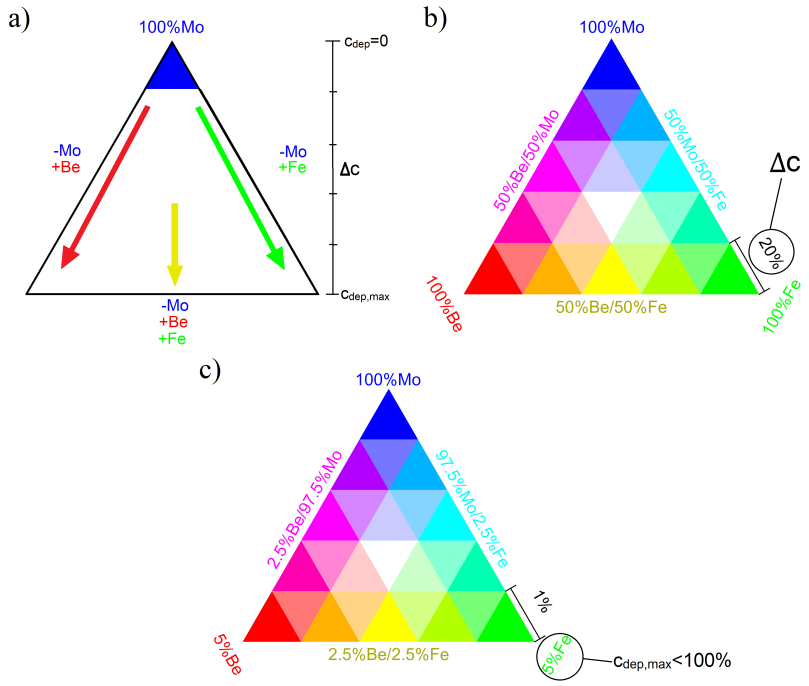

Figure A.1: Colour mapping (legend) of composition plots. a) Simplified view. b) Legend with full range ($\Delta c = 20\%$). c) Legend with reduced range around $c_{\mathrm{Mo}} = 100\,\%$.

colours for easier interpretation. $N_b = 5$ bins along each axis are chosen for all cases in this work, leading to a total of $N_c = N_b^2 = 25$ colours. Usually, a bin width $\Delta c = 20\%$ is chosen in this work, so that the full domain $c_i \in (0, 1)$ is depicted by the colour scale. In the case of $\Delta c = 0.2$ for example, the pure blue colour represents a Mo concentration of 80–100 %. If the concentration of deposited material $c_{\mathrm{dep}} := c_{\mathrm{Be}} + c_{\mathrm{Fe}}$ is very low ($c_{\mathrm{dep}} < 20\%$), local differences on the mirror surface would not be resolved by this colour scale, therefore a smaller bin width Δc is chosen for cases with low c_{dep}. The range $c_{\mathrm{dep,max}} = N_b \cdot \Delta c$ of possible deposited concentration values resolved by the colour mapping is then reduced, since N_b is kept constant for easier identification of the colours. However, the dark blue colour always represents the maximum Mo concentrations up to 100%. In the main analysis, Δc is adapted in a way that ensures that $> 95\%$ of the values depicted in the respective graphics are resolved by the chosen $c_{\mathrm{dep,max}}$, and Δc is displayed in the bottom right of the colour scale (see Figure A.1b)+c).

With the chosen colour mapping, the composition of all surface cells of the mirror can be determined. Example depictions of this type are shown in Figure A.2. For easier interpretation, the mean value of the composition, averaged over a selected

subsurface of the mirror (e.g. “centre” and “edge”, while “mean” implies that the full surface was taken into account) are shown in black boxes around the colour scale.

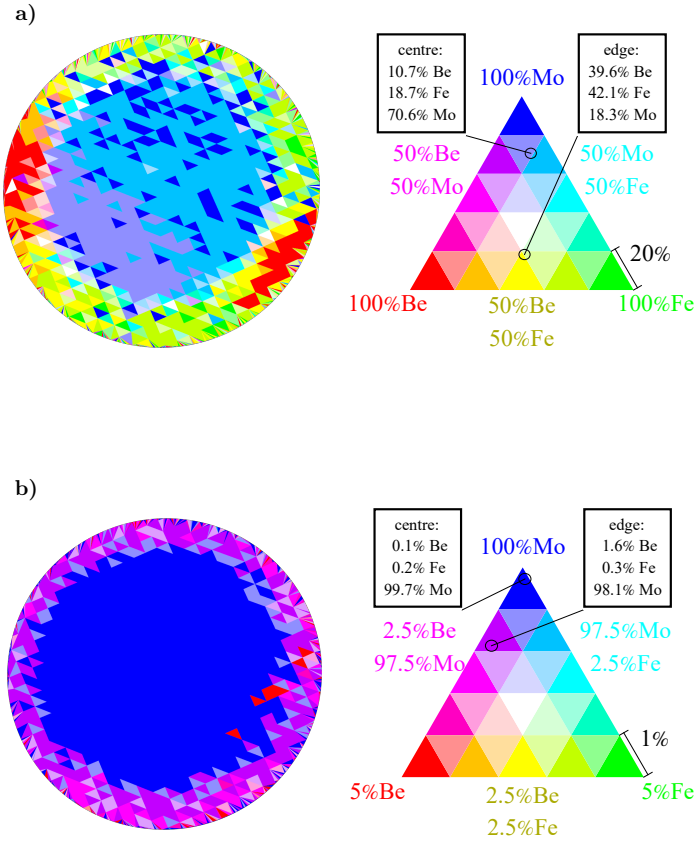

Figure A.2: Examples of composition plots from the main analysis. a) Case with full range of the colour mapping ($\Delta c = 20\%$). b) Case with reduced range of the colour mapping due to the low amounts of deposited material. $c_{\mathrm{dep}} < 5\,\%$ is resolved by the colour scale. Note: the definitions of mirror centre and edge are shown in Figure 6.16.

Appendix B

Overview of ITER Studies

Figure B.1 gives a structural overview of all ITER studies performed in this work, showcasing the modular approach of the multi-stage simulation workflow developed. The main ITER study is presented in section 6.2. In the "d=100 nm"-(section 6.3.1) and "Be covered DFW"- (section 6.3.2) studies, earlier results from the main study can be re-used. In the "full-W ITER"-study (section 6.3.3), only the first simulation stage is performed, due to the negligible fluxes into the DFWs in comparison to the main study. Only the "boronized ITER"-study (section 6.3.4) required a full repeat of all three simulation stages, since the material in the global simulation volume (stage 1) was altered, and the fluxes into the DFW were not deemed negligible. Further details and results of the studies are presented in their respective section.

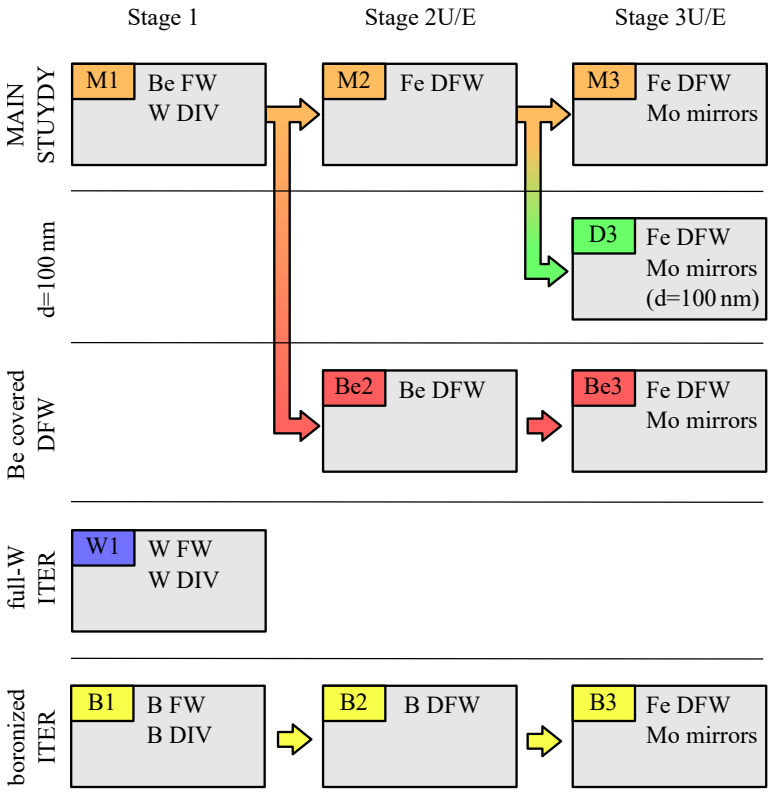

Figure B.1: Overview of all ITER studies performed in this work in the multi-stage simulation workflow. The coloured boxes label the simulation, respectively. Split arrows signify the re-use of earlier studies' results, followed by a simulation with altered assumptions about the first wall (FW), divertor (DIV) or mirror properties. Note: the stage 2 and stage 3 simulations include the two branches U and E in the UPP and EPP DFW, respectively, which are not shown here separately for simplicity and use identical settings described in the boxes.

Appendix C

Comparison of EIRENE CXN Angular Distributions

EIRENE simulations were performed for the analysis of recessed volumes in this work, providing critical information about the incoming hydrogenic particles entering the ITER-like mirror test assembly (ILMTA) in JET and the diagnostic first wall (DFW) ports in ITER. In the stage 1 EIRENE Monte-Carlo simulation of the multi-stage simulation approach (see Figure 5.1), the angular and energy distributions of impacting hydrogenic particles on the EIRENE catcher planes E were collected. The full process is described in detail in section 5.3. For the ITER simulations, the original data used for the main analysis in this work was based on an EIRENE code version which had an error in the collection of the angular distribution. In detail, particles hitting the backside of the EIRENE catcher plane, i.e. particles travelling towards the core plasma, were registered with an impact angle of $\alpha = 90°$. The impact angle is measured relative to the surface normal of the EIRENE catcher plane E, which faces outwards. For particles travelling inwards, this angle is larger than 90°, which was registered in the final bin ($\alpha \simeq 90°$) of the angular distribution during the collection of the data. In the corrected code version, only the particles travelling outwards are registered, correctly defining an impact angle $0° \leq \alpha < 90°$.

This error only affects EIRENE simulations for ITER, and led to a shift and deformation of the angular distributions towards 90° impact angle, i.e. towards hydrogenic particles more likely entering the DFW ports nearly parallel to the catcher plane. The original and corrected angular spectra for all plasma scenarios analysed for ITER simulations in this work are depicted in Figure C.1. The implications of this error are discussed in the main analysis (sections 5.3 and 6.2). The error only affected angular distributions simulated for ITER. For later parts

of this work (sections 6.3.2 and 6.3.4), the corrected distributions were used. The ITER hydrogenic energy distributions and all JET angular and energy distributions are unaffected by the error. The conceptually similar collection of impact angles of impurity particles in the stage 1 ERO2.0 simulation is unaffected as well, since the C1 catcher planes used in ERO2.0 are defined in 3D, covering the entrance to the DFWs leak-tight.

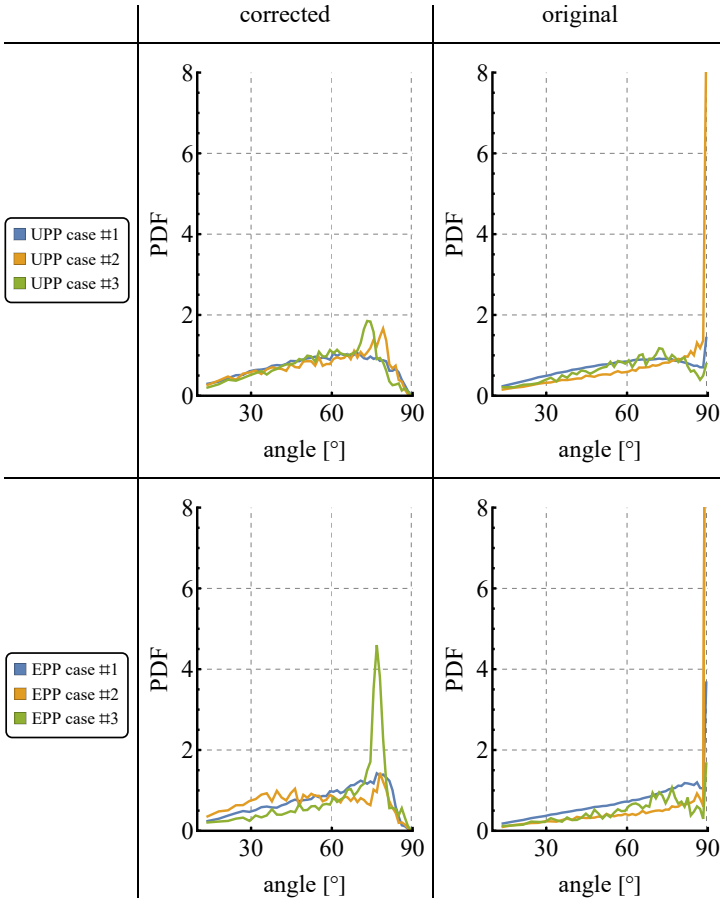

Figure C.1: Corrected and original CXN angular distributions of deuterium (H-mode scenarios #1 and #2)/hydrogen (L-mode scenario #3) neutrals in the ITER Upper Port Plug (UPP, top) and Equatorial Port Plug (EPP, bottom) DFW. The distributions were collected in stage 1 EIRENE simulations on the catcher planes E_{UPP} and E_{EPP}, respectively. The plasma scenarios are defined in Table 6.8.

Appendix D

ITER Second Mirrors

Second Mirrors (SMs) are placed in the ITER EPP and UPP DFWs in the optical path connecting the diagnostics to the plasma. In this section, a graphical overview for the SM front surfaces is shown for the main study assuming a Be/W ITER material composition, a Fe DFW and 5 nm surface interaction layer thickness on the mirrors. The results are from the same simulations as the first mirrors (FMs) presented in section 6.2, where the SM results were briefly discussed and summarised (Table 6.14), but were not shown graphically for brevity. The front surfaces of the SMs are not in direct line-of-sight with the plasma. Therefore, the fluxes onto them are in general significantly lower than on the respective FM.
Figures D.1-D.3 illustrate the net fluence of Be, Fe, and Mo as well as the surface composition on the SM front surfaces for all plasma scenarios. In contrast to all FM results from the main analysis, Mo is net deposited on all SMs, since Mo sputtered from the respective FM can reach the SM surface. It clearly visible that the deposition of all elements on the SMs is much more uniform than on the FMs, which is why mean values of the composition are shown averaged over the whole front surface. The uniformity is caused by the additional reflections of particles needed to reach the SM, so the cone structure leading up to the aperture hole of the respective DFW has a much less significant impact on the incoming fluxes than on the FM. The deposition is at most around 1 nm (plasma case `#1`, Fe). However, the deposition is all around negligible and thus operability of the SMs is not expected to decrease over the ITER lifetime. Comparing between the different plasma cases, the main findings are the same as discussed already in the main analysis for FMs – the most deposition is found in the high density H-mode plasma case, while the deposition in L-mode is negligible in comparison and the low density H-mode case lies in-between. Notably, the mean Be deposition on the SM is always 4–5 % relative to the FM in all scenarios and both analysed geometries (EPP/UPP), while the mean Fe deposition varies between 3–15 %.

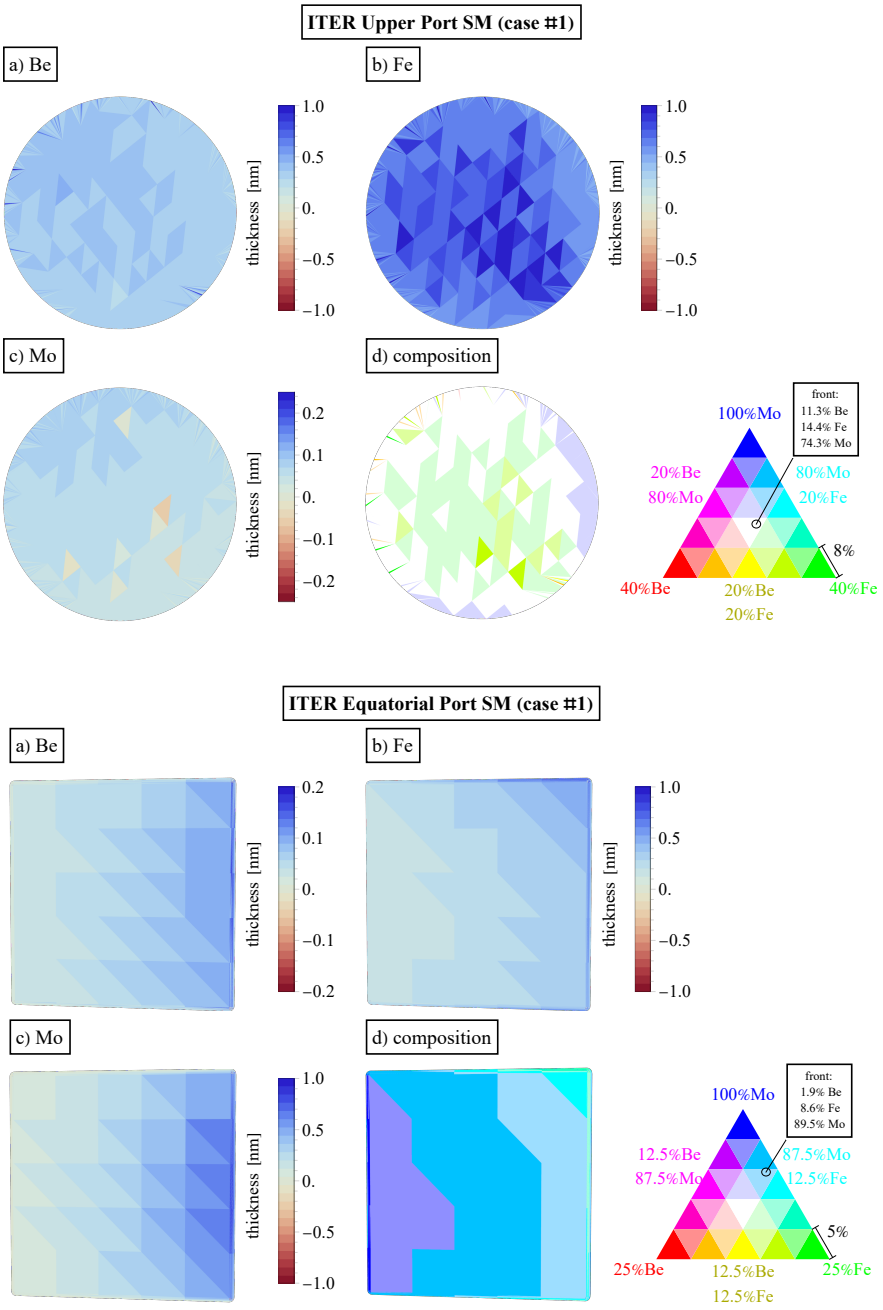

Figure D.1: UPP (top) and EPP (bottom) second mirrors in the main study, plasma case #1: net fluences of Be, Fe, and Mo (a-c) and surface composition in a 5 nm layer on the mirror front surface (d), respectively.

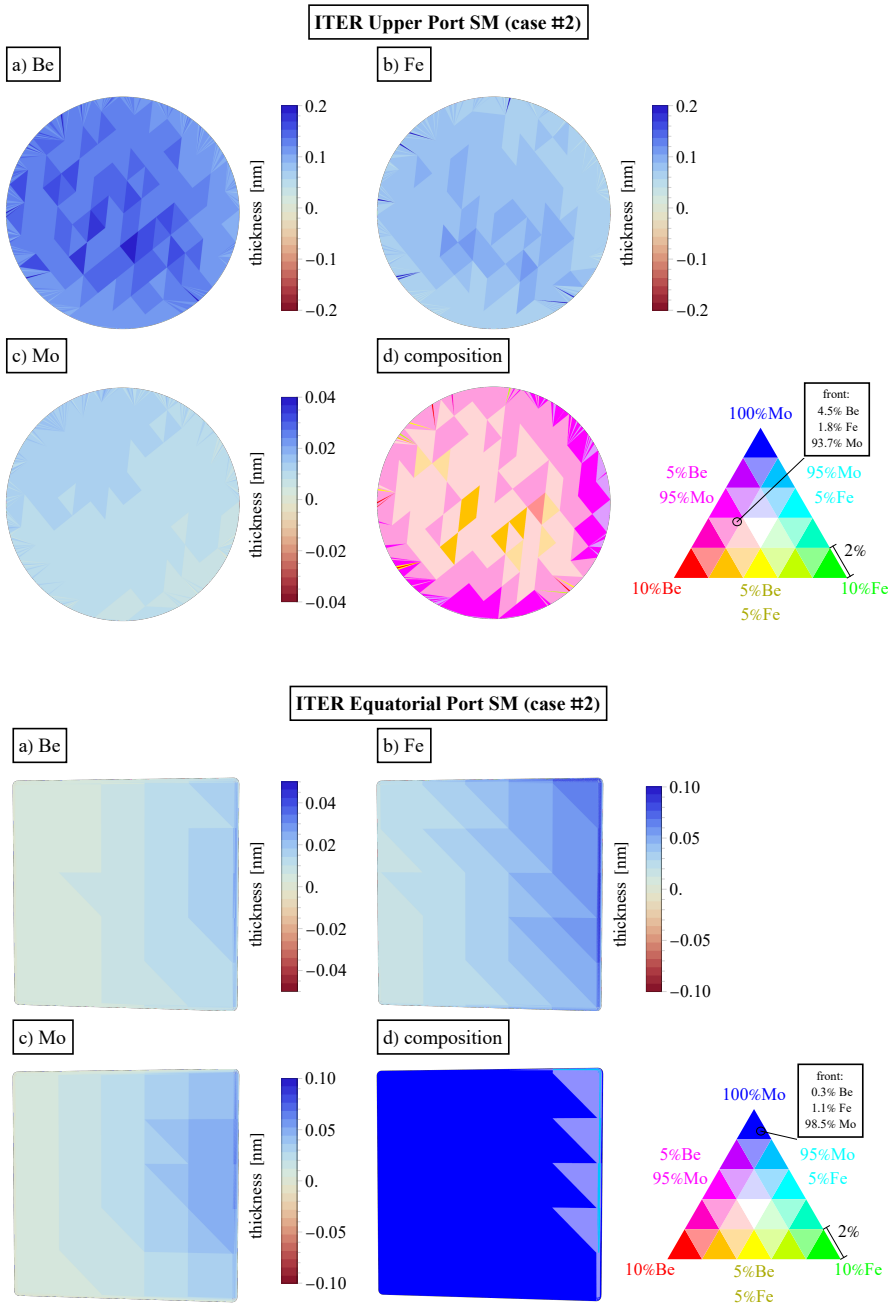

Figure D.2: UPP (top) and EPP (bottom) second mirrors in the main study, plasma case #2: net fluences of Be, Fe, and Mo (a-c) and surface composition in a 5 nm layer on the mirror front surface (d), respectively.

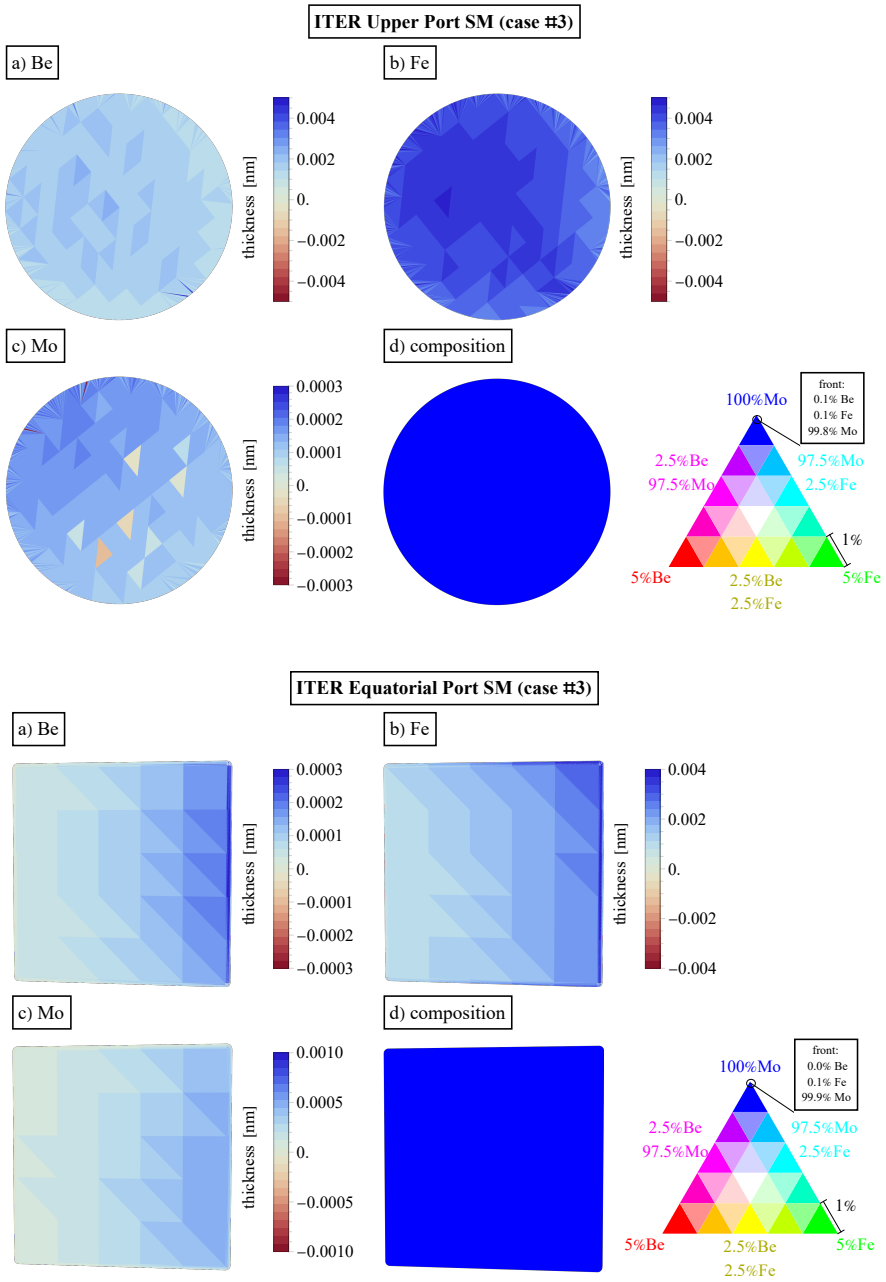

Figure D.3: UPP (top) and EPP (bottom) second mirrors in the main study, plasma case #1: net fluences of Be, Fe, and Mo (a-c) and surface composition in a 5 nm layer on the mirror front surface (d), respectively – all surface cells retain more than 99% Mo concentration.

Bibliography

1. H. Abu-Shawareb *et al.*, *Physical Review Letters* **129**, 075001 (2022).
2. L. Aho-Mantila *et al.*, *Contributions to Plasma Physics* **50**, 12th International Workshop on Plasma Edge Theory in Fusion Devices, Rostov State Hist Museum, Rostov Veliky, Russia, Sep 02-04 2009, 439–444 (2010).
3. J. A. Alonso *et al.*, *Nuclear Fusion* **62**, 036024 (2022).
4. I. Balboa *et al.*, *Plasma Physics and Controlled Fusion* **65**, 064005 (2023).
5. P. Banks, *Planetary and Space Science* **14**, 1105–1122 (1966).
6. S. S. Batsanov, *Inorganic Materials* **37**, 871–885 (2001).
7. R. Behrisch, W. Eckstein, *Sputtering by Particle Bombardment* (Springer Berlin Heidelberg, 2007), vol. 110.
8. A. Bojar *et al.*, *Journal of Physics: Energy* **5**, 035001 (2023).
9. A. Bondi, *The Journal of Physical Chemistry* **68**, 441–451 (1964).
10. D. Borodin *et al.*, *Nucl. Mater. Energy* (2017).
11. S. I. Braginskii, *Transport processes in a plasma*, 1965.
12. S. Brezinsek, *J. Nucl. Mater.* **463**, 11–21 (2015).
13. S. Brezinsek *et al.*, *Nucl. Fusion* **55**, 63021 (2015).
14. S. Brezinsek *et al.*, *Nuclear Materials and Energy* **18**, 50–55 (2019).
15. S. Brezinsek, PhD thesis, Heinrich-Heine Universität Düsseldorf, 2002.
16. S. Cabrera, E. Rincón, M. Medrano, F. L. Guern, E. Rodríguez, *Fusion Engineering and Design* **201**, 114273 (2024).
17. J. Coenen *et al.*, *Journal of Nuclear Materials* **438**, Proceedings of the 20th International Conference on Plasma-Surface Interactions in Controlled Fusion Devices, S27–S33 (2013).
18. D. Coster *et al.*, *Contributions to Plasma Physics* **40**, 334–339 (2000).
19. G. De Temmerman *et al.*, *Journal of Applied Physics* **102**, 083302 (2007).

20. S. Devaux, G. Manfredi, *Plasma Physics and Controlled Fusion* **50**, 025009 (2008).

21. L. Dittrich *et al.*, *Nuclear Materials and Energy* **37**, 101548 (2023).

22. S. Droste *et al.*, *Plasma Phys. Control. Fusion* **50**, 015006 (2008).

23. S. Droste *et al.*, *Contrib. to Plasma Phys.* **46**, 628–634 (2006).

24. S. Droste, PhD thesis, Heinrich-Heine Universität Düsseldorf, 2007.

25. G. Duxbury, M. F. Stamp, H. P. Summers, *Plasma Physics and Controlled Fusion* **40**, 361–370 (1998).

26. W. Eckstein, *Vacuum* **82**, 930–934 (2008).

27. W. Eckstein, *Vacuum* **82**, 930–934 (2008).

28. A. Eksaeva *et al.*, *Physica Scripta* **T171** (2020).

29. A. Eksaeva *et al.*, *Physica Scripta* **97**, 014001 (2022).

30. A. Eksaeva *et al.*, *Nuclear Materials and Energy* **19**, 13–18 (2019).

31. G. Federici, C. Baylard, A. Beaumont, J. Holden, *Fusion Engineering and Design* **173**, 112960 (2021).

32. Y. Feng *et al.*, *Contrib. to Plasma Phys.* **44**, 57–69 (2004).

33. O. P. Ford *et al.*, *Review of Scientific Instruments* **91**, 023507 (2020).

34. W. R. Fundamenski, O. E. Garcia, presented at the EFDA–JET–R(07)01.

35. A. Gallo *et al.*, *Physica Scripta* **T171**, 014013 (2020).

36. S. Garitta *et al.*, *Fusion Engineering and Design* **170**, 112471 (2021).

37. H. Grote *et al.*, *Journal of Nuclear Materials* **266-269**, 1059–1064 (1999).

38. M. Groth *et al.*, *Nuclear Fusion* **53**, 093016 (2013).

39. C. Guillemaut *et al.*, *Nuclear Fusion* **54**, 093012 (2014).

40. J. Gunn *et al.*, *Nuclear Fusion* **57**, 046025 (2017).

41. F. Guzmán, M. O'Mullane, H. Summers, *Journal of Nuclear Materials* **438**, Proceedings of the 20th International Conference on Plasma-Surface Interactions in Controlled Fusion Devices, S585–S588 (2013).

42. A. Hakola *et al.*, *Journal of Nuclear Materials* **463**, 162–165 (2015).

43. H. J. Hartfuss, in *Advanced Diagnostics for Magnetic and Inertial Fusion*, ed. by P. E. Stott, A. Wootton, G. Gorini, E. Sindoni, D. Batani (Springer US, Boston, MA, 2002), pp. 371–374.

44. M. Hemmous, A. Layadi, A. Guittoum, A. Bourzami, A. Benabbas, *Microelectronics Journal* **39**, 1545–1549 (2008).

45. E. Hirvijoki, PhD thesis, Aalto University, 2014.

46. L. Horton, presented at the Fusion Eng. Des. Vol. 88, pp. 434–439.

47. J. Huang *et al.*, *Physics of Plasmas* **30** (2023).

48. A. Huber *et al.*, *Nuclear Materials and Energy* **18**, 118–124 (2019).

49. D. Humphreys *et al.*, *Physics of Plasmas* **22**, 021806 (2015).

50. W. Hunter, *Vacuum Ultraviolet Spectroscopy*, 183–204 (2000).

51. IAEA, *Summary of the ITER Final Design Report* (International Atomica Energy Agency, Vienna, 2001).

52. F. Iannone *et al.*, *Fusion Engineering and Design* (2017).

53. R. K. Janev, D. Reiter, U. Samm, "Collision processes in low-temperature hydrogen plasmas", tech. rep., Atomic and Molecular Physics (Germany, 2003), p. 190.

54. P. P. B. Johnson, *Phys. Rev. B* **8** (1974).

55. Jülich Supercomputing Centre, *JLSRF* **2** (2016).

56. A. Kirschner, V. Philipps, J. Winter, *Nucl. Fusion* **40**, 989 (2000).

57. A. Kirschner *et al.*, *Plasma Physics and Controlled Fusion* **60**, 014041 (2018).

58. A. Kirschner *et al.*, presented at the J. Nucl. Mater. Vol. 337-339, pp. 17–24.

59. A. Kirschner *et al.*, *J. Nucl. Mater.* **290-293**, 238–244 (2001).

60. A. Kirschner *et al.*, *Contributions to Plasma Physics* **56** (2016).

61. A. Kirschner *et al.*, presented at the J. Nucl. Mater. Vol. 313-316, pp. 444–449.

62. A. Kirschner *et al.*, *J. Nucl. Mater.* **363-365**, 91–95 (2007).

63. T. Klinger *et al.*, *Nuclear Fusion* **59**, 112004 (2019).

64. A. Komori *et al.*, *Plasma Physics and Controlled Fusion* **42**, 1165 (2000).

65. A. E. Kramida, J. Reader, *Atomic Data and Nuclear Data Tables* **92**, 457–479 (2006).

66. A. Kreter *et al.*, *Fusion Science and Technology* **68**, 8–14 (2015).

67. K. Krieger *et al.*, *Journal of Nuclear Materials* **438**, Proceedings of the 20th International Conference on Plasma-Surface Interactions in Controlled Fusion Devices, S262–S266 (2013).

68. A. L. Kritcher *et al.*, *Physics of Plasmas* **31**, 70502 (2024).

69. P. Krstic, D. Schultz, presented at the Atomic and Plasma–Material Interaction Data for Fusion.

70. A. Leontyev *et al.*, *Fusion Engineering and Design* **86**, Proceedings of the 26th Symposium of Fusion Technology (SOFT-26), 1728–1731 (2011).

71. S. Lisgo, A. Kukushkin, R. Pitts, D. Reiter, *Journal of Nuclear Materials* **438**, Proceedings of the 20th International Conference on Plasma-Surface Interactions in Controlled Fusion Devices, S580–S584 (2013).

72. E. Marenkov *et al.*, *Journal of Nuclear Materials* **496**, 18–23 (2017).

73. V. Martin *et al.*, *Fusion Engineering and Design* **146**, 2446–2449 (2019).

74. Y. Martin, T. Takizuka, *Journal of Physics: Conference Series* **123**, 012033 (2008).

75. M. Maslov *et al.*, *Nuclear Fusion* **63**, 112002 (2023).

76. D. Matveev *et al.*, *Plasma Physics and Controlled Fusion* **52**, 075007 (2010).

77. P. Mertens *et al.*, *Fusion Engineering and Design* **146**, SI:SOFT-30, 2514–2518 (2019).

78. V. Mertens *et al.*, *Fusion Engineering and Design* **66-68**, 22nd Symposium on Fusion Technology, 119–127 (2003).

79. J. Miettunen *et al.*, *J. Nucl. Mater.* **438**, S612–S615 (2013).

80. S. Moon *et al.*, *Nuclear Materials and Energy* **19**, 59–66 (2019).

81. A. Mutzke *et al.* (2019).

82. D. Naujoks, R. Behrisch, J. Coad, L. De Kock, *Nuclear Fusion* **33**, 581–590 (1993).

83. M. Navarro *et al.*, presented at the 24th International Conference on Plasma Surface Interactions in Controlled Fusion Devices (PSI 2020, virtuell), 25 - 29 Jan 2021.

84. M. Navarro *et al.*, *Physics of Plasmas* **31** (2024).

85. J. Nührenberg *et al.*, *Fusion Technology* **27**, 71–78 (1995).

86. D. Palumbo, *The JET Project* (Commission of the European Communities, Brussels, 1975).

87. V. Philipps, P. Mertens, G. Matthews, H. Maier, *Fusion Engineering and Design* **85**, Proceedings of the Ninth International Symposium on Fusion Nuclear Technology, 1581–1586 (2010).

88. R. A. Pitts *et al.*, *Nuclear Materials and Energy* **20**, 100696 (2019).

89. W. H. Press, W. T. Vetterling, S. A. Teukolsky, B. P. Flannery, *Numerical Recipes in C++: The Art of Scientific Computing* (Cambridge University Press, USA, 2nd, 2001).

90. A. Pukhov, *Journal of Plasma Physics* **61**, 425–433 (1999).

91. A. D. Rakić, A. B. Djurišić, J. M. Elazar, M. L. Majewski, *Appl. Opt.* **37**, 5271–5283 (1998).

92. R. Reichle *et al.*, *ANIMMA 2009 - 2009 1st International Conference on Advancements in Nuclear Instrumentation, Measurement Methods and their Applications* (2009).

93. D. Reiser, PhD thesis, Heinrich-Heine Universität Düsseldorf, 1998.

94. D. Reiter, M. Baelmans, P. Börner, *Fusion Sci. Technol.* **47**, 172–186 (2005).

95. M. T. Robinson, in *Sputtering by Particle Bombardment I: Physical Sputtering of Single-Element Solids*, ed. by R. Behrisch (Springer Berlin Heidelberg, Berlin, Heidelberg, 1981), pp. 73–144.

96. S. Rode, MA thesis, Heinrich-Heine Universität Düsseldorf, 2021.

97. S. Rode *et al.*, *Contrib. Plasma Phys* **62**, 202100172 (2022).

98. F. Romanelli *et al.*, *Nuclear Fusion* **55**, 104001 (2015).

99. J. Romazanov *et al.*, *Phys. Scr.* **T170**, 014018 (2017).

100. J. Romazanov *et al.*, *Nuclear Materials and Energy* **26**, 100904 (2021).

101. J. Romazanov *et al.*, *Nuclear Fusion* **62**, 036011 (2022).

102. J. Romazanov *et al.*, *Nuclear Materials and Energy* **18**, 331–338 (2019).

103. J. Romazanov, PhD thesis, Ruhr-Universität Bochum, 2017.

104. J. Romazanov *et al.*, *Nuclear Fusion* **64** (2024).

105. M. Rubel *et al.*, *Nuclear Fusion* **61**, 046022 (2021).

106. F. Sanchez *et al.*, *Journal of Nuclear Materials* **581**, 154382 (2023).

107. K. Schmid, T. Lunt, W. Zhang, *Physica Scripta* **T171**, 014006 (2020).

108. M. Shoji *et al.*, *Plasma and Fusion Research* **16**, 2403004–2403004 (2021).

109. M. Siccinio *et al.*, *Fusion Engineering and Design* **176**, 113047 (2022).

110. R. Simonini, G. Corrigan, G. Radford, J. Spence, A. Taroni, *Contributions to Plasma Physics* **34**, 368–373 (1994).

111. K. Soni *et al.*, *Journal of Nuclear Materials* **564**, 153671 (2022).

112. P. Stangeby, *The Plasma Boundary of Magnetic Fusion Devices* (Taylor & Francis, 2000).

113. P. Stangeby, J. Elder, *Journal of Nuclear Materials* **196-198**, Plasma-Surface Interactions in Controlled Fusion Devices, 258–263 (1992).

114. P. Stangeby *et al.*, *Journal of Nuclear Materials* **313-316**, Plasma-Surface Interactions in Controlled Fusion Devices 15, 883–887 (2003).

115. S. Sudo *et al.*, *Review of Scientific Instruments* **72**, 483–491 (2001).

116. H. P. Summers, M. G. O'Mullane, A. D. Whiteford, N. R. Badnell, S. D. Loch, *AIP Conference Proceedings* **901** (2007).

117. H. P. Summers, M. G. O'Mullane, *AIP Conference Proceedings* **1344**, 179–187 (2011).

118. P. R. Thomas *et al.*, *Phys. Rev. Lett.* **80**, 5548–5551 (1998).

119. M. W. Thompson, *Philos. Mag.* **18**, 377–414 (1968).

120. S. Togo *et al.*, *Plasma and Fusion Research* **13**, 3403022–3403022 (2018).

121. M. Z. Tokar, M. Koltunov, *Nucl. Fusion* **53**, 093014 (2013).

122. M. Z. Tokar, R. Ding, M. Koltunov, *Plasma Phys. Control. Fusion* **52**, 075003 (2010).

123. Z. Vizvary *et al.*, *Fusion Engineering and Design* **123** (2017).

124. F. Waelbroeck *et al.*, *Plasma Physics and Controlled Fusion* **31**, 185 (1989).

125. F. Wagner *et al.*, *Physical Review Letters* **49**, 1408–1412 (1982).

126. M. Wakatani *et al.*, *Nuclear Fusion* **39**, 2175 (1999).

127. F. Warmer *et al.*, *Fusion Engineering and Design* **123**, 47–53 (2017).

128. J. Wesson, D. Campbell, *Tokamaks* (OUP Oxford, 2011).

129. S. Wiesen *et al.*, *J. Nucl. Mater.* **463**, 480–484 (2015).

130. J. Winter *et al.*, *Journal of Nuclear Materials* **162-164**, 713–723 (1989).

131. M. Wisse *et al.*, *Fusion Engineering and Design* **88**, 388–399 (2013).

List of Figures

List of Tables

List of Abbreviations

1D/2D/3D	One-/two-/three-dimensional
3D-GAPS	(MC neutrals transport code)
ADAS	Atomic Data and Analysis Structure
AGCA	Adaptive GCA (hybrid simulation mode in ERO2.0)
ASCOT	(Transport code)
B	Boron
B2	(Plasma edge code)
BCA	Binary collision approximation
Be	Beryllium
C	Carbon
C++	(Programming language)
C1, C2	Catcher planes (ERO2.0)
CAPS	Chemically assisted physical sputtering
CFC	Carbon fibre composite
Cr	Chromium
CRM	Collisional-Radiative Model
CX	Charge exchange
CXN	Charge exchange neutrals
D	Deuterium
DFW	Diagnostic First Wall
DIV	Divertor
DIVIMP	DIVertor IMPurity (MC impurity transport code)
DT	Deuterium-Tritium
E	Catcher plane (EIRENE)
EDGE2D	(Plasma edge code)
EFIT	Equilibrium FITting (magnetic equilibrium code)
EIRENE	(MC neutrals transport code)
ELM	Edge-localized mode

EMC3	(Plasma edge code)
EPP	Equatorial Port Plug
ERO	Erosion and RedepOsition (MC PWI and impurity transport code)
ERO2.0	(MC PWI and impurity transport code, successor of ERO)
EU-DEMO	Conceptual nuclear fusion power plant
Fe	Iron
FM	First Mirror
FO	Full-orbit
FPO	Fusion-power operation
FW	First wall
GCA	Guiding center approximation
H	Hydrogen
He	Helium
HELIAS	(Advanced stellarator concept)
HIERDA	Heavy Ion Elastic Recoil Detection Analysis
HMM	Homogeneous mixing model
HPC	High-performance computing
ICF	Inertial Confinement Fusion
ILMTA	ITER-like Mirror Test Assembly
ILW	ITER-like wall
IO	ITER Oranization
ITER	Latin: 'the way' (tokamak)
IWC	Inner wall cladding
IWGL	Inner wall guard limiter
IWPB	Inner wall protection bars
JET	Joint European Torus (tokamak)
JPN	JET pulse number
JURECA	Jülich Research on Exascale Cluster Architectures (supercomputer)
KSTAR	(Tokamak)
LCFS	Last closed flux surface
LHD	Large Helical Device (stellarator)
LOS	Line of sight
MA	Mirror Assembly
MARCONI	(Supercomputer)
MC	Monte-Carlo
MCF	Magnetic Confinement Fusion

MD	Molecular dynamics
Mo	Molybdenum
N	Nitrogen
NBI	Neutral beam injection
Ni	Nickel
NMAE	Normalized mean absolute error
O	Oxygen
OEDGE	(Code suite for plasme edge modelling)
OMP	Outer Mid-Plane
OPL	Outer poloidal limiter
PFC	Plasma-facing component
PFM	Plasma-facing material
PFPO	Pre-fusion-power operation
PIC	Particle-In-Cell
POI	Point of interest
PSI-2	(linear plasma device)
pure FO	(simulation mode in ERO2.0
PWI	Plasma-wall interaction
Rh	Rhodium
RK	Runge-Kutta
SDTrimSP	(BCA code)
SM	Second Mirror
SOL	Scrape-off layer
SOLPS-4.3	(Plasma edge code package)
T	Tritium
TEXTOR	Tokamak EXperiment for Technology Oriented Research (Tokamak)
UDP	Upper dump plate
UPP	Upper Port Plug
VisIR	Visible + infrared
VLPL	Virtual Laser Plasma Laboratory (PIC code)
W	Tungsten
W7-X	Wendelstein 7-X (stellarator)
WAVS	Wide-Angle Viewing System (diagnostic)
WEST	(tokamak)

List of Symbols

A	Area
a_0	Minor radius in toroidal geometry
B	Magnetic field strength
$\mathbf{B}$	Magnetic field vector
$\mathbf{b}$	Magnetic field direction
c	Surface concentration
$\boldsymbol{D}$	Diffusion tensor
$D_\perp$	Anomalous diffusion coefficient
d	Surface interaction layer thickness (HMM parameter)
dE_{bin}	Energy binning width (EIRENE binning parameter)
$d\cos(\alpha)$	Impact angle binning width (EIRENE binning parameter)
$\mathbf{E}$	Electric field vector
E	Energy
$E_{\mathrm{bin,max}}$	Maximal binning energy (EIRENE binning parameter)
E_{SB}	Surface binding energy
E_{T}	Threshold energy for (typically physical) sputtering
e	Elementary charge; Euler's number
$\boldsymbol{F}_L$	Lorentz force
f	Distribution function
$\mathbf{K}$	Drift vector
k_{B}	Boltzmann constant
m	Mass
n	Particle density
n^0	Neutron
$\hat{n}$	Surface normal vector
$n_{\mathrm{e/i}}$	Electron/ion density
P	Power
Q	Power amplification factor

q	Electric charge
R_0	Major radius in toroidal geometry
R	Reflectivity
$\mathbf{R}$	Guiding-centre position
R_N	Reflection coefficient
$\mathbf{r}$	Particle position
r_d	Debye length
r_L	Larmor (gyration) radius
r_vdW	Van-der-Waals radius
s	Stencil length for gradient calculation
T_L	Gyration time period
T	Temperature
$T_\mathrm{e/i}$	Electron/ion temperature
T_surf	Surface temperature
t	Time
V	Volume
$\mathbf{v_{GC}}$	Guiding-Centre velocity
$\mathbf{v}$	Velocity vector
$v_\parallel$	Velocity component parallel to magnetic field
$v_\perp$	Velocity component perpendicular to magnetic field
Y	Sputtering yield
Z	Ion charge state; atomic number
$\hat{z}$	z-axis
α	Impact angle (EIRENE)
Δt_PWI	Time discretization (PWI)
Δt	Time discretization (particle transport)
ϵ_0	Vacuum permittivity
η	Distance buffer factor applied in AGCA
Γ	Particle flux
γ	Energy transfer factor for sputtering
$\gamma^\mathrm{rel}_\mathrm{sputt}$	Relative sputtering contribution
λ	Wave length; decay length
λ_mfp	Mean free path distance
μ	Magnetic moment
∇	Differential nabla-operator

ω_{L}	Larmor (gyration) frequency
φ	Poloidal angle; polar angle
ρ	Radial flux coordinate
ρ_N	Atomic number density
σ	Cross-section (esp. for collisions)
τ_E	Energy confinement time
ϑ	Toroidal angle; azimuthal angle
θ	Impact angle

List of Publications

The following first-author publications were published by the author of this thesis during the time as a PhD student:

1) **Implementation and validation of guiding centre approximation into ERO2.0** by S. Rode, J. Romazanov, D. Reiser, S. Brezinsek, Ch. Linsmeier and A. Pukhov, published in *Contributions to Plasma Physics* on 14 March 2022 (DOI: 10.1002/ctpp.202100172)

2) **Multi-staged ERO2.0 simulation of material erosion and deposition in recessed ITER mirror assemblies** by S. Rode, S. Brezinsek, A. Kirschner, L. Moser, R.A. Pitts, J. Romazanov, A. Terra, T. Wauters and S. Wiesen, published in *Nuclear Materials and Energy* on 05 December 2023 (DOI: 10.1016/j.nme.2023.101564)

3) **Multi-staged ERO2.0 simulation of material erosion and deposition in recessed mirror assemblies in JET and ITER** by S. Rode, S. Brezinsek, M. Groth, A. Kirschner, D. Matveev, L. Moser, R.A. Pitts, J. Romazanov, A. Terra, T. Wauters and S. Wiesen, published in *Nuclear Fusion* on 25 June 2024 (DOI: 10.1088/1741-4326/ad556d)

The author of this thesis performed the ERO2.0 simulations, main data analysis and code optimizations in these publications. All plasma backgrounds used were based on existing plasma solutions, and the EIRENE post-processing step was performed by the EIRENE experts Sven Wiesen and Mathias Groth. As the first author, the production of all figures and the writing of the manuscripts were conducted by the author of this thesis. Both text and figures from these publications are used either in their original or adapted form throughout this thesis without explicit citation. This mostly involves parts of chapter 4 for publication 1), chapter 5 for publication 2), and chapter 6 for publication 3).

Acknowledgements

This work benefited from HPC resources from CINECA Marconi-Fusion projects FUA34_WPJET1, FUA35_WPJET1, and FUA36_WPJET1.

The authors gratefully acknowledge the computing time granted by the JARA Vergabegremium and provided on the JARA Partition part of the supercomputer JURECA at Forschungszentrum Jülich.

Parts of this work have been carried out within the framework of the EUROfusion Consortium, funded by the European Union via the Euratom Research and Training Programme (Grant Agreement No 101052200—EUROfusion). Views and opinions expressed are those of the author(s) and do not necessarily reflect those of the European Union or the European Commission. Neither the European Union nor the European Commission can be held responsible for them.

Parts of this work have been carried out within the framework of an ITER service contract with the ID IO/20/CT/4300002242. The views and opinions expressed herein do not necessarily reflect those of the ITER Organization.

Usage of generative AI tools

AI-based writing tools were used in the following scope for this work:

- *DeepL* for the first translation of the abstract into the German language, with subsequent manual checking and editing by the author
- *LanguageTool* for a final check of grammar and punctuation throughout the otherwise finished thesis

No full-text sections were produced by the use of generative AI tools for this work.

Danksagung

Im Zuge dieser Arbeit durfte ich mit unzähligen fantastischen Personen zusammenarbeiten und meine Zeit verbringen, die ich leider im folgenden nicht alle nennen kann. Mein besonderer Dank gebührt aber folgenden Menschen:
Dr. Juri Romazanov, meinem täglichen Betreuer während der Doktorarbeit – für die immerwährende Hilfe, das Korrekturlesen dieser Arbeit, den Optimismus, die zahlreichen Ideen und die coole Zeit innerhalb und außerhalb des FZJ.
Prof. Dr. Sebastijan Brezinsek, meinem Doktorvater – der einfach alles über Fusionsplasmen weiß und ohne den heute vermutlich (i) die Plasmaphysik nicht auf demselben Stand wäre, und (ii) ich nicht am FZJ wäre.
Den weiteren Mitgliedern des ERO2.0-Teams am FZJ: Dr. Christoph Baumann, Dr. Andreas Kirschner, Dr. Dmitry Matveev und Dr. Henri Kumpulainen – für die tolle Atmosphäre im Team (wie war das nochmal, sind wir jetzt ein Team oder eine Gruppe?!) und die zahlreichen fruchtbaren Diskussionen und Ratschläge.
Dr. Sven Wiesen und Dr. Mathias Groth – für die Simulation der EIRENE Spektren im Zuge dieser Arbeit und Hilfe bei Nachfragen, und weiterhin Dr. Derek Harting – für das weitere Verständnis von EIRENE und die angenehme Zusammenarbeit im EIRENE-KIT/ERO2.0-Benchmark.
Dr. Richard Pitts, Dr. Tom Wauters, and Dr. Lucas Moser from the ITER Organization – for the fruitful discussions during the progress meetings.
Den restlichen Doktoranden des IFN-1 – für die positive Stimmung auch in oft komplizierten Lagen, und die schönen Erlebnisse auf Reisen.
Weiterhin danke ich:
Meinen Eltern, die immer alles daran gesetzt haben, mir meinen Weg zu ermöglichen, und mir immer Hilfe und Geborgenheit bieten.
Meiner Schwester, und meinem Freund, die mich auch in den schlimmsten Zeiten der Doktorarbeit erleben mussten und nicht weggerannt sind.
Und zuletzt meinen Freunden, die ich monatelang vernachlässigen musste, die aber immer wieder für Lichtblicke in der Dunkelheit sorgen konnten.

Danke euch allen! Thank you everyone!

Band / Volume 669
Quantifying Recombination Losses and Charge Extraction in Halide Perovskite Solar Cells
L. Krückemeier (2025), vi, 286 pp
ISBN: 978-3-95806-835-3

Band / Volume 670
Investigation of Dynamic Material Changes During the Preparation of ZnPd Nanoparticles Supported on ZnO and their Catalytic Application in Methanol Steam Reforming on the Atomic Level
A. Meise (2025), xviii, 175 pp
ISBN: 978-3-95806-838-4

Band / Volume 671
Improving Energy Efficiency of Public Buildings by Influencing Occupant Behaviour using Dashboards and Gamification
E. Ubachukwu (2025), xxi, 191 pp
ISBN: 978-3-95806-840-7

Band / Volume 672
Exploring Plant Responses to Changing Environments: Integrating Phenotyping and Modeling Across Scales
F. M. Bauer (2025), xxix, 188 pp
ISBN: 978-3-95806-845-2

Band / Volume 673
A constitutive theory to represent non-idealities in contacting of SOC interconnect contacts
R. M. Pinto (2025), xii, 139 pp
ISBN: 978-3-95806-846-9

Band / Volume 674
Strontium titanate based materials for use as oxygen transport membranes in membrane reactors
Y. Tang (2025), XIV, 132 pp
ISBN: 978-3-95806-849-0

Band / Volume 675
Scaling Methods for the Production of Tungsten Fiber-Reinforced Composites via Chemical Vapor Deposition
A. Lau (2025), untersch. Pag.
ISBN: 978-3-95806-851-3

Band / Volume 676
Nanoscale analysis of high-temperature oxidation mechanisms of Cr_2AlC MAX phase and W-Cr-Y self-passivating tungsten alloy
A.J. S. Reuban (2025), ix, 142 pp
ISBN: 978-3-95806-855-1

Band / Volume 677
First principles simulations of high-entropy materials for energy storage
Y. Ting (2025), xviii, 169 pp
ISBN: 978-3-95806-858-2

Band / Volume 678
Deployment of Fuel Cell Vehicles in Road Transport and the Expansion of the Hydrogen Refueling Station Network
T. Grube, M. Sander (2025), iv, 61 pp
ISBN: 978-3-95806-859-9

Band / Volume 679
Entwicklung von nickelbasierten katalysatorbeschichteten Diaphragmen für die alkalische Wasserelektrolyse
C. B. Karacan (2025), 146 pp
ISBN: 978-3-95806-860-5

Band / Volume 680
Bewertung lokaler Eigenspannungsverteilungen bei der lokalen Bauteilreparatur durch Kaltgasspritzen
J.-C. Schmitt (2025), 154, xxvii pp
ISBN: 978-3-95806-861-2

Band / Volume 681
First principles study of the effect of substitution\doping on the performance of layered oxide cathode materials for secondary batteries
N. Yacoob (2025), iii, 126 pp
ISBN: 978-3-95806-864-3

Band / Volume 682
Field assisted sintering technology/spark plasma sintering in the direct recycling of hot-deformed Nd-Fe-B scrap and PM T15 steel swarf
M. T. M. Keszler (2025), viii, 173 pp
ISBN: 978-3-95806-866-7

Band / Volume 683
Assessment of erosion in recessed areas of fusion devices using multi-scale computer simulations
S. Rode (2025), viii, 196 pp
ISBN: 978-3-95806-867-4

Weitere ***Schriften des Verlags im Forschungszentrum Jülich*** unter
http://wwwzb1.fz-juelich.de/verlagextern1/index.asp

Energie & Umwelt / Energy & Environment
Band / Volume 683
ISBN 978-3-95806-867-4

Mitglied der Helmholtz-Gemeinschaft

JÜLICH
Forschungszentrum